Multi-Scale Life Cycle Design of Synthetic Fuels for Sustainable Mobility

Multiskalen Lebenszyklusdesign synthetischer Kraftstoffe für nachhaltige Mobilität

Von der Fakultät für Maschinenwesen der
Rheinisch-Westfälischen Technischen Hochschule Aachen
zur Erlangung des akademischen Grades eines Doktors
der Ingenieurwissenschaften genehmigte Dissertation

vorgelegt von

Simon Völker

Berichter: Univ.-Prof. Dr.-Ing. Niklas von der Aßen
Univ.-Prof. Dr.-Ing. André Bardow
Univ.-Prof. Dr. rer. nat. Walter Leitner

Tag der mündlichen Prüfung: 6. Dezember 2024

Aachener Beiträge zur Technischen Thermodynamik Band 55

Simon Völker
Multi-Scale Life Cycle Design of Synthetic Fuels for Sustainable Mobility

Multiskalen Lebenszyklusdesign synthetischer Kraftstoffe für nachhaltige Mobilität

ISBN: 978-3-95886-544-0

Bibliografische Information der Deutschen Bibliothek
Die Deutsche Bibliothek verzeichnet diese Publikation in der Deutschen Nationalbibliografie; detaillierte bibliografische Daten sind im Internet über http://dnb.ddb.de abrufbar.

Herstellung & Vertrieb:

1. Auflage 2025
© Wissenschaftsverlag Mainz GmbH - Aachen
Süsterfeldstr. 83, 52072 Aachen
Tel. 0241 / 87 34 34 00
www.Verlag-Mainz.de

ISSN: 2198-4832

Satz: nach Druckvorlage des Autors
Umschlaggestaltung: Druckerei Mainz

printed in Germany
D82 (Diss. RWTH Aachen University, 2024)

Danksagung

Die vorliegende Arbeit entstand im Rahmen meiner Tätigkeit als wissenschaftlicher Mitarbeiter am Lehrstuhl für Technische Thermodynamik der RWTH Aachen. Besonders danke ich meinem Doktorvater, Prof. Dr.-Ing. Niklas von der Aßen, für die hervorragende Betreuung. Danke für dein Vertrauen, deine wertvollen Anregungen und deine Unterstützung während der letzten Jahre. Weiterhin danke ich Prof. Dr.-Ing. André Bardow für das konstruktive Feedback, die anhaltende Unterstützung trotz des Wechsels an die ETH Zürich, sowie die Übernahme des Koreferats. Herrn Prof. Dr. rer. nat. Walter Leitner danke ich für die intensive und spannende Zusammenarbeit im Zuge des HyFiT-Papers und die Übernahme des Koreferats. Zudem danke ich Prof. Dr.-Ing. Jakob Andert für die Übernahme des Prüfungsvorsitzes.

Mein besonderer Dank gilt meinen aktiven und ehemaligen Kollegen am LTT für die schönen Jahre am Lehrstuhl, die mir durch die vielen fachlichen und persönlichen Gespräche und das grandiose Arbeitsklima in besonderer Erinnerung bleiben werden. Insbesondere möchte ich mich auch bei meiner Arbeitsgruppe, der Energiesystemtechnik, für die tolle Zeit bedanken. Bei Sarah von Pfingsten bedanke ich mich für die Zusammenarbeit im Zuge meiner ersten HiWi-Stelle am Lehrstuhl, die mir in der Folge die spannenden Forschungsthemen des LTT eröffnet hat. Ein riesiges Dankeschön geht an Leonard Müller und Sarah Deutz für die Unterstützung, das kritische Feedback und die motivierenden Gespräche während meiner gesamten Promotion. Meinen ehemaligen Bürokollegen Hesam Ostovari, Sarah Deutz, Hannah Minten, Dörthe Hagedorn und Benedikt Nilges danke ich besonders herzlich für das tolle Büroklima und die vielen Gespräche. Bei Dörthe Hagedorn und Benedikt Nilges möchte ich mich außerdem für die gemeinsame Zeit als Gruppenleitung der E$T bedanken.

Außerdem möchte ich meinen Studis für Ihren Beitrag zu meiner Forschung danken. Insbesondere Niklas Groll und Marcel Granderath haben maßgeblich zum Gelingen dieser Arbeit beigetragen.

Zuletzt gilt mein größter Dank meiner Familie. Von ganzem Herzen danke ich meinen Eltern, Gabi und Frank, sowie meiner Schwester Judith. Ihr habt mich stets motiviert und aufgebaut und wart immer für mich da. Meinem Sohn Levi danke ich für das Glück, was er mir jeden Tag schenkt. Abschließend möchte ich meiner Frau Theresa danken: Danke für deine bedingungslose Unterstützung und dafür, dass du immer an meiner Seite bist. Danke für alles!

Köln, im März 2025 *Simon Völker*

'Whatever it is you're seeking
won't come in the form you're expecting.'

Haruki Murakami
"Kafka on the Shore" (2005)

Contents

List of Figures

List of Tables

Notation

Abbreviations and acronyms

A	acidification
abs	absolut
ADU	atmospheric distillation unit
AFIDA	advanced fuel ignition delay analyzer
aq	aqueous
ASF	Anderson-Schulz-Flory
ASTM	American Society for Testing and Materials
B2L	biomass-to-liquid
BECCS	bioenergy carbon capture and storage
BEV	battery-electric vehicle
CAaTDC	crank angle after top dead center
CAN	Canada
CCS	carbon capture and storage
CCU	carbon capture and utilization
CDR	carbon dioxide removal
CEPCI	chemical engineering plant cost index
CF	carbon footprint
CFB	circulating fluidized bed
CGSB	Canadian General Standards Board
CH	Switzerland
COP	coefficient of performance
DAC	direct air capture
DACCS	direct air carbon capture and storage
DB	displacement body
DCN	derived cetane number
DOC	diesel oxidation catalyst
DOE	design of experiment

DPF	diesel particulate filter
E_{fw}	eutrophication, freshwater
E_m	eutrophication, marine
E_t	eutrophication, terrestrial
EATS	exhaust gas aftertreatment system
EF	environmental footprint
EGR	exhaust gas recirculation
EI	environmental impact
EN	European standard (German: Europäische Norm)
EO	engine-out
EPA	Environmental Protection Agency
ET	ecotoxicity, freshwater
EU	European Union
FAME	fatty acid methyl ester
FC	fuel cell
FCEV	fuel cell electric vehicle
FKM	fluorine rubber
FR	France
FT	Fischer-Tropsch
GB/T	national standard of the People's Republic of China (Chinese: Guobiao)
GHG	greenhouse gas
GOST	governmental standard (Russian: gosudarstvennyy standart)
GWI	global warming impact
HFRR	high frequency reciprocating rig
HNBR	hydrogenated nitrile butadiene rubber
HT_c	human toxicity, carcinogenic
HT_{nc}	human toxicity, non-carcinogenic
HT-Aq	high-temperature aqueous solution
HT-FT	high-temperature Fischer-Tropsch
HVO	hydrogenated vegetable oil
HyFiT	hydroformylated Fischer-Tropsch
ICE	internal combustion engine
IEA	International Energy Agency
iLUC	indirect land-use change
Imep	indicated mean effective pressure
IR	ionizing radiation, human health
IS	Indian standard

ISO	International Organization for Standardization
JIS	Japanese industrial standard
LCA	life cycle assessment
LCI	life cycle inventory
LCIA	life cycle impact assessment
LH_2	liquefied hydrogen
LHV	lower heating value
LOHC	liquid organic hydrogen carrier
LPG	liquefied petroleum gas
LT-FT	low-temperature Fischer-Tropsch
LU	land use
LUC	land-use change
m-FTS	modified Fischer-Tropsch synthesis
MAA	Modeling All Alternatives
max	maximal
MGA	Modeling to Generate Alternatives
MILP	mixed-integer linear programming
min	minimal
MOP	multi-objective optimization problem
NBR	nitrile butadiene rubber
NDC	nationally determined contribution
NET	negative emissions technology
NLP	nonlinear program
NMVOC	non-methane volatile organic compounds
NO	Norway
OD	ozone depletion
P2G	power-to-gas
PCA	principal component analysis
PEM	polymer electrolyte membrane
PM	particulate matter
PNFA	process network flux analysis
POF	photochemical ozone formation
PV	photovoltaic
RE	respiratory effects
RED II	renewable energy directive II
RNFA	reaction network flux analysis
RU_e	resource use, energy carriers
RU_m	resource use, minerals and metals

SAF	sustainable aviation fuel
SANS	South African national standard
SCE	single-cylinder engine
SCR	selective catalytic reduction
SMR	steam methane reforming
SOC	state of charge
ST	solar-thermal
TEA	techno-economic assessment
TP	tailpipe
TRL	technology readiness level
TSA	temperature swing adsorption
UHEE	ultra-high efficiency engine
UNEP	United Nations Environment Programme
US	United States
VDU	vacuum distillation unit
VGO	vacuum gas oil
VOC	volatile organic compound
vol	volume
WLTC	worldwide harmonized light vehicles test cycle
WLTP	worldwide harmonized light vehicles test procedures
WSD	wear scar diameter
wt	weight
WU	water use

Chemicals

C_1-C_4	tail gas cut
C_5-C_{10}	naphtha cut
C_{11+}	distillate cut
CH_4	methane
C_3H_8	propane
C_nH_{2n}	generic olefin of chain length n
$C_nH_{2(n+1)}$	generic alkane of chain length n
$C_nH_{2n}O$	generic aldehyde of chain length n
$C_nH_{2n+1}OH$	generic alcohol of chain length n
CO	carbon monoxide
CO_2	carbon dioxide

DME	dimethyl ether
DMM	dimethoxymethane (OME_1)
FA	formaldehyde
H_2	hydrogen
H_2O	water
HC	hydrocarbon
KEAA	ketone-ester-alcohol-alkane
MeOH	methanol
2-MTHF	2-methyltetrahydrofuran
NO_x	nitrogen oxides
O_2	oxygen
OME_n	polyoxymethylene dimethyl ethers of chain length n
TRI	trioxane

Latin symbols

a	project lifetime
b	by-product flux
BR	blending ratio
C	production cost
cap	capacity
CM	correlation matrix
$Conv$	conversion
COP	coefficient of performance
e	energy consumption
E	energy
$\dot{E}$	exergy flow
ei	specific environmental impact factor
EI	environmental impact
f	feedstock flux
F	force
FC	fuel consumption
g	gravitational constant
H	enthalpy
H_u	lower heating value
IC	investment costs

ir	interest rate
k	objective subset size
LHV	lower heating value
m	mass
M	molar mass
$MILEAGE$	mileage
n, N	number
OB	number of omitted objectives
OF	objective function value
P	power
PR	price parameter
q	size of the objective space
Q	heat consumption
$\dot{Q}$	heat flow
r	waste flux
$r_{X_1X_2}$	Pearson correlation coefficient for two variables X_1 and X_2
s	distance
$Selec$	selectivity
$SHARE$	share
SOC	state of charge
T	temperature
V	volume
w	work, specific
W	work
WSD	wear scar diameter
x	mole fraction
y, Y	mass fraction
$Yield$	yield
YP	auxiliary binary variable for objective reduction
ZD	auxiliary binary variable for objective reduction
ZO	auxiliary binary variable for objective reduction
ZOD	auxiliary binary variable for objective reduction

Greek symbols

α	chain growth probability
β	annual fuel production

δ	δ-error
Δ	difference
η	efficiency
λ	air–fuel equivalence ratio
μ	friction coefficient
ρ	density

Subscripts

avg	average
Batt	battery
boil	boiling
C	carbon
Ch	charging
comb	combustion
cycle	driving cycle
Dch	discharging
el	electrical
eq	equivalent
feedstock	feedstock
filtered	filtered
grav	gravitational
in	input
initial	initial
invest	investment
L	liquid
meas	measured
min	minimal
norm	normalized
OB	number of omitted objectives
prod	product
reac	reaction
reduced	reduced
refinery	refinery
rel	relative
S	sample
sep	separation

spec	specific
tan	tangential
total	total
transfer	transferred
util	utility
utils	utilities
VGO	vacuum gas oil
vol	volumetric
waste	waste disposal

Superscripts

avg	average
EU	European Union
future	'future' scenario
max	maximum
norm	normalized
today	'today' scenario
$*$	threshold

Sets

$i \in F$	set of objectives
$m \in EI$	set of environmental impacts
$s \in S$	set of solutions

Kurzfassung

Der Verkehrssektor gehört zu den Hauptemittenten von Treibhausgasemissionen, was die Abkehr von der Verbrennung fossiler Kraftstoffe hin zur Integration erneuerbarer Energien erfordert. Während die Integration erneuerbarer Energien mittels direkter Elektrifizierung am sinnvollsten ist, sind einige Teilsektoren des Verkehrs nur schwer direkt zu elektrifizieren. Für diese Teilsektoren stellen synthetische Kraftstoffe eine vielversprechende Ergänzung zur direkten Elektrifizierung dar. Die vermuteten Umweltvorteile synthetischer Kraftstoffe bedürfen jedoch umfassender Validierung. Diese Arbeit unterstützt daher die Ökobilanz und das Design synthetischer Kraftstoffe, indem sie Forschungsfragen beim *Screening*, der *Auswahl* und der *Verteilung* adressiert.

Für das *Screening* identifizieren wir diejenigen ökologischen Zielfunktionen, die die wichtigsten Zielkonflikte im integriertem Prozess- und Kraftstoffdesign abdecken. Ein ganzheitliches Kraftstoffdesign mit vertretbarem Rechenaufwand ist bereits mit den drei Zielfunktionen Landnutzung, Mineralien- und Metallverbrauch sowie Produktionskosten möglich. Das integrierte Kraftstoffdesign mit diesen Zielfunktionen zeigt, dass Bio-Hybridkraftstoffe die Zielkonflikte reiner Bio- und E-Kraftstoffe reduzieren.

Von den *gescreenten* Kraftstoffen sollten nur diejenigen für detailliertere Analysen *ausgewählt* werden, die vier zentrale Herausforderungen aktueller synthetischer Kraftstoffe adressieren. Unsere Studie zu hydroformylierten Fischer-Tropsch (HyFiT) Kraftstoffen zeigt, dass HyFiT-Kraftstoffe diese vier Herausforderungen erfüllen können: Sie (1) sind skalierbar durch die Nutzung reifer Technologien, (2) sind kompatibel mit Kraftstoffstandards und aktueller Motorentechnologie, (3) reduzieren Luftschadstoffe und (4) ermöglichen den Übergang zu netto-null Treibhausgasemissionen.

Die *ausgewählten* synthetischen Kraftstoffe könnten in Flotten als reine Kraftstoffe an nur wenige oder als Blend mit fossilem Kraftstoff an alle Fahrzeuge *verteilt* werden. Unsere Flottenanalyse demonstriert, dass die ökologisch optimale Verteilung davon abhängt, wie sich die Verbrennungsemissionen mit steigender Blendrate entwickeln. Die Analyse von Polyoxymethylendimethylether der Kettenlänge drei bis fünf ($OME_{3\text{-}5}$) zeigt, dass die Verteilung als Blend mit fossilem Kraftstoff dann optimal ist, wenn die Verbrennungsemissionen mit steigender Blendrate überproportional sinken.

Abstract

Global transport is among the main emitters of greenhouse gas (GHG) emissions, requiring a paradigm shift away from burning fossil fuels towards integrating renewable energy. While renewable energy integration via direct electrification is most sensible, some transport subsectors are hard to electrify directly: aviation, shipping, and long-haul heavy-duty trucks. For these subsectors, renewable synthetic fuels pose promising complements for direct electrification. However, the environmental benefits of synthetic fuels are not a given and require thorough validation. Therefore, this thesis guides the life cycle assessment and design of synthetic fuels by addressing major research questions in the *screening*, *filtering*, and *distribution* of synthetic fuels.

For synthetic fuel *screening*, we identify those key environmental objectives that cover the major trade-offs of integrated process and fuel design. Our findings suggest that the objectives land use, resource use of minerals and metals, and production cost are sufficient to design spark-ignition engine fuels holistically but with manageable computational cost. Integrated process and fuel design with these objectives reveals that bio-hybrid fuels can balance the burden-shifting of pure bio- and e-fuels.

The group of synthetic fuels obtained from *screening* has to be further narrowed by *filtering* out only those for more detailed analyses that address the four key challenges of current synthetic fuels. Our study on hydroformylated Fischer-Tropsch (HyFiT) fuels demonstrates that HyFiT-fuels can fulfill these key challenges simultaneously: they (1) are scalable by using mature technologies, (2) are compatible with fuel standards and current engine technology, (3) reduce urban air pollutants, and (4) enable the transition to net-zero GHG emissions.

In a fleet, the *filtered* out synthetic fuels could be *distributed* either as pure fuels to few or as blends with fossil fuel to all vehicles. Our fleet analysis shows that the environmentally optimal distribution depends on how combustion emissions develop with increasing blending ratios. For polyoxymethylene dimethyl ethers of chain length three to five ($OME_{3\text{-}5}$), distribution as a blend is optimal since increasing blending ratios of $OME_{3\text{-}5}$ in diesel decrease combustion emissions disproportionately strong.

Chapter 1

Introduction

Climate change mitigation is arguably one of the main challenges of this century. The primary reason for climate change are greenhouse gas (GHG) emissions, predominantly carbon dioxide (CO_2), due to the burning of fossil fuels, i.e., coal, gas, and oil (UNEP, 2022). As a consequence, the global surface temperature is already today, on average, around 1.3 °C above the pre-industrial levels, and GHG emissions have not even peaked yet (IEA, 2023c). Many nations have, therefore, adopted national climate policies to mitigate climate change. Although these climate policies are already bearing fruit, e.g., investment in clean energy technologies rose by 40 % since 2020, limiting global warming to 1.5 °C requires much more ambition in the coming years (IEA, 2023c).

In this context, Ban Ki-moon, the former secretary-general of the United Nations, remarked at the *Climate Summit 2014*:

> *'Climate change is the single greatest threat to a sustainable future. But, at the same time, addressing the climate challenge presents a golden opportunity to promote prosperity, security and a brighter future for all.'*
>
> Ban Ki-moon,
> 8th secretary-general of the United Nations,
> remarks at the *Climate Summit 2014*

Most GHG emissions are emitted in the energy, industry, transport, and agriculture sectors (UNEP, 2020). Around 15 % of these GHG emissions stem from today's global transport sector (Jaramillo et al., 2022). Road vehicles are by far the greatest emitters with 70 % of the transport sector's global GHG emissions, followed by aviation and shipping with 12 % and 11 %, respectively. Additionally, global transport demands are growing, e.g., freight transport by around 70 % between 2000 and 2015, with even

larger growth projected for the coming decades (Jaramillo et al., 2022). Thus, large reductions of GHG emissions are necessary, which require turning away from fossil fuel use towards integration of renewable energy.

Faster expansions of renewables and electrification are considered key measures to accelerate climate change mitigation (IEA, 2023b). In transportation, scarce renewable energy is used most efficiently by direct electrification in electric vehicles (Agora Verkehrswende, 2017). Today, global sales of electric vehicles are already steeply rising and have surpassed 13 % of the car market in 2022 (IEA, 2023a). However, hard-to-electrify transport subsectors, such as aviation, shipping, and long-haul heavy-duty trucks, are anticipated to remain partly reliant on liquid energy carriers with high energy density (Shukla et al., 2022). Furthermore, it is to be expected that at least a small proportion of passenger cars will remain vehicles with internal combustion engines.

For these hard-to-electrify subsectors, viable options to mitigate GHG emissions and climate change are synthetic fuels. Synthetic fuels can be produced bio-based, using biogenic carbon sources (Leitner et al., 2017), or electricity-based, electrifying these transport subsectors indirectly. Electricity-based fuels can be carbon-free, e.g., hydrogen and ammonia, or carbon-based, e.g., methanol. For electricity-based synthetic fuels containing carbon, CO_2 is captured and used as a feedstock (Artz et al., 2018), which is called carbon capture and utilization (CCU). Besides their use in mobility applications, synthetic fuels can also be used for long-term storage of renewable energy, bridging temporal and spatial gaps between high energy demand and low renewable energy supply (Baumgärtner et al., 2021).

Environmental benefits such as climate change mitigation are, however, not given and require thorough validation. For this purpose, the standardized methodology of life cycle assessment (LCA) is commonly used (ISO, 2006a,b). LCA evaluates a wide range of environmental impacts along the entire life cycle, quantifying burden-shifting between life cycle stages and impact categories. Using LCA in model-based fuel design, environmental impacts of synthetic fuels can be minimized already at early development stages.

However, the current assessment practice of synthetic fuels lacks an overarching approach that guides synthetic fuel design in different stages. In early-stage model-based fuel design, identifying key environmental objectives covering the major burden shifts would be desirable to design synthetic fuels holistically but with manageable computational cost. Since model-based fuel design presents many promising synthetic fuels, this group of fuels has to be further narrowed by more detailed analyses. These analyses should check whether the key challenges of current synthetic fuels are ad-

dressed. Thereafter, synthetic fuels fulfilling these key challenges could be distributed either as pure fuel or as blend with fossil fuel to vehicle fleets. From an environmental perspective, the optimal distribution is still to be derived.

In this thesis, we[1] provide an LCA-based fuel design procedure that aims to support the design and deployment of renewable synthetic fuels for the transport sector. Herein, we apply this procedure to synthetic fuels for road applications. The procedure comprises three stages with each stage spanning different model scales. In the first stage, the *screening* of synthetic fuels, we identify which environmental impact categories are key for early-stage model-based fuel design. The *filtering* stage further narrows the group of promising synthetic fuels obtained from *screening*. Only those fuels are *filtered* out for further studies that can overcome the key challenges of current synthetic fuels. In the last stage, we determine the environmentally optimal *distribution* of limited amounts of synthetic fuels in vehicle fleets.

1.1 Structure of this thesis

This thesis is structured in six chapters. In **Chapter 2**, we give an overview of the state of the art in life cycle assessment and design of synthetic fuels. We begin with describing the transport sector's transformation from fossil fuels towards electrification complemented by synthetic fuels. Subsequently, fundamentals of life cycle assessment and a model-based framework for integrated process and fuel design are described. Next, recent scientific literature on the life cycle assessment and design of synthetic fuels is reviewed with focus on road transport. Based on the literature review, scientific gaps are identified in the recent assessment practice. Lastly, the contribution of this thesis is outlined, describing how the identified scientific gaps can be narrowed with the three-stage fuel design procedure proposed herein.

In **Chapter 3**, key environmental objectives are identified for the early-stage screening of synthetic fuels. For this purpose, an existing fuel design framework is extended to include a wide range of environmental impact categories as additional objectives to production cost. The key environmental objectives are subsequently identified, using a dominance-based optimization approach. Lastly, synthetic fuels are generated by multi-objective optimization with the identified key objectives.

[1] This thesis is written in the *pluralis modestiae*, first to avoid the excessive use of passive voice and second to emphasize that the research behind this thesis is done in collaboration with colleagues and my supervisor. The contribution of the author is pointed out at the beginning of each chapter.

Chapter 4 narrows the group of synthetic fuels obtained from the early-stage screening in Chapter 3. For this purpose, key challenges of synthetic fuels are outlined to filter out those synthetic fuels by more detailed analyses that can contribute to accelerating the transition towards clean transportation. The key challenges are evaluated on the example of hydroformylated Fischer-Tropsch (HyFiT) fuels, illustrating that tailored synthetic fuels can address all key challenges simultaneously.

In **Chapter 5**, the focus is on distributing synthetic fuels to existing vehicle fleets. The production volume of synthetic fuels can be expected to be limited by feedstock availability in the coming decades. Consequently, limited amounts of synthetic fuel could be distributed either as blend with fossil fuel to all vehicles or as pure fuel to only few vehicles in a fleet. The environmentally optimal distribution is analyzed on the example of the synthetic fuel polyoxymethylene ether of chain length three to five ($OME_{3\text{-}5}$).

Finally, **Chapter 6** summarizes the thesis and draws conclusions on each chapters' findings. The thesis concludes with perspectives for future research.

Chapter 2

State of the art in life cycle assessment and design of synthetic fuels

This chapter gives a general overview about the role of synthetic fuels in transforming the transport sector as well as the environmental assessment and design of synthetic fuels. Section 2.1 outlines the transport sector's transformation from fossil fuels towards electrification complemented by synthetic fuels. In Section 2.2, we describe the methodology of LCA and a model-based framework for integrated process and fuel design. This section also includes a literature review of recent assessments and fuel design studies on synthetic fuels and outlines the identified scientific gaps. Lastly, Section 2.3 discusses the contribution of this thesis with respect to the identified scientific gaps.

Parts of this chapter are reproduced by permissions of the Royal Society of Chemistry and Springer Nature from:

Völker, S., Ackermann, P., Granderath, M., Kortmann, C., Viell, J., Mitsos, A., and von der Aßen, N. (2024). Identifying key environmental objectives for integrated process and fuel design. *Sustainable Energy & Fuels*, **8**(9), 1966-1982.

Völker, S., Groll, N., Bachmann, M., Müller, L., Neumann, M., Kossioris, T., Muthyala, P., Lehrheuer, B., Hofmeister, M., Vorholt, A., Schmitz, K., Pischinger, S., Leitner, W., and Bardow, A. (2024). Towards carbon-neutral and clean propulsion in heavy-duty transportation with hydroformylated Fischer-Tropsch fuels. *Nature Energy*, **9**(10), 1220-1229.

Völker, S., Deutz, S., Burre, J., Bongartz, D., Omari, A., Lehrheuer, B., Mitsos, A., Pischinger, S., Bardow, A., and von der Aßen, N. (2022). Blend for all or pure for few? Well-to-wheel life cycle assessment of blending electricity-based OME_{3-5} with fossil diesel. *Sustainable Energy & Fuels*, **6**(8), 1959-1973.

2.1 Transforming the transport sector

This sections starts with a description of today's fossil-based transport sector as part of the *linear carbon economy* (Section 2.1.1). Thereafter, the role of synthetic fuels is outlined as a complement to electrification in transforming the transport sector towards a *low-carbon economy* (Section 2.1.2). For this transformation, two pathways are discussed: a *carbon-free* and a *circular carbon pathway*.

2.1.1 Present transport sector: fossil fuels and rising electrification

Today's transport sector relies predominantly on the use of fossil fuels, satisfying transportation demands to move passengers and goods (IEA, 2023c). In 2022, the total final energy consumption of the global transport sector amounted to 116 EJ comprising 91 % oil, 4 % natural gas, 4 % biofuels, and only 1 % electricity (Figure 2.1A). Among transport subsectors, 76 % of this final energy is consumed by road transport, followed by aviation and shipping with 10 % each (Figure 2.1B). Noticeably, global transport activities are projected to increase even further: transport by passenger cars, heavy-duty trucks, and shipping is projected to double while aviation activities are estimated to triple until 2050 (Figure 2.1C).

On a global scale, oil refineries produce around 4 Gt of oil derivatives to satisfy primarily the large fossil fuel consumption of the transport sector (IEA, 2021). Of

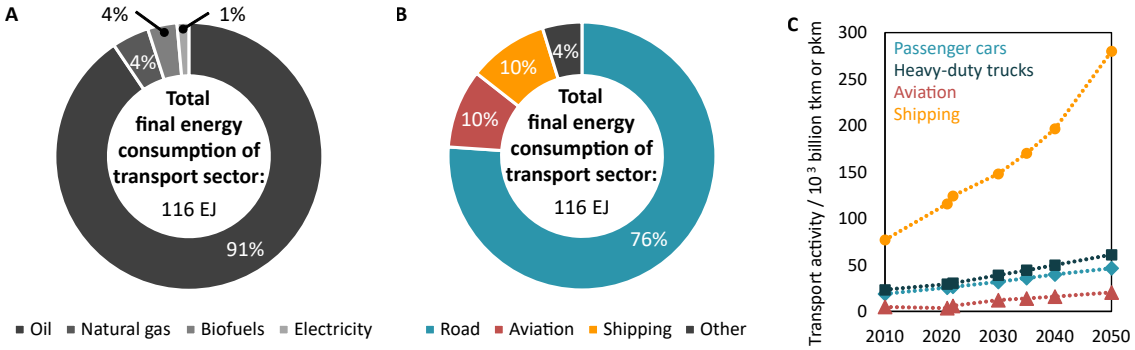

Figure 2.1: Total final energy consumption and transport activity of the global transport sector, adapted from IEA (2023c). The total final energy consumption in 2022 is shown by (A) energy carrier and (B) subsector. (C) The current and projected transport activity is shown by subsector in 10^3 billion tonnes-km (shipping, heavy-duty trucks) and passenger-km (passenger cars, aviation), respectively.

these oil derivatives, diesel and gasoline account for 60 % while fuel oil and aviation fuels amount to 20 % in 2019.

The oil derivatives are produced by a sequence of several processes of which the atmospheric distillation unit (ADU) and vacuum distillation unit (VDU) are the most important units (Riazi et al., 2013). In the ADU, the crude oil is separated into the liquefied petroleum gas (LPG), naphtha, kerosene, light- and heavy-gas oil fractions, according to their boiling ranges. The atmospheric residue of the ADU is further fractionated in the VDU, producing vacuum gas oils and vacuum residue. To meet product specifications, ADU products undergo further finishing processes, e.g., hydrotreating, and blending, whereas vacuum gas oil (VGO) products require additionally a series of conversion processes, e.g., hydrocracking.

Owing to its reliance on fossil fuels, the present transport sector is part of what is termed the *linear carbon economy* (Figure 2.2). In the *linear carbon economy*, products are produced from finite fossil-based carbon feedstocks that have been extracted from underground (Meys et al., 2021). Thus, fossil carbon is incorporated into products such as fuels. At the product's end of life, this carbon is ultimately released to the atmosphere as CO_2 emission, e.g., through fuel combustion, contributing to climate change. As a consequence of burning fossil fuels, the transport sector therefore contributes to the depletion of fossil resources and emits large amounts of GHG emissions. With around 8 Gt CO_2 eq., the transport sector emits, in fact, third-most GHG emissions after the energy and industry sectors, according to UNEP (2020). Road transport is primarily responsible for these GHG emissions (74 %), followed by international (16 %) and non-road transport (10 %) (UNEP, 2020).

Besides GHG emissions, the transport sector is also among the main contributors to air pollution. The Environmental Protection Agency (EPA) of the United States (US) reports that highway vehicles and non-road mobile sources, e.g., marine vessels and planes, emit around half of all carbon monoxide (CO) and nitrogen oxides (NO_x) emissions, followed by around 10 % to 15 % of particulate matter (PM) and volatile organic compound (VOC) emissions in the US (Figure 2.3). In urban environments, road transport is reported as the major source of PM and NO_x emissions (European Environment Agency, 2018), causing risks to human health. In addition to fuel combustion, road dust as well as tyre and brake wear add on top of these emissions.

Reducing both GHG emissions and air pollution of the transport sector requires a paradigm shift away from fossil fuels towards the integration of renewable energy (IEA, 2023c). Governments' national energy and climate targets aim to accelerate this shift with so-called nationally determined contributions (NDCs) as well as long-term and net-zero pledges (UNEP, 2022). Although this shift is already ongoing, e.g.,

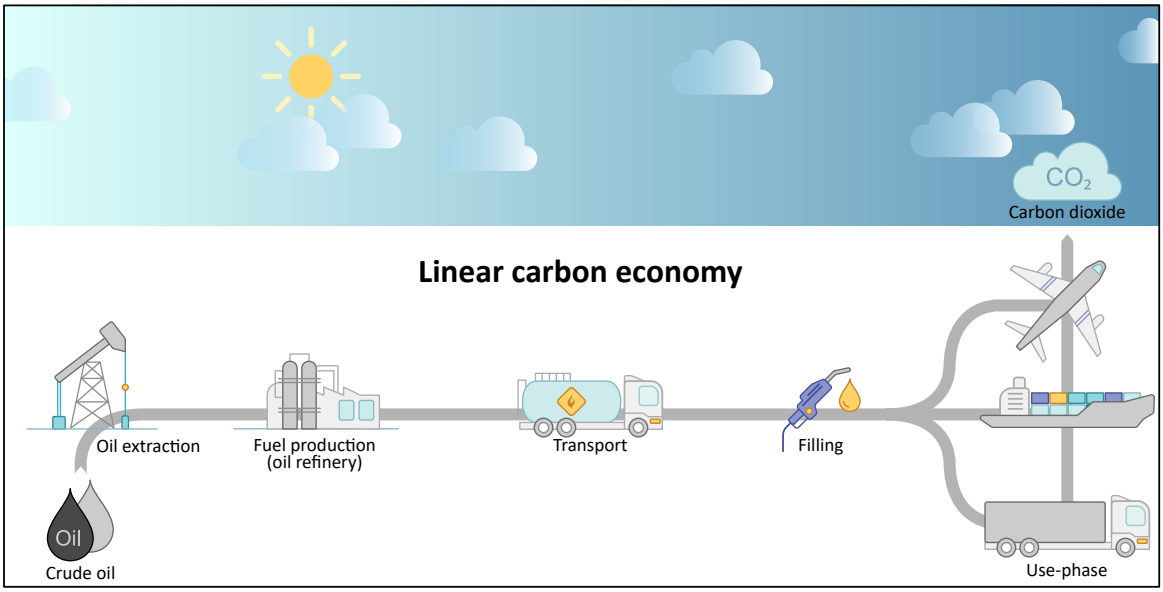

Figure 2.2: Scheme of today's fossil fuel production as part of the *linear carbon economy*. The solid arrow denotes the main carbon flow, while other CO_2 emissions from oil extraction, fuel production, transport, and filling have been omitted for simplicity.

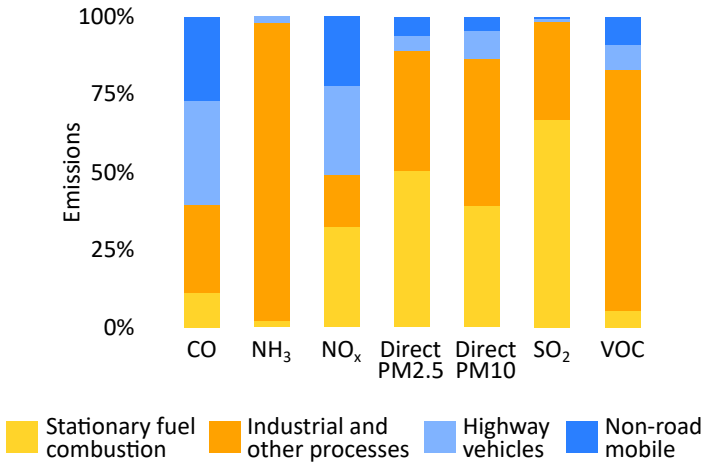

Figure 2.3: Emissions of air pollution in the United States by source category, adapted from U.S. Environmental Protection Agency (2022). CO: carbon monoxide, NH_3: ammonia, NO_x: nitrogen oxides, PM: particulate matter, SO_2: sulfur dioxide, VOC: volatile organic compound.

electric passenger car sales are steeply rising (IEA, 2023a), more ambitious action is necessary to limit global warming to 1.5 °C. As renewable energy will likely remain a scarce resource, it should be integrated preferably in those applications where it is used most efficiently.

Sternberg and Bardow (2015) demonstrated that direct electrification is by far the most efficient use of renewable electricity to mitigate climate change, as shown for battery-electric vehicles (BEVs) in Figure 2.4. Direct electrification should therefore always be the first choice wherever possible. In fact, electric car sales and investments in battery manufacturing are already ramping up rapidly. Sales made up more than 20 % of the market in the European Union (EU) in 2022 and are expected to reach around 14 million sold vehicles globally in 2023 (IEA, 2023c). Moreover, capacity of battery manufacturing for electric vehicles increased by around 60 % in 2022 (IEA, 2023b).

However, the subsectors aviation, shipping, and heavy-duty trucks in long-haul applications require energy carriers of higher energy densities than batteries can currently provide (Shukla et al., 2022). Although aviation and shipping with electric power may become feasible in short-range applications, both are expected to remain largely dependent on fuels. These subsectors are therefore referred to as hard-to-electrify. In hard-to-electrify subsectors, renewable synthetic fuels are considered as key technologies to mitigate climate change. Section 2.1.2 outlines in detail how synthetic fuels can complement direct electrification in the future transport sector.

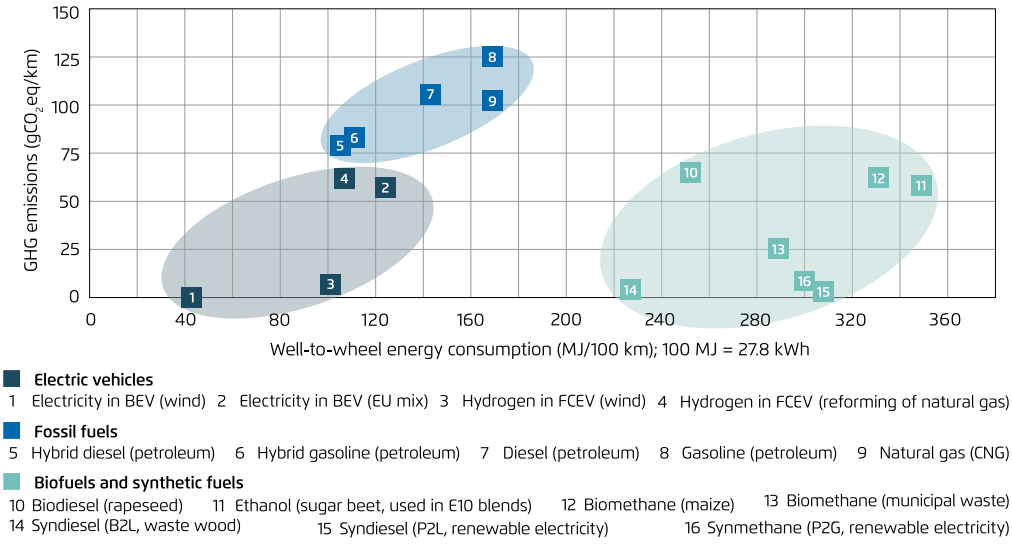

Figure 2.4: Greenhouse gas (GHG) emissions and energy consumptions of road transport technologies, adapted from Agora Verkehrswende (2017). BEV: battery-electric vehicle, FCEV: fuel cell electric vehicle, B2L: biomass-to-liquid, P2G: power-to-gas.

2.1.2 Future transport sector: synthetic fuels complementing electrification

In the previous section, we outlined the present transport sector that still uses predominantly fossil fuels as part of the *linear carbon economy*. Here, we proceed with the future transport sector, describing in particular the role of synthetic fuels as complements for direct electrification in hard-to-electrify subsectors. In these hard-to-electrify subsectors, synthetic fuels can be used in vehicles with both today's and tomorrow's propulsion technology, comprising internal combustion engines (ICEs), gas turbines, and fuel cells (FCs) combined with an electric motor. However, the FC technologies differ in terms of their intended application, the fuel used, and technological maturity (Mekhilef et al., 2012; Sharaf and Orhan, 2014; van Biert et al., 2016; Sazali et al., 2020).

In scientific literature, many terms are used to describe fuels of non-fossil origin, depending on whether the focus is on the feedstock, application, or process:

- *advanced fuels* (Leitner et al., 2017; Artz et al., 2018),
- *alternative fuels* (Thavornprasert et al., 2016; Niethammer et al., 2018; Liu et al., 2019; Okolie et al., 2023),
- *biomass-based fuels (bio-fuels)* (Leitner et al., 2017),
- *biomass-to-fuel* (Gnanasekaran et al., 2023; Xu et al., 2023),
- *biomass-to-liquid* (Ail and Dasappa, 2016; Putta et al., 2022),
- *CO_2-based fuels* (Artz et al., 2018),
- *electricity-based fuels (e-fuels)* (Borning et al., 2020; Skov and Schneider, 2022),
- *electrofuels* (Brynolf et al., 2022),
- *power-to-fuel* (Schemme et al., 2017; Bargiacchi et al., 2019),
- *power-to-liquid* (Schmidt et al., 2018; Putta et al., 2022),
- *renewable fuels* (Leitner et al., 2017; König et al., 2019; Chen et al., 2021; Lark et al., 2022),
- *solar fuels* (Artz et al., 2018; Gong et al., 2022),
- *synthetic biofuels* (Baranowski et al., 2017),
- *synthetic fuels (synfuels)* (Schemme et al., 2017; Baranowski et al., 2017; Artz et al., 2018; Sun et al., 2019),
- and more.

In the following, we stick to the term *synthetic fuels* and define it as follows to avoid ambiguity:

Synthetic fuels refer to fuels produced from renewable feedstocks, encompassing both bio- and electricity-based fuels that contain or are free of carbon.

In hard-to-electrify transport subsectors, synthetic fuels produced from renewable feedstocks are considered as key technologies to integrate renewable energy and feedstocks for climate change mitigation (Shukla et al., 2022). Depending on the fuel composition, two pathways are possible to transition from the present *linear carbon economy* to a future *low-carbon economy* with synthetic fuels (Figure 2.5): Synthetic fuels may follow a *carbon-free pathway* if they do not contain carbon (Figure 2.5A), or they may adopt a *circular carbon pathway* if they do contain carbon (Figure 2.5B). Electricity-based synthetic fuels can follow both pathways since they can be either carbon-free, e.g., hydrogen, or carbon-based, e.g., methane. In contrast, bio-based synthetic fuels are usually carbon-based, as they are made from carbon-containing organic materials, leaving only the *circular carbon pathway* open to them. In the following, we describe both pathways in more detail.

Carbon-free pathway (Figure 2.5A). The most discussed carbon-free synthetic fuels are hydrogen and ammonia (Shukla et al., 2022). In aviation, liquefied hydrogen (LH_2) is expected to play a decisive role: LH_2 could be used in either FCs for shorter flight ranges or in gas turbines for longer flights. Hydrogen is also discussed, in addition to ammonia, as future fuel for shipping (IEA, 2023b). Both fuels could be used either in engines or FCs (Muthukumar et al., 2021; Pramuanjaroenkij and Kakaç, 2023; Jeerh et al., 2021). In particular, ammonia is expected to be promising for future shipping where it could be also used as transport vector for hydrogen. Ammonia and so-called liquid organic hydrogen carriers (LOHCs) are, in fact, expected to become cheaper than LH_2 for hydrogen transport by ship, according to IEA (2023a). For long-haul heavy-duty road transport, both fuels are discussed as carbon-free energy carrier in fuel cell electric vehicles (FCEVs) (IEA, 2023c; Shukla et al., 2022). Although FCEVs do not use electricity as efficiently as BEVs, they are still much more efficient than ICEs burning synthetic fuels (Figure 2.4).

Overall, the *carbon-free pathway* via the synthetic fuels hydrogen and ammonia is likely the future for new vehicle fleets in hard-to-electrify transport subsectors. However, using hydrogen and ammonia in today's propulsion technology is considered challenging due to limited compatibility with existing engines and fuel infrastructure. Both fuels require retrofitting of existing propulsion systems and the development of safe procedures for handling and storage (Tornatore et al., 2022; Shukla et al., 2022;

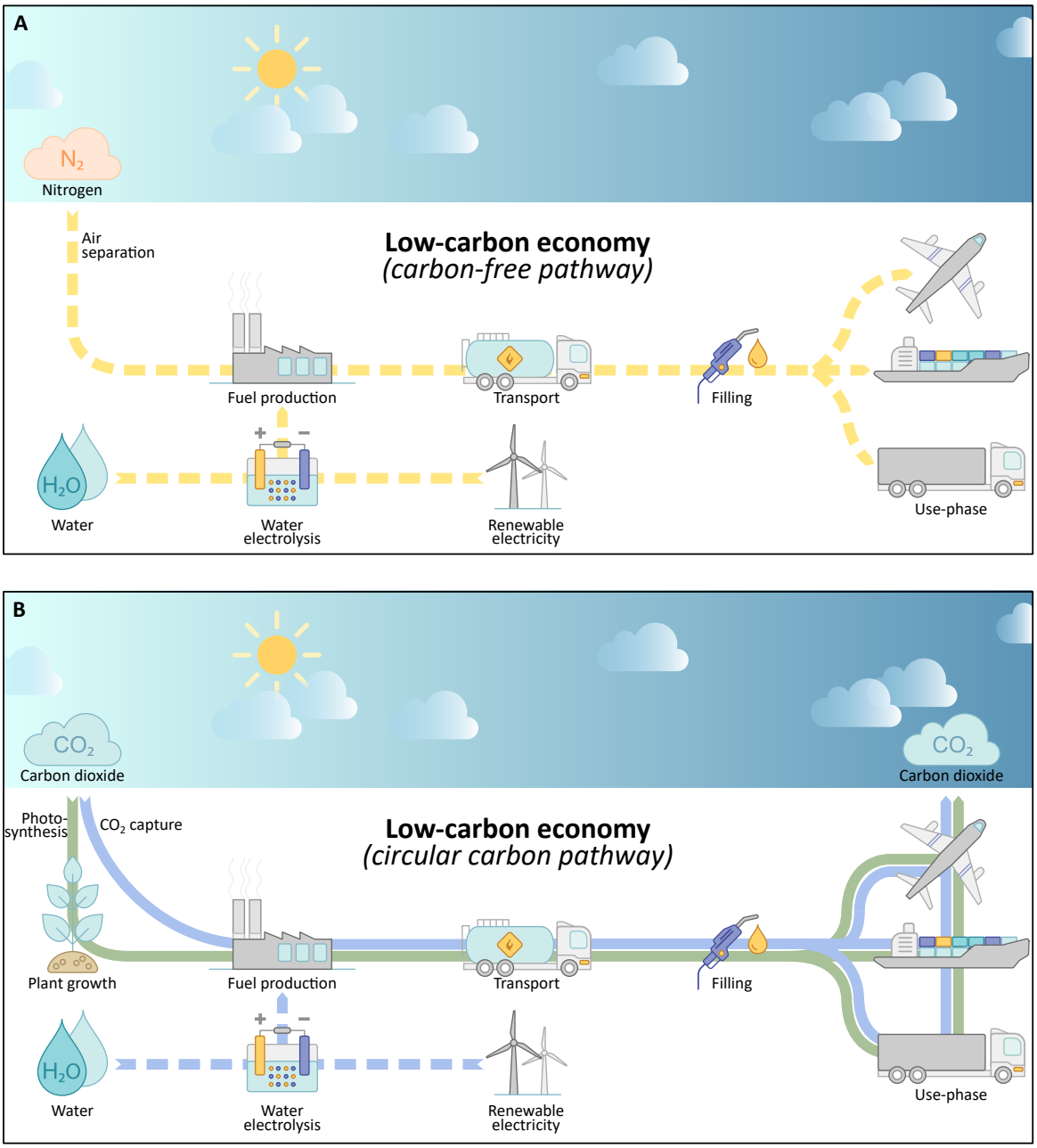

Figure 2.5: Scheme of two pathways for tomorrow's synthetic fuel production as part of the *low-carbon economy*. Synthetic fuels may follow a (A) *carbon-free pathway* if they do not contain carbon or (B) *circular carbon pathway* via biomass (green) or direct air capture (blue) if they do contain carbon. Solid arrows denote the main carbon flow while dashed arrows denote other material and energy flows. Other CO_2 emissions from fuel production, transport, and filling have been omitted for simplicity.

Ma et al., 2023). As aviation fuel, liquid hydrogen even requires an entire redesign of today's aircrafts.

Circular carbon pathway (Figure 2.5B). In contrast to carbon-free synthetic fuels, many carbon-based synthetic fuels have the advantage of potentially maintaining compatibility with today's existing propulsion technology and fuel infrastructure. Carbon-based synthetic fuels are thus promising to mitigate climate change in already existing vehicle fleets, with only slight or even no retrofitting (Shukla et al., 2022). Notable, FCs could also use carbon-based synthetic fuels, e.g., methanol (İnci et al., 2021) and ethanol (Barbaro and Bianchini, 2009). In particular, methanol is discussed for future shipping where it could be used as fuel and LOHC to transport hydrogen. All carbon-based synthetic fuels have in common that they utilize biomass or CO_2 as carbon feedstocks. If carbon is sourced from CO_2, a high-energetic co-reactant is required to activate the inert CO_2 molecule for fuel production (Ampelli et al., 2015). This high-energetic co-reactant is usually hydrogen that can be produced renewably by water electrolysis if low-carbon electricity is used. The major drawback of water electrolysis is its high electricity consumption (Kätelhön et al., 2019): Large amounts of scarce low-carbon electricity are required to align carbon-based synthetic fuels produced from renewable hydrogen with a future *low-carbon economy*.

The most discussed carbon-based synthetic fuels are, for aircrafts, sustainable aviation fuels (SAFs) (Okolie et al., 2023; IEA, 2023b) as well as, for shipping, primary alcohols (ethanol and methanol), liquefied methane, and synthetic diesel (Shukla et al., 2022). In road applications, in particular heavy-duty trucks, a wide range of carbon-based synthetic fuels has been investigated: synthetic gasoline and diesel (Fischer-Tropsch (FT) and methanol-to-gasoline), methane, primary alcohols (ethanol and methanol), ethers (dimethyl ether (DME), dimethoxymethane (DMM), polyoxymethylene ethers (OMEs) of chain length three to five), and more (Baranowski et al., 2017; Schemme et al., 2017; Deutz et al., 2018; Niethammer et al., 2018; Artz et al., 2018; Sun et al., 2019; Brynolf et al., 2022). For all of the aforementioned fuels, production routes exist that use biomass or CO_2 as carbon feedstock. Both carbon feedstocks are described in more detail in the following.

Biomass as carbon feedstock. The feedstock biomass is typically divided into three generations (Lee and Lavoie, 2013): First-generation biomass includes food crops like corn, sugarcane, soybean, and palm oil. Chemicals and fuels that are produced from first-generation biomass are derived from the sugars, starch, or vegetable oils contained in these crops. However, biomass of this generation has the major disadvantage of fueling the so-called "food versus fuel" conflict, which describes the competition for arable land between food and fuel production (Saini et al., 2015). Second-generation

biomass attempts to defuse this conflict by utilizing non-food crops, biowaste, and agricultural residues. This generation comprises, for instance, municipal wastes and lignocellulosic biomass such as energy crops (e.g., miscanthus and switchgrass), forest residues (e.g., bark and wood chips), and agricultural residues (e.g., bagasse and corn stover). A potential disadvantage associated with first- and second-generation biomass are land-use change (LUC) emissions (Dunn et al., 2013). Direct LUC occurs if land is converted for biomass cultivation. If this land was originally used for other purposes, e.g., agriculture, indirect land-use change (iLUC) may also occur: the displaced original land demand still remains and induces additional LUC somewhere else. Third-generation biomass is intended to defuse this LUC problem and encompasses the use of algae. Algae grows much faster and uses less land compared to lignocellulosic biomass, according to Fenton and Ó hUallacháin (2012). As alternative to biomass, CO_2 can be used as carbon feedstock, which is described next.

CO_2 as carbon feedstock. For decades, CO_2 is utilized in various applications: carbonation of beverages, enhanced oil recovery from oil fields, urea production, in solid form as so-called dry ice for cooling in the food industry, and more (Bui et al., 2018). In recent years, CCU has emerged as a promising concept to convert CO_2 into value-added products within a *low-carbon economoy* (Müller et al., 2020b). In this concept, CO_2 is captured and utilized as a chemical carbon feedstock for various applications, e.g., cement (Ostovari et al., 2020), foams (von der Assen and Bardow, 2014), chemicals (Kätelhön et al., 2019), and fuels (Deutz et al., 2018). Prior to utilization, CO_2 is captured from either industrial point sources or ambient air. Industrial point sources comprise, for instance, cement and steel plants while CO_2 capture from ambient air requires a direct air capture (DAC) system (von der Assen et al., 2016). Notably, the CO_2 concentration varies among point sources and is lowest in ambient air. As a consequence, GHG emission reductions of CCU vary among CO_2 sources since the lower the CO_2 concentration the higher the energy demand required for capture (Müller et al., 2020b).

Besides CCU, CO_2 could be also captured and stored, e.g., underground in geological formations or carbonates, which is called carbon capture and storage (CCS) (Bui et al., 2018; Ostovari et al., 2022). If the stored CO_2 is captured from biogenic carbon sources or the atmosphere, net-negative CO_2 emissions are possible since CO_2 is permanently removed from the natural carbon cycle (Anderson and Peters, 2016). The corresponding negative emissions technologies (NETs) are called bioenergy carbon capture and storage (BECCS) and direct air carbon capture and storage (DACCS) (Fuss et al., 2018). In this thesis, we do not consider CCS since we investigate CO_2 as carbon feedstock for synthetic fuel production.

Overall, synthetic fuels appear promising for climate change mitigation in hard-to-electrify transport subsectors—both in vehicles with today's and tomorrow's propulsion technology. Still, climate change mitigation through synthetic fuels is not a given but requires thorough verification. Moreover, burden-shifting to other areas of concern, e.g., excessive land use, should be quantified and avoided or at least kept at a minimum. For these purposes, the methodology of LCA was developed and standardized. However, in addition to the fuels mentioned above, there are many other candidates that could be used either as pure substances or as components in mixtures, i.e., fuel blends. To cope with so many options, model-based fuel design can aid in identifying those synthetic fuels that are most suitable for their intended application.

2.2 Life cycle assessment and design of synthetic fuels

In the following, we describe the methodology of LCA in Section 2.2.1. Section 2.2.2 proceeds with an introduction of the integrated process and fuel design framework as an early-stage screening tool for model-based fuel design. A literature review of recent assessments and fuel design studies on synthetic fuels follows in Section 2.2.3. This section concludes with outlining the identified scientific gaps in Section 2.2.4.

2.2.1 Fundamentals of life cycle assessment

The methodology of LCA evaluates the environmental impacts of a product or service throughout its entire life cycle (ISO, 2006a). LCA covers all activities of the product system from *cradle-to-grave*, i.e., starting from the extraction of raw materials through production, transport, and product use to recycling and final disposal of the product and related wastes. Throughout the product system's life cycle, all material and energy flows are quantified that the product system exchanges with its environment. These exchanges are consumed natural resources, e.g., freshwater, and emitted pollutants, e.g., nitrous oxide, that LCA characterizes according to their contribution to environmental impact categories such as water use and climate change. Owing to LCA's holistic approach, potential burden shifting between life cycle stages and impact categories can be identified and quantified. In the 1990s, the International Organization for Standardization (ISO) developed the ISO 14040 and ISO 14044 to standardize the LCA methodology (ISO, 2006a,b). Following these standards, LCAs

are commonly performed iteratively in four phases that are explained in more detail below (Figure 2.6):

Phase 1: Goal and scope definition

Phase 2: Life cycle inventory analysis

Phase 3: Life cycle impact assessment

Phase 4: Interpretation

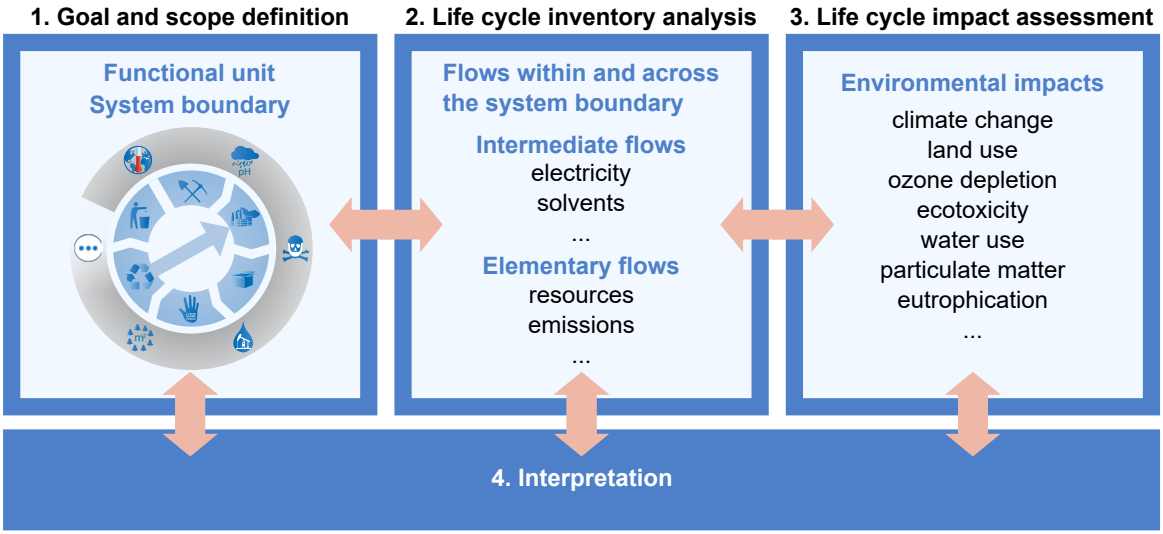

Figure 2.6: The four phases of the life cycle assessment framework according to ISO 14040 and ISO 14044 (ISO, 2006a,b).

Phase 1: Goal and scope definition. In the first phase, the *goal and scope definition*, LCA practitioners define the *goal* of the study: the reasons for evaluating this product system as well as the intended application and audience. Based on the goal definition, the study's *scope* is defined, which encompasses describing the product system under study and its function(s), the so-called functional unit, and the system boundary. The scope also includes the description of methodological choices such as solving multi-functionality, selected impact categories with their corresponding life cycle impact assessment (LCIA) methods, and critical assumptions and limitations of the study.

The *functional unit* is a means to quantify the product system's function(s) and serves as a basis to which calculated environmental impacts are related. If several product systems are studied in a comparative LCA, the functional unit represents a common basis that ensures comparability of impacts. The quantitative output to fulfill the product system's function is called the *reference flow* (Müller et al., 2020a).

For instance, a passenger car's function can be quantified with the functional unit "the provision of 1 km of transportation in a medium-sized passenger car" and the reference flow "1 km-driven."

The *system boundary* includes all processes and life cycle stages that are required to fulfill the product system's function(s) and to reach the LCA's goal. In principle, it is recommended to apply a *cradle-to-grave* system boundary ensuring that all environmental impacts associated with the product's entire life cycle are considered. In comparative LCAs, however, a *cradle-to-gate* system boundary can be sufficient if the products under study exhibit equal environmental impacts in the neglected life cycle stages. In LCAs of road vehicles, the terms *well-to-wheel* and *well-to-tank* are commonly used to describe a system boundary that encompasses all life cycle stages either including or excluding the use-phase, respectively.

Phase 2: Life cycle inventory analysis. In the second phase, the *life cycle inventory analysis*, the life cycle inventory (LCI) is gathered, which comprises material and energy balances for all processes that are within the system boundary. Therefore, all flows are covered that processes exchange with each other (*technosphere*) and with the environment (*ecosphere*). Exchanges between processes are called *intermediate flows* while *elementary flows* denote exchanges, e.g., resources and emissions, across the system boundary. Among LCA practitioners, it is common practice to divide the system into a foreground and a background system (Frischknecht, 1998). While the *foreground system* describes processes that decision-makers can control, the *background system* comprises processes that cannot be directly influenced. The background system is typically modeled with aggregated datasets from LCA databases, e.g., the ecoinvent (Wernet et al., 2016) and GaBi (GaBi, 2019) databases.

A product system can show *multi-functionality* due to (1) multiple outputs (e.g., a co-produced product), (2) multiple inputs (e.g., several treated wastes), and (3) in- and output systems that simultaneously produce product(s) and treat waste(s). ISO 14044 provides a stepwise procedure to deal with multi-functionality that is briefly summarized in the following (ISO, 2006b). Multi-functionality should be resolved, if possible, by either dividing the multi-functional process into sub-processes or including the additional function into the functional unit by system expansion. If the aforementioned steps are not possible, allocation procedures are required to partition environmental impacts between several inputs and/or outputs. For allocation, physical relationships should be applied preferably, followed by other relationships such as the products' economic value or exergy.

In the context of CCU, industrial CO_2 point sources are prominent examples of multi-functional processes, e.g., a steel plant with carbon capture co-produces steel

and CO_2. In this thesis, we solve multi-functionality of CO_2 point sources by substitution via system expansion: we give a credit, i.e., so-called *avoided burden*, for CO_2 utilization that represents *"the environmental burdens avoided by the substitution of the conventional production system which would have been used otherwise"* (Müller et al., 2020a). In this example, the substituted "conventional production system" is the steel plant without carbon capture.

Phase 3: Life cycle impact assessment. In the third phase, the *life cycle impact assessment*, all elementary flows of the LCI are characterized regarding their impact to various environmental impact categories, e.g., climate change and land use. Each elementary flow is multiplied with so-called characterization factors that describe the elementary flow's contribution to a certain impact category compared to a reference flow. For example, methane's characterization factor regarding climate change of 29.8 kg_{CO_2eq} kg^{-1} expresses that methane absorbs 29.8 times more infrared radiation over 100 years than the reference flow CO_2 (European Commission, 2018b). The overall impact, e.g., on climate change, of the product system can be calculated by summing up all characterized elementary flows. The set of environmental impact categories under study is defined in the first phase, the goal and scope definition, and should cover a wide range to identify potential burden shifting between impact categories. In this thesis, we consider the environmental impact categories of the LCIA method Environmental Footprint (EF) that is recommended by the Joint Research Centre of the European Commission (European Commission, 2018b).

Phase 4: Interpretation. In phase four, the *interpretation*, the results are reviewed and interpreted regarding their ability to fulfill the stated goal of the LCA study. This review includes identifying major issues, so-called "hot-spots," of the product system, e.g., a specific process or substance that contributes most to the environmental impacts. For this purpose, LCA practitioners typically conduct contribution analyses that reveal these hot-spots. Furthermore, the results should be critically analyzed regarding their limitations and robustness, i.e., assumptions made while conducting the LCA, consistency of underlying process data, and sensitivity and uncertainty of calculated results. Finally, sound conclusions should be derived to give recommendations for decision-makers. As the LCA methodology is an iterative approach, changes in the other three phases may be required, e.g., refining the goal and scope of the study or including additional environmental impact categories.

2.2.2 The integrated process and fuel design framework

This section proceeds with the introduction of the integrated process and fuel design framework as an early-stage screening tool for model-based fuel design. In scientific literature, several approaches exist for model-based fuel design (see Section 2.2.3). So far, the integrated process and fuel design framework by König et al. (2021) is the only approach that considers the fuel's well-to-wheel life cycle, rendering it compliant with the LCA methodology. In the following, we concisely describe the framework and refer to König et al. (2021) for an in-depth description.

The integrated process and fuel design framework combines a pathway model based on process network flux analysis (PNFA) (Ulonska et al., 2016; König et al., 2019) with the fuel property model of Dahmen and Marquardt (2017). The most important characteristics of the pathway and fuel property models are described in the following. Subsequently, the resulting optimization problem is explained.

Pathway model. The pathway model based on PNFA was developed as an early-stage screening tool that evaluates reaction pathways and subsequent processing options. The model comprises an array of possible production pathways that can be depicted as a reaction network. The reaction network links feedstocks to products via multiple biomass and hydrogen conversion routes and intermediates. Product and side-product flows are calculated based on stoichiometry and yield data from literature. Thus, direct emissions that might occur during fuel production in industrial facilities are not modeled. The production cost and environmental impacts of side-products are allocated to the main product, i.e., the fuel. Moreover, the model takes into account energy consumptions of reactions and separation sequences, encompassing electricity, process heat, and cooling demands. Based on this reaction network and energy consumptions, economic and environmental metrics are estimated. Previous studies focused on estimating production cost and global warming impact (GWI) although other metrics can be implemented as well. These estimations comprise the prices and environmental impacts of feedstocks, auxiliaries, and waste disposal as well as investment costs. More details on the pathway model are presented in Ulonska et al. (2016) and König et al. (2019).

Fuel property model. Fuel property models are used to ensure that properties of designed fuels are within specifications to fulfill requirements of targeted fuel standards. These fuel properties are predicted based on priori determined data that stems from either experiments or model-based approaches, using mixture property models relying on pure-component properties. For more details on the fuel property model, see Dahmen and Marquardt (2017) and König et al. (2019, 2021).

Optimization problem. The continuous nonlinear program (NLP) of integrated process and product design is briefly summarized in Equation (2.1). In König et al. (2020, 2021), integrated process and product design was formulated as bi-objective optimization problem with the objectives specific production cost C_{spec} and GWI. In this bi-objective optimization problem, design variables are the resulting fuel composition and the mole fluxes of the reaction network. Trade-offs among objectives can be evaluated by using the ϵ-constraint method (Haimes et al., 1971; Mavrotas, 2009). See Section A.2.2.1 and König et al. (2021) for more details regarding the optimization problem including all constraints.

$$\min \begin{bmatrix} C_{\text{spec}} \\ GWI \end{bmatrix} \tag{2.1}$$

$s.t.$ **pathway model:**

mole balances for products and by-products

utility requirements of reactions and separation steps

costs (feedstocks, utilities, disposal, investment)

GWI estimation of feedstocks and processes

fixed annual fuel production β

property model:

mole and mass fractions of fuel

fuel property models and mixing rules

fuel specifications

2.2.3 Current status of environmental assessment and design of synthetic fuels

In literature, several approaches have been developed for model-based fuel design. Additionally, many LCAs of synthetic fuels have been conducted for a wide range of possible propulsion technologies and transport subsectors. In this thesis, we apply the herein proposed fuel design procedure exemplary on carbon-based synthetic fuels for today's vehicles with ICEs in road applications (*circular carbon pathway* in Figure 2.5B). We thus focus on these applications in our concise literature review below. Since natural gas has only a small share of around 4 % of total final energy

consumption in today's road transport (Figure 2.1A), we concentrate on gasoline- and diesel-type fuels.

2.2.3.1 Model-based fuel design

With model-based fuel design, promising components or blends for synthetic fuels can be identified that exhibit a priori defined properties. Most fuel design studies focus on screening molecules or mixtures that lie in a pre-defined range of physico-chemical and combustion-related properties with the aim of identifying a feasible fuel (Dahmen and Marquardt, 2016; McCormick et al., 2017; Gschwend et al., 2019; Fioroni et al., 2019; Huo et al., 2019; vom Lehn et al., 2021; Rittig et al., 2023; Fleitmann et al., 2023). Many of these studies target fuel properties that allow for increased engine efficiency, e.g., through high octane numbers which in turn can lead to a reduced GWI (Dahmen and Marquardt, 2016; McCormick et al., 2017; Gschwend et al., 2019; vom Lehn et al., 2021; Rittig et al., 2023; Fleitmann et al., 2023). In contrast, only few studies consider the impact of fuel chemistry on emission formation (Dahmen and Marquardt, 2016; Fioroni et al., 2019; Huo et al., 2019; Fleitmann et al., 2023) or the eco-toxicity and human toxicity of the fuel (Fleitmann et al., 2023; Yunus et al., 2014; Zhang et al., 2018a).

Additionally, several studies focus solely on designing the blend, neglecting other phases of the fuel's life cycle. For instance, designing blends with minimal amount of fossil fuel and maximal amount of synthetic fuel aims to reduce both fossil resource depletion and GWI (Yunus et al., 2014; Zhang et al., 2018a; Hashim et al., 2017; Kalakul et al., 2018). However, to estimate the environmental impact of a fuel over its whole life cycle, fuel production needs to be considered as well. Identifying optimal synthetic fuels or blends thereof is thus a complex task that can be supported by mathematical optimization, e.g., with methods that combine process and product design in an integrated manner. To this end, Marvin et al. (2013) combined a reaction network generator with linear fuel property models to design a blend of biomass-based components with fossil gasoline that complies with standards of the American Society for Testing and Materials (ASTM). Their approach targeted different objectives such as energy loss, catalyst requirement and heat duty of reactions.

Dahmen and Marquardt (2017) built on the method by Marvin et al. (2013) and combined mass-based screening by reaction network flux analysis (RNFA) (Voll and Marquardt, 2012) with nonlinear fuel property models to design fuel blends for high efficiency engines with minimal resource consumption. RNFA was further developed towards PNFA (Ulonska et al., 2016; König et al., 2019). PNFA also considers energy

demands of separation steps based on shortcut models for distillation columns by Bausa et al. (1998). Combining PNFA with predictive fuel property models enabled the integrated early-stage design of production processes and fuels, minimizing the objectives production cost and GWI (König et al., 2020). The application of integrated process and fuel design on a case study for spark-ignition engine fuels identified a ketone-ester-alcohol-alkane (KEAA) blend as a promising Pareto-optimal process and fuel design that compromises the conflicting objectives production cost and GWI (König et al., 2021; Ackermann et al., 2021).

While a lot of studies address the environmental impacts of the fuel, so far, the approach of König et al. (2020) is the only design approach that considers the well-to-wheel life cycle of the fuel. It uses a bi-objective optimization, minimizing production cost and GWI as the only environmental impact category, which may overlook a potential burden shift to other currently neglected impact categories. Electricity-based synthetic fuels, for instance, can reduce GWI substantially compared to fossil fuels if produced from renewable electricity and carbon sources at the cost of increases in other impact categories, e.g., resource use of minerals and metals (Hank et al., 2019; Medrano-García et al., 2022). In contrast, biomass-based synthetic fuels, e.g., ethanol, are known to increase agricultural land occupation substantially compared to their fossil-based counterpart (Muñoz et al., 2014). Therefore, a holistic design approach should cover a wide range of impact categories as additional objectives to quantify and avoid potential burden-shifting (Kleinekorte et al., 2020).

2.2.3.2 Environmental assessments of synthetic fuels

Recent literature discusses several synthetic fuels as promising substitutes or blend components for gasoline and diesel. Some synthetic fuels, e.g., hydrogen (H_2) and ammonia, may be of interest for future applications but are incompatible with existing gasoline and diesel engines, requiring entirely new engine concepts. For near-term applications, drop-in synthetic fuels are of particular interest that require only minor or even no adaption of existing engines and infrastructure. Currently intensively studied synthetic fuels are the *ethers* DME, DMM and $OME_{3\text{-}5}$, the so-called *renewable diesel fuels* hydrogenated vegetable oil (HVO) and fatty acid methyl ester (FAME), *FT gasoline and diesel*, and *primary alcohols*. Besides these most-discussed synthetic fuels, other fuel candidates are also investigated, e.g., the biofuel candidates furans, tetrahydrofuran, and alkyl tetrahydrofurans (Leitner et al., 2017). However, these fuel candidates are still technologically immature and thus neglected in the following.

All of the aforementioned synthetic fuels differ regarding their (1) technological maturity for large-scale production, (2) compatibility with existing engine technology and fuel infrastructure, (3) pollutants from fuel combustion, and (4) GHG emissions. However, all four aspects are important criteria to accelerate climate change mitigation with synthetic fuels in today's vehicles. Therefore, we also review briefly the technological maturity, compatibility, and combustion pollutants in addition to LCAs for these fuels. In literature, technological maturity is commonly expressed in terms of the technology readiness level (TRL) ranging from one to nine, with nine representing the most mature technology (European Commission, 2017).

Ethers: DME, DMM, and $OME_{3\text{-}5}$. The ethers DME, DMM, and $OME_{3\text{-}5}$ are mostly discussed as substitutes or blend components for diesel fuel. While the technological maturity of DME production via methanol is high with a TRL of nine (Breuer et al., 2022; Schemme et al., 2019), DME's TRL is estimated as four in case of direct synthesis via H_2 and CO_2 (Schemme et al., 2018). DMM and $OME_{3\text{-}5}$ have estimated TRLs of four to five (Breuer et al., 2022; Schemme et al., 2019; Roh et al., 2020) and three to five (Breuer et al., 2022; Schemme et al., 2019; Mantei et al., 2022), respectively. Regarding their compatibility with existing fuel infrastructure, these fuels require minor adaptions to today's diesel engine systems. Importantly, all three would need new sealing materials if used as pure substitutes for diesel (Pélerin et al., 2020; Park and Lee, 2014; Schröder and Görsch, 2020). DME and DMM would also require pressurized tanks (Omari et al., 2017a; Park and Lee, 2014) and DME additionally an adapted fuel-injection system (Park and Lee, 2014). Moreover, DME, DMM, and $OME_{3\text{-}5}$ have much lower heating values than diesel, resulting in increased fuel consumption (Arcoumanis et al., 2008; Pélerin et al., 2020). All three have shown to burn almost without PM formation which can be leveraged to also reduce NO_x emissions (Zubel et al., 2019, 2021; Ying et al., 2008; Omari et al., 2017a, 2019).

Well-to-wheel GHG emissions can be reduced strongly if these oxygenated fuels are produced renewably from biomass or CO_2. DME can be produced bio-based via syngas from biomass gasification (Landälv et al., 2014; Lecksiwilai et al., 2016), for which Lecksiwilai et al. (2016) reported GHG emission reductions of up to 62 % compared to fossil diesel. Other LCAs focused on DME production from CO_2 and hydrogen either via syngas (Uddin et al., 2020; Fernández-Dacosta et al., 2019; Schakel et al., 2016), methanol (Matzen and Demirel, 2016), or direct synthesis (Bongartz et al., 2018). Reported GHG emission reductions are up to 80–86 % compared to fossil diesel (Matzen and Demirel, 2016; Bongartz et al., 2018). DMM, also known as OME_1, can be produced CO_2-based via several pathways using methanol: reaction of methanol with formaldehyde, direct reduction of CO_2, as well as by oxidation,

dehydrogenation, or transfer-hydrogenation of methanol (Deutz et al., 2018; Burre et al., 2021). For these pathways, GHG emission reductions of up to 92 % compared to fossil diesel have been reported. However, Deutz et al. (2018) demonstrate that the carbon footprint of electricity supply is decisive for the climate change mitigation potential of electricity-based DMM.

$OME_{3\text{-}5}$ can be produced from methanol via anhydrous and aqueous routes, using either biomass or CO_2 as feedstock. In these routes, methanol is produced via syngas from biomass gasification or via direct CO_2 hydrogenation. Anhydrous routes use trioxane and either DMM or DME as intermediates, whereas the aqueous routes directly utilize methanol and typically aqueous formaldehyde (FA) for $OME_{3\text{-}5}$ formation. Only a few LCAs exist that assess the well-to-wheel GHG emissions of $OME_{3\text{-}5}$ from biomass or CO_2 (see Section C.1), with reported GHG emission reductions of up to 86–93 %. Notably, the anhydrous route via trioxane and DME has not yet been investigated in LCAs. While all studies confirm that the well-to-wheel GHG emissions largely depend on the electricity source for e-fuel production, each study focuses on specific phases of the entire $OME_{3\text{-}5}$ life cycle or on selected environmental impact categories. Bokinge et al. (2020) focus solely on fuel production, while any use-phase emissions from fuel combustion remain uninvestigated. Hank et al. (2019) and Rodríguez-Vallejo et al. (2021) use proxy data for fuel combustion, neglecting the environmental promises of combustion research that OMEs enable lower PM and thus NO_x emissions than diesel (Omari et al., 2019, 2017a; Richter and Zellbeck, 2017). Moreover, only one study considers a blend of $OME_{3\text{-}5}$ and diesel besides pure $OME_{3\text{-}5}$ (Mahbub et al., 2017). The study of Hank et al. (2019) underlines that mitigating climate change with electricity-based fuels may shift burdens to other environmental impact categories, e.g., resource use of minerals and metals.

Renewable diesel: HVO and FAME. The biofuels HVO and FAME, known as biodiesel, are commercially established technologies with TRLs of nine (Breuer et al., 2022; Müller-Langer et al., 2014; Puricelli et al., 2021; Paris et al., 2021), and both are compatible with the existing fuel infrastructure (Puricelli et al., 2021; Hartikka et al., 2012). However, FAME application has shown degradation of elastomer materials (Fazal et al., 2011), and using it as pure fuel requires slight engine modifications to prevent deterioration of engine efficiency (Patel et al., 2016). PM and NO_x emissions are reduced with HVO (Hartikka et al., 2012; Lapuerta et al., 2011; Kuronen et al., 2007; Aatola et al., 2009), whereas measurements are inconclusive for FAME: Some studies report reductions in PM and increases in NO_x emissions (Hoekman and Robbins, 2012; Murtonen et al., 2009; Wyatt et al., 2005; Johansson et al., 2013), but others highlight increases for both (Wu et al., 2007; Karavalakis et al., 2016).

Nonetheless, HVO and FAME have shown to reduce well-to-wheel GHG emissions by around 50 % compared to fossil diesel (Puricelli et al., 2021; Arvidsson et al., 2011). They can be produced from vegetable oil, e.g., rapeseed, soybean, and palm oil, as well as used cooking oil that stems from vegetable oil or animal fat (Puricelli et al., 2021). However, first-generation biofuels produced from vegetable oil are in the "food versus fuel" conflict (Mohr and Raman, 2013), and palm oil is additionally associated with indirect land-use change and deforestation (Fargione et al., 2008). Both issues render used cooking oil the only suitable feedstock for large-scale production of HVO and FAME, making their production inflexible regarding feedstock choice. Additionally, the sustainability of used cooking oil as a feedstock remains controversial: In the future, the global demand for used cooking oil is expected to exceed its supply by far, which may trigger the displacement of used cooking oil by virgin oil in exporting countries, e.g., palm oil in Southeast Asia (van Grinsven et al., 2020).

FT gasoline and diesel. The FT synthesis is a well-established technology that has been available at large scale for decades (Klerk, 2011). FT products consist mainly of alkanes and olefins (Maitlis and Klerk, 2013), and can be tailored in composition towards desired fuels, e.g., jet fuel, FT gasoline, and FT diesel (Ail and Dasappa, 2016; Brynolf et al., 2018). These FT fuels can be produced via syngas from biomass or CO_2 (Dieterich et al., 2020). FT gasoline and diesel exhibit good compatibility with existing engines and fuel infrastructure, e.g., FT diesel is similar in composition to fossil diesel since both consist mostly of alkanes (Lappas and Heracleous, 2016; Dieterich et al., 2020). Regarding combustion emissions, FT diesel can reduce PM emissions only slightly compared to fossil diesel (Alleman and McCormick, 2003).

The GHG reduction potential of FT fuels was already evaluated in many LCAs with the feedstocks biomass (Okeke et al., 2020; Samavati et al., 2018; Zhang et al., 2018b; de Jong et al., 2017; Liu et al., 2017; van den Oever et al., 2023; Weyand et al., 2023) and CO_2 (Medrano-García et al., 2022; Freire Ordóñez et al., 2021; Zang et al., 2021a; Liu et al., 2020; Cuéllar-Franca et al., 2019; Hombach et al., 2019; Delgado et al., 2023). Most of these LCAs investigate FT diesel, with only three studies focusing on FT gasoline (Freire Ordóñez et al., 2021; Hombach et al., 2019; Zhang et al., 2018b). Reported GHG reductions of FT diesel and gasoline range between 70 % and 98 % compared to their fossil fuel comparator. For a detailed overview of recent LCAs, techno-economic assessments (TEAs), and reviews on FT fuels, see Section B.1.

Primary alcohols. Typically, short-chain $C_{<5}$ alcohols, e.g., methanol and ethanol, are considered as substitutes or blend components for gasoline, whereas long-chain C_{5+} alcohols, e.g., 1-octanol, are investigated for diesel-type applications (Hosseinzadeh-Bandbafha et al., 2024). Methanol can be directly produced from CO_2 and hydrogen

(Sternberg et al., 2017; Bongartz et al., 2018) while Schemme et al. (2019) present a CO_2-based route to ethanol via DME and syngas from reverse water-gas shift. The TRLs of both production routes are estimated to 9 and 4, respectively (Schemme et al., 2019). Alternatively, both can be produced from biomass with high technological maturity. Methanol produced from lignocellulosic biomass has a reported TRL of 8 (Breuer et al., 2022). Bio-based ethanol production routes exist with TRLs of 7–9, using a sequence of saccharification, fermentation, and dehydration (Müller-Langer et al., 2014). Note that methanol could also serve as intermediate for synthetic gasoline production via the established methanol-to-gasoline process (Schemme et al., 2019).

Regarding compatibility with existing spark-ignition engines, corrosion of metal surfaces is a major issue due to the polarity and hygroscopic nature of methanol and ethanol (Dharma et al., 2016; Verhelst et al., 2019). Additionally, elastomers in the fuel injection system tend to change in volume and hardness (Shahir et al., 2014; Verhelst et al., 2019). However, according to Wouters et al. (2020, 2023), both methanol and ethanol can reduce NO_x emissions substantially compared to gasoline, whereas unburned hydrocarbon emissions remain a challenge during cold-start conditions. Both methanol and ethanol can reduce well-to-wheel GHG emissions substantially compared to gasoline. GHG emission reductions of bio- and CO_2-based methanol are in the range of 80–90 % (Matzen and Demirel, 2016; Bongartz et al., 2018). For bio-based ethanol, the review paper by Müller-Langer et al. (2014) reports GHG emission reductions of 65–88 %, depending on the biomass feedstock.

The long-chain alcohol 1-octanol is conventionally produced fossil-based, starting from either ethylene (Alfen process) or n-heptene (SHOP process). Besides its fossil-based production, 1-octanol can be also produced from biomass-derived platform chemicals, e.g., furfural and acetone (Julis and Leitner, 2012). However, the technological maturity of this route can be expected to be still low; Breuer et al. (2022) estimate a TRL of three. Some of 1-octanol's properties are disadvantageous for using it as a pure fuel, e.g., its low cetane number (García et al., 2018; Zubel et al., 2017a). However, 1-octanol shows exceptionally low PM emissions: PM emissions are halved compared to fossil diesel at high part load and almost gone at lower part load (Zubel et al., 2016, 2017b). So far, no LCAs exist for renewable 1-octanol production from biomass or CO_2 feedstock.

Concluding remarks on FT diesel and long-chain alcohols. In summary, all of the aforementioned synthetic fuels are unable to meet several or even all of the following key challenges: (1) scalability in a timely manner, (2) compatibility with existing fuel standards and engine components for retrofitting, (3) reducing urban air pollutants, and (4) enabling the transition to net-zero GHG emissions with flexible

feedstocks. However, accelerating the transition towards a clean transport sector requires synthetic fuels that address these four key challenges simultaneously. Towards this goal, previous studies highlight that blends of FT diesel and the long-chain alcohol 1-octanol may yield promising synthetic fuels to address these key challenges (Lehrheuer et al., 2018; Neumann et al., 2018, 2019). These blends can combine their advantages and reduce their drawbacks, i.e., suitable fuel properties are maintained while reducing PM emissions by up to 94 % compared to fossil diesel. The gain in lower PM emissions could be further leveraged to also lower NO_x emissions with an adapted exhaust gas recirculation (EGR) rate.

2.2.4 Scientific gaps

The following major scientific gaps have been identified, based on the current status of environmental assessment and model-based design of synthetic fuels.

Gap 1: Model-based fuel design with key environmental objectives. Currently, most model-based fuel design approaches consider only single environmental objectives. In contrast, LCA recommends to include a wide range of environmental impact categories to avoid shifting burdens to unconsidered categories. However, with many environmental objectives included, the computational cost of fuel design increases exponentially, and decision-making in fuel design is hampered. Therefore, identifying the key environmental objectives of integrated process and fuel design is desirable to keep the computational cost and decision-making manageable. These key environmental objectives should cover the major trade-offs in fuel design to prevent overlooking of burden shifts in LCA.

Gap 2: Synthetic fuels addressing key challenges. So far, recently discussed synthetic fuels cannot simultaneously address all key challenges postulated above. While first results on reducing urban air pollutants are promising for blends of FT diesel and long-chain alcohols, their overall potential to meet all key challenges has to be checked. More precisely, a process concept is missing for the integrated production of blends of FT diesel and long-chain alcohols, based on mature technological concepts. Additionally, material compatibility, compliance with fuel standards, and combustion emissions have to be evaluated. Finally, the potential to enable the transition to net-zero GHG emissions has to be verified for these blends by a comprehensive well-to-wheel LCA.

Gap 3: Comprehensive well-to-wheel LCA on electricity-based OME_{3-5}. The already existing LCAs on electricity-based OME_{3-5} focus on specific fuel production routes and life cycle phases. No LCA exists that covers aqueous OME_{3-5} production via the intermediates trioxane and DME. All studies assume proxy data for combustion emissions or consider only a well-to-tank system boundary. Consequently, the environmental promises of combustion research are neglected that OMEs enable substantially lower NO_x emissions than diesel. Thus, a comparative well-to-wheel LCA is missing that covers all major anhydrous and aqueous production routes for electricity-based OME_{3-5}. For the use phase, this LCA should also include actual NO_x and soot tailpipe emissions from a driving cycle to capture the combustion benefits of OME_{3-5} accurately.

Gap 4: Optimal LCA-based distribution of synthetic fuels to fleets. The production volume of synthetic fuels will be likely limited by the availability of their feedstocks biomass and renewable electricity. So far, none of the LCAs on synthetic fuels analyzes how these limited fuel amounts should be distributed optimally to vehicle fleets from an environmental perspective. Depending on the fuel, it might be more beneficial to distribute limited synthetic fuel as pure fuel to only few vehicles or as blend with fossil fuel to all vehicles in a fleet. To answer this distribution question, the effect of variable blending ratios of synthetic fuel in fossil fuel has to be analyzed from a fleet perspective.

2.3 Contribution of this thesis

The literature review in Section 2.2.3 revealed major scientific gaps in current LCAs and design of synthetic fuels for road applications. In this thesis, we aim to narrow these gaps with a three-stage fuel design procedure guiding the progress in fuel design. This fuel design procedure spans from *screening* through *filtering* to *distribution* of synthetic fuels for existing vehicle fleets (Figure 2.7).

In the *screening* stage, a large amount of synthetic fuel candidates is screened regarding its potential to substitute fossil fuels in terms of production cost and environmental impacts. This stage represents early-stage fuel design, covering the model scales *stoichiometry* to *process*. The *filtering* stage further narrows the group of eligible synthetic fuels obtained from *screening*, evaluating their suitability to meet four key challenges of synthetic fuels. In this stage, more detailed models and analyses are required than in fuel screening, spanning the model scales *process* to *plant*. Lastly, the *distribution* stage analyzes how limited amounts of synthetic fuels should be dis-

tributed in vehicle fleets from an environmental perspective, i.e., as pure fuel or as blend with fossil fuel. Here, the model scale goes beyond *plant*, answering questions on a *fleet* scale. More precisely, the thesis provides the following contributions by applying the proposed fuel design procedure on carbon-based synthetic fuels for existing vehicles with ICEs in road applications.

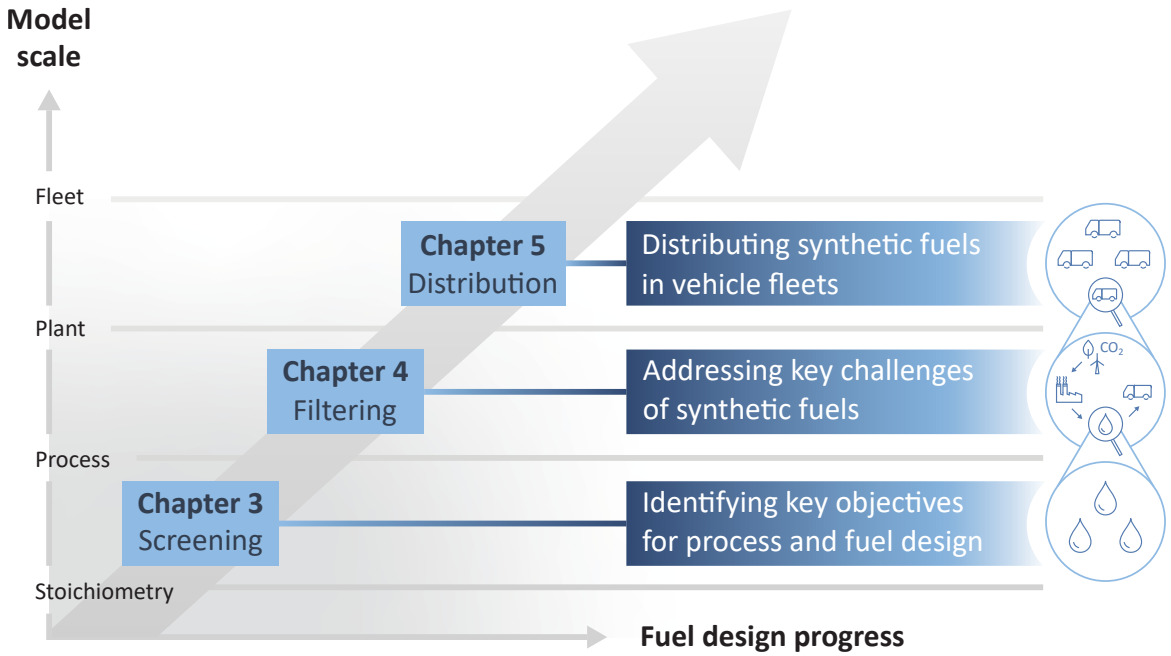

Figure 2.7: Contribution of this thesis: a three-stage fuel design procedure based on life cycle assessment, spanning from *screening* through *filtering* to *distribution* of synthetic fuels.

Chapter 3: Identifying key objectives for model-based fuel design. Chapter 3 focuses on the first stage of the proposed fuel design procedure: the *screening* of synthetic fuels via model-based fuel design. In model-based fuel design, it is desirable to include only those objectives that cover an optimization problem's major trade-offs since computational cost increases exponentially with the number of objectives. In contrast, LCA recommends to analyze a wide range of environmental impact categories to avoid burden-shifting to unconsidered categories. Focusing on the screening of spark-ignition engine fuels, we identify those environmental impact categories that represent key objectives for integrated process and fuel design. Therefore, we keep the computational cost of model-based fuel design manageable but without overlooking burden shifts in LCA.

Chapter 4: Addressing key challenges of synthetic fuels. Accelerating the transition towards clean road transport requires synthetic fuels that can address four key challenges. Synthetic fuels have to (1) be scalable in a timely manner, (2) be compatible with existing fuel standards and engine components for retrofitting, (3) reduce urban air pollutants, and (4) enable the transition to net-zero GHG emissions. Therefore, the group of eligible synthetic fuels obtained from *screening* is further narrowed in the fuel design procedure's second stage. In this stage, only those synthetic fuels are *filtered* out by more detailed analyses that can meet all key challenges simultaneously. Chapter 4 evaluates these four key challenges exemplary for so-called hydroformylated Fischer-Tropsch (HyFiT) fuels, which are blends of FT diesel and long-chain alcohols. For these HyFiT fuels, a process concept for fuel production is presented, material compatibility and compliance with fuel standards are investigated, combustion emissions are evaluated, and a comprehensive well-to-wheel LCA is conducted with fossil diesel and a BEV as benchmarks.

Chapter 5: Distributing synthetic fuels in vehicle fleets. In the third stage, we address how synthetic fuels, *filtered* out in the second stage, should be *distributed* in vehicle fleets in the coming decades. Since the production scale of synthetic fuels will be likely limited by feedstock availability, e.g., biomass and renewable electricity, their production volume can be expected to remain limited as well. In vehicle fleets, these limited fuel amounts could be distributed either as pure fuel for only few vehicles or as blend with fossil fuel for all vehicles. In Chapter 5, we answer how synthetic fuels should be distributed in vehicle fleets for minimal environmental impacts. For this analysis, we choose electricity-based $OME_{3\text{-}5}$ produced from CO_2 and renewable hydrogen as exemplary synthetic fuel. We conduct a comprehensive well-to-wheel LCA that covers all major anhydrous and aqueous production routes for electricity-based $OME_{3\text{-}5}$. To capture the reported combustion benefits of $OME_{3\text{-}5}$, we include actual tailpipe emissions from driving cycle tests.

Chapter 3

Identifying key environmental objectives for integrated process and fuel design

In this chapter, we identify key environmental objectives for the *screening* of spark-ignition engine fuels via integrated process and fuel design. For this purpose, we extend the existing process and fuel design framework (see Section 2.2.2) by all environmental impact metrics recommended for LCA by the European Commission (European Commission, 2018b). Applying a dominance-based optimization approach, we identify those objectives that are key to cover the major trade-offs of the optimization problem. With these key objectives, we generate Pareto-optimal process and fuel designs that we evaluate regarding a potential burden shift. Additionally, these process and fuel designs are benchmarked against both the KEAA blend of previous studies and fossil gasoline.

Section 3.1 gives a general introduction on approaches to identify key objectives of optimization problems. The overall solution procedure is outlined with all steps in Section 3.2. The case study on spark-ignition engine fuels is described in Section 3.3. Section 3.4 presents the identified key objectives and generated Pareto-optimal process and fuel designs. We discuss and conclude our findings in Section 3.5–3.6.

Major parts of this chapter are reproduced by permission of the Royal Society of Chemistry from:

> Völker, S., Ackermann, P., Granderath, M., Kortmann, C., Viell, J., Mitsos, A., and von der Aßen, N. (2024). Identifying key environmental objectives for integrated process and fuel design. *Sustainable Energy & Fuels*, **8**(9), 1966-1982.

Contribution report: Writing the draft, principal author, conceptualization, implementing the objective reduction, expanding the case study, calculation, evaluation and visualization of the results.

3.1 Determining key objectives of optimization problems

With many additional LCA objectives included, the optimization formulation for integrated process and fuel design (see Equation (2.1) in Section 2.2.2) becomes a multi-objective optimization problem (MOP). However, solving MOPs is challenging for two reasons: The computational effort of approximating a well-resolved Pareto front increases exponentially with the number of objectives (Li et al., 2015). Additionally, human decision-making is difficult as visualizing, interpreting, and weighing many different objectives is a complex and subjective task.

In MOPs, the number of actual trade-offs among all objectives is often fewer than expected a priori since at least some objectives are highly correlated (Steinmann et al., 2016). These correlated objectives may be less important or even redundant for optimization. According to Gal and Leberling (1977), an objective is redundant if its removal does not change the original Pareto front. Consequently, both challenges of MOPs may be resolved by considering only those objectives as key objectives for optimization that are most conflicting and thus covering the major trade-offs of the original MOP. However, identifying the key objectives of an optimization problem is challenging.

In literature, several methods have been proposed to identify a key objective subset that adequately represents the trade-offs of the original MOP, see the review article by Li et al. (2015) for an extensive overview. These methods are commonly referred to as "dimensionality reduction" or "objective reduction" methods since they reduce the dimensionality of the objective space, i.e., the number of objectives (Vaskan et al., 2014; Vázquez et al., 2018c). For the sake of brevity, we will use the term "objective reduction" whenever we refer to reducing the number of objectives in the objective space. Methods for objective reduction can be roughly categorized by the timing of objective reduction and the expression of the key objective subset: Objective reduction may take place during (*online*) or after (*offline*) the generation of a Pareto-optimal solution set (Li et al., 2015), and the key objectives are either expressed as a subset (*selection*) or linear combination (*extraction*) of the full objective vector (Saxena et al., 2013). Most of these methods are correlation-based or aim to preserve the original MOP's Pareto dominance structure (Singh et al., 2011). Note that some approaches are also based on feature similarity measures (López Jaimes et al., 2008), the analytic hierarchy process (Wheeler et al., 2017), objective clustering (Pal et al., 2018; Oliva et al., 2013), and representative and extreme criteria (Thoai, 2012).

Saxena and Deb (2007) developed correlation-based methods for both linear and nonlinear objective reduction (Deb and Saxena, 2006; Saxena et al., 2013), using principal component analysis (PCA) to evaluate the degree of correlation among objectives. PCA transforms a set of correlated objectives linearly into a smaller set of uncorrelated objectives, i.e., the so-called principal components, capturing the maximum variance in the underlying data (Deb and Saxena, 2005). Correlation-based objective reduction with PCA has, however, two major drawbacks (Brockhoff and Zitzler, 2009): Transformed objectives can be difficult to interpret for decision makers since they represent no longer distinct objectives but linear combinations thereof. Additionally, existing PCA-based methods do not take the dominance relation among solutions into account. Thus, preserving the dominance structure cannot be guaranteed.

In contrast, the dominance-based method by Brockhoff and Zitzler (2006) evaluates changes in the Pareto dominance structure induced by objective reduction. These changes in the dominance structure are quantified by the so-called δ-error. The δ-error can be interpreted as the maximum distance between the Pareto fronts of the original and the reduced objective spaces. Following this approach, objectives are considered redundant if omitting them does not change the dominance structure, resulting in a δ-error of zero. Consequently, a minimum key objective subset without changes to the dominance structure is identified if omitting further objectives would increase the δ-error above zero. The approach also allows to reduce the number of objectives even further, accepting changes in the dominance structure in favor of a smaller objective subset.

Guillén-Gosálbez (2011) and Kostin et al. (2012) introduced a mixed-integer linear programming (MILP) formulation for this approach to minimize the error of omitting objectives with common branch and bound algorithms. The advantage of this dominance-based method is twofold: Identified key objectives represent a true subset instead of transformations of the full objective space. Additionally, the Pareto dominance structure can be preserved, as reported by Guillén-Gosálbez (2011). It should be noted though that identified key objective subsets are not guaranteed to preserve the Pareto dominance structure. The number of input datasets, the approach to generate them, e.g., heuristics, and their normalization may affect Pareto dominance preservation.

The aforementioned objective reduction methods have been already applied on several case studies with environmental objectives to identify key objective subsets (see Section A.1). So far, for integrated process and fuel design, key environmental objectives have not yet been identified. However, their identification is crucial to quantify

potential burden shifts and enable early-stage fuel design with manageable computational cost. Due to the problem size of integrated process and fuel design, identifying these key environmental objectives requires the use of optimization-based techniques.

In this chapter, we apply the objective reduction method by Guillén-Gosálbez (2011) and Kostin et al. (2012) to identify key environmental objectives of integrated process and fuel design for spark-ignition engine fuels. Key objectives are derived for two scenarios to consider potential technology changes in energy and feedstock supply in the next decades.

3.2 Solution procedure to identify key objectives

First, the overall solution procedure to identify key objectives for integrated process and fuel design is outlined. Afterwards, the applied approaches within this procedure are described: the framework for integrated process and fuel design, normalization of solutions, the objective reduction method, and correlation between variables.

The applied solution procedure is based on the work of Guillén-Gosálbez (2011) and Kostin et al. (2012) and divided into nine steps (Figure 3.1). First, an initial Pareto-optimal solution set is generated by applying the integrated process and fuel design method in the full objective space F (Step 1). To generate this solution set, we minimize each single objective separately and subsequently determine the range of each objective. With these ranges, we next apply bi-objective optimization on every combination of objective pairs, using the ϵ-constraint method with solely four partitions in favor of manageable computational effort (Haimes et al., 1971; Mavrotas, 2009). From the 17 objectives considered in this work, there are 136 possible objective pairs with four partitions per pair, resulting in 544 initial solutions S_{initial}.

After repeated and dominated solutions have been sorted out (Step 2), we obtain the filtered solutions S_{filtered}. Note that the aforementioned procedure represents a heuristic approach to limit the computational cost: The generated initial solutions are weakly Pareto-optimal since, by bi-objective optimization, we solely optimize two-dimensional projections of the 17-dimensional objective space. Thus, the remaining dimensions of the objective space are not optimized for. The filtered solutions S_{filtered} are used for the objective reduction algorithm and to construct a correlation matrix (left and right branch, Figure 3.1).

In the left branch of Figure 3.1, we proceed with normalizing the filtered solutions to obtain a normalized solution set S_{norm} (Step 3). These normalized solutions are used as input for the objective reduction method applied in Step 4. By applying the

objective reduction method, we calculate the δ-error, which quantifies the change of the Pareto dominance structure, as function of the number of omitted objectives (OB). In Step 5, we can identify the key objectives representing an acceptable compromise of omitted objectives and induced δ-error. Lastly, in Step 6, we generate the set of Pareto-optimal process and fuel designs S_{reduced} in the reduced objective space F'. We apply multi-objective optimization on all key objectives, using again the ϵ-constraint method (Haimes et al., 1971; Mavrotas, 2009). In contrast to the first step, we increase the number of partitions from four to 32 in favor of a higher resolution of the Pareto front. Additionally, we refrain from using heuristics to generate these Pareto-optimal solutions, accepting increased computational cost that is partly offset by the smaller number of objectives considered.

In the right branch of Figure 3.1, we use the filtered solutions S_{filtered} to construct a correlation matrix CM (Step 7). Next, the degree of correlation among the objectives is analyzed to gain a first notion about redundancy and conflict (Step 8). Lastly, in Step 9, we compare the conflicting objectives from the correlation matrix with the key objectives identified by objective reduction. Based on this comparison, we derive conclusions about the suitability of correlation matrices to identify the key objectives covering an optimization problem's major trade-offs.

3.2.1 Integrated process and fuel design

In previous studies, integrated process and product design was formulated as bi-objective optimization problem with the objectives production cost and GWI per functional unit, i.e., \$ per GJ_{fuel} and kg CO_2 eq. per GJ_{fuel} (see Section 2.2.2) (König et al., 2020, 2021). In this study, we reformulate the optimization problem as MOP with the objectives production cost (C) in € and 16 environmental impacts (EI) per functional unit. See Table 3.1 for a list of considered environmental impact categories.

$$\min \begin{bmatrix} C \\ EI_1 \\ \cdots \\ EI_{16} \end{bmatrix} \tag{3.1}$$

$s.t.$ **pathway model:**

mole balances for products and by-products

utility requirements of reactions and separation steps

costs (feedstocks, utilities, disposal, investment)

EI estimation of feedstocks and processes

fixed annual fuel production β

property model:

mole and mass fractions of fuel

fuel property models and mixing rules

fuel specifications

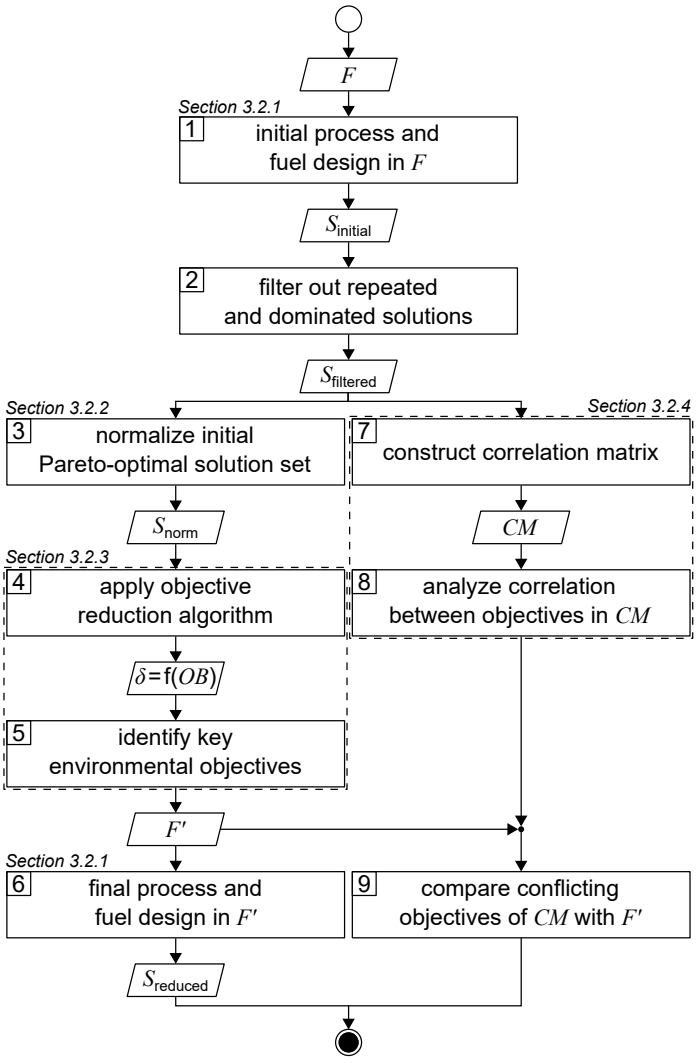

Figure 3.1: Flowsheet of the applied solution procedure for objective reduction based on the work of Guillén-Gosálbez (2011) and Kostin et al. (2012). F: full objective space, F': reduced objective space, S: solution set, δ: delta-error, OB: number of omitted objectives, CM: correlation matrix.

Table 3.1: List of the considered environmental impact categories with their specified units as determined in the Environmental Footprint (EF) 3.0 framework recommended by the Joint Research Centre of the European Commission (European Commission, 2018b). We adhere to the prescribed units outlined in the EF 3.0 framework for all impact categories. Altering units, e.g., from megajoule (RU_e) to gigajoule, is possible but would affect all results related to the adjusted impact category equally.

Abbreviation	**Impact category**	**Unit**
GWI	Climate change	kg CO_2 eq.
OD	Ozone depletion	kg CFC-11 eq.
PM	Particulate matter	disease incidence
A	Acidification	mol H^+ eq.
E_{fw}	Eutrophication, freshwater	kg P eq.
E_m	Eutrophication, marine	kg N eq.
E_t	Eutrophication, terrestrial	mol N eq.
IR	Ionizing radiation, human health	kBq U^{235} eq.
POF	Photochemical ozone formation	NMVOC eq.
ET	Ecotoxicity, freshwater	CTUe
HT_c	Human toxicity, carcinogenic	CTUh
HT_{nc}	Human toxicity, non-carcinogenic	CTUh
LU	Land use	points
RU_e	Resource use, energy carriers	MJ
RU_m	Resource use, minerals and metals	kg Sb eq.
WU	Water use	m^3 world eq.

3.2.2 Normalization of solutions

There are good reasons to normalize solutions prior to objective reduction: The herein considered objectives differ regarding their physical units, e.g., GWI in kg CO_2 eq. and water use in m^3 eq. Thus, without normalization, the δ-error's unit would also differ depending on the omitted objective since the error is directly calculated from the objective function values (see Equations (3.6) and (3.7) below). Moreover, the scales among objectives can vary by several orders of magnitude, depending on the objectives' units. Therefore, without normalization, objectives with a small scale would be omitted preferentially, as the δ-error of omitting these objectives would be also small. However, solutions can be normalized in different ways, rendering the choice of the applied normalization variant arbitrary. We emphasize, therefore, that normalization is a critical step that induces ambiguity to the identification of key objective sets (Vázquez et al., 2018a). In fact, the identified key objective subsets

and the corresponding approximation errors might change if different normalization variants are used.

Solutions are usually normalized with mathematical or environmental reference values. As mathematical reference values, the objective-specific minimum and maximum values of all solutions are commonly used to normalize the range of each objective. Environmental reference values are typically the environmental impacts of a reference system, e.g., a country's environmental impacts or planetary boundaries of the Earth. These environmental reference values can be optionally weighted, e.g., based on expert judgment, to rank the importance among objectives. Both mathematical and environmental reference values have advantages and drawbacks. While mathematical normalization attributes arbitrarily equal relevance to all objectives, mathematical reference values can be objectively calculated. In contrast, environmental normalization derives the relevance of objectives by comparison with the reference system. However, the reference system can be chosen arbitrarily and derived reference values are often uncertain, e.g., global environmental impacts or the Earth's planetary boundaries. Additionally, optional weighting based on experts' judgements is highly subjective. For energy system optimization, Postels et al. (2015) have analyzed the influence of normalization variants based on mathematical and environmental reference values on the identified key objective subset. The authors show that, in their case study, mathematical normalization variants lead to similar results while the identified key objective subsets differed substantially for the environmental reference values.

In this work, we focus on comparing four mathematical normalization variants regarding the key objective subsets identified by subsequent objective reduction. The variants (N1–N4) normalize each objective value $OF_{s,i}$ of solution s regarding objective i. For this purpose, the objective-specific minimum $\underline{OF}_i$ and maximum $\overline{OF}_i$ of all solutions are used as reference values, following Marler and Arora (2004):

$$\text{N1:} \quad OF_{s,i}^{\text{norm,N1}} = \frac{OF_{s,i} - \underline{OF}_i}{\overline{OF}_i - \underline{OF}_i} \tag{3.2}$$

$$\text{N2:} \quad OF_{s,i}^{\text{norm,N2}} = \frac{OF_{s,i} - \underline{OF}_i}{\underline{OF}_i} \tag{3.3}$$

$$\text{N3:} \quad OF_{s,i}^{\text{norm,N3}} = \frac{OF_{s,i}}{\underline{OF}_i} \tag{3.4}$$

$$\text{N4:} \quad OF_{s,i}^{\text{norm,N4}} = \frac{OF_{s,i}}{\overline{OF}_i}. \tag{3.5}$$

3.2.3 Objective reduction

To identify key objectives of integrated process and fuel design, we apply the dominance-based MILP approach for objective reduction by Guillén-Gosálbez (2011) and Kostin et al. (2012). This approach reduces the number of objectives in the objective vector using mathematical optimization such that changes in the Pareto dominance structure are minimized, i.e., the major trade-offs of the original problem are covered. Before objective reduction is applied, it is required to normalize Pareto-optimal solutions used as input for objective reduction (see Section 3.2.2). In the following, we briefly explain the formulation of the optimization problem for the objective reduction. See Section A.2.3 for an exemplary minimization problem describing the underlying idea of this approach.

Here, the optimization problem for objective reduction is briefly summarized for completeness. For a more extensive description of the MILP formulation, see the work of Guillén-Gosálbez (2011) and Kostin et al. (2012). This MILP formulation is based on the problem of computing a "minimum objective subset of size k with minimum error" (k-EMOSS) by Brockhoff and Zitzler (2006). For q objectives in the full objective space F, the optimization problem seeks to minimize the maximum δ-error induced by omitting objectives:

$$\min_{s,s',i} \left(\delta_{s,s',i}\right) \tag{3.6}$$
$$s.\,t.\ \text{Equations (3.7)–(3.14)}$$

All solutions of the minimization problem must satisfy a set of constraints that are described in the following. The δ-error is the difference between solution s and solution s' regarding the ith objective (Equation 3.7). In this constraint, $OF_{s,i}$ represents the normalized value of the ith objective of Pareto solution s, whereas ZO_i and $ZD_{s,s'}$ are two binary variables. ZO_i is 1 if the ith objective is omitted while $ZD_{s,s'}$ is 1 if solution s dominates solution s' in the reduced objective space.

$$\delta_{s,s',i} = \left(OF_{s',i} - OF_{s,i}\right) ZO_i ZD_{s,s'} \quad \forall s \neq s',i \tag{3.7}$$

In Equations (3.8) and (3.9), $ZD_{s,s'}$ is calculated using a third binary variable $YP_{s',s,i}$, which is 1 if solution s is better than solution s' in the ith objective.

$$\left(q - \sum_i ZO_i\right) - q\,(1 - ZD_{s,s'}) \leq \sum_i YP_{s',s,i}\,(1 - ZO_i) \tag{3.8}$$

$$\leq \left(q - \sum_i ZO_i\right) + q\,(1 - ZD_{s,s'}) \quad \forall s \neq s'$$

$$\sum_i YP_{s',s,i}\,(1 - ZO_i) \leq \left(q - \sum_i ZO_i\right) - 1 + qZD_{s,s'} \qquad \forall s \neq s' \tag{3.9}$$

The following four equations are used to linearize the product of the binary variables ZO_i and $ZD_{s,s'}$ in Equation (3.7):

$$(OF_{s',i} - OF_{s,i})\,ZOD_{s,s',i} = \delta_{s,s',i} \qquad \forall s \neq s', i \tag{3.10}$$

$$ZOD_{s,s',i} \leq ZO_i \qquad \forall s \neq s', i \tag{3.11}$$

$$ZOD_{s,s',i} \leq ZD_{s,s'} \qquad \forall s \neq s', i \tag{3.12}$$

$$ZOD_{s,s',i} \geq ZO_i + ZD_{s,s'} - 1 \qquad \forall s \neq s', i \tag{3.13}$$

Lastly, the number of objectives to be omitted OB is prescribed:

$$\sum_i ZO_i = OB. \tag{3.14}$$

Note that alternative objective subsets may exist that exhibit equal δ-errors. To find those alternatives for a prescribed number of omitted objectives, we iteratively exclude previously found objective subsets from the solution space by adding integer cut constraints.

3.2.4 Correlation between two variables

Calculating the correlation coefficient is a common means to get a notion of the trade-off between variables. Often, the Pearson correlation coefficient is used to evaluate the degree of correlation between two variables for a given sample. Applied to our work, the variables are two objectives i and i', e.g., production cost and GWI. The sample comprises n solutions of the integrated process and fuel design. Regarding the

ith objective, $OF_{s,i}$ denotes the objective function value of the sth solution, whereas OF_i^{m} is the mean value of objective i. To calculate the degree of correlation between two objectives i and i', the Pearson correlation coefficient $r_{i,i'}$ is calculated as the ratio between the covariance of both objectives and the product of their standard deviations:

$$r_{i,i'} = \frac{\sum_{s=1}^{n} \left(OF_{s,i} - OF_i^{\mathrm{m}}\right)\left(OF_{s,i'} - OF_{i'}^{\mathrm{m}}\right)}{\sqrt{\sum_{s=1}^{n} \left(OF_{s,i} - OF_i^{\mathrm{m}}\right)^2}\sqrt{\sum_{s=1}^{n} \left(OF_{s,i'} - OF_{i'}^{\mathrm{m}}\right)^2}}. \tag{3.15}$$

Noteworthy, the Pearson correlation coefficient ranges between -1 and 1. Perfectly negative or positive correlation is implied by values of -1 or 1, whereas a value of zero implies that no linear correlation exists. For q objectives, a correlation matrix CM of size $q \times q$ can be constructed whose (i,i') entry is

$$cm_{i,i'} = r_{i,i'}. \tag{3.16}$$

In such a correlation matrix, all diagonal entries equal 1 since each variable is perfectly correlated with itself ($i = i'$). Negative or positive correlation may indicate a conflicting or redundant pair of objectives, respectively.

3.3 Integrated process and fuel design for spark-ignition engine fuels

We apply the above described solution procedure on a case study on integrated process and fuel design for spark-ignition engine fuels by König et al. (2021). In the following, we briefly review the main features of this case study and describe which aspects we adapt in this work. The case study considers 47 pre-screened fuel species as suitable fuel components for spark-ignition engines. For these fuel species, reaction routes for biomass and hydrogen conversion have been collected from literature and the authors' previous studies for the pathway model. Energy demands for downstream processing have been calculated with thermodynamically sound intermediate-fidelity methods for distillation columns (Bausa et al., 1998). As possible feedstocks, biomass, CO_2, and hydrogen are considered for fuel production.

For the fuel property model, pure-component data have been incorporated for all fuel species from databases, literature, and property prediction models. Fuel requirements for so-called ultra-high efficiency engine (UHEE) fuels have been adapted from previous studies (König et al., 2020). These UHEE fuel requirements have been derived for highly boosted spark-ignition engines with a high compression ratio, targeting high engine efficiency and low combustion-induced pollutant emissions. Considered fuel properties are the research octane number, density, oxygen content, olefin and aromatic content, surface tension, kinematic viscosity, enthalpy of vaporization, bubble point pressure, and distillation curve.

Goal and scope definition. The overall aim of this case study is to identify those environmental metrics that are key for the integrated process and fuel design of renewable spark-ignition engine fuels. For this purpose, this LCA's goal is to analyze the environmental impacts of production-optimal fuels with tailor-made properties for spark-ignition engines within a German fuel production setting. These environmental impacts are benchmarked with fossil gasoline and the KEAA blend of previous studies (König et al., 2021; Ackermann et al., 2021). For a consistent comparison among different fuels, we define the functional unit as "the provision of 1 GJ of enthalpy of combustion," as recommended by Müller et al. (2020a) and following previous work by König et al. (2021). The fuel production model comprises a well-to-wheel system boundary that considers the supply of feedstocks and utilities, the pathway model for fuel production, and fuel combustion with air (Figure 3.2). In contrast to previous studies, we do not allow fossil gasoline as a blending component since our aim is to design fully renewable fuels.

We characterize all material and energy flows exchanged with the environment according to the LCIA method EF 3.0, which is recommended by the Joint Research Centre of the European Commission (European Commission, 2018b). We, therefore, extend the objective space by 15 environmental objectives of the EF 3.0 method, in addition to the objectives production cost and GWI considered in previous case studies (König et al., 2021; Ackermann et al., 2021). An overview of the included impact categories with the corresponding abbreviations, units, and recommendation levels is presented in Table 3.1. The environmental impact categories have been classified with respect to their maturity into three recommendation levels: "Level I" is recommended and satisfactory, "Level II" is recommended but needs some improvements, and "Level III" is recommended but has to be applied with caution (European Commission, 2011). Consequently, the resulting objective vector contains in total one economic and 16 environmental objectives. Note that, in this work, solely environ-

mental objectives can be omitted by objective reduction to keep the only economic objective, production cost, in the key objective subset.

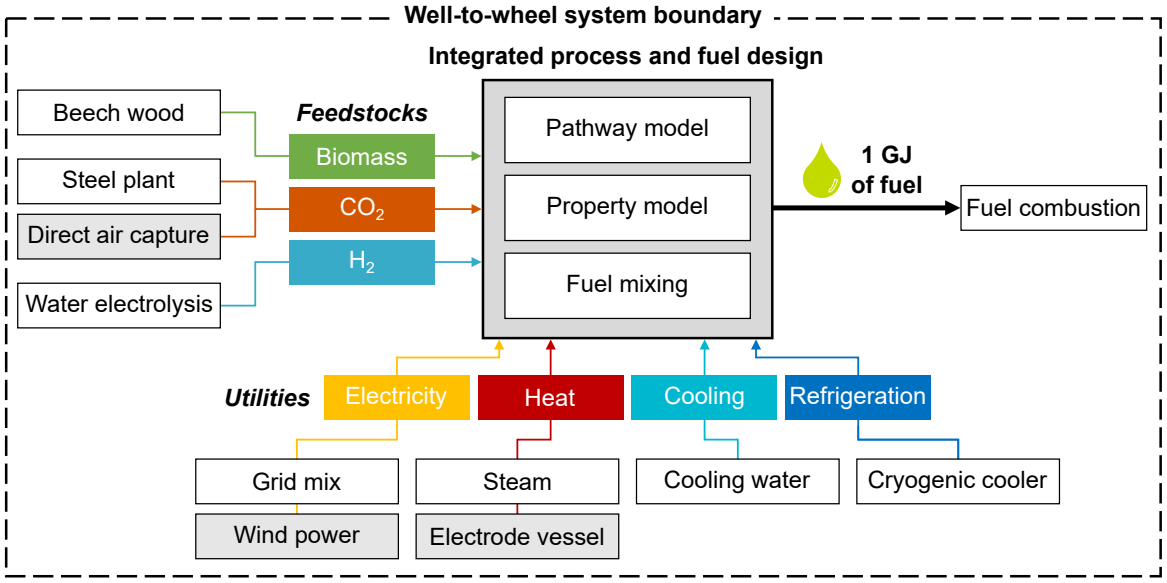

Figure 3.2: Well-to-wheel system boundary of fuels optimized by integrated process and fuel design. The functional unit is "the provision of 1 GJ of enthalpy of combustion." Light grey boxes denote technologies that are used in the 'future' scenario, e.g., electricity from wind power instead of the power grid.

Life cycle inventory. For the case study, we distinguish between a 'today' and a 'future' scenario to consider potential technology changes in feedstock and energy supply (Table 3.2). While the 'today' scenario represents incumbent technologies, the 'future' scenario portrays a likely, fully renewable energy system. As our 'today' scenario slightly adjusts LCA datasets and prices compared to the work of König et al. (2020, 2021), we analyze the implications of these adjustments in Section A.2.2.2. Overall, our adjustments result in a similar Pareto front for GWI and production cost, with slight increases in GWI scores due to our changes regarding the modeled steam and refrigeration supply. In the following, we briefly describe the inventory data used for the LCA as well as assumed prices for each scenario. A detailed overview of the LCA datasets is presented in Section A.2.1.

The feedstock CO_2 is either supplied by carbon capture at a steel plant or DAC. Carbon capture at a steel plant requires 0.87 MJ of electricity and 0.95 MJ of process heat per kg of captured CO_2, according to von der Assen et al. (2016). For DAC, we consider the predicted energy requirements of a temperature swing adsorption (TSA) system, following Deutz and Bardow (2021). Each kg of captured CO_2 via DAC requires 1.80 MJ of electricity and 5.40 MJ of process heat. The process heat for DAC is supplied by heat pumps with a modeled coefficient of performance of 3.28

Table 3.2: Scenario-specific technologies of the life cycle inventory for the integrated design of advanced spark-ignition engine fuels.

Inputs	**Scenario**	
	today	future
Feedstocks		
Carbon dioxide	Steel plant	Direct air capture
Biomass	Beech wood	
Hydrogen	Water electrolysis[a]	
Utilities		
Electricity[a]	Grid mix	Wind power
Process heat	Steam	Electrode vessel
Cooling	Cooling water	
Refrigeration	Cryogenic cooler	

[a] For water electrolysis, electricity from wind power is considered independent of the scenario.

(David et al., 2017). Beech wood is assumed as representative lignocellulosic biomass, using process data from the LCA database ecoinvent (Wernet et al., 2016). Note that no carbon credit, i.e., avoided burden, is given for CO_2 that is removed from the atmosphere by either biomass growth or DAC since this CO_2 is released again to the atmosphere at the fuel's end-of-life (König et al., 2021).

Designing renewable fuels necessitates renewable hydrogen production in both scenarios. Therefore, hydrogen is assumed to be supplied renewably via polymer electrolyte membrane (PEM) water electrolysis in both scenarios, using electricity from wind power. Using electricity from wind power for electrolysis also in the 'today' scenario reflects a realistic scenario of importing renewable energy via hydrogen. Already today, so-called green hydrogen hubs are developed by several large ports, e.g., those of Antwerp-Bruges, Rotterdam and Hamburg, to import and produce green hydrogen. These green hydrogen hubs are scheduled to start operating already by 2025 ("Shell Holland 1," "HyoffWind," "Plugpower") and 2026 ("Hamburg Green Hydrogen Hub"). The modeled PEM electrolysis requires 8.94 kg of water and 47.6 kWh of electricity from wind power per kg of hydrogen, using process data by Reuß et al. (2017).

Regarding utilities, we consider the provision of electricity, process heat, cooling, and refrigeration. We assume that electricity for other processes than water electrolysis is mainly supplied by the German grid in the 'today' scenario and by clean electricity from wind power in the 'future' scenario, using process data from ecoinvent (Wernet et al., 2016). Process heat is provided via steam or electrode vessel with a

power-to-heat efficiency of 95 % (Müller et al., 2020a). For cooling and refrigeration, the use of cooling water (Wernet et al., 2016) and cryogenic coolers is assumed, respectively. In this early-stage design, we assume a constant refrigeration temperature of $-100\,°C$ as a rough estimation and model cryogenic coolers with an energy efficiency ratio of 0.25, based on curve fit functions of Ladner (2011).

Use phase pollutants from non-ideal fuel combustion are not covered in integrated process and fuel design. Soot emissions for hydrocarbon fuels can be predicted using the particulate matter index by Aikawa et al. (2010), which predicts engine-out emissions based on the fuel's volatility and its chemical tendency to form soot. As a measure for the latter, the number of double bonds is used. However, soot chemistry becomes more complicated for oxygenated hydrocarbons since different oxygen functionalities reduce the formation of soot precursors in different degrees (Westbrook et al., 2006). While this effect is captured by the Yield Sooting Index by Das et al. (2018), the Yield Sooting Index does however not predict engine-out emissions. Further pollutant emissions like unburned hydrocarbons, carbon monoxide, and nitrogen oxides depend strongly on the engine operation and can therefore not be predicted at an early design stage. Additionally, engine efficiencies are disregarded for simplicity, i.e., it is assumed that different fuels could be used equally-efficient in spark-ignition engines (König et al., 2021).

For price estimations, we adopt prices from previous studies on integrated process and fuel design by König et al. (2020, 2021) where possible, maintaining comparability with preceding studies as much as possible. Due to the German scope of this study, the following prices are converted from United States dollar ($) to euro (€), using 2022's average exchange rate of 1.05 $ per €. These adopted prices comprise 7.5 $-ct per kWh of electricity from the grid (El-Halwagi, 2012), 9.5 $ per ton of steam (El-Halwagi, 2012), 6.5 $-ct per m^3 of cooling water (El-Halwagi, 2012), 5.78 $ per kg of hydrogen from water electrolysis using electricity from wind power (Grube and Höhlein, 2014), 50 $ per ton of biomass (Ruth, 2011), and 40 $ per ton of CO_2 captured at a steel plant (Quader et al., 2016). We further assume prices of 6.0 $-ct per kWh of electricity from wind power (Ueckerdt et al., 2013), 6.3 $-ct per kWh of process heat from electrode vessels using electricity from wind power with a power-to-heat efficiency of 95 %, and 200 $ per ton of CO_2 captured from ambient air (Sabatino et al., 2021; McQueen et al., 2021). Cryogenic refrigeration costs are modeled for the assumed refrigeration temperature of $-100\,°C$ and a two-stage compression refrigeration system, according to Luyben (2017): Refrigeration costs result in 22.4 or 18.9 $-ct per kWh of refrigeration if electricity from the grid or wind power is used, respectively.

3.4 Results

Both the continuous NLP of integrated process and fuel design and the MILP of the objective reduction approach are implemented in GAMS v35.2.0 and solved on a computer with an Intel E5-1660 v4 3.2 GHz processor and 128 GB of RAM. The continuous NLP is solved with the deterministic global solver BARON v21.1.13, using one thread, a branching priority of 20 on the molar fuel fraction, a time limit of 1000 seconds, and a relative optimality tolerance of 0.1 % (single objective optimization) or 1 % (bi- and multi-objective optimization). For the MILP, we use the solver CPLEX v20.1.0.1 and four parallel threads. Any other solver settings are left at default values. Similar to König et al. (2021), some solutions of the continuous NLP are globally optimal while other runs do not converge to the specified optimality even though we increased the time limit drastically. Likewise to previous work, the lower bound convergence stagnates for these runs, and we follow the assumption of König et al. (2021) that the found solutions are globally optimal.

After filtering out the initial 544 solutions S_{initial} (see Section 3.2), 156 and 158 unique solutions $S^{\text{today}}_{\text{filtered}}$ and $S^{\text{future}}_{\text{filtered}}$ remain for the 'today' and 'future' scenario, respectively. With these unique Pareto-optimal solutions, we construct correlation matrices for both scenarios to gain a first notion about conflicting and redundant objective pairs (see Section A.3.1). The correlation matrices indicate that the most conflicting objectives are land use in the 'today' scenario as well as land use and freshwater eutrophication in the 'future' scenario. Furthermore, weakly correlated objectives are production cost in both scenarios and freshwater eutrophication in the 'today' scenario. All other objective pairs show large coefficients in the correlation matrices, indicating redundancy among these objectives. We next normalize the scenario-specific filtered solutions with each normalization variant (see Section 3.2.2), yielding four normalized solution sets per scenario, e.g., $S^{\text{today}}_{\text{norm,N1}}$, $S^{\text{today}}_{\text{norm,N2}}$ and so on.

3.4.1 Identifying key environmental objectives

After generating the normalized solution sets, we identify key environmental objectives and redundant ones for each scenario. To analyze how the problem's dominance structure may change if we omit redundant objectives, we apply the dominance-based objective reduction approach (see Section 3.2.3). Thus, we quantify this change, i.e., the δ-error, as function of the number of omitted objectives for each normalization variant (Figure 3.3). Note that the normalization variants lead to different ranges of values regarding the normalized solutions and, consequently, resulting δ-errors. To en-

able comparability between δ-errors calculated with different normalization variants, we use the relative δ-error δ_{rel} introduced by Postels et al. (2015): For each normalization variant, the δ-error is referenced to its maximum value that occurs if all but one, i.e., 16 out of 17, objectives are omitted. Additionally, we specify a threshold δ^* of 0.1 to identify small objective subsets with still acceptable δ-error (Figure 3.3, dotted horizontal line).

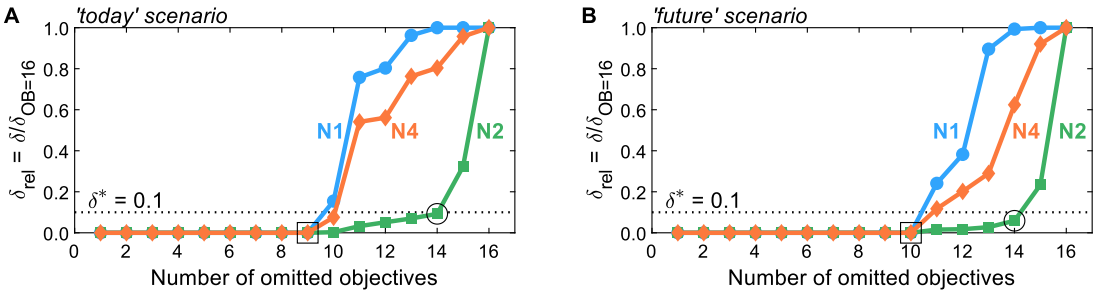

Figure 3.3: The δ_{rel}-error as function of the number of omitted objectives for normalization variants N1, N2, and N4 in the (A) 'today' and (B) 'future' scenario. Note that normalization variant N3 is not shown since it yields identical results as N2 because both variants differ only by a constant offset of 1. The threshold δ^* of 0.1 is introduced to identify small objective subsets with acceptable δ-error. For numerical results and the corresponding identified objective subsets, see Table A.6–A.7.

Regarding the determined threshold δ^* of 0.1, two numbers of omitted objectives are of greater interest: The maximum number of omitted objectives for which all (square, Figure 3.3) or at least one (circle, Figure 3.3) normalization variant is below the threshold. For both scenarios, many objectives can be omitted without inducing a δ-error, i.e., a change to the dominance structure of integrated process and fuel design. Without inducing a δ-error, up to nine and ten objectives can be omitted in the 'today' and 'future' scenario (square, Figure 3.3), respectively. In the 'today' scenario, all normalization variants result in the same minimal reduced objective subset without δ-error of $F_{OB=9}^{\text{today}} = (C, LU, RU_{\text{m}}, RU_{\text{e}}, WU, E_{\text{fw}}, HT_{\text{c}}, PM)^{\text{T}}$. In contrast, in the 'future' scenario, two minimal reduced objective subsets without δ-error are identified by all normalization variants: $F_{OB=10}^{\text{future,1}} = (C, LU, RU_{\text{m}}, RU_{\text{e}}, WU, ET, HT_{\text{nc}})^{\text{T}}$ and $F_{OB=10}^{\text{future,2}} = (C, LU, RU_{\text{m}}, RU_{\text{e}}, WU, ET, IR)^{\text{T}}$. Hence, the objectives production cost (C), land use (LU), resource use of minerals and metals (RU_{m}) and energy carriers (RU_{e}), and water use (WU) are present in the reduced objective subsets without δ-error of both scenarios.

With normalization variant N2, further objectives can be omitted while still maintaining a δ-error below the threshold δ^*. In both scenarios, up to 14 objectives can be omitted (circle, Figure 3.3), resulting in equal reduced objective subsets of $F_{OB=14}^{\text{N2,today}} = F_{OB=14}^{\text{N2,future}} = (C, LU, RU_{\text{m}})^{\text{T}}$ with δ-errors of 0.09 and 0.06, respectively.

The other normalization variants, N1 and N4, result in the same reduced objective subsets but with much greater δ-errors. In fact, normalization variant N1 reaches the maximal δ-error of one for 14 omitted objectives in the 'today' scenario, rendering the choice of the three objectives arbitrary. Notable, alternative objective subsets with equivalent approximation error and three objectives were not found. However, in near-optimal objective subsets, other sets of three objectives can be seen (e.g., land use (LU) and water use (WU)).

Overall, we find that the normalization variants considered herein do not affect the minimal reduced objective subsets without δ-error identified in both scenarios (square, Figure 3.3). If even smaller reduced objective subsets are targeted, normalization affects, however, both the identified reduced objective subsets and the induced δ-error. Nonetheless, land use (LU) and resource use of minerals and metals (RU_{m}) stand out against the other objectives since they are present in all reduced objective subsets for up to 14 objectives omitted, irrespective of the scenario and normalization variant (see Table A.6–A.7). We, therefore, suggest using land use (LU) and resource use of minerals and metals (RU_{m}) as key environmental objectives for integrated process and fuel design of spark-ignition engine fuels.

When we compare these findings with the constructed correlation matrices (see Section A.3.1), we find, as a priori expected, that correlation matrices alone provide insufficient information to select reduced objective subsets. Land use is the only objective that is conflicting with any other objective in the 'today' scenario while, in the 'future' scenario, land use and freshwater eutrophication are both in conflict with the other objectives. On the one hand, this degree of conflict matches our findings from objective reduction that land use is a key objective. On the other hand, the correlation matrices indicate that resource use of minerals and metals is correlated with the other objectives although it is also a key objective from objective reduction. Therefore, correlation matrices alone appear unsuitable for choosing key objectives since the error inherent to omitting objectives cannot be quantified.

3.4.2 Integrated process and fuel design with key environmental objectives

Based on our findings from objective reduction, we proceed with generating Pareto-optimal process and fuel designs for spark-ignition engine fuels in a reduced objective space (Figure 3.4). It would be sensible to perform the integrated fuel design with the minimal objective subset that does not induce a δ-error irrespective of the normalization variant (see square, Figure 3.3). However, multi-objective optimiza-

tion with eight objectives comes at the cost of high computational effort for a well-resolved Pareto front. Here, we thus choose the smaller reduced objective subset $F_{OB=14}^{\mathrm{N2,today}} = F_{OB=14}^{\mathrm{N2,future}} = (C, LU, RU_{\mathrm{m}})^{\mathrm{T}}$ containing both key environmental objectives land use (LU) and resource use of minerals and metals (RU_{m}) to gain a well-resolved Pareto front with manageable computational effort. Note though that this reduced objective subset induces a δ-error that is small for normalization variant N2 but large for N1 and N4 (see Section 3.4.1). We obtain 43 and 46 unique Pareto-optimal solutions for the 'today' and the 'future' scenario, respectively. The majority of Pareto-optimal solutions are bio-hybrid fuels, followed by bio-fuels and only one e-fuel (Table 3.3). For contribution analyses of these solutions, see Section A.3.4.

Table 3.3: Number of unique Pareto-optimal solutions by fuel type.

	Scenario	
	today	future
Total	*43*	*46*
Bio-fuels	19	18
E-fuels	1	1
Bio-hybrid fuels	23	27

In both scenarios, the bio-fuels yield the lowest production cost (C) and resource use of minerals and metals (RU_{m}) but highest land use (LU) (Figure 3.4A and B). In contrast, the e-fuel has minimal land use (LU) but highest scores in both other objectives (Figure 3.4C and D). Notably, in the 'future' scenario, e-fuels exhibit slightly higher production cost and resource use of minerals and metals: CO_2 supply by DAC is expected to be much more expensive than CO_2 capture from industrial point sources, e.g., capture at steel plants, resulting in increased production cost (see Figure A.5C and D). Additionally, the demand for minerals and metals increases as electrification with renewable energy is rising in all life cycle phases (see Figure A.6C and D). The bio-hybrid fuels can balance all three objectives (Figure 3.4E and F), leveling the advantages and drawbacks of bio- and e-fuels: lower land use (LU) scores than those of bio-fuels are possible but at the cost of increases in the other objectives and vice versa.

Based on the generated Pareto-optimal solutions, we next analyze trends in the full objective space and benchmark the generated solutions with gasoline and the KEAA blend, which was designed in a previous study considering only production cost and GWI (König et al., 2021). For the analysis of trends among the generated solutions, we normalize the solutions with variant N2 (Figure 3.5A and B). For the

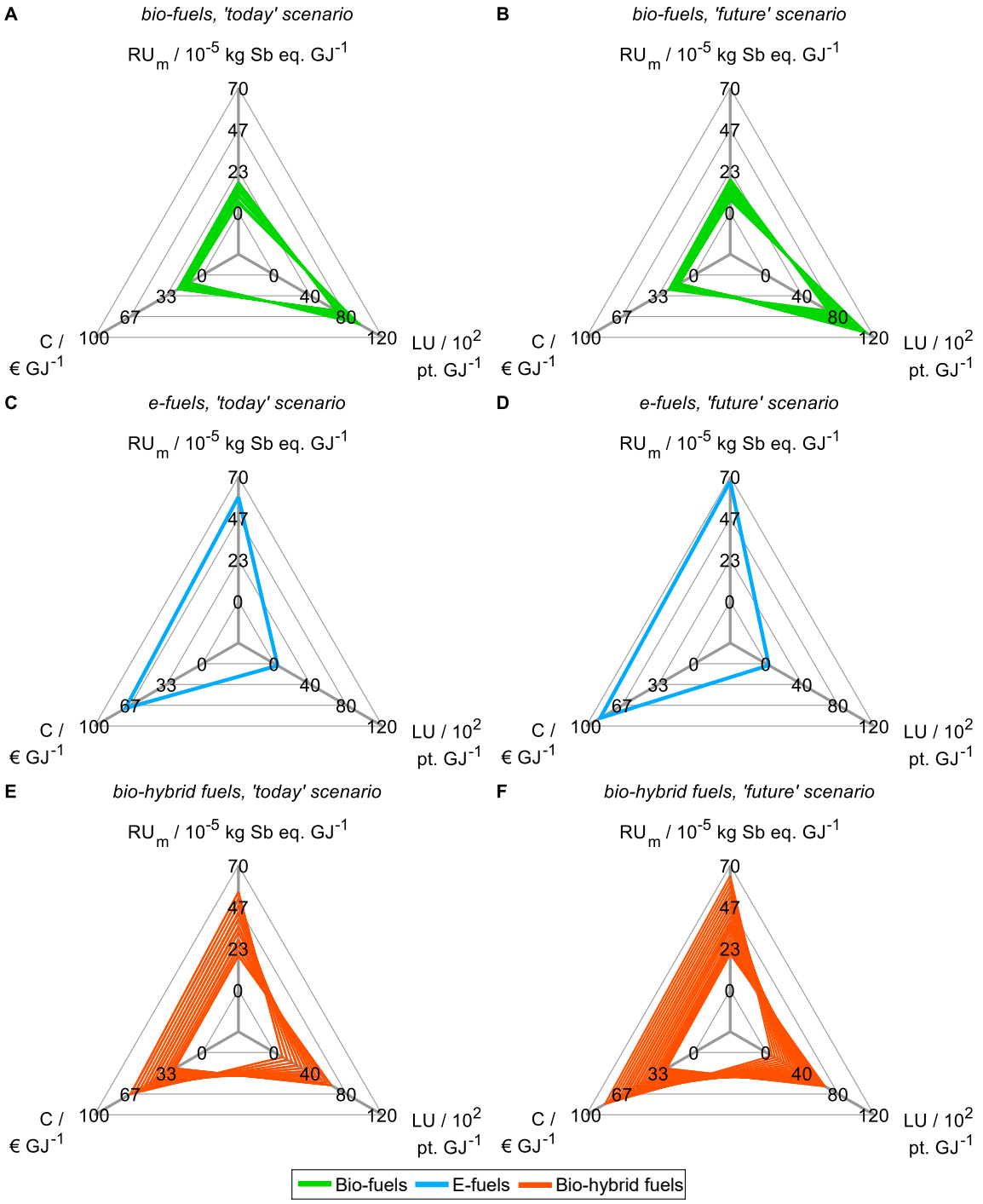

Figure 3.4: Pareto-optimal process and fuel designs of bio-, e-, and bio-hybrid fuels regarding the reduced objective space of the 'today' (A, C, E) and 'future' (B, D, F) scenario. See Figure A.3 for an alternative figure showing the single-objective minima of the Pareto-optimal solutions generated with the reduced objective subsets. For contribution analyses of these solutions, see Section A.3.4.

comparison with both benchmarks in Figure 3.5C and D, we normalize with variant N1 instead. With variant N1, all objectives are scaled to the range [0,1], facilitating the comparison especially for objectives with small variance among all generated solutions, e.g., acidification (A).

When we evaluate the Pareto-optimal solutions in the full objective space (Figure 3.5A and B), we see that land use (LU) and resource use of minerals and metals (RU_{m}) represent, as expected, the most apparent trade-off in both scenarios and for all fuels, i.e., the higher the land use the lower the resource use of minerals and metals and vice versa. Besides land use (LU) and resource use of minerals and metals (RU_{m}), there is also larger variance among solutions regarding production cost (C) and human toxicity (HT) for the 'today' scenario as well as additionally ecotoxicity (ET) and particulate matter (PM) for the 'future' scenario. Overall, the e-fuel performs worst in all objectives except for land use in the 'today' scenario and additionally in freshwater eutrophication (E_{fw}) in the 'future' scenario. Conversely, the bio-fuels rank worst for these objectives and best for all others. As already indicated by the results from the reduced objective space (see Figure 3.4), bio-hybrid fuels level the impacts of bio- and e-fuels in most objectives.

Comparing the generated solutions with the benchmark gasoline reveals that the designed synthetic fuels can achieve better or at least similar scores compared to gasoline in many objectives (Figure 3.5C and D). However, in both scenarios, gasoline has the lowest production cost (C), freshwater eutrophication (E_{fw}), human toxicity (HT), land use (LU), resource use of minerals and metals (RU_{m}), and water use (WU). For human toxicity (HT), electricity consumption is the main driver for the generated solutions (see Figure A.18–A.19). Depending on whether electricity from wind power or the grid is consumed, the major contributors are the production of either metals or lignite and hard coal, respectively, and associated waste treatment processes. Conversely, gasoline performs worse, if not worst, in ionizing radiation (IR) and ozone depletion (OD), acidification (A), GWI, ecotoxicity (ET), and resource use of fossil energy carriers (RU_{e}).

Benchmarking the generated solutions with the KEAA blend from previous fuel design studies (König et al., 2021; Ackermann et al., 2021) shows that the KEAA blend is still an exceptionally promising synthetic fuel, except for land use (LU). Apart from land use, the KEAA blend yields the lowest scores among all synthetic fuels for almost every objective in the 'today' scenario. Moreover, the KEAA blend is also among the best synthetic fuels in our 'future' scenario although the blend was originally designed for a scenario considering solely today's technologies (König et al., 2021; Ackermann et al., 2021). Nonetheless, we can identify bio-fuel designs among

our generated solutions that yield better scores than the KEAA blend in all objectives for the 'future' scenario (see Figure A.4).

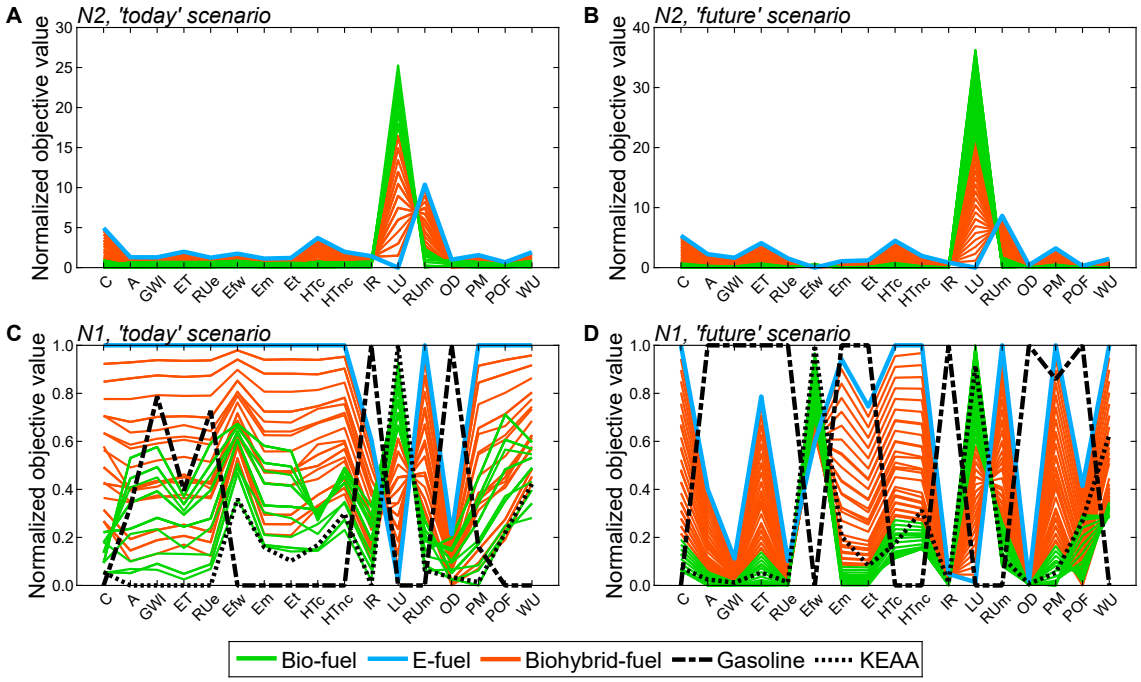

Figure 3.5: Pareto-optimal process and fuel designs of bio-, e-, and bio-hybrid fuels evaluated in the full objective space for the 'today' (A, C) and 'future' (B, D) scenario. In (A) and (B), each objective is normalized according to normalization variant N2 to analyze trends among the generated solutions. In (C) and (D), objectives are normalized with variant N1 to facilitate the comparison with both benchmarks gasoline and the bio-based KEAA blend. For consistency, the KEAA blend of previous studies is recalculated with our 'today' and 'future' scenario.

3.5 Discussion

Our findings indicate that up to nine or ten of 17 objectives can be omitted in early-stage fuel design for our 'today' or 'future' scenario, respectively. For these objective subset sizes, no error is induced regarding the approximated Pareto front, irrespective of the applied normalization variant. If even smaller objective subsets are desired for fuel design, one has to weigh the benefit of a decreasing computational effort in fuel design against the drawback of an increasing approximation error. Notably, the approximation error differs depending on the normalization variant applied. Normalization is thus a critical, arbitrary step since various normalization variants exist.

By reducing the objective space even further, we find that land use and resource use of minerals and metals are present in all reduced objective subsets irrespective of the scenario, normalization variant, and objective subset size. In our view, these results underline the relevance of both objectives to cover the major trade-offs in the design of bio-, e-, and bio-hybrid fuels for spark-ignition engines. We, therefore, consider land use and resource use of minerals and metals as key environmental objectives and suggest to include both, in addition to production cost, for fuel design.

Our integrated process and fuel design with these key environmental objectives and production cost demonstrates that bio-fuels yield among the best scores in most objectives but shift burdens to large increases in land use due to biomass cultivation. Conversely, the e-fuel has the lowest land use but the highest scores regarding all other objectives. We show that the generated bio-hybrid fuels can step in as balanced fuel designs: by using both biomass and renewable electricity as feedstocks, they can balance the benefits and drawbacks of bio- and e-fuels. Compared to the KEAA blend of previous studies (König et al., 2021; Ackermann et al., 2021), most blend components of the generated bio-hybrid fuels have similar shares, e.g., ethanol and ethyl acetate (see Section A.3.5). However, some blend components differ to a larger extent: the bio-hybrid fuels contain more than twice as much methyl acetate (45 %) as the KEAA blend, whereas methyl isopropyl ketone, one of KEAA's main components, is completely absent.

In the following, we discuss the generalizability of our findings towards a universal assessment of renewable fuels in terms of the considered product, the production scale, data gaps in the process model, and the methodological maturity of the environmental impact categories. We underline that the herein identified key environmental objectives are case-specific for the design of advanced spark-ignition engine fuels. However, we are confident that the key environmental objectives hold also for other liquid carbon-based energy carriers produced from renewable feedstocks, e.g., diesel-type fuels, since the involved processing steps are similar among different synthetic fuels. The two identified key environmental objectives land use and resource use of minerals and metals account for the fact that the production of renewable carbon-based energy carriers involves a step to chemically reduce CO_2, which is present in the atmosphere. In case of biomass, CO_2 reduction through photosynthesis requires land for biomass cultivation. For e-based energy carriers, CO_2 is reduced by hydrogen from renewable electricity via water electrolysis, which requires minerals and metals for the construction of wind parks and photovoltaic plants. These findings suggest that, for renewable fuels, both key environmental objectives also cover the trade-offs of GWI, which is strongly interconnected with CO_2.

The scale of fuel production modeled might change the identified subset of key environmental objectives. While we assume constant prices and environmental impacts of feedstocks and auxiliaries as input parameters for our model, these parameters can be expected to vary for different production scales. With increasing production scale, prices and environmental impacts of feedstocks and auxiliaries might change due to market effects such as the price elasticity of demand and LUC emissions induced by the development of new land for biomass cultivation or wind parks. Although such scaling effects could be modeled, in principle, by incorporating integrated assessment models into our framework, solving these models would further increase computational cost drastically.

Regarding data gaps in the process model, our findings might change if more detailed models of the transportation, production, and use phase are developed for the fuel design framework. Currently, the cost and environmental impacts of feedstock transportation are neglected. However, the supply of feedstocks, in particular renewable hydrogen, may require their production or cultivation in regions with high renewable energy potential and subsequent transportation around the globe. During fuel production, potential direct emissions are not covered since the fuel design framework was developed as an early-stage screening tool based on stoichiometry and yield data. In the use phase, combustion-induced pollutants, e.g., soot, nitrogen oxides, and carbon monoxide, are neglected since, so far, they cannot be predicted accurately at an early design stage.

Noteworthy, the environmental impact categories considered herein vary regarding their methodological maturity (Table 3.1), which might be an additional source of uncertainty for the identified key environmental objectives. Only three of 16 impact categories are classified as recommended and satisfactory. Although also recommended, the remaining 13 impact categories are still classified as in need of some improvement or to be applied with caution. For instance, human toxicity (HT) and the identified key environmental objectives land use (LU) and resource use of minerals and metals (RU_m) are recommended but should be applied with caution. Regarding human toxicity, it is questionable whether gasoline is actually less toxic to humans over the entire life cycle than all renewable fuels generated herein (see Figure 3.5C and D). This finding might hint at data gaps in the underlying LCIA methods because gasoline is well-known for its acute toxicity.

As a consequence, we recommend to verify our findings with the approach described herein if another product or production scale is studied. Likewise, the identified key environmental objectives should be verified if the fuel design framework is enhanced,

e.g., by a sophisticated engine model, or environmental impact categories are improved that are currently immature.

3.6 Summary and conclusion

In this chapter, we identify key environmental objectives for the *screening* of spark-ignition engine fuels via the integrated process and fuel design framework. For this purpose, we add 15 common environmental impact metrics of the LCA methodology as additional objectives to the integrated process and fuel design framework by König et al. (2021). We analyze a 'today' and a 'future' scenario to consider technology changes in feedstock and utility supply. To identify a reduced objective subset covering the problem's key trade-offs, we use a dominance-based optimization approach to reduce the number of objectives in the objective vector with minimal changes to the problem's dominance structure. As it is advantageous to normalize input data for this objective reduction approach, we evaluate the normalization's influence on the identified reduced objective subset and the induced change to the problem's dominance structure. Lastly, Pareto-optimal process and fuel designs are generated for the identified reduced objective subset.

Overall, we consider land use as well as resource use of minerals and metals as key environmental objectives, covering the major trade-offs of integrated process and fuel design for advanced spark-ignition engine fuels. Therefore, we recommend to include both as additional objectives to production cost in future fuel design studies. As demonstrated herein, we suggest to evaluate the identified key objectives regarding their robustness towards different normalization variants since normalization of input data for objective reduction is arbitrary. Using these three objectives for integrated process and fuel design, we show that the obtained bio-hybrid spark-ignition engine fuels can balance the benefits and drawbacks of pure bio- and e-fuels.

Lastly, we stress that our recommendations on key environmental objectives refer explicitly to early-stage process and fuel design. In this context, the emphasis is on using as few objectives as possible to reduce the computational effort without neglecting major trade-offs of the optimization problem. Therefore, our recommendations by no means imply that objectives identified as redundant for fuel design are negligible for overall decision-making. For instance, the objective global warming impact is surprisingly not suggested as key environmental objective for early-stage fuel design, indicating that its trade-offs with the other objectives can be adequately captured by the reduced objective subsets identified in this work. Nonetheless, global warming

impact represents one of the most important metrics in decision-making to evaluate the climate change mitigation potential of new technologies.

As the next step of the herein proposed fuel design procedure, the *screened* synthetic fuels need to be further narrowed by *filtering* out only those fuels that can meet key challenges of synthetic fuels.

Chapter 4

Addressing key challenges of synthetic fuels

In the previous chapter, we identified key environmental objectives for the *screening* of synthetic fuels. This group of synthetic fuels needs to be further narrowed by *filtering* out only those fuels that can meet four key challenges: (1) technological maturity for timely production at scale, (2) compatibility with fuel standards and sealing materials, (3) reducing urban air pollutants, and (4) enabling net-zero GHG emissions.

In this chapter, we check on the example of HyFiT-fuels whether all key challenges can be addressed simultaneously (Figure 4.1). For this purpose, a production concept is developed based on mature technological concepts. We also measure common fuel properties, conduct material compatibility tests, and determine combustion-related NO_x and PM emissions. Additionally, a well-to-wheel LCA for a heavy-duty vehicle benchmarks HyFiT-fuels with fossil diesel and a fully electrified powertrain.

Section 4.1 describes the measurement of fuel properties, material compatibility, and combustion emissions as well as the LCA. The process concept for HyFiT-fuel production is presented in Section 4.2. Results for HyFiT-fuel usage are described in Section 4.3. In Section 4.4, environmental impacts of HyFiT-fuels are evaluated and benchmarked. We conclude our findings in Section 4.5.

Major parts of this chapter are reproduced by permission of Springer Nature from:

Völker, S., Groll, N., Bachmann, M., Müller, L., Neumann, M., Kossioris, T., Muthyala, P., Lehrheuer, B., Hofmeister, M., Vorholt, A., Schmitz, K., Pischinger, S., Leitner, W., and Bardow, A. (2024). Towards carbon-neutral and clean propulsion in heavy-duty transportation with hydroformylated Fischer-Tropsch fuels. *Nature Energy*, **9**(10), 1220-1229.

Contribution report: Writing the draft, principal author, conceptualization, process modeling, the LCA case study, evaluation and visualization of LCA results and key performance indicators.

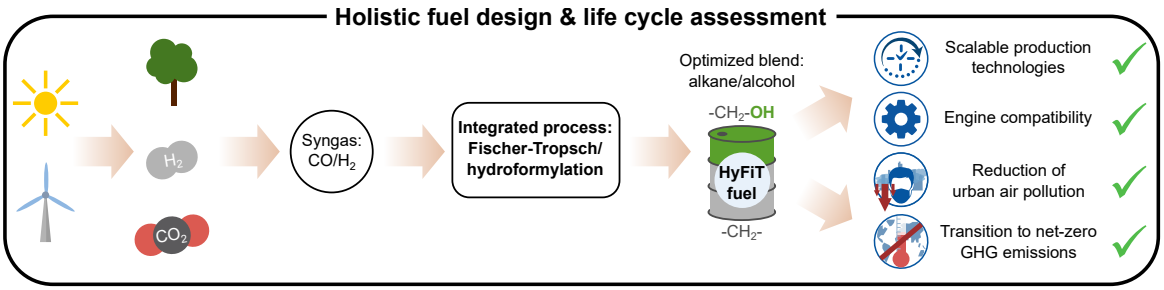

Figure 4.1: Holistic approach comprising fuel design and life cycle assessment of hydroformylated Fischer-Tropsch (HyFiT) fuels to validate their potential as possible diesel substitutes.

4.1 Methods

In this section, we briefly describe the methods to determine fuel properties, material compatibility, combustion emissions, and environmental impacts of HyFiT-fuels. For more details on calculations and conducted experiments, see Section B.2.

4.1.1 Fuel properties and material compatibility

Experiments were conducted for both pure and additivated HyFiT-fuels to investigate fuel properties and material compatibility. For the additivated fuel, 2000 ppm of the additive R655 are blended with the fuel, which is within the range suggested by Luecke and Zigler (2021). Determined fuel properties are the lower heating value (LHV) and, as standardized in the EN 590: density, viscosity, lubricity, and derived cetane number (DCN). While the HyFiT-fuel's LHV is calculated, the other properties are measured in experiments. The density is determined by buoyancy tests using the Archimedes principle. The viscosity is measured using an Ubbelohde type viscometer, according to DIN 51562. For the lubricity, high-frequency reciprocating rig tests were conducted, as described in DIN EN ISO 12156-1. The DCN was determined using the Advanced Fuel Ignition Delay Analyzer (AFIDA) (Seidenspinner et al., 2015), following the ASTM D6890 and D8183 standards. The experiments on compatibility with sealing materials follow DIN ISO 1817. Therein, the change of mass, hardness, and volume is evaluated for the three reference elastomers fluorine rubber (FKM), nitrile butadiene rubber (NBR), and hydrogenated nitrile butadiene rubber (HNBR), according to DIN ISO 13226. For more details, see Section B.2.1.

4.1.2 Fuel combustion

For vehicle testing, a light commercial van was investigated that has a vehicle mass of 3.3 t, a plug-in hybrid powertrain with a battery capacity of 14 kWh, and an electric motor with 95 kW peak power (Schaub et al., 2020a,b). Based on its maximum vehicle mass of 5.5 t when fully loaded, the baseline conventional vehicle was certified according to the Euro 6d heavy-duty standards. Emissions from fuel combustion were measured for diesel and additivated HyFiT-fuels in the Worldwide Harmonized Light Vehicles Test Cycle (WLTC) (European Commission, 2019) with the maximum speed limited to 120 km h^{-1}. To ensure the reproducibility of the provided emissions results in the WLTC and under these testing boundary conditions, the vehicle tests were repeated several times for each fuel, in order to primarily eliminate the driver's effect on the results. For plug-in hybrid vehicles, the test procedure provides a charge sustain mode: the difference between the state of charge (SOC) of the battery at the beginning and end of the test cycle must not exceed 1 %. However, SOC deviations greater than 1 % occurred for two reasons (see Figure B.5): the LHVs of HyFiT-fuels do not correspond to that of diesel, and the vehicle calibration was not adjusted to the HyFiT-fuels. Consequently, fuel consumption, PM, and NO_x emissions were corrected according to these SOC deviations to maintain comparability between different fuels. For more details, see Section B.2.2.

4.1.3 Life cycle assessment

In this section, we outline the goal and scope definition of the LCA of HyFiT-fuels, comprising goal and scope, system boundary, functional unit, and impact assessment. Additionally, we describe the inventory data used in the LCA in more detail.

Goal and scope. The goal of this LCA is to assess the well-to-wheel environmental impacts of using HyFiT-fuels in a heavy-duty van in 2030 within a global setting. These environmental impacts are compared with two benchmarks: a heavy-duty van powered by fossil diesel as today's benchmark and a fully battery-electric van as a future benchmark. The applied system boundary comprises the supply of feedstocks and utilities, the production of syngas, HyFiT-fuel, and the battery, as well as driving the van to provide the service of transportation (Figure 4.2).

Our analysis considers a large-scale HyFiT-fuel production plant for which we neglect plant construction since environmental impacts of FT plants are mostly dominated by energy and feedstock demands (Freire Ordóñez et al., 2021; Liu et al., 2020; Cuéllar-Franca et al., 2019). Moreover, the scale-up analysis on FT plants by Cuéllar-

Franca et al. (2019) underscores that environmental impacts due to plant construction decrease substantially with increasing plant capacity until they are even negligible for large-scale production capacities, e.g., the Bintulu gas-to-liquid plant in Malaysia. We thus focus on the influence of energy and feedstock demands. Further scaling-effects on environmental impacts that might occur, e.g., through changes in heat integration and energy efficiency, are not considered since our first conceptual analysis focuses on developing and evaluating a suitable process concept. Moreover, we neglect vehicle construction except for the battery since the environmental impacts of fuel-powered and battery-electric vans differ mostly in terms of direct emissions, battery production, and the supply of energy carriers for driving, i.e., fuel or electricity (Sacchi et al., 2022).

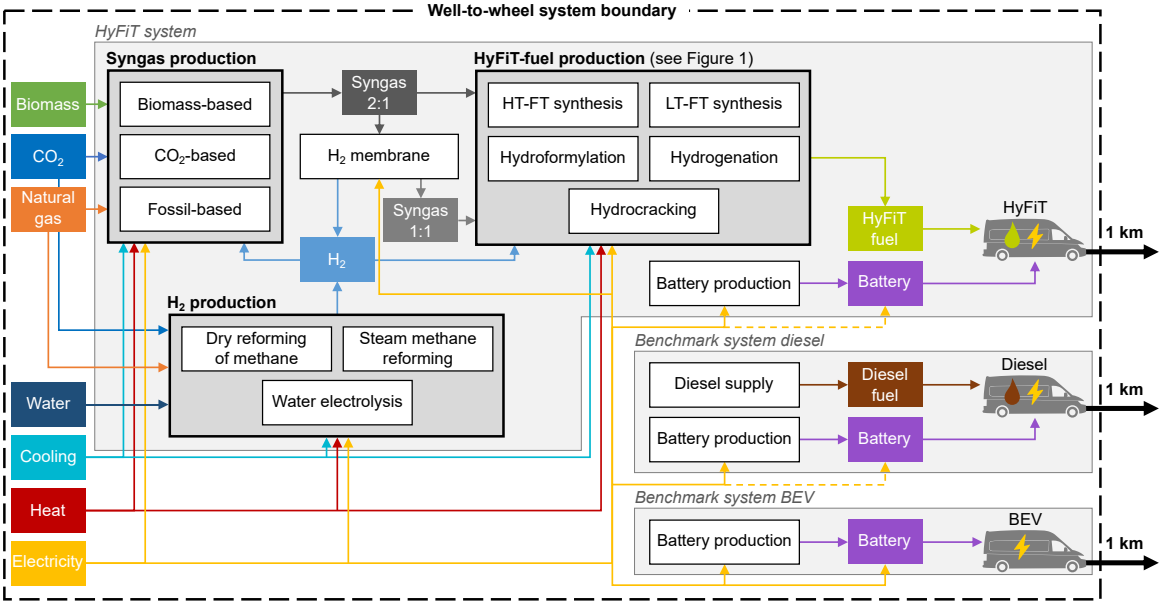

Figure 4.2: The system boundary for the well-to-wheel LCA of the HyFiT system (top), benchmark system diesel (middle), and benchmark system BEV (bottom). The functional unit for all three systems is "the provision of 1 km of transportation in a van." In the HyFiT and diesel benchmark systems, the hybrid van has a battery with a capacity of 14 kWh in addition to its internal combustion engine. In contrast, in the BEV benchmark system, the fully electric van has a battery capacity of 153 kWh. Syngas for HyFiT-fuel production can be produced from either biomass, CO_2, or natural gas. Note that the battery is recharged by fuel combustion at the end of a hybrid vehicle's test cycle, which is why electricity for battery charging is shown as dashed arrow for the hybrid vans.

Functional unit and impact assessment. Comparing production systems consistently requires a common basis. This common basis is called functional unit in LCA. Here, we define the functional unit as "the provision of 1 km of transportation in a heavy-duty van," following the recommendations of Müller et al. (2020a). We

characterize all material and energy flows exchanged with the environment according to the method EF 3.0 recommended by the Joint Research Centre of the European Commission (European Commission, 2018b). Thereby, we consider all impact categories covered by the EF 3.0 method (see Table B.6). Note that from here on, we use the term carbon footprint when referring to climate change. In Section 4.4, we optimize the HyFiT-fuel supply chain for minimal carbon footprint and evaluate this carbon-footprint-optimal supply chain for other impact categories.

Life cycle inventory. Here, we present the inventory data for the LCA (Figure 4.2), except for HyFiT-fuel production which is described in detail in Section 4.2. As feedstocks, we consider natural gas, biomass, and CO_2 for syngas production. For the supply of natural gas, process data from the LCA database ecoinvent is used (Wernet et al., 2016). As biomass feedstock, we use miscanthus as a perennial energy crop and second-generation biomass to avoid the "food versus fuel" conflict of first-generation biomass. Process data for miscanthus supply is taken from ecoinvent (Wernet et al., 2016). Note that we do not consider LUC emissions in the manuscript but present a sensitivity analysis in Section B.5.4.2. For CO_2 supply, we assume DAC and include the energy requirements from the predicted energy targets of an industrial TSA DAC system of Deutz and Bardow (2021). We give a credit for CO_2 that is used after removing it from the atmosphere by biomass growth or DAC (Müller et al., 2020b). However, this CO_2 is released again during the combustion of the HyFiT-fuel, by-products, and purge gas streams, and is accounted for in the LCA.

As the FT synthesis and hydroformylation both require syngas as input, we incorporate the syngas production network by Bachmann et al. (2023a). Here, we give a concise summary of the most important aspects of this network and refer the reader to Bachmann et al. (2023a) for an in-depth description. This syngas production network supplies syngas from natural gas, biomass, or CO_2 at 30 bar with an H_2:CO ratio of 2:1, based on engineering-level data. Since the HT-FT synthesis and hydroformylation both require syngas with an H_2:CO ratio of 1:1, we model a ceramic membrane separation unit in which excess H_2 can be separated by membrane permeation to lower the syngas' H_2:CO ratio (see Section B.3.1).

For fossil-based syngas, steam reforming and partial oxidation of methane are considered. In the case of steam methane reforming, syngas has an H_2:CO ratio of 3:1. This ratio is adjusted to 2:1 by either separating additional H_2 after the reactor (H_2 skimming) or feeding additional CO_2 to the reactor (CO_2 import). Bio-based syngas is either produced in a pressurized direct oxygen-steam blown circulating fluidized bed (CFB) or in an atmospheric indirect air-blown dual fluidized bed gasifier. The syngas' H_2:CO ratio is adjusted to 2:1 by water-gas shift or addition of H_2. For CO_2-

based syngas, three technologies are considered: dry reforming of methane with CO_2 as co-reactant, reverse water-gas shift of CO_2 and H_2, and the Sabatier process for methane production from CO_2 and H_2. Methane from the Sabatier process is subsequently converted to syngas via steam reforming, partial oxidation, or dry reforming of methane. Note that, in contrast to Bachmann et al. (2023a), we do not consider high-temperature CO_2-electrolysis and co-electrolysis of CO_2 and water since both are still technologically immature for large-scale syngas production (Jarvis and Samsatli, 2018).

The co-reactant H_2 can be produced fossil-based or from renewables. While fossil-based H_2 is supplied via steam reforming of natural gas, renewable H_2 can be produced via three pathways: (1) by water electrolysis using low-carbon electricity or via renewable methane from the Sabatier reaction and its subsequent (2) steam reforming or (3) dry reforming (with CO as co-product). Process data for water electrolysis is taken from the PEM electrolysis by Bareiß et al. (2019).

For cooling purposes, we distinguish between cooling water above 10 °C and refrigeration below 10 °C. Cooling water is modeled with process data from ecoinvent (Wernet et al., 2016), a specific heat capacity of $4.18\,\mathrm{kJ\,kg^{-1}\,K^{-1}}$, and a maximum temperature increase of 10 K. Refrigeration is modeled by cryogenic coolers based on curve fit functions by Ladner (2011): The electricity consumption to provide refrigeration is calculated as a function of the required refrigeration temperature.

Process heat demand is differentiated between heat below 100 °C, between 100 °C and 250 °C, and above 250 °C. We include fossil-based and power-to-heat technologies whose application depend on the temperature level of the heat demand. As fossil-based technologies, we consider generic natural gas boilers (heat above 250 °C) and steam production in the chemical industry (heat below 250 °C), using process data from ecoinvent for both (Wernet et al., 2016). For power-to-heat, we assume electrode boilers with a power-to-heat efficiency of 95 % (heat above 100 °C) (Müller et al., 2020a) and heat pumps with a constant coefficient of performance (COP) of 3.28 (heat below 100 °C). The COP is averaged from heat pumps built since 2006 with condenser temperatures of about 90 °C and evaporator temperatures between 9 to 15 °C, according to David et al. (2017). Note that we perform pinch-based heat integration ($\Delta T_{\mathrm{min}} = 10$ K) after supply chain optimization to minimize external heating and cooling demands.

Electricity is supplied either by the grid or wind power which serves as a best-case proxy for a future low-carbon grid. As a consequence, each kilowatt-hour of wind power is assumed to be directly used although, in reality, intermittent wind energy would require energy storage to ensure steady-state operation of CO_2 supply

by direct air capture, syngas production from CO_2 and biomass, and fuel production. To capture systemic changes in the underlying electricity grid, we follow the approach by Reinert et al. (2020) and model the EU grid mix in 2030 based on the "2 °C scenario" of the International Energy Agency (2017). Process data to model the EU grid mix 2030 and electricity from wind power is taken from ecoinvent (Wernet et al., 2016).

Driving the fully battery-electric van is modeled with the python package "carculator" of version 1.7.0 by Sacchi et al. (2022). For this purpose, we evaluate a BEV in 2030 and adjust the parameters cargo and battery mass, such that a minimum driving range of 400 km is maintained. The total driving mass, including battery mass, is adjusted to the 3.3 t of the van with ICE (see Section 4.1.2). The remaining parameters are left at default values. The most important default parameters are 200,000 lifetime kilometers for both the vehicle and the battery, 12,000 driven kilometers per year, an NMC-622 battery with a cell energy density of 0.3 $kW\,h\,kg^{-1}$, and China as the country of battery production. The adjustments lead to a modeled BEV with a battery weighing 680 kg and a capacity of 153 kWh, resulting in a driving range of 430 km. The electricity consumption for battery production and driving the van results in 0.051 $MJ\,km^{-1}$ and 1.195 $MJ\,km^{-1}$, respectively. In Section B.5.4.1, battery lifetime and capacity are varied in sensitivity analyses.

For driving the van with ICE, we consider the LHV of HyFiT-fuel (see Figure 4.5A) and diesel (42.8 $MJ\,kg^{-1}$) and the required chemical energy per kilometer (see Figure B.12). Combustion-related CO_2, PM, and NO_x emissions are presented in Section 4.3.2 and stem from our vehicle tests with diesel and additivated HyFiT-fuels described in Section 4.1.2. Note though that the production-related environmental impacts of the fuel additive R655 are not considered since data on its production and composition is proprietary and thus lacking. However, the additive's contribution to the overall well-to-wheel environmental impacts can be expected to be negligible due to its low concentration of 2000 ppm in the fuel blend. For the battery of the hybrid van with ICE (see Section 4.1.2), we model a battery with a capacity of 14 kWh in the "carculator," leaving the remaining parameters again at default values. The electricity consumption for battery production results in 0.005 $MJ\,km^{-1}$. Note that the battery is recharged by fuel combustion at the end of a hybrid vehicle's test cycle, as defined by the battery charge sustain mode of the Worldwide Harmonized Light Vehicles Test Procedures (WLTP). Therefore, for battery recharging, no electricity is consumed but additional fuel. Process data for the supply of fossil diesel is taken from ecoinvent (Wernet et al., 2016). For more details on the used LCA datasets, see Table B.7.

4.2 HyFiT-fuel production

The promising initial results for blends of FT diesel and long-chain alcohols (see Section 2.2.3.2) shifted the focus to the next step of systematic fuel design: developing a process concept for the integrated production of blends of FT diesel and long-chain alcohols with a targeted carbon range of C_6-C_{11}. Blends of FT diesel and alcohols could in principle be produced by higher alcohol synthesis, e.g., modified Fischer-Tropsch synthesis (m-FTS), or by combining FT synthesis and hydroformylation. While "higher alcohols" of m-FTS denote typically C_3-C_5 alcohols beyond ethanol (Surisetty et al., 2011), the combination of FT synthesis and hydroformylation can also generate alcohols with longer chains. Additionally, m-FTS can only reach high selectivities to C_{2+} alcohols at the expense of CO conversion (Luk et al., 2017).

In contrast, the combination of FT synthesis and hydroformylation allows to maximize the carbon yield for all components in the resulting fuel by integrating streams of alkanes and olefins of various chain length from the crude FT fraction. Moreover, using the crude FT fraction directly can be expected to positively influence the cost structure: Today's hydroformylation processes use single-chain-length olefins as substrates, which are the major cost driver as their production requires several process steps in the petrochemical value chain (e.g., ALFEN or SHOP process). In this study, we thus focus on the combination of FT synthesis and hydroformylation to produce blends of FT diesel and long-chain alcohols.

Like FT synthesis, hydroformylation is a well-established process (Wiese and Obst, 2006). In the proposed concept, FT synthesis is tailored beyond the alkane fraction towards a product that is rich in olefins. These olefins in the FT product are subsequently converted with syngas to alcohols by a hydroformylation and hydrogenation sequence (Franke et al., 2012). Consequently, the product is a hydroformylated Fischer-Tropsch fuel (HyFiT-fuel) consisting of the desired blend of long-chain alcohols and alkanes. This approach combines the well-established FT synthesis and hydroformylation therefore in a way that we regard as "drop-in technologies leading to a drop-in fuel." While we see great potential to improve the production chain through technologies such as one-pot synthesis, novel catalysts and process intensification, the urgency of the climate issue motivates us to focus on a solution which could be implemented today.

The combination of FT synthesis and hydroformylation has been explored in the REDIFUEL project of the EU (Heuser et al., 2020). In this project, novel FT catalysts (Jeske et al., 2021) and hydroformylation processes (Rösler et al., 2021; Püschel et al., 2021, 2022a,b) as well as a tandem integration of FT synthesis and hydroformylation

for one-pot REDIFUEL production were developed (Jeske et al., 2022). Based on these novel concepts, a blend of REDIFUEL and used cooking oil was shown to reduce GHG emissions by 27-64 % compared to fossil diesel (van den Oever et al., 2022, 2023). However, such novel FT catalysts and process concepts are not yet industrially established and subject of ongoing research, rendering their timely availability on large scale unlikely.

Consequently, herein, we present a concept for the near-term production of HyFiT-fuels. The major process steps of the proposed HyFiT-fuel production are shown in Figure 4.3 (details in Section B.3). In this concept, syngas for FT synthesis and hydroformylation is either produced from natural gas, biomass, or CO_2. H_2 from water electrolysis is considered as highly energetic co-reactant for the conversion of the inert CO_2. As water electrolysis requires large amounts of electricity, renewable or low-carbon electricity is required to keep environmental impacts at minimum. The FT synthesis is tailored in such a way that its product spectrum is shifted from alkanes towards olefins in the naphtha cut (C_5-C_{10}), since these olefins are desired intermediates to produce alcohols via subsequent hydroformylation and hydrogenation. Hydrocarbons in the distillate cut (C_{11+}) are sent to a hydrocracking unit, such that the resulting HyFiT-fuel consists of C_6-C_{11} alcohols and C_5-C_{17} alkanes.

The overall carbon efficiency of the process concept is strongly affected by the fate of unconverted CO that is treated in the gas loop (Klerk, 2011). This study considers

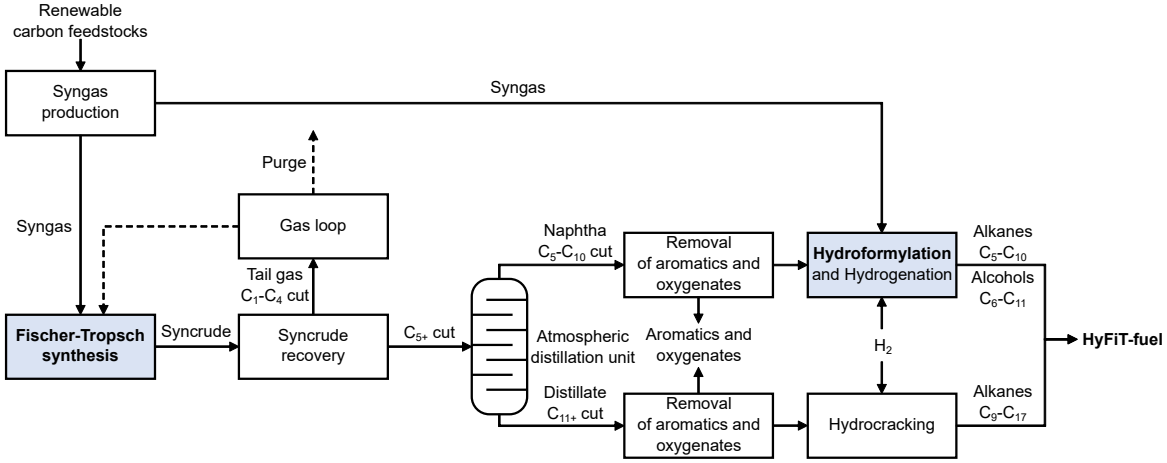

Figure 4.3: Simplified process concept for the production of HyFiT-fuels. Note that we do not differentiate between the low-temperature and high-temperature FT synthesis for the sake of better readability. Depending on the supply chain optimization, by-products, e.g., aromatics and oxygenates, are either incinerated for heat recovery followed by optional CO_2 capture or flared. For detailed process flowsheets of all involved process steps see Section B.3.2.

the two extremes of the gas loop: an open-loop and a closed-loop design (Dry and Steynberg, 2006). Here, we show results for the open-loop design without tail gas recycle. Results for the closed-loop design are presented in Section B.5.1. To enable rapid deployment, the proposed HyFiT-fuel production integrates mature technologies, yet in an unprecedented design framework. As a consequence, the resulting HyFiT-fuels match and even exceed the carbon efficiency of previous FT-fuels, in particular for the bio-based route (see Section B.5.5). At the same time, the resulting yields of up to 83 % at CO conversions above 95 % match and even exceed the C_2-C_5 alcohols formed with state-of-the-art m-FTS systems (Figure 4.4) (Luk et al., 2017).

The HyFiT-fuels' alcohol-alkane ratio influences fuel properties, material compatibility, combustion emissions, and environmental impacts. To adjust the alcohol-alkane ratio, this conceptual analysis models and combines two types of FT synthesis: low-temperature (LT) and high-temperature (HT) FT synthesis. LT-FT synthesis uses cobalt-based catalysts which yield a syncrude of mostly long-chain alkanes, only few oxygenates, and almost no aromatics (Klerk, 2011). Iron-based catalysts are usually used for HT-FT synthesis for less hydrogenation. Thus, the syncrude of HT-FT synthesis contains much more short-chain olefins in addition to alkanes.

By combining both LT-FT and HT-FT synthesis, we can vary the alcohol-alkane ratio and study its impact on fuel properties and material compatibility (Section 4.3.1), emissions from fuel combustion (Section 4.3.2), and environmental impacts (Section 4.4). Such combined LT-FT and HT-FT synthesis have already been industrially

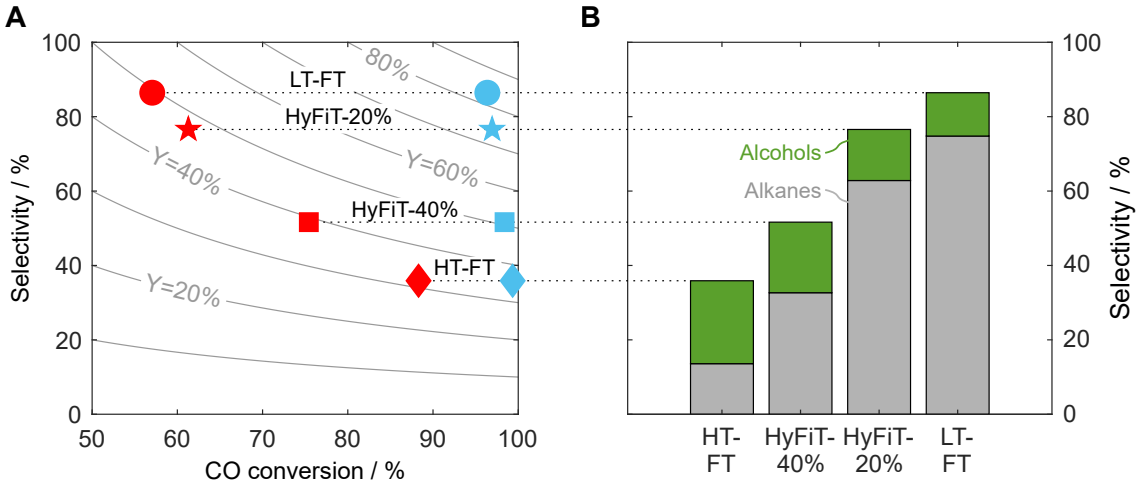

Figure 4.4: (A) HyFiT-fuel selectivity as a function of CO conversion, with yield (Y) values as contour curves. Results are presented for the open (red) and closed (blue) gas loop design. (B) Alcohols and alkanes selectivities of HyFiT-fuels. For further details, see Section B.3.4. LT: low-temperature, HT: high-temperature, FT: Fischer-Tropsch.

demonstrated in the Sasol 1 and PetroSA FT facilities (Klerk, 2011). Note that, alternatively, dedicated catalysts can be designed to produce either tailored olefin-alkane ratios with one FT reactor or even desired alcohol-alkane ratios by tandem integration of FT and hydroformylation catalysts in one-pot reactors, as demonstrated by Jeske et al. (2021, 2022). However, such concepts are still subject of ongoing research and not yet industrially established.

4.3 HyFiT-fuel usage

The HyFiT-fuel's alcohol-alkane ratio was varied between 15 wt% (LT-FT synthesis) and 65 wt% (HT-FT synthesis) to study its effect on fuel usage, i.e., fuel properties, material compatibility, and fuel combustion.

4.3.1 Fuel properties and material compatibility

Experiments were conducted for both pure and additivated HyFiT-fuels. Following current fuel standards, we considered the LHV, DCN, density, viscosity, and lubricity (Figure 4.5A). For material compatibility, we analyze the change of mass, hardness, and volume for the reference elastomers FKM, NBR, and HNBR that are common in diesel and gasoline systems (Figure 4.5B). The shown limits are taken from common fuel standards, e.g., the EN 590, and Richter (2014, 2022).

No alcohol content is optimal for all examined fuel properties (Figure 4.5A): With increasing alcohol content in the HyFiT-fuel, density and viscosity increase while LHV, DCN, and lubricity decrease. The LHV is not limited in fuel standards and is in the range of fossil diesel ($42.8\,\mathrm{MJ\,kg^{-1}}$) for alcohol contents between 15 and 40 wt%. Experiments for DCN, density, viscosity, and lubricity were additionally conducted with using the additive R655. Thereby, lubricity values were strongly improved but DCN, density, and viscosity showed no effect. For the DCN, an alcohol content of less or equal to 40 wt% is preferable to stay above the EN 590 limit of 51. None of the density values is within the limits of EN 590, although the density increases with higher alcohol contents. Still, all density values are within the range of common country-specific fuel standards. In terms of viscosity, alcohol contents of 20 wt% or greater meet the requirements of EN 590, while lower alcohol contents are still acceptable for the broader range of fuel standards. Determined lubricity values are far outside the tolerated fuel limits if no additive is blended into the fuel. However, with the R655 additive, all lubricity values comply with EN 590.

For material compatibility, no optimal alcohol content exists for all reference elastomers and examined parameters (Figure 4.5B). While mass and volume change only slightly with increasing alcohol content, hardness is strongly affected, yet without a clear trend. For the different alcohol contents, the tolerated limits are realized almost fully with FKM, at least partly with HNBR, and rarely with NBR. FKM shows negligible mass changes and is within limits except for one value. For HNBR, mass increases by 7-8 %, and hardness and volume changes are tolerable with alcohol contents between 20 wt% and 35 wt%. NBR has the greatest increase in mass, and only one measured value is within limits. Consequently, compatible reference elastomers for HyFiT-fuels are FKM and, with limitations, HNBR.

Overall, no alcohol content can be clearly identified as optimal, but the range between 20 and 40 wt% appears promising for most of the parameters investigated. In the following, we therefore focus on the HyFiT-fuels with 20 wt% (HyFiT-20%) and 40 wt% alcohol (HyFiT-40%) for the analyses of combustion emissions in Section 4.3.2 and environmental impacts in Section 4.4. Further increasing compatibility with existing standards requires investigations with suitable fuel additives, e.g., viscosity improvers, as we demonstrated for lubricity. Such investigations need to consider interactions between additives and their influence on fuel properties. A tailored design of additive mixtures for HyFiT-fuels is, however, beyond the scope of this study.

4.3.2 Fuel combustion

Combustion-related CO_2, NO_x, and PM emissions of diesel and additivated HyFiT-fuels (HyFiT-20% and HyFiT-40%) are evaluated for three engine calibration cases (Figure 4.6): measured emissions from vehicle tests with the manufacturer's engine calibration, denoted as "drop-in," and estimated emissions of HyFiT-fuels with an engine calibration that targets either the same tailpipe NO_x emissions or engine-out PM emissions as diesel.

When used as drop-in fuels (white circles in Figure 4.6), HyFiT-fuels reduce CO_2 and PM tailpipe emissions while NO_x emissions slightly increase. CO_2 emissions are even moderately reduced by 3-5 % compared to diesel if HyFiT-fuels are used (Figure 4.6A), mainly due to the more favorable carbon-to-hydrogen ratio of 0.45 for HyFiT-fuels compared to 0.53 for diesel (Omari et al., 2017a). A minor drawback of HyFiT-fuels is the slight increase in engine-out NO_x emissions of around 8 % (see Figure B.13). In combination with lower average exhaust gas temperatures and a correspondingly slower warm-up of the exhaust gas aftertreatment system, higher engine-out NO_x emissions result in higher NO_x tailpipe emissions for

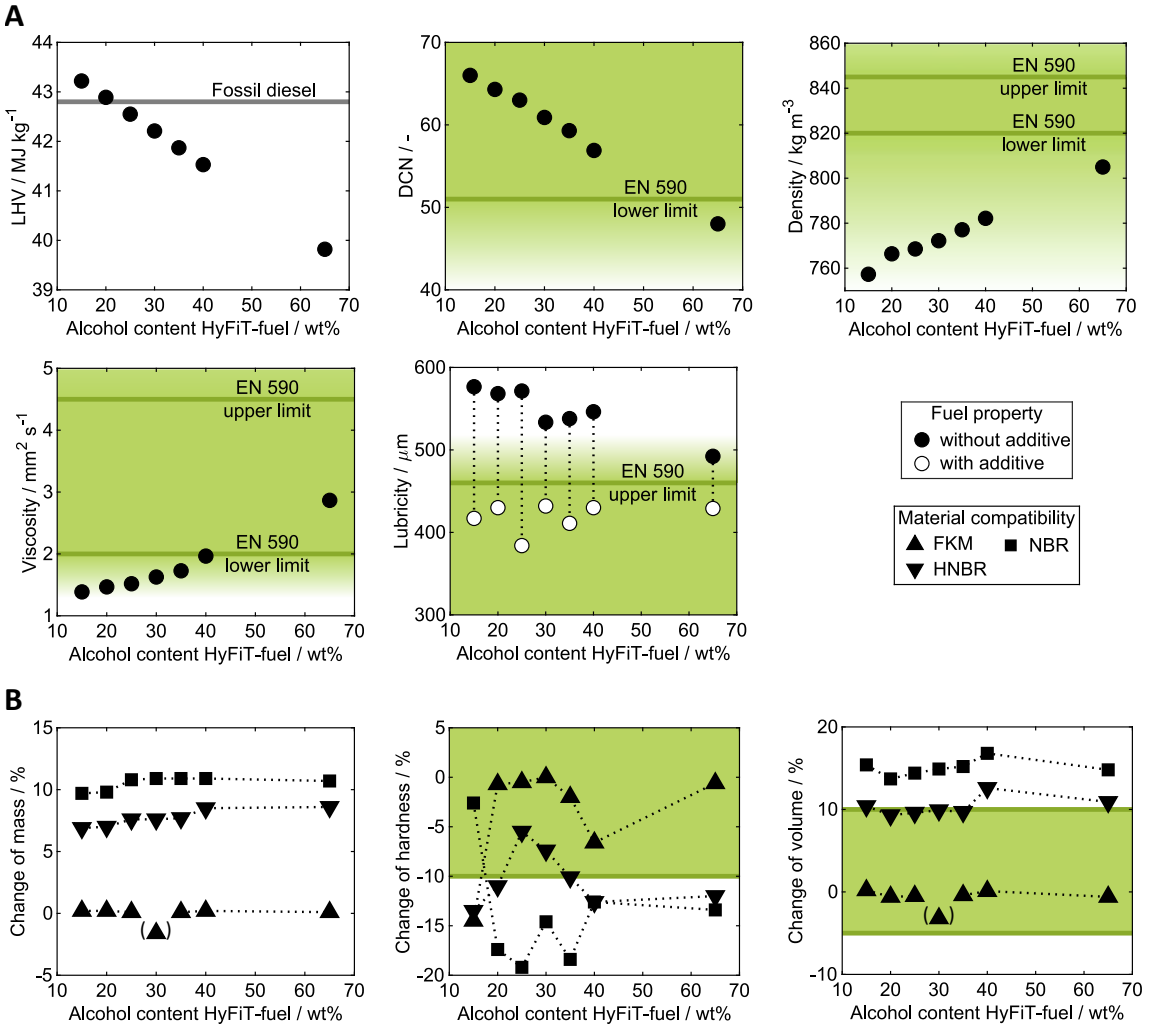

Figure 4.5: (A) Fuel properties and (B) material compatibility at 23 °C of HyFiT-fuels with alcohol contents between 15 and 65 wt%. Fuel properties are compared to the EN 590 diesel standard (green area) and a range of common country-specific standards (green color gradient) that are listed in Table B.2. For material compatibility, limits are taken from Richter (2014, 2022). The measurements for the change of mass and volume of FKM and 30 wt% alcohol gave inconsistent results. This data point is shown in brackets and not included in the further analysis. For numerical values, see Table B.12.

HyFiT-20% (29 mg km^{-1}) and HyFiT-40% (35 mg km^{-1}) than for diesel (24 mg km^{-1}) (Figure 4.6B). It should be noted, however, that these NO_x tailpipe emissions are still way below the limits of the upcoming Euro 7 legislation (75 mg km^{-1}).

The main advantages of HyFiT-fuels are substantially reduced PM engine-out emissions (see Figure B.13) by 55 % for HyFiT-20% and 70 % for HyFiT-40% compared to fossil diesel. Reasons for these PM reductions are threefold: (1) HyFiT-fuels ben-

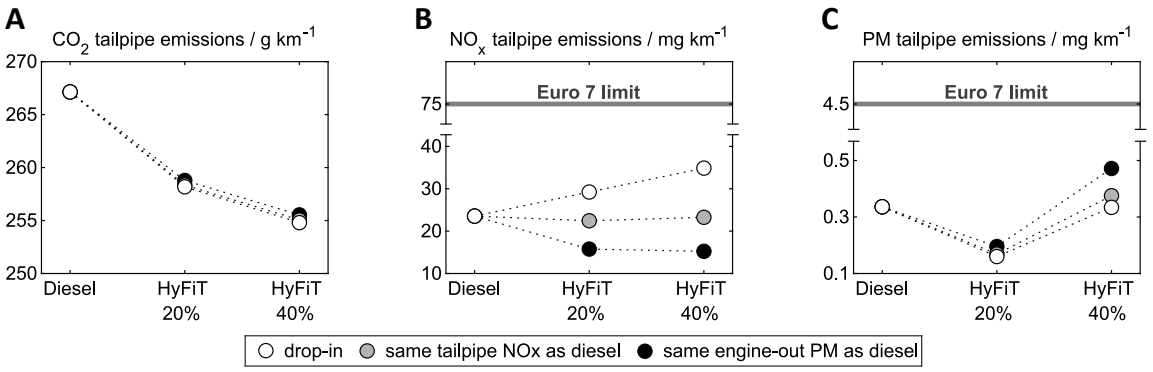

Figure 4.6: (A) CO_2, (B) NO_x, and (C) PM tailpipe emissions from the combustion of diesel, HyFiT-20%, and HyFiT-40%. Results are shown for additivated HyFiT-fuels and three engine calibration cases: measured emissions from vehicle tests with the manufacturer's engine calibration, denoted as "drop-in," (white circles) and estimated emissions of HyFiT-fuels with an engine calibration that targets either the same tailpipe NO_x emissions (grey circles) or engine-out PM emissions as diesel (black circles). Numerical values of emissions are presented in Table B.13. An alternative figure showing PM over NO_x tailpipe emissions is presented in Figure B.14.

efit from a much higher oxygen content (2.5-5.0 wt%) than fossil diesel (0.8 wt%) (Omari et al., 2017a), due to the incorporated alcohols. Previous studies already described the benefits of oxygen and the functional group of linear alcohols on PM emissions (Leitner et al., 2017). In addition, (2) HyFiT-fuels contain no aromatics and (3) feature high volatility for better mixture formation. Due to the particulate filter, almost no PM emissions can be measured in the exhaust gas after the tailpipe (Figure 4.6C). However, low engine-out PM emissions enable extended regeneration intervals of the particulate filter, which can further reduce CO_2 emissions. Significantly reduced PM engine-out emissions may also enable reducing NO_x emissions by adapting the EGR rate, as discussed in the following. Additionally, the injection strategy could be adapted to reduce the proportion of premixed combustion; that is, however, beyond the scope of this study.

By adapting the EGR rate, we estimate to what extent the PM reduction potential of HyFiT-fuels can be leveraged to reduce NO_x emissions of HyFiT-fuels. We adapt the EGR rate until HyFiT-fuels had either same tailpipe NO_x (grey circles) or engine-out PM emissions as diesel (black circles). In the second case, NO_x tailpipe emissions are reduced to 16 mg km^{-1} (HyFiT-20%) and 15 mg km^{-1} (HyFiT-40%), corresponding to a reduction of 33-38 % compared to the 24 mg km^{-1} of diesel. However, in both cases, NO_x reductions come at the cost of slightly increased CO_2 and tailpipe PM emissions.

In summary, both HyFiT-20% and HyFit-40% show promising combustion emissions. As drop-in fuels, PM and NO_x tailpipe emissions are already in the same

range as diesel and below the limits of the upcoming Euro 7 legislation. With an adapted calibration of the EGR strategy, the potential of HyFiT-fuels can be further exploited to reduce NO_x emissions substantially. In comparison, HyFiT-20% is favorable over HyFiT-40% since it yields lower or equal PM and NO_x tailpipe emissions with only slightly higher CO_2 emissions. Consequently, for the analysis of environmental impacts in Section 4.4, we focus on HyFiT-20% with adapted EGR rate for "same engine-out PM as diesel," which represents a good compromise for reducing all three combustion-related emissions simultaneously.

4.4 Environmental impacts of HyFiT-fuels

Here, we present the well-to-wheel LCA of using HyFiT-20% in a hybrid heavy-duty van in 2030 within a global setting. These environmental impacts are compared with two benchmarks: a hybrid heavy-duty van powered by fossil diesel as today's benchmark and a fully battery-electric van as a future benchmark. The functional unit of this LCA is "the provision of 1 km of transportation in a heavy-duty van."

First, we focus on climate change by optimizing HyFiT-fuel supply chains for minimal carbon footprint (Section 4.4.1). Subsequently, potential burden-shifting to other environmental impacts is analyzed for these climate-optimal supply chains (Section 4.4.2). Note that results are presented for the open-gas-loop design, resulting in the lowest carbon footprint; see Section B.5.1 for results with closed-gas-loop design and HyFiT-40%.

4.4.1 Carbon footprint

In the following, we analyze the HyFiT-fuels' potential for net-zero GHG emissions by minimizing the carbon footprint of the HyFiT-fuel supply chain (Figure 4.7A). As HyFiT-fuels can be produced from multiple feedstocks, we optimize the supply chain for each feedstock, i.e., biomass, CO_2, and natural gas. Previous studies have shown that the carbon footprint of CO_2-based fuels depends strongly on the carbon footprint of electricity (Hank et al., 2019; Deutz et al., 2018). In the optimization, we thus vary the carbon footprint of electricity to assess its influence on the potential of, in particular, CO_2-based HyFiT-fuels.

Strikingly, bio-based HyFiT-fuel depends much less on low-carbon electricity than CO_2-based HyFiT-fuel to become competitive with diesel and the BEV (Figure 4.7A), since much less electricity is required for bio-based than for CO_2-based HyFiT-fuel

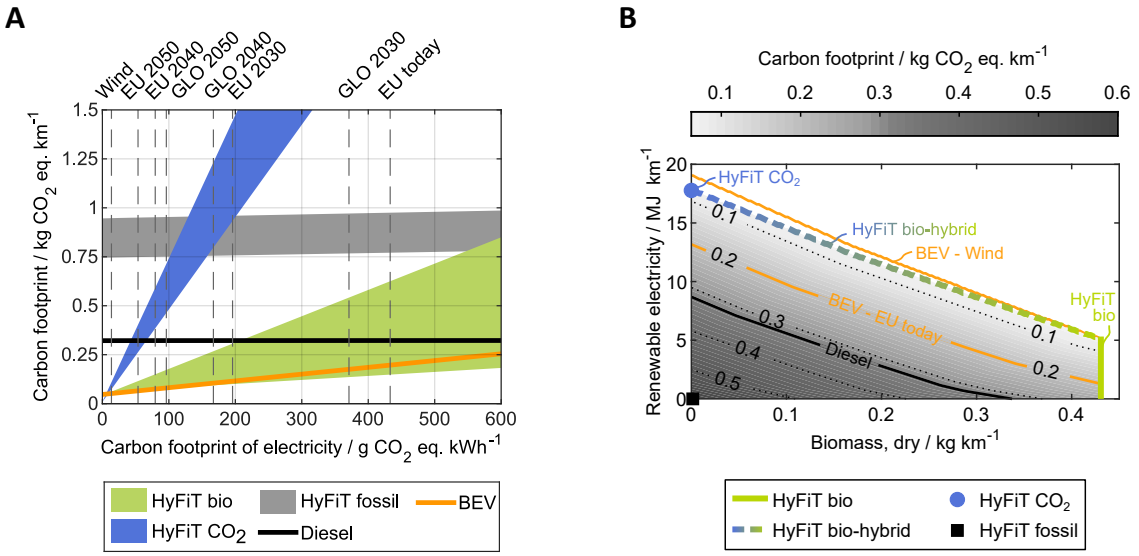

Figure 4.7: (A) The well-to-wheel carbon footprint of the van powered by bio-, CO_2-, or fossil-based HyFiT-fuel as function of the carbon footprint of electricity. Since multiple production routes exist for each feedstock, we show colored ranges for the feedstock-specific carbon footprints. The lower and upper margin of each range represents the supply chain with the lowest and highest carbon footprint. Benchmark results of diesel and the BEV are additionally shown. At the top, exemplary carbon footprints are shown for various electricity supplies. See Section B.5.4.1 for a sensitivity analysis of the BEV's battery lifetime and capacity. EU: European Union, GLO: global. (B) The well-to-wheel carbon footprint of HyFiT-fuels as function of available renewable electricity and biomass. If renewable electricity is not sufficiently available, additional electricity is taken from the power grid to meet the electricity demand. A purely bio-based HyFiT-fuel supply chain is indicated by the green vertical line, whereas the dashed curve represents a bio-hybrid, i.e., bio- and CO_2-based, supply chain. The circle and rectangle show a HyFiT-fuel supply chain purely based on CO_2 and fossils, respectively. For reference, contour curves are shown for the carbon footprint of diesel and a BEV with either electricity from today's EU grid or wind power. In (A) and (B), results are shown for the supply chain with open gas loop, HyFiT-20%, and the engine calibration "same engine-out PM as diesel" (see Figure 4.6). The results of the closed-gas-loop design and HyFiT-40% are presented in Section B.5.1.

(Figure 4.7B). The carbon footprint of bio-based HyFiT-fuel is lower than diesel and even competitive with the BEV over the entire range of electricity impacts. Thus, bio-based HyFiT-fuel is most promising in terms of carbon footprint. In contrast, CO_2-based HyFiT-fuel requires low-carbon electricity below 65 g CO_2 eq. kWh^{-1} to break-even with diesel, which is even cleaner electricity than the forecasted EU grid mix in 2050. Even if electricity with a carbon footprint of wind power is used for fuel production, the BEV has still a slightly lower carbon footprint than CO_2-based HyFiT-fuel. Fossil-based HyFiT-fuel never reaches a lower carbon footprint than either benchmark. Note that reasonable variations of battery lifetime and capacity (see Section B.5.4.1) and LUC emissions of biomass (see Section B.5.4.2) influence the

carbon footprint of the BEV and bio-based HyFiT-fuel only slightly by adding 0.04 to 0.07 kg CO_2 eq. km^{-1} and −0.07 to 0.04 kg CO_2 eq. km^{-1}, respectively.

For minimal carbon footprints, HyFiT-fuel is produced bio-based via biomass gasification in a CFB gasifier with water-gas shift, CO_2-based via reverse water-gas shift and water electrolysis, and fossil-based via steam methane reforming with H_2 skimming. Carbon footprints are the highest if HyFiT-fuel is produced bio-based via biomass gasification in a CFB gasifier with addition of H_2, CO_2-based via methane from the Sabatier process followed by steam methane reforming with H_2 skimming, and fossil-based via steam methane reforming with CO_2 import.

Although bio- and CO_2-based HyFiT-fuels are both promising, the availability of their inputs, i.e., biomass and low-carbon electricity, may be limited in the FT plant's proximity for large-scale applications. Thus, we again minimize the carbon footprint of HyFiT-fuels, but now with constrained availability of renewable electricity and biomass (Figure 4.7B). If there is not enough renewable electricity available, additional electricity is taken from the power grid. In this optimization, we do not predefine feedstock-specific technology sets such that the optimizer can freely choose and combine all included HyFiT-fuel production routes.

If at least 0.43 kg km^{-1} of biomass is available, the optimal HyFiT-fuel is purely bio-based (green vertical line), regardless of whether electricity stems from the grid or renewables. The carbon footprint of 0.43 kg km^{-1} corresponds to 0.12 kg MJ^{-1}, which is at the lower end of recent studies on bio-based FT fuels (0.10-0.37 kg MJ^{-1}) and bioethanol (0.12-0.22 kg MJ^{-1}) (see Section B.5.2). With less than 0.43 kg km^{-1} of biomass but sufficient amounts of renewable electricity available, the optimal HyFiT-fuel is bio-hybrid, using both bio- and CO_2 based production routes (dashed curve). The HyFiT-fuel is purely CO_2-based if at least 17.5 MJ km^{-1} of renewable electricity and no biomass are available (circle). If both resources are unavailable, the HyFiT-fuel is produced purely fossil-based (square).

Consequently, the flexibility of the HyFiT-fuel concept enables adapting the supply chain design according to the local availability of biomass and renewable electricity. Thereby, several supply chain designs can be identified that yield lower carbon footprints than diesel and are in the range of the BEV. However, the BEV is by far the most efficient technology in terms of renewable electricity use: It requires 1.3 MJ km^{-1} of electricity compared to the 17.5 MJ km^{-1} of CO_2-based HyFiT-fuel and has a carbon footprint in the range of 0.05 to 0.25 kg CO_2 eq. km^{-1} (Figure 4.7). Therefore, large amounts of biomass and renewable electricity are required to achieve similar climate benefits as those of the BEV. Note, though, that electricity consumption of CO_2-based HyFiT-fuel can be reduced by 25 % to 13.1 MJ km^{-1} with the closed in-

stead of the open-gas-loop design. With the closed-gas-loop design, electricity for water electrolysis is reduced by 38 % to 9.0 MJ km^{-1}, benefitting from H_2 in the recycled unconverted syngas. However, this benefit is partly offset by 1.5 MJ km^{-1} of additional electricity required for cryogenic separation in the closed-gas-loop design (see Section 4.2). Detailed process optimization might allow to further reduce the energy demand for HyFiT-fuel production.

4.4.2 Impacts beyond carbon footprint

As shown by Freire Ordóñez et al. (2021) and Medrano-García et al. (2022), close-to-zero GHG emissions of FT fuels come at the cost of burden-shifting to other impact categories. For HyFiT-fuels, we therefore analyze a potential burden shift from carbon footprint to other environmental impacts in Figure 4.8. Environmental impacts of HyFiT-fuels and diesel are normalized to those of the BEV. Here, we evaluate all carbon-footprint-optimal supply chains with electricity from wind power as a best-case proxy for a future low-carbon grid, and we present the results with electricity from the EU 2030 grid in Figure B.23. We list abbreviated impact categories in Table B.6 and present contribution analyses in Section B.5.3.

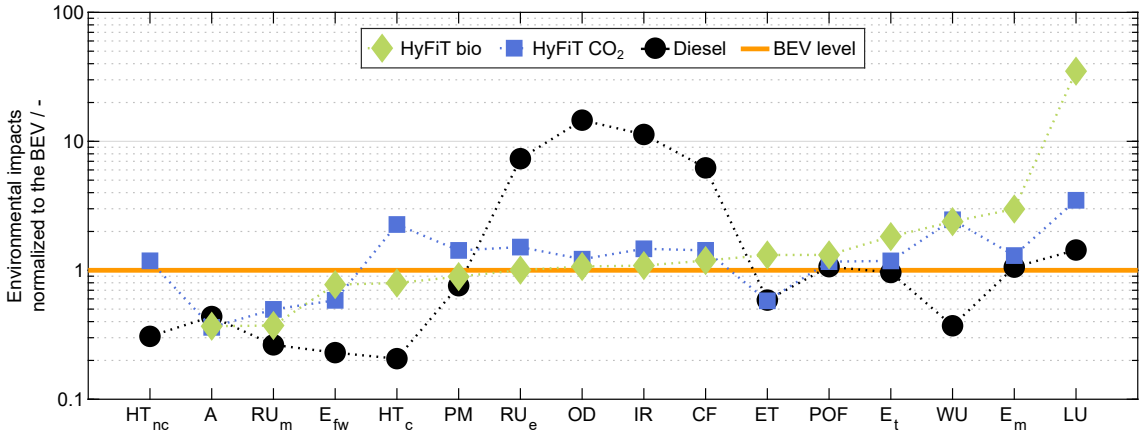

Figure 4.8: The well-to-wheel environmental impacts of bio-based (green) and CO_2-based (blue) HyFiT-20% fuel and diesel (black) normalized to the environmental impacts of the BEV (yellow). The impact categories on the x-axis are sorted by the normalized impacts of the bio-based HyFiT-fuel. Results are shown for the feedstock-specific optimal supply chain with electricity from wind power as a best-case proxy for a future low-carbon grid (see Figure 4.7A) and open gas loop as well as the engine calibration "same engine-out PM as diesel" (see Figure 4.6). For contribution analyses and a list of all abbreviated impact categories, see Section B.5.3 and Table B.6, respectively. See Figure B.22–B.23 for sensitivity analyses of the BEV's battery lifetime and capacity.

The HyFiT-fuels' and BEV's advantage of a close-to-zero carbon footprint comes at the cost of trade-offs in other impact categories. No single technology reduces all impact categories simultaneously. Compared to the BEV (yellow), bio-based HyFiT-fuel (green) is superior in terms of human toxicity (HT_{nc}, HT_c), resource use of minerals (RU_m), acidification (A), and freshwater eutrophication (E_{fw}). In the aforementioned impact categories, battery production is the major contributor for the BEV (see Figure B.17). Due to biomass cultivation and cooling water consumption, bio-based HyFiT-fuel is inferior for terrestrial and marine eutrophication (E_t, E_m), land use (LU), and water use (WU). The remaining impact categories are in the same range for bio-based HyFiT-fuel and the BEV. Environmental impacts of CO_2-based HyFiT-fuel (blue) are almost exclusively dominated by its large electricity consumption (see Figure B.17). CO_2-based HyFiT-fuel performs only better than its bio-based counterpart for eutrophication (E_{fw}, E_t, E_m), ecotoxicity (ET), and land use (LU).

If electricity is supplied from the power grid instead of wind power, bio-based HyFiT-fuel performs even better than the BEV in five additional impact categories. However, with electricity from the power grid, CO_2-based HyFiT-fuel performs worst in all impact categories, except for the BEV in the impact category resource use of minerals (RU_m) (see Figure B.23).

In a sensitivity analysis, we decrease the BEV's battery lifetime and increase battery capacity, i.e., driving range, to evaluate the influence of both parameters on all impact categories (see Figure B.22). As expected, all impacts of the BEV increase. Yet, the largest increase is observed in resource use of minerals (RU_m) for lower battery lifetimes since more batteries are required and thus constructed per vehicle lifetime. Moreover, we find that the higher the required driving range, i.e., battery capacity of the BEV, the more superior are bio-based HyFiT-fuels: For driving ranges of at least 550 km, bio-based HyFiT-fuels have lower environmental impacts in 10 to 12 out of 16 impact categories (see Figure B.22B).

4.5 Summary and conclusion

In this chapter, we check whether HyFiT-fuels can address all stated key challenges of synthetic fuels simultaneously. For this purpose, a production concept based on mature technological concepts is developed. Furthermore, we analyze compliance with fuel standards, evaluate material compatibility, and determine NO_x and PM emissions from fuel combustion. Lastly, a comprehensive well-to-wheel LCA compares environ-

mental impacts, including GHG emissions, of a heavy-duty vehicle using HyFiT-fuel with the benchmarks fossil diesel and a BEV.

Our multi-disciplinary study demonstrates that HyFiT-fuels can address all four key challenges of synthetic fuels simultaneously. The presented process concept allows HyFiT-fuels to be produced flexibly from biomass, CO_2, bio- and natural gas based on mature technologies by combining Fischer-Tropsch synthesis and hydroformylation. All HyFiT-fuel properties are shown to lie within the range of common global fuel standards. The only exception is lubricity which could be rendered standard-compliant by an additive. HyFiT-fuels are fully or partly compatible with two standard reference elastomers in terms of mass, hardness, and volume change. Consequently, HyFiT-fuels are promising for retrofitting today's vehicle fleets. Our vehicle testing highlights that HyFiT-fuels show exceptional emission behavior: Both PM and NO_x emissions can be reduced substantially compared to fossil diesel and are far below the limits of the upcoming Euro 7 legislation already when used as drop-in fuels.

The potential of HyFiT-fuels to enable the transition to net-zero GHG emissions is confirmed in the well-to-wheel LCA for a heavy-duty vehicle. Bio-based HyFiT-fuels are most promising since they yield less GHG emissions than fossil diesel and can compete with fully battery-electric vans even with today's electricity grid mix of the EU. In contrast, CO_2-based HyFiT-fuels require low-carbon electricity to compete with fossil diesel, in line with other electricity-based fuels (Hank et al., 2019; Deutz et al., 2018; Burre et al., 2021). However, both HyFiT-fuels and the battery-electric van shift burdens to other impact categories such as resource use of minerals and metals, water and land. These trade-offs should be considered in future technology development. In particular, land use is large for bio-based HyFiT-fuels and needs to be carefully assessed regionally for large-scale deployment.

It should be noted that battery-electric vans are by far the most efficient technology when it comes to the amount of electricity required per kilometer driven: While vans using CO_2-based HyFiT-fuel need $17.5\,\mathrm{MJ\,km^{-1}}$ of clean electricity, the battery-electric van requires only $1.3\,\mathrm{MJ\,km^{-1}}$. Energy use could be substantially reduced by an optimized gas loop design, showing the potential for further process optimization of HyFiT-fuel production. However, the fundamentally larger energy demand and the LCA results suggest that HyFiT-fuels should target complementary applications where battery-electric vans are limited. One such area is the drop-in use in the current fleet. Furthermore, the battery-electric van has a rather low driving range of 430 km and shows large impacts in mineral resource use due to battery production, rendering bio-based HyFiT-fuels the most promising option for long-haul applications: The

battery-electric van shows higher environmental impacts than bio-based HyFiT-fuel in 10 to 12 of 16 impact categories if driving ranges greater than 550 km are required.

The next step in the proposed fuel design procedure is to optimally *distribute* the *filtered* out synthetic fuels to vehicle fleets in order to minimize environmental impacts.

Chapter 5

Distributing synthetic fuels in vehicle fleets

In the previous chapter, the group of eligible synthetic fuels was narrowed by *filtering* out only those fuels that could meet key challenges. However, synthetic fuels will likely remain limited by the availability of their feedstocks. It is still unanswered how limited synthetic fuels should be distributed in vehicle fleets for minimal environmental impacts: as pure fuel for only few vehicles or blended with fossil fuel for all vehicles.

In this chapter, we answer this *distribution* question from a fleet perspective, considering the effect of variable blending ratios of synthetic in fossil fuel as additional degree of freedom. For this analysis, we evaluate electricity-based $OME_{3\text{-}5}$ as exemplary synthetic fuels. OMEs are promising synthetic fuels since they can escape the traditional NO_x-soot trade-off of fossil diesel (Omari et al., 2019). For $OME_{3\text{-}5}$, a comprehensive LCA is still missing that analyzes all major production routes, actual tailpipe emissions of NO_x and soot, and variable blending ratios with fossil diesel.

Section 5.1 describes the blending ratio serving as additional degree of freedom. The LCA's goal and scope is defined in Section 5.2. Section 5.3 presents the inventory data for $OME_{3\text{-}5}$ synthesis and combustion. Environmental impacts of diesel-$OME_{3\text{-}5}$ blends are shown in Section 5.4. We conclude our findings in Section 5.5.

Major parts of this chapter are reproduced by permission of the Royal Society of Chemistry from:

Völker, S., Deutz, S., Burre, J., Bongartz, D., Omari, A., Lehrheuer, B., Mitsos, A., Pischinger, S., Bardow, A., and von der Aßen, N. (2022). Blend for all or pure for few? Well-to-wheel life cycle assessment of blending electricity-based $OME_{3\text{–}5}$ with fossil diesel. *Sustainable Energy & Fuels*, **6**(8), 1959-1973.

Contribution report: Writing the draft, principal author, conceptualization, the LCA case study, evaluation and visualization of LCA results.

5.1 The blending ratio as a degree of freedom

The blending ratio is defined as the volumetric share of $OME_{3\text{-}5}$ within the blended fuel. From a market-perspective, the average blending ratio is limited by the available volume of $OME_{3\text{-}5}$. Still, the blending ratio provides an additional degree of freedom by choosing individual blending ratios, e.g., for individual vehicles within a fleet. One extreme is distributing limited $OME_{3\text{-}5}$ as a fixed blend with fossil diesel to the entire fleet ("blend for all"), whereas the opposite extreme is to use $OME_{3\text{-}5}$ as a pure fuel in only some vehicles of the fleet ("pure for few"). An environmental assessment of these two extremes is equivalent to the question how limited $OME_{3\text{-}5}$ amounts should be allocated within a fleet to minimize environmental impacts. This allocation question is important since electricity-based $OME_{3\text{-}5}$ production will be limited by the availability of scarce, clean electricity, which is required to render $OME_{3\text{-}5}$ production environmentally favorable according to previous LCA studies (Bokinge et al., 2020; Hank et al., 2019; Rodríguez-Vallejo et al., 2021). In fact, the EU's demand for renewable electricity in 2050 due to e-fuel production is estimated to be about eight times bigger than the current annual electricity production in the EU (Siegemund et al., 2017). Using scarce, clean electricity most efficiently in $OME_{3\text{-}5}$ production processes is thus crucial.

In this chapter, we analyze the environmental effect of blending $OME_{3\text{-}5}$ gradually into a fleet, depending on the availability of additional electricity and its environmental impacts. We choose the EU fleet of diesel passenger cars as exemplary fleet. Nevertheless, the qualitative results and conclusions of this fleet-wide analysis also apply to other, harder-to-electrify transport subsectors, e.g., long-haul heavy-duty trucks. In particular, we analyze whether limited $OME_{3\text{-}5}$ from scarce renewable power should be distributed to the entire fleet as a blend or to selected vehicles as full diesel substitute. In other words, we answer the question whether we should use identical "blends for all" vehicles or supply "pure $OME_{3\text{-}5}$ for few" vehicles in the fleet.

5.2 Goal and scope definition

Here, we outline the goal and scope of the LCA of diesel-$OME_{3\text{-}5}$ blends. We describe the goal, system boundary, functional unit, environmental impact categories, and exergy analysis.

5.2.1 Goal and system boundary

The goal of this LCA is to analyze the environmental impacts of blending the e-fuel $OME_{3\text{-}5}$ into a fleet on the example of the EU's fleet of diesel passenger cars. For this goal, we apply a well-to-wheel (cradle-to-grave) system boundary that includes all processes required for $OME_{3\text{-}5}$ production, subsequent blending with fossil diesel, and fuel combustion in the engine (Figure 5.1, dashed box). Since pure $OME_{3\text{-}5}$ and diesel-$OME_{3\text{-}5}$ blends are intended to substitute fossil diesel, we benchmark LCA results of the blends to fossil diesel.

For the production phase, we analyze four alternative production routes of $OME_{3\text{-}5}$ in more detail, using a well-to-tank (cradle-to-gate) system boundary (Figure 5.1, dotted box). All routes for $OME_{3\text{-}5}$ production use CO_2-based methanol and FA as intermediates: We consider the two anhydrous routes (1) via trioxane and OME_1 (TRI+OME_1) and (2) via trioxane and DME (TRI+DME) as well as the two aqueous routes (3) via methanol and FA by partial oxidation of methanol (MeOH POX) and (4) via methanol and FA by dehydrogenation of methanol (MeOH DEHY). We neglect vehicle constructions, road infrastructure emissions, and the fuel distribution because they are likely equal for fossil diesel as well as diesel-$OME_{3\text{-}5}$ blends and therefore cancel out in a comparison. The construction of chemical plants for $OME_{3\text{-}5}$ production is also neglected due to the lack of data. For the use phase, combustion-related emissions are measured on a single-cylinder engine and subsequently used to simulate the tailpipe emissions for the fuel variants pure fossil diesel, pure $OME_{3\text{-}5}$, and diesel-$OME_{3\text{-}5}$ blends in a driving cycle for passenger cars including an exhaust gas after-treatment system.

We define a best-case and a worst-case scenario in terms of the carbon footprint of diesel-$OME_{3\text{-}5}$ blends (Table 5.1). As previously shown by Hank et al. (2019), a best-case scenario with the lowest carbon footprint is achieved with Power-to-X technologies for H_2 and heat supply, combined with renewable electricity and CO_2 from high-purity industrial point sources, e.g., ammonia plants (Figure 5.1, blue boxes). We contrast this best-case scenario with a worst-case scenario that considers today's conventional H_2 and heat supply, the average EU grid mix, and CO_2 from DAC (Figure 5.1, orange boxes). In Section 5.4.3, the supply chain of diesel-$OME_{3\text{-}5}$ blends is optimized for a minimum carbon footprint as function of the carbon footprint of electricity, with the choice among all considered technologies in Table 5.1 as free optimization variable.

Eventually, we bring the EU fleet of diesel passenger cars into focus by comparing whether "blend for all" or "pure for few" is more favorable from an environmental per-

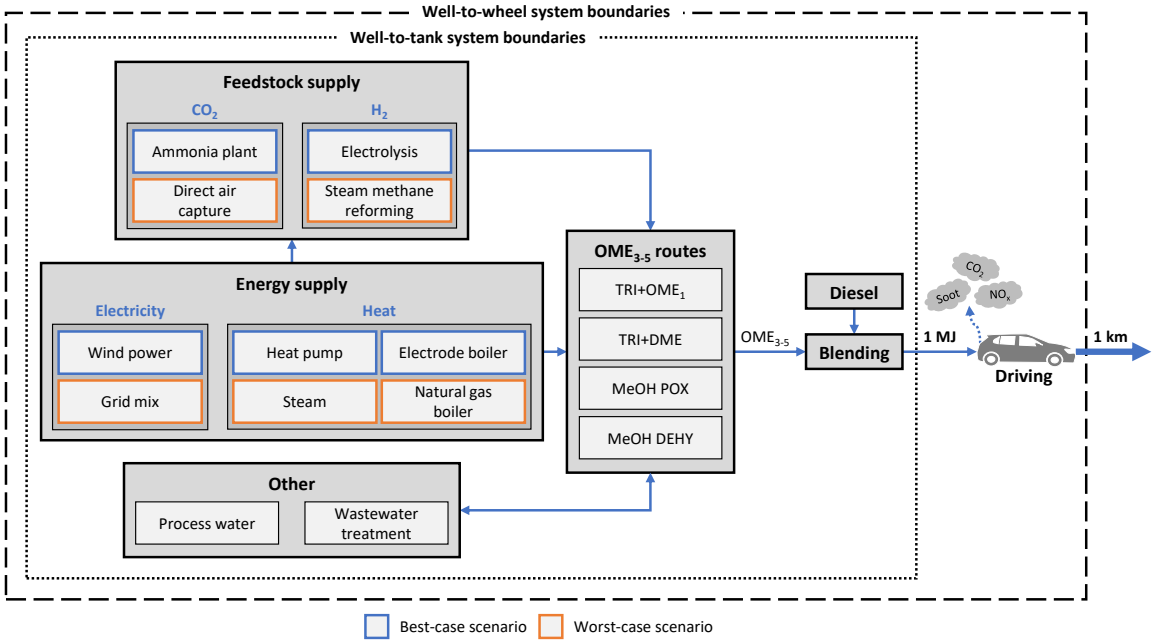

Figure 5.1: System boundary of the life cycle of diesel-$OME_{3\text{-}5}$ blends. Solid boxes represent production processes, while arrows represent material and energy flows between processes. The dotted arrow indicates use-phase emissions from fuel combustion in the passenger car. The dotted box represents the well-to-tank (cradle-to-gate) system boundary of the $OME_{3\text{-}5}$ production and subsequent blending with fossil diesel: the functional unit is "the provision of 1 MJ of enthalpy of combustion." For the well-to-tank system boundary, the use phase of $OME_{3\text{-}5}$ is neglected since a constant energy consumption is assumed for the passenger car, rendering the use phase equal for all routes. The dashed box represents the well-to-wheel (cradle-to-grave) system boundary of the entire life cycle of diesel-$OME_{3\text{-}5}$ blends, including fuel combustion with the release of CO_2, soot, and NO_x emissions: the functional unit is "the provision of 1 km of transportation in a medium-size passenger car." Four $OME_{3\text{-}5}$ production routes are investigated: $OME_{3\text{-}5}$ (1) via trioxane and OME_1 (TRI+OME_1), (2) via trioxane and DME (TRI+DME), (3) via methanol and FA by partial oxidation of methanol (MeOH POX), and (4) via methanol and FA by dehydrogenation of methanol (MeOH DEHY). Alternative technologies for the supply of feedstocks and energy are either pre-defined in best- and worst-case scenarios or treated as free optimization variable.

spective. For this fleet-wide analysis, introducing $OME_{3\text{-}5}$ as "blend for all" can have two effects regarding environmental impact reductions. The first effect is the difference in environmental impacts between pure fossil diesel and diesel-$OME_{3\text{-}5}$ blends. The second effect refers to additional, nonlinear synergies from blending $OME_{3\text{-}5}$ with fossil diesel, e.g., small blending ratios of $OME_{3\text{-}5}$ lead to disproportionately high reductions in combustion emissions (see Section 5.3.2). Both effects can be evaluated simultaneously in the relative metric blending effectiveness factor (BEF) (Deutz et al., 2018). However, we report results in absolute environmental impacts (e.g. g CO_2 eq.)

per functional unit (e.g. km) to be able to evaluate both effects separately and compare results to common fuel standards. For the "pure for few" case, we use a linear combination of pure $OME_{3\text{-}5}$ and pure fossil diesel in analogy to Mancini and Mitsos (2011).

5.2.2 Functional unit

Consistent comparisons between production systems require a common basis. In LCA, this common basis for comparing environmental impacts of production systems is the so-called functional unit. The functional unit is a quantitative measure for all functions of a production system. For the detailed analysis of four $OME_{3\text{-}5}$ production routes from well-to-tank, we choose "the provision of 1 MJ of enthalpy of combustion" as the functional unit. In the well-to-tank analysis, we neglect the use phase of $OME_{3\text{-}5}$ since a constant energy consumption is assumed for the passenger car, rendering the use phase equal for all four routes. In our well-to-wheel analysis, we choose "the provision of 1 km of transportation in a medium-size passenger car" as the functional unit for comparing different diesel-$OME_{3\text{-}5}$ blends to fossil diesel.

5.2.3 Environmental impact categories

Using diesel-$OME_{3\text{-}5}$ blends is mainly motivated by reducing both the impact on climate change of driving a diesel passenger car and the impacts on human health by the local pollutants soot and NO_x from fuel combustion. Therefore, we focus on three environmental impact categories in the LCIA: climate change in g CO_2 eq., respiratory effects in disease incidence, and photochemical ozone formation in kg NMVOC eq. In

Table 5.1: Best-case and worst-case scenario in terms of the carbon footprint for the considered technologies. For more details on the underlying LCA datasets, see Table C.17.

	Best case	**Worst case**
CO_2	Ammonia plant	Direct air capture system
H_2	Electrolysis	Steam methane reforming
Electricity	Wind power	Grid mix
Heat		
$< 90\,°C$	Heat pump	Steam
90-250 °C	Electrode boiler	Steam
$> 250\,°C$	Electrode boiler	Natural gas boiler

the following, we use the term carbon footprint for the impact on climate change. We assess these environmental impact categories according to the LCIA method EF at midpoint level, as recommended by the Joint Research Centre of the European Commission. Other impact categories are also relevant but beyond the scope of this study.

5.2.4 Exergy analysis

We conduct an exergy analysis for the $OME_{3\text{-}5}$ production to gain a deeper knowledge of the exergy losses and the differences between the four considered $OME_{3\text{-}5}$ routes (Figure 5.1, well-to-tank). Details regarding the calculation of the exergy efficiency as well as the specific exergies of the considered mass and heat flows are presented in Section C.3.1.

5.3 Life cycle inventory for diesel-$OME_{3\text{-}5}$ blends

In this section, we describe the inventory data used in our LCA in more detail. First, we describe the anhydrous and aqueous production routes for $OME_{3\text{-}5}$ as well as the supply of feedstocks and energy. Second, we analyze the combustion of diesel-$OME_{3\text{-}5}$ blends.

5.3.1 $OME_{3\text{-}5}$ production

All considered routes for $OME_{3\text{-}5}$ have two common intermediates: methanol and FA. Following the Power-to-X concept, methanol can be produced by direct CO_2 hydrogenation (Van-Dal and Bouallou, 2013) and is partly used to produce FA in all considered $OME_{3\text{-}5}$ routes. Dependent on whether water coexists in the final process step of $OME_{3\text{-}5}$ formation, $OME_{3\text{-}5}$ routes can be divided into two types: anhydrous and aqueous routes (Figure 5.2). In the following, we consider both anhydrous and aqueous routes in our investigation to understand their advantages and drawbacks. All processes are based on similar assumptions and detailed process models created by the respective authors in the simulation software Aspen Plus or CHEMASIM from BASF. For more details on the considered $OME_{3\text{-}5}$ production routes and the underlying modeling assumptions see Section C.2. Pinch-based heat integration has been applied for all routes, using the target values for the heating and cooling demand.

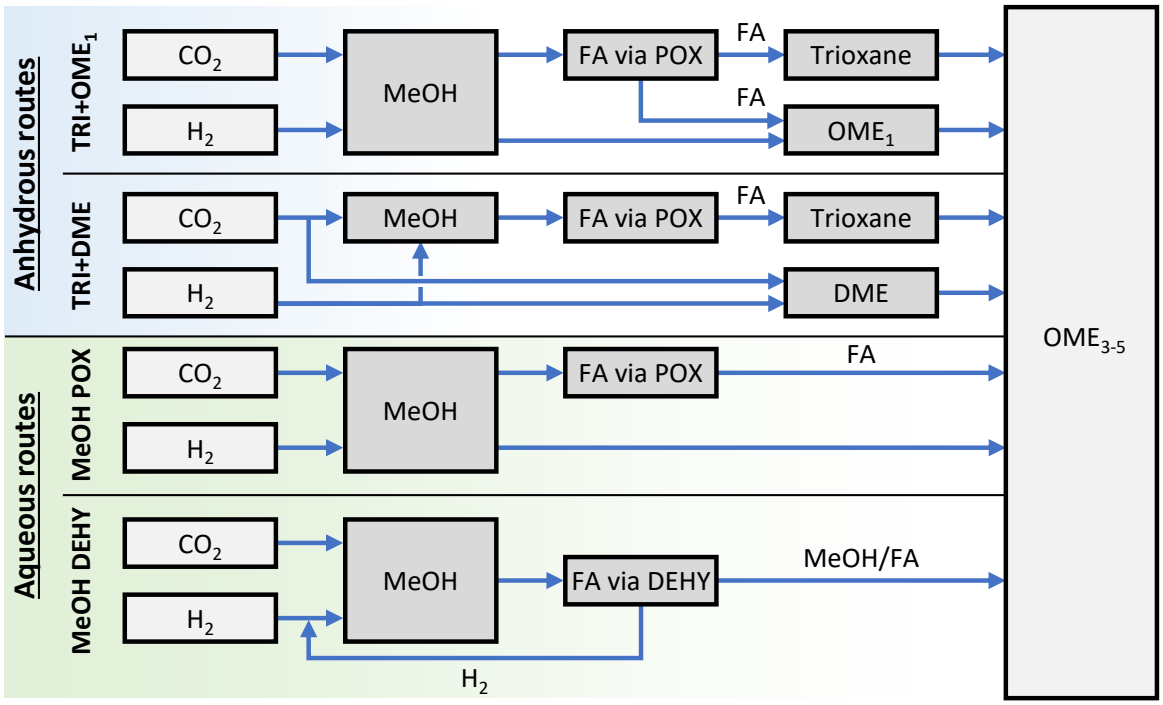

Figure 5.2: Flowchart of both anhydrous and both aqueous routes to OME$_{3\text{-}5}$. Boxes represent production processes, while arrows represent material flows between processes. Both anhydrous routes use trioxane (TRI) as an intermediate with either OME$_1$ (TRI+OME$_1$) or DME (TRI+DME) as the capping source. Both aqueous routes use methanol (MeOH) and formaldehyde (FA) as intermediates: FA is either produced via partial oxidation of methanol (MeOH POX) or via dehydrogenation of methanol (MeOH DEHY). In case of the MeOH DEHY route, significant amounts of H_2 are co-produced and thus recycled to the preceding methanol production, reducing the overall H_2 consumption.

Anhydrous routes (TRI+OME$_1$ and TRI+DME). Anhydrous OME$_{3\text{-}5}$ production can either use OME$_1$ or DME as intermediate (Figure 5.2). The concept of OME$_{3\text{-}5}$ production via trioxane and OME$_1$ (TRI+OME$_1$) (Schmitz et al., 2016) is based on the work of Burger et al. (2010). For our study, we use the process models of Bongartz et al. (2019) and Burre et al. (2019) that analyzed this process concept in detail. Their process chain considers OME$_1$ production from H_2 and CO_2 via methanol and aqueous FA solution.

For the concept of producing OME$_{3\text{-}5}$ from trioxane and DME (TRI+DME), a process similar to OME$_{3\text{-}5}$ production via the TRI+OME$_1$ route has been developed and evaluated by Breitkreuz et al. (2018), using chemical equilibrium calculations for the reaction and detailed distillation models for the separation part. For the DME production step, we use a model for direct DME production from H_2 and CO_2, using equilibrium-based models for both the reaction and the separation via rectification

(Bongartz et al., 2018). Methanol, FA, and trioxane production is taken from the TRI+OME_1 route.

Aqueous routes (MeOH POX and MeOH DEHY). In contrast to the anhydrous routes, aqueous routes directly utilize methanol and typically aqueous FA for $OME_{3\text{-}5}$ formation (Figure 5.2). For the $OME_{3\text{-}5}$ route via methanol and FA by partial oxidation of methanol (MeOH POX), the process concept is adopted from Held et al. (2019) with methanol production from H_2 and CO_2.

For the $OME_{3\text{-}5}$ route via methanol and FA by dehydrogenation of methanol (MeOH DEHY), we combine methanol dehydrogenation with FA absorption in water to selectively separate FA from the gaseous reactor effluent. Thereby, we accept the disadvantage of introducing unfavorable amounts of water into the process: This way, we can use the catalysts and process concept for $OME_{3\text{-}5}$ synthesis from methanol and aqueous FA considered by Held et al. (2019). In principle, it might be possible to synthesize $OME_{3\text{-}5}$ from methanol and gaseous FA, which would eliminate the need for FA removal from the gas stream altogether, but this synthesis pathway has only recently been proposed (Grünert et al., 2018). Ouda et al. (2018b) proposed a similar process concept to the one considered herein, but without introducing water for separating FA from the gaseous reactor effluent, thus potentially benefiting from smaller amounts of water in the process. However, the downstream distillation models used in their work do not account for oligomerisation reactions whose effects on distillation boundaries need to be considered (Schmitz et al., 2017). Therefore, we do not use their results for our analysis but rather those of Held et al. (2019), who do use detailed distillation models including these reactions.

In the MeOH DEHY route, we assume a selective separation of H_2 from CO and methane (CH_4) by a membrane for H_2 recycling. For such membranes, high selectivities of up to 1000 and 27,000 have been reported (Ockwig and Nenoff, 2007; Prabhu and Oyama, 2000). Part of the H_2 is recycled and accumulated in the dehydrogenation reactor to dilute the gaseous methanol feed to the desired 1:1 ratio of H_2 to methanol. The rest is recycled to the methanol plant. As the final product, the same ratio of FA to water as in the partial oxidation of methanol is realized such that both can be used for the same proceeding $OME_{3\text{-}5}$ process of Held et al. (2019). See Figure C.1 for a flowsheet of the MeOH DEHY route.

Background data for feedstocks, energy, and others. We also take into account the environmental impacts from technologies providing the feedstocks CO_2 and H_2, electricity, heat, process water and wastewater treatment. For aggregated process datasets, we consider LCA inventories from the GaBi LCA database if datasets are available. Thus, we rely on the ecoinvent LCA database only if LCA inventories

are unavailable in GaBi. We do so to ensure that the data basis of our study is as consistent as possible. Furthermore, ecoinvent does not provide a suitable dataset for H_2 from steam methane reforming (SMR), which we consider in our worst-case scenario (Table 5.1). The considered technologies are described in the following.

For the CO_2 supply, we consider a DAC system as well as high-purity sources from the chemical industry, e.g., ethylene oxide or ammonia plants. In case of the DAC system, CO_2 is captured from the atmosphere. In the atmosphere, CO_2 is much more diluted (410 ppm, Dunn et al. (2020)) than in industrial exhaust streams. Therefore, the energy consumption for capturing CO_2 from the atmosphere is higher, making the DAC system the least efficient technology for CO_2 supply (von der Assen et al., 2016). For the energy requirements of the DAC system, we use the predicted energy targets for industrial DAC plants based on TSA, according to Deutz and Bardow (2021). Note that Madhu et al. (2021) compared a high-temperature aqueous solution (HT-Aq) DAC to a TSA DAC, and conclude that the TSA DAC outperforms the HT-Aq DAC in all considered impact categories. In current ammonia plants, CO_2 is co-produced during steam reforming of methane and the water-gas shift reaction. In subsequent gas scrubbing, nearly pure CO_2 is separated (Farla et al., 1995). Note that the ammonia plant with CO_2 separation is thus a multifunctional product system since it co-produces CO_2 besides ammonia. We therefore apply the avoided burden approach and credit for CO_2 utilization in accordance to Müller et al. (2020b). Since CO_2 is separated in conventional ammonia plants anyway, we attribute the environmental impact of CO_2 capture to the ammonia plant. We model the CO_2 supply from the ammonia plant according to von der Assen et al. (2016).

H_2 is either supplied by conventional steam reforming from natural gas (GaBi, 2019) or a PEM electrolysis. We model the PEM electrolysis with an overall electricity consumption of 47.6 kWh per kg H_2, representing an overall efficiency of 70 %, a water demand of 0.01 m^3 per kg H_2, and an outlet pressure of 30 bar according to Reuß et al. (2017). Co-produced oxygen is assumed to be vented to the atmosphere. The construction of the PEM electrolysis is neglected: It accounts for maximum 4 % of the total carbon footprint of the PEM electrolysis when renewable electricity is used (Bareiß et al., 2019). Respiratory effects and photochemical ozone formation depend almost exclusively on the electricity supply and are thus not affected by the electrolyser construction. In contrast, the electrolyser construction affects the environmental impact categories ozone depletion and metal depletion that are however beyond the scope of this study (Bareiß et al., 2019).

For electricity supply, we consider the average EU grid mix as well as the average wind electricity of the EU (GaBi, 2019). We also include the country-specific grid

mixes of Italy, Denmark, Austria, Finland, Belgium, Switzerland, France, and Norway as well as the average electricity production from photovoltaics and solar-thermal energy in the EU for our analysis of the environmental impacts due to electricity supply (GaBi, 2019). For heat supply, we differentiate between three temperature levels: below 90 °C, between 90 °C and 250 °C, and above 250 °C. Depending on the temperature level, we consider steam production in the chemical industry (Wernet et al., 2016), natural gas boilers (GaBi, 2019), heat pumps, and electrode boilers. For the heat pump, we assume a COP of 3.28: The COP is averaged from heat pumps built since 2006, with evaporator temperatures between 9-15 °C and condenser temperatures of about 90 °C according to David et al. (2017). For the electrode boiler, we assume a Power-to-Heat efficiency of 95 % according to Müller et al. (2020a).

Additional process data for other processes, i.e., diesel supply, process water supply, and wastewater treatment are taken from the GaBi and ecoinvent LCA databases (Wernet et al., 2016; GaBi, 2019). For the diesel supply, we consider the EU market mix that is provided at a filling station, using the corresponding dataset from the GaBi database (GaBi, 2019). This diesel supply process includes the entire supply chain from drilling through crude oil production and oil refining to transportation to the filling station. The diesel fuel of this dataset contains about 6 wt% of bio-components. The dataset is mainly based on industry data and considers contributions of all delivering countries to the EU fuel mix based on national statistics. More details on the underlying LCA datasets of all processes are listed in Table C.17.

5.3.2 Diesel-OME$_{3\text{-}5}$ blend combustion

The combustion-related raw emissions of diesel-OME$_{3\text{-}5}$ blends are characterized by engine tests with a single-cylinder engine (SCE). These SCE tests comprise variations of the EGR rate at different load points with blending ratios of 0 vol%, 20 vol%, 35 vol%, 50 vol%, and 100 vol% OME in fossil diesel as described in previous studies (Omari et al., 2019, 2017a; Omari, 2021) and additionally new analyses in form of a design of experiment (DOE) approach. Subsequently, the DOE models are implemented in a mean-value engine model (Lee et al., 2018, 2019) (including vehicle, engine, driver, transmission, and after-treatment system) to determine the corresponding vehicular tailpipe emissions in a given driving cycle. Specifications of the SCE, the emission measurement equipment, and the main parameters from the vehicle model are given in Table C.35-Table C.37.

Within the global DOE test campaign on the SCE, the WLTP cycle is covered by varying the speed and load range. To include the fuel's effect on the emissions, the

DOE is conducted three times namely with pure fossil diesel, with 35 vol% $OME_{3\text{-}5}$ in fossil diesel, and with pure $OME_{3\text{-}5}$. A blend with 35 vol% $OME_{3\text{-}5}$ generates a sufficient amount of soot that can be measured with high accuracy as required for the DOE. If instead a blend with 50 vol% $OME_{3\text{-}5}$ would be used, the soot emissions would be too low to be measured with sufficiently high accuracy. For the subsequent creation of DOE models, 600 points are available in total: The DOE domain covers 40 load points for each considered fuel and 5 variations of calibration parameters per load point on average. The parameters varied in the DOE input domain are given in Table C.39. Subsequently, global DOE models are created from the measured data from the SCE with the ETAS ASCMO software. The measured data is fitted to the DOE input domain by a multiple Gaussian regression analysis procedure within the software.

After evaluating the generated DOE models, we find the trends to be within expectations; in particular, considering that only three fuels have been investigated in the DOE (0 vol%, 35 vol%, and 100 vol% $OME_{3\text{-}5}$ in fossil diesel). The observed trends of soot and NO_x emissions are in good agreement with the observations in previous work (Omari et al., 2019, 2017a; Omari, 2021), where multiple blending ratios were investigated at different load points. With the generated DOE models, an optimal set of engine calibration maps is obtained with the ETAS ASCMO optimizer tool, targeting the best compromise between NO_x, soot, and CO_2 emissions for each fuel. After obtaining the optimized engine calibration maps and the emission models, an in-house transient-capable mean-value engine model is used to simulate the cumulative tailpipe emissions during a WLTP cycle. This WLTP cycle simulation assumes a D-segment passenger car (mid-size vehicle) with a representative rolling resistance curve, a 1.6-Liter four-cylinder engine, and an after-treatment system consisting of a diesel oxidation catalyst, a selective NO_x reduction catalyst, and a diesel particulate filter. The resulting tailpipe emissions of CO_2, soot, and NO_x are shown in Figure 5.3 and summarized in Table C.38. Note that we expect the qualitative trends of the obtained results to be also valid for other vehicles, e.g., long-haul heavy-duty trucks.

The tailpipe CO_2 emissions increase almost linearly with the $OME_{3\text{-}5}$ content (Figure 5.3A). This increase in CO_2 emissions is not caused by efficiency losses but is attributed to the fact that $OME_{3\text{-}5}$ has a higher specific carbon content per heat of combustion compared to fossil diesel ($22\,g\,MJ^{-1}$ and $20\,g\,MJ^{-1}$, respectively) (Omari, 2021). In contrast to CO_2 emissions, soot and NO_x tailpipe emissions reduce nonlinearly with increasing blending ratios of $OME_{3\text{-}5}$ in fossil diesel (Figure 5.3B and C). Both pollutants are mostly convex functions of the blending ratio except for soot emissions at low blending ratios. Thus, even small blending ratios of $OME_{3\text{-}5}$ in fossil

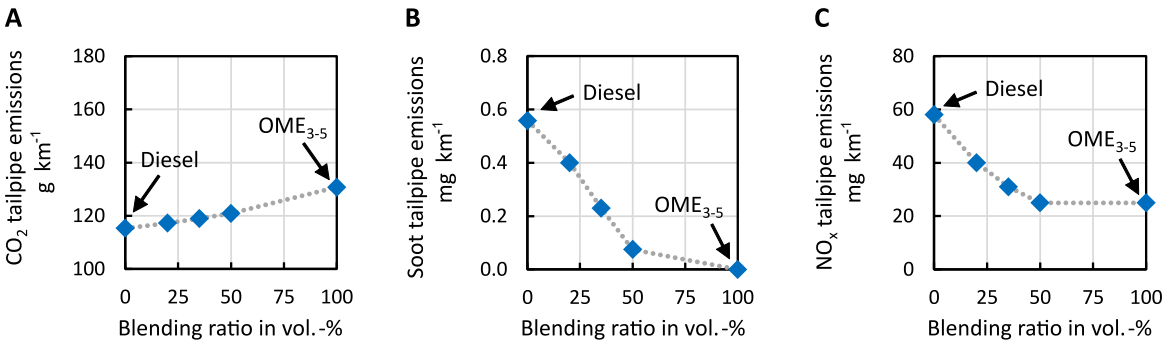

Figure 5.3: (A) CO_2, (B) soot, and (C) NO_x tailpipe emissions of diesel-OME_{3-5} blend combustion for various volumetric blending ratios. CO_2 emissions are calculated by the carbon balance for each blending ratio. Soot and NO_x emissions are obtained by single-cylinder engine tests for each blending ratio, using a global design of experiments approach and subsequently simulating a complete driving cycle for a mid-size passenger car.

diesel drastically reduce both local pollutants soot and NO_x. In contrast to soot, NO_x shows a saturation behavior after about 50 vol% OME_{3-5} content, where an additional increase of OME_{3-5} does not reduce NO_x further. This saturation is attributed to the maximum attainable EGR rate to maintain the relative air-fuel ratio above 1.15 such that efficiency does not deteriorate. An alternative solution to limiting the EGR rate would be the increase of boost pressure, e.g., by means of sophisticated two-stage boosting systems. This system is however beyond the scope of the current work.

For the LCIA in Section 5.4, we model the emissions from fuel combustion as emitted in the environmental sub-compartment urban air close to ground. Thereby, we assume driving in an urban environment for which NO_x and soot emissions are characterized with higher, i.e., stricter, characterization factors. For the environmental impact category respiratory effects, the characterization factors of NO_x and soot emissions are 6.6 and 78 times higher in urban air close to ground than in non-urban air or from high stacks, respectively.

5.4 Environmental impacts of diesel-OME_{3-5} blends

In this section, we analyze the environmental impacts of diesel-OME_{3-5} blends. First, we identify the most promising route of four OME_{3-5} production routes in a well-to-tank analysis: For this purpose, we conduct exergy analyses and an LCA for the environmental impacts of all routes. Second, we analyze the entire life cycle of diesel-OME_{3-5} blends for various blending ratios from well-to-wheel for the most promising

$OME_{3\text{-}5}$ route. Third, we analyze the well-to-wheel carbon footprint of the diesel-$OME_{3\text{-}5}$ blends depending on the carbon footprint of electricity supply. Finally, we conclude with an analysis of blending $OME_{3\text{-}5}$ gradually into a fleet on the example of the EU's fleet of diesel passenger cars, depending on the availability of additional electricity and its environmental impacts.

5.4.1 Well-to-tank: $OME_{3\text{-}5}$ production

Exergy analysis. The exergy flows for producing 1 kg $OME_{3\text{-}5}$ of all four $OME_{3\text{-}5}$ production routes are visualized in Sankey diagrams in Figure 5.4. See Section C.3.1 for numerical results of the exergy analysis. The largest exergy losses occur in both anhydrous routes (Figure 5.4A and B). The overall exergy efficiency is 57 % for the TRI+OME_1 route and 55 % for the TRI+DME route, with the highest exergy losses occurring due to the high heat demand during trioxane production. Second highest exergy losses occur in the FA production step: These losses are mainly due to the combustion of side products in the off-gas and the conversion of chemical energy to heat in the partial oxidation of methanol. Although the TRI+OME_1 route requires 28 wt% less trioxane than the TRI+DME route, its overall exergy efficiency is only slightly higher: Exergy losses are higher during OME_1 production than during DME production, reducing the advantage of a lower trioxane demand for the TRI+OME_1 route.

The aqueous routes MeOH POX and MeOH DEHY yield overall exergy efficiencies of 65 % and 71 %, respectively (Figure 5.4C and D). For the MeOH POX route, the largest exergy losses occur during FA and $OME_{3\text{-}5}$ production. In contrast, the MeOH DEHY route benefits twofold from the significant co-production of H_2. First, less side products are produced and thus burned during FA production, reducing its exergy losses. Second, the H_2 recycle to the preceding methanol production reduces the overall H_2 demand and thereby increases the overall exergy efficiency. The exergy analysis of both anhydrous routes and aqueous routes shows that the MeOH DEHY route results in the highest overall exergy efficiency and uses H_2 most efficiently.

LCA. The well-to-tank environmental impacts of the four $OME_{3\text{-}5}$ production routes are shown in Figure 5.5 for the best-case scenario. See Figure C.6 for the worst-case scenario. From a well-to-tank perspective, all routes have negative carbon footprints in the best-case scenario since CO_2 emitted otherwise from the CO_2 source ammonia plant is avoided. However, for the carbon footprint, we additionally indicate the end-of-life of $OME_{3\text{-}5}$ as hatched area to emphasize that the full life cycle of $OME_{3\text{-}5}$ is no carbon sink: All carbon is eventually released again as CO_2 dur-

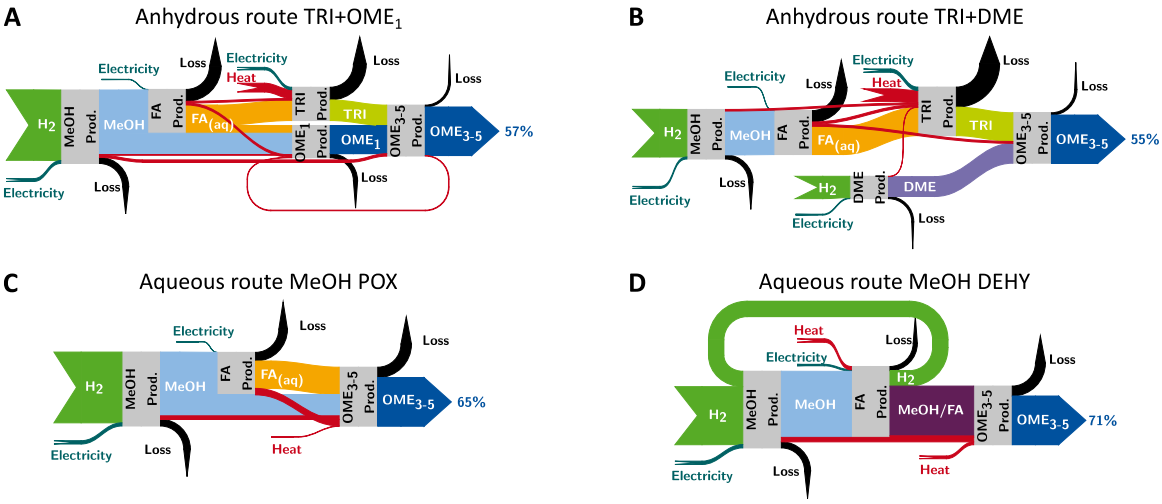

Figure 5.4: Sankey diagrams of the exergy analysis for producing 1 kg of $OME_{3\text{-}5}$. Boxes represent process steps, whereas arrows denote exergy flows. The presented $OME_{3\text{-}5}$ routes are the anhydrous routes via (A) trioxane and OME_1 (TRI+OME_1) and via (B) trioxane and DME (TRI+DME), as well as the aqueous routes via (C) methanol and FA by partial oxidation of methanol (MeOH POX) and via (D) methanol and FA by dehydrogenation of methanol (MeOH DEHY). The amount of exergy of each mass and energy flow is represented by the width of the arrow.

ing fuel combustion, making CO_2-based $OME_{3\text{-}5}$ carbon-neutral at best, but only if carbon-neutral electricity is used for fuel production and all other supply chains are also carbon-neutral.

In the best-case scenario, already very low-carbon electricity from wind power is used, leading to almost carbon-neutral $OME_{3\text{-}5}$ production. All routes have nearly identical life-cycle carbon footprints of about 7 g CO_2 eq. per MJ (Figure 5.5A). Although both aqueous routes MeOH POX and MeOH DEHY require more CO_2 and thereby benefit from higher credits for CO_2 utilization, they also have higher CO_2 purge streams compared to both anhydrous routes. Additionally, the H_2 recycle of the MeOH DEHY route results in the lowest H_2 demand and thus in the lowest overall electricity consumption because H_2 is supplied via PEM electrolysis in this scenario. However, the benefit of the more efficient H_2 usage is rather low in terms of the carbon footprint in the best-case scenario: Electricity is supplied by wind power with an already low carbon footprint, making the efficient usage of electricity less important for the overall carbon footprint. Nevertheless, a high efficiency in H_2 and electricity usage is beneficial in order to keep the demand for low carbon electricity as low as possible.

In terms of respiratory effects and photochemical ozone formation (Figure 5.5B and C), the aqueous routes MeOH POX and MeOH DEHY have the lowest environmental

impacts. Both impact categories are almost exclusively dominated by the upstream impacts of electricity supply: Electricity is mostly used for the Power-to-X technologies PEM electrolysis, heat pumps, and electrode boilers, followed by OME$_{3\text{-}5}$ production and CO_2 supply. The MeOH DEHY route shows the lowest H_2 consumption due to the H_2 recycle from the FA production to the preceding methanol production. This benefit is, however, partly offset by a higher heat consumption during FA and OME$_{3\text{-}5}$ production compared to the MeOH POX route. Consequently in the best-case scenario, respiratory effects and photochemical ozone formation are more decisive for the choice of the route than the carbon footprint since the carbon footprints are almost equal.

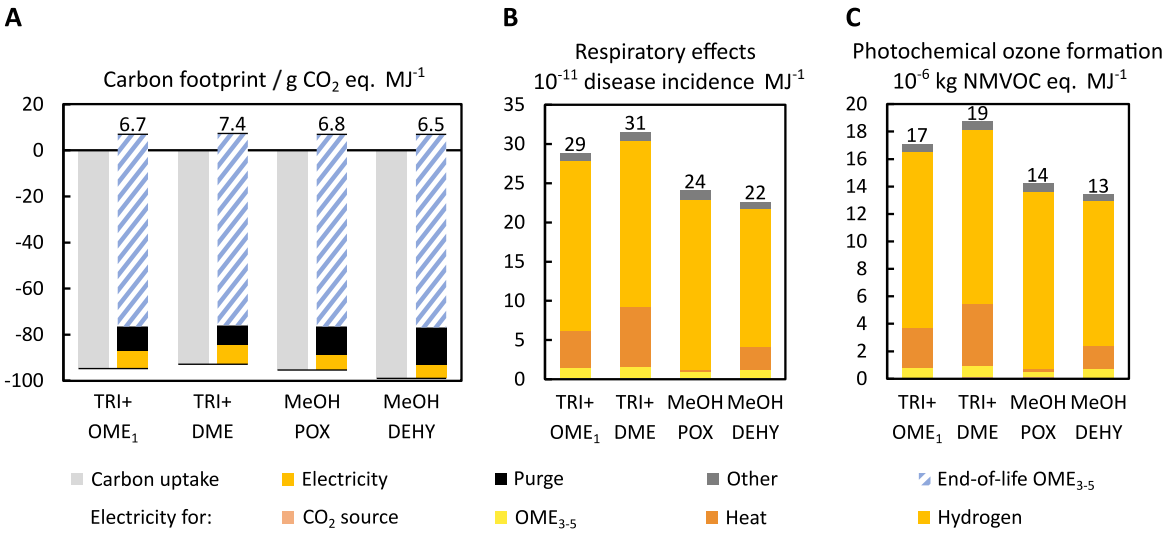

Figure 5.5: Well-to-tank (A) carbon footprint in g CO_2 eq. per MJ, (B) respiratory effects in 10^{-11} disease incidence per MJ, and (C) photochemical ozone formation in 10^{-6} kg NMVOC eq. per MJ of the four OME$_{3\text{-}5}$ production routes for the best-case scenario. The carbon footprint of the carbon uptake due to CO_2 utilization is negative (light grey). Positive environmental impacts result from direct CO_2 emissions in purge gases from OME$_{3\text{-}5}$ production (black), minor emissions due to process water supply and wastewater treatment (dark grey), and electricity supply (yellow). The electricity supply is further subdivided in electricity for hydrogen, heat, OME$_{3\text{-}5}$, and CO_2 supply in (B) and (C). Note however that environmental impacts due to electricity for CO_2 supply are very small and thus barely visible. Although not inside the system boundary of a well-to-tank analysis, we additionally indicate the end-of-life emissions from OME$_{3\text{-}5}$ combustion for the carbon footprint (A, hatched blue): The entire life cycle of CO_2-based fuels cannot be carbon-negative and is thus carbon-neutral at best. The same figure is shown with CO_2 from DAC in the best-case scenario in Figure C.7.

In the worst-case scenario (Figure C.6), the differences between the four routes are greater in all considered impact categories than in the best-case scenario, and both aqueous routes MeOH POX and MeOH DEHY show the lowest environmental impacts. Note that we considered a TSA DAC in the worst-case scenario, which performs

better than a HT-Aq DAC, according to Madhu et al. (2021). We thus expect our results to worsen slightly if we would instead assume a HT-Aq DAC. In this scenario, H_2 is supplied by conventional steam methane reforming, resulting in high contributions to the overall carbon footprint (Figure C.6A). In terms of the carbon footprint, the aqueous routes MeOH POX and MeOH DEHY benefit from a lower heat consumption compared to both anhydrous routes. Respiratory effects and photochemical ozone formation are both dominated by the fossil-based supply of heat in the worst-case scenario (Figure C.6B and C). Although the MeOH DEHY route still profits from a lower H_2 consumption due to its H_2 recycle, its higher heat consumption affects the environmental impacts more strongly in the worst-case scenario. Consequently, in contrast to the best-case scenario, the MeOH DEHY route has higher environmental impacts than the MeOH POX route in the worst-case scenario.

All in all, the aqueous routes MeOH POX and MeOH DEHY yield the lowest environmental impacts in both the worst-case (Figure C.6) and the best-case scenario (Figure 5.5). In the proceeding well-to-wheel analysis of diesel-$OME_{3\text{-}5}$ blends, we focus on the aqueous MeOH DEHY route as it has the highest overall exergy efficiency of all four routes in addition to its environmental advantages (Figure 5.4D). Note though that considering exergy efficiency alone is not sufficient to rank the $OME_{3\text{-}5}$ routes in terms of environmental impacts: While the MeOH DEHY route has the highest exergy efficiency, it shows lower environmental impacts in the best-case scenario and higher ones in the worst-case scenario compared to the MeOH POX route.

5.4.2 Well-to-wheel: the entire life cycle of diesel-$OME_{3\text{-}5}$ blends

Figure 5.6 shows the well-to-wheel analysis of diesel-$OME_{3\text{-}5}$ blends for the best-case scenario: Investigated fuel blends are pure diesel, 20, 35 and 50 vol% $OME_{3\text{-}5}$ in fossil diesel as well as pure $OME_{3\text{-}5}$ (see Section 5.3.2). Over the entire life cycle, diesel-$OME_{3\text{-}5}$ blends can reduce not only the carbon footprint but also respiratory effects and photochemical ozone formation compared to fossil diesel (Figure 5.6). These results partly contradict earlier findings that $OME_{3\text{-}5}$ performs worse than fossil diesel in terms of particulate matter and photochemical ozone formation (Rodríguez-Vallejo et al., 2021). However, in this previous study (Rodríguez-Vallejo et al., 2021), NO_x emissions of $OME_{3\text{-}5}$ combustion (Hank et al., 2019) are assumed to be one order of magnitude higher than those of fossil diesel combustion (Simons, 2016). In contrast to the previous study, $OME_{3\text{-}5}$ combustion has actually shown to enable large reductions of NO_x emissions compared to fossil diesel in current literature (Omari et al., 2019;

Richter and Zellbeck, 2017). This discrepancy may influence the authors' findings strongly since NO_x emissions contribute not only to photochemical ozone formation but also, as a precursor, to respiratory effects. Our findings are in line with recent literature from OME combustion showing the combustion benefits of OME$_{3\text{-}5}$. In any case, this highlights the necessity to use measured combustion emissions as reliable data basis for LCA studies.

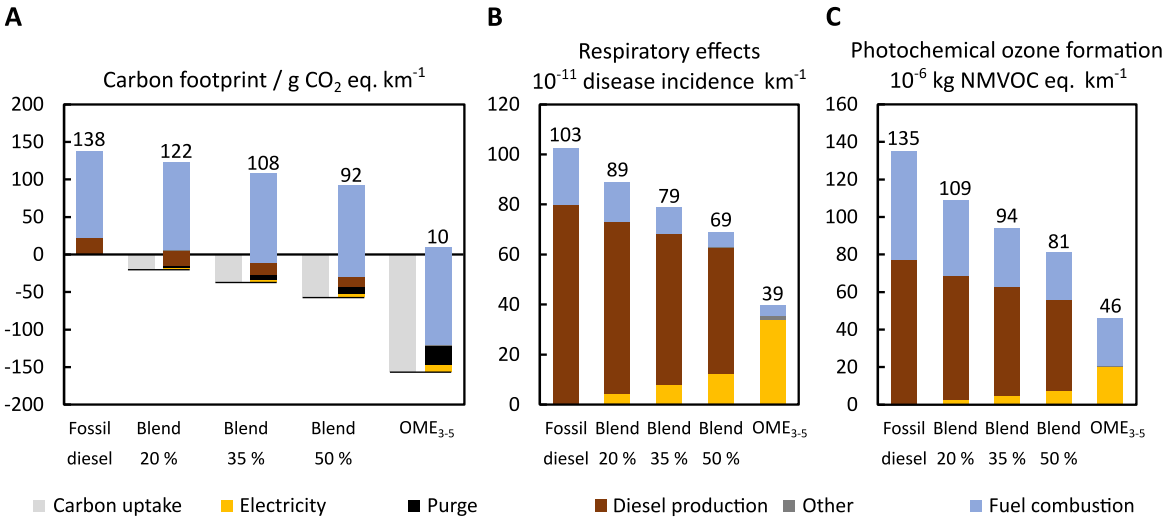

Figure 5.6: Well-to-wheel (A) carbon footprint in g CO_2 eq. per km, (B) respiratory effects in 10^{-11} disease incidence per km, and (C) photochemical ozone formation in 10^{-6} kg NMVOC eq. per km of pure fossil diesel, blends of OME$_{3\text{-}5}$ in fossil diesel, and pure OME$_{3\text{-}5}$ for the best-case scenario. OME$_{3\text{-}5}$ is produced via the MeOH DEHY route. The carbon footprint of the carbon uptake due to CO_2 utilization is negative (light grey). Positive environmental impacts result from electricity supply (yellow), direct CO_2 emissions in purge gases from OME$_{3\text{-}5}$ production (black), diesel production (brown), fuel combustion (light blue), and minor emissions due to process water supply and wastewater treatment (dark grey). The same figure is shown with CO_2 from DAC in the best-case scenario in Figure C.9.

In terms of the carbon footprint, the combustion, i.e., use phase, of the fuels contributes most to the overall impact in the best-case scenario (Figure 5.6A). Note that the combustion of OME$_{3\text{-}5}$ slightly increases CO_2 emissions compared to fossil diesel due to the lower heating value (see Section 5.3.2). However, the production of OME$_{3\text{-}5}$ overcompensates increased CO_2 emissions from fuel combustion, reducing the overall carbon footprint of the entire life cycle: Blending ratios of 20, 35 and 50 vol% OME$_{3\text{-}5}$ in fossil diesel reduce the carbon footprint by 12 %, 22 % and 33 %, respectively. Pure OME$_{3\text{-}5}$ reduces the carbon footprint by 93 %. Respiratory effects are dominated by the production of fossil diesel and, for increasing blending ratios, also by the electricity supply (Figure 5.6B). Blending 20, 35 and 50 vol% OME$_{3\text{-}5}$ with fossil diesel reduces respiratory effects by 14 %, 23 % and 33 %, respectively, while pure OME$_{3\text{-}5}$

reduces respiratory effects by 62 %. In terms of photochemical ozone formation, fuel combustion and diesel production are the most important contributors (Figure 5.6C). Photochemical ozone formation reduces by 19 %, 30 % and 40 %, due to the blending of 20, 35 and 50 vol% $OME_{3\text{-}5}$ in fossil diesel, respectively. Pure $OME_{3\text{-}5}$ reduces photochemical ozone formation by 66 %.

In the worst-case scenario (Figure C.8), all environmental impact categories increase strongly with increasing blending ratios because fossil-based technologies are considered instead of wind power and the Power-to-X technologies of the best-case scenario (see Section 5.2.1). The largest increase is thus found for pure $OME_{3\text{-}5}$ for which the carbon footprint increases by 161 %, respiratory effects by 409 %, and photochemical ozone formation by 199 %. Note though that diesel-$OME_{3\text{-}5}$ blends would still reduce the local tailpipe emissions of NO_x and soot (see Section 5.3.2). Technological choices for electricity, H_2, and heat supply are therefore crucial and further investigated in the proceeding analysis.

5.4.3 Blending $OME_{3\text{-}5}$ gradually into a fleet

The preceding well-to-wheel analysis for the best-case and worst-case scenario highlights that Power-to-X technologies and low-carbon electricity are decisive to realize environmental benefits of diesel-$OME_{3\text{-}5}$ blends. In Figure 5.7, we therefore minimize the carbon footprint of the supply chain of diesel-$OME_{3\text{-}5}$ blends for the MeOH DEHY route as function of the carbon footprint of electricity supply. In this optimization, technological choices in the supply chain depend solely on the carbon footprint of electricity supply since we do not predefine any scenario-specific technology sets (see Section 5.2.1).

Below a carbon footprint of electricity supply of 360 g CO_2 eq. per kWh, heat supply between 90 and 250 °C changes from steam production in the chemical industry to electrode boilers, while heat supply above 250 °C changes from natural gas to electrode boilers below 235 g CO_2 eq. per kWh. H_2 supply changes from fossil-based steam methane reforming to PEM electrolysis below 227 g CO_2 eq. per kWh. As a result, the production system is solely based on Power-to-X technologies below 227 g CO_2 eq. per kWh. Consequently, further reducing the carbon footprint of electricity supply strongly reduces the well-to-wheel carbon footprint of pure $OME_{3\text{-}5}$ (Figure 5.7, strongly negative slope). The well-to-wheel carbon footprints of diesel-$OME_{3\text{-}5}$ blends and pure $OME_{3\text{-}5}$ are lower than that of pure fossil diesel, once the carbon footprint of electricity supply is below 140 g CO_2 eq. per kWh.

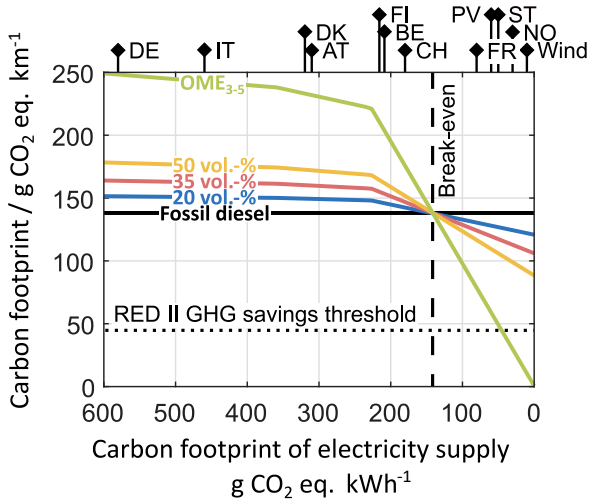

Figure 5.7: The well-to-wheel carbon footprint as function of the carbon footprint of electricity supply for pure OME$_{3\text{-}5}$, blends of 20, 35, and 50 vol% OME$_{3\text{-}5}$ in diesel as well as pure fossil diesel. The well-to-wheel impacts include emissions along the entire life cycle of diesel-OME$_{3\text{-}5}$ blends. Note that pure fossil diesel is a horizontal line since aggregated process data from the GaBi LCA database is used. Thereby, changes due to the decarbonization of electricity and electrification of the refinery cannot be reflected. In reality, the line of pure fossil diesel would thus slightly decrease if electricity is decarbonized and heat supply is electrified. The theoretical lower bound of fossil diesel would be 115 g CO_2 eq. per km, with diesel combustion being the only contributor, if fossil diesel production would be carbon-neutral (see Figure 5.6A). Note though that the curves of diesel-OME$_{3\text{-}5}$ blends would then also decrease slightly. The dashed vertical line represents the break-even carbon footprint of electricity supply below which diesel-OME$_{3\text{-}5}$ blends reduce the well-to-wheel carbon footprint compared to fossil diesel. The dotted horizontal line represents the GHG savings threshold from the renewable energy directive II (RED II) of the European Commission. The RED II states that GHG emissions savings from fuels of non-biological origin shall be at least 70 % compared to a fossil fuel comparator with 94 g CO_2 eq. per MJ (European Commission, 2018a), corresponding to 148 g CO_2 eq. per km with an energy consumption of 1.57 MJ per km. CO_2 is supplied by an ammonia plant. See Figure C.10 for the same figure with CO_2 from DAC. DE: Germany, IT: Italy, DK: Denmark, AT: Austria, FI: Finland, BE: Belgium, CH: Switzerland, FR: France, PV: photovoltaic, ST: solar-thermal, NO: Norway, wind: wind power.

An even more ambitious electricity carbon footprint of 45 g CO_2 eq. per kWh or lower is required if OME$_{3\text{-}5}$ is to comply with the European Commission's RED II (European Commission, 2018a). In the RED II, fuels from non-biological origin, e.g., e-fuels, shall reduce GHG emissions by at least 70 % compared to a fossil fuel comparator (Figure 5.7, dotted horizontal line). See Figure C.10 for the same analysis recalculated for CO_2 from DAC instead of an ammonia plant. Our recalculations show that the cleaner the electricity supply the less sensitive are the environmental impacts towards the considered CO_2 supply, e.g., different DAC systems such as TSA or HT-Aq DAC.

Reducing the well-to-wheel carbon footprint with diesel-$OME_{3\text{-}5}$ blends is thus only possible if Power-to-X technologies for heat and H_2 supply are combined with low-carbon electricity. For example, today's country-specific grid mixes of France and Norway as well as wind and photovoltaic power would already enable reducing the well-to-wheel carbon footprint with diesel-$OME_{3\text{-}5}$ blends. However in the future, such low-carbon electricity will also be demanded by competing Power-to-X applications and will remain scarce. Environmental impact reductions of diesel-$OME_{3\text{-}5}$ blends will therefore depend on both the availability of additional electricity for $OME_{3\text{-}5}$ production and the environmental impacts of that electricity supply.

In the following, we further analyze this dependence in more detail on the example of the EU's current fleet of diesel passenger cars. In this analysis, we focus on those electricity supply grid mixes and technologies that showed the potential to reduce the carbon footprint compared to fossil diesel in the preceding supply chain optimization. We determine the current annual mileage of the EU fleet of diesel passenger cars as 1.34 trillion km: Today, the EU fleet of diesel passenger cars amounts to about 95.7 million cars (Eurostat, 2020b), while the average annual mileage by EU passenger cars is estimated as 14,000 km (Siegemund et al., 2017). We assume this mobility demand with diesel-like passenger cars to be constant. For this estimated mobility demand, we then calculate the blending ratio of $OME_{3\text{-}5}$ in fossil diesel, depending on additionally available electricity for $OME_{3\text{-}5}$ production. This blending ratio corresponds to distributing diesel-$OME_{3\text{-}5}$ blends for the entire EU fleet of diesel passenger cars ("blend for all"). For more details on the calculations see Section C.3.2.

Figure 5.8 shows the volumetric blending ratio, the carbon footprint, respiratory effects, and photochemical ozone formation as function of additionally available electricity for $OME_{3\text{-}5}$ production. The aforementioned impact categories are evaluated for different technology- and country-specific grid mixes for electricity supply as well as for the theoretical limit of a burden-free electricity supply. The solid curves show the environmental impacts of diesel-$OME_{3\text{-}5}$ blends for the entire fleet ("blend for all"), while the dashed lines represent the linear combination of using pure fossil diesel and pure $OME_{3\text{-}5}$ in the fleet ("pure for few"). We show "pure for few" only for one electricity supply for the sake of better readability.

The blending ratio of $OME_{3\text{-}5}$ in diesel is a concave nonlinear function of the additional electricity supply (Figure 5.8A). This concave function results from $OME_{3\text{-}5}$ being no direct substitute for fossil diesel since $OME_{3\text{-}5}$ has a lower specific heating value than fossil diesel: Substituting 1.0 L of fossil diesel requires 1.8 L of $OME_{3\text{-}5}$ to provide the same amount of enthalpy of combustion. Therefore, more $OME_{3\text{-}5}$ is required than fossil diesel is replaced, resulting in an increase of the total fuel mass for

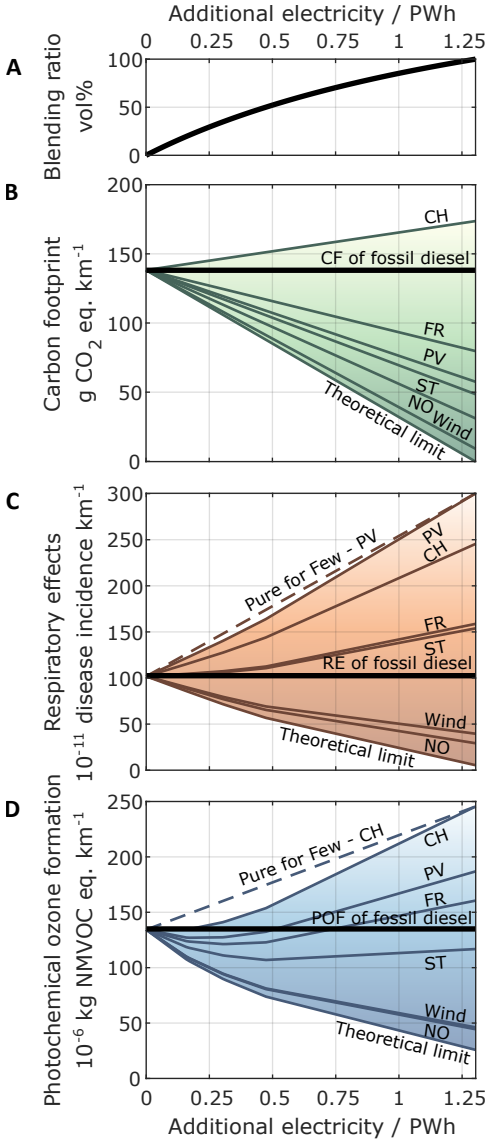

Figure 5.8: The volumetric blending ratio (A), the well-to-wheel carbon footprint (CF) (B), respiratory effects (RE) (C), and photochemical ozone formation (POF) (D) as function of additionally available electricity for OME$_{3\text{-}5}$ production. Results are presented for country- and technology-specific environmental impacts of electricity. Solid curves indicate the environmental impacts of blending OME$_{3\text{-}5}$ with fossil diesel for the entire fleet ("Blend for All"), while dashed lines show the results for switching only some diesel passenger cars to pure OME$_{3\text{-}5}$ usage ("Pure for Few"). "Pure for Few" is the linear combination of pure diesel and pure OME$_{3\text{-}5}$ and is, for the sake of better readability, shown for only two examples. The black bold lines indicate the environmental impacts of pure fossil diesel for reference. CO_2 is supplied by an ammonia plant. See Figure C.11 for the same figure with CO_2 from DAC. CH: Switzerland, FR: France, NO: Norway, PV: photovoltaic, ST: solar-thermal. The theoretical limit of a burden-free electricity supply is also included as lower bound.

increasing blending ratios. Using pure $OME_{3\text{-}5}$ for the entire fleet, i.e., a blending ratio of 100 vol%, would require 1.3 PW h of additional electricity to substitute the entire EU diesel demand for passenger cars. This additional demand corresponds to almost half of the 2.8 PW h of electricity currently produced in the EU states (Eurostat, 2020a).

The well-to-wheel carbon footprint of diesel-$OME_{3\text{-}5}$ blends depends linearly on the amount of additional electricity (Figure 5.8B). Thus, each additional unit of electricity for $OME_{3\text{-}5}$ production has the same marginal impact on the overall carbon footprint irrespective of the blending ratio. Consequently for the carbon footprint, there would be no difference between blending the produced $OME_{3\text{-}5}$ with fossil diesel for the entire fleet ("blend for all") and switching only some vehicles to pure $OME_{3\text{-}5}$ usage instead ("pure for few").

In contrast to the carbon footprint, the well-to-wheel respiratory effects and photochemical ozone formation of diesel-$OME_{3\text{-}5}$ blends depend nonlinearly on the amount of additional electricity (Figure 5.8C and D): In the use phase of diesel-$OME_{3\text{-}5}$ blends, NO_x and soot emissions reduce nonlinearly with increasing blending ratios (see Section 5.3.2). For respiratory effects and photochemical ozone formation, the curves of "blend for all" are always below the lines of "pure for few," i.e., "blend for all" has always less environmental impacts than "pure for few." Consequently, blending $OME_{3\text{-}5}$ gradually with fossil diesel for the entire fleet ("blend for all") is always better than switching only some vehicles to pure $OME_{3\text{-}5}$ usage ("pure for few"). We discuss the significantly higher environmental impacts for electricity from photovoltaic compared to electricity from wind power in Section C.5.3.

The benefit of "blend for all" over "pure for few" is maximal at a blending ratio of 50 vol% for both respiratory effects and photochemical ozone formation with higher benefits for photochemical ozone formation. This blending ratio of 50 vol% requires 0.47 PW h of electricity for $OME_{3\text{-}5}$ production. Moreover, we find that the cleaner the electricity supply (see Figure 5.7, top axis for exemplary values), the greater the benefit of "blend for all" over "pure for few." When applying "blend for all" instead of "pure for few," photochemical ozone formation reduces by 12 % with Swiss (CH) electricity and by 21 % with Norwegian (NO) electricity at a blending ratio of 50 %. Similarly, respiratory effects reduce by 7 % with Swiss (CH) electricity and by 13 % with Norwegian (NO) electricity.

Consequently, blending $OME_{3\text{-}5}$ with fossil diesel for the entire fleet can contribute to reducing the carbon footprint, photochemical ozone formation, and respiratory effects compared to pure fossil diesel. However, fuel suppliers should always distribute $OME_{3\text{-}5}$ as a blend with fossil diesel to the filling stations to maximize the environ-

mental benefits for the entire fleet. The blending ratio should then be gradually increased, when more additional electricity is available for $OME_{3\text{-}5}$ production. Besides the availability of electricity, the reductions in each environmental impact category depend also on the environmental impacts of electricity supply. Today, electricity from wind power and the Norwegian electricity grid mix are already sufficiently clean to reduce all three environmental impact categories with diesel-$OME_{3\text{-}5}$ blends simultaneously (Figure 5.8). For contribution analyses of "blend for all" in Figure 5.8 for various country- and technology-specific electricity supplies, see Section C.5.3.

5.5 Summary and conclusion

In this chapter, we answer from a fleet perspective how limited synthetic fuels should be *distributed* in vehicle fleets for minimal environmental impacts: as pure fuel for only few vehicles or blended with fossil fuel for all vehicles? For this purpose, we consider the effect of variable blending ratios of synthetic in fossil fuel as additional degree of freedom. Electricity-based $OME_{3\text{-}5}$ is investigated as exemplary synthetic fuel, which enables to escape the traditional NO_x-soot trade-off of fossil diesel.

Our well-to-tank LCA of four anhydrous and aqueous $OME_{3\text{-}5}$ production routes underlines that both aqueous routes are preferable regarding exergy efficiency and environmental impacts. The aqueous routes exhibit exergy efficiencies of up to 71 % and have lowest environmental impacts. Future studies should thus focus on routes via methanol dehydrogenation, such as that proposed by Ouda et al. (2018a) and the variant considered herein. The well-to-wheel LCA demonstrates that blending $OME_{3\text{-}5}$ with fossil diesel can reduce environmental impacts for all considered impact categories in the best-case scenario. In this LCA, we integrate measured NO_x and soot emissions from diesel-$OME_{3\text{-}5}$ blend combustion for various blending ratios. Notable, our results contradict earlier findings for respiratory effects and photochemical ozone formation by Rodríguez-Vallejo et al. (2021) who used proxy data for combustion emissions. In general, we thus emphasize to use measured data as reliable basis for sound conclusions.

The fleet analysis demonstrates that increasing blending ratios of $OME_{3\text{-}5}$ in fossil diesel can reduce all considered impacts compared to fossil diesel. Reduction potentials depend however strongly on the environmental impacts of electricity supply, the desired blending ratio, and the availability of additional electricity for $OME_{3\text{-}5}$ production. We further show that the environmentally optimal distribution of synthetic fuels depends on how combustion-induced NO_x and soot emissions develop with increasing

blending ratios. Distribution as a blend with fossil fuel is optimal for synthetic fuels whose NO_x and soot emissions reduce disproportionately strong with increasing blending ratio, as demonstrated for blends of $OME_{3\text{-}5}$ and fossil diesel. Reversely, synthetic fuels should be distributed as pure fuel if combustion-induced emissions increase disproportionately with increasing blending ratio. In case of a linear relationship between combustion emissions and blending ratio, both distribution options are equivalent.

For minimal environmental impacts, fuel suppliers should thus distribute $OME_{3\text{-}5}$ as a blend component to the filling stations and gradually increase the blending ratio as soon as more electricity is available for $OME_{3\text{-}5}$ production. Noteworthy, a blending ratio of 100 vol% $OME_{3\text{-}5}$ would require a massive expansion of current renewable electricity capacities. Yet, the blending ratio would likely increase over time for a constant amount of electricity for $OME_{3\text{-}5}$ production: With battery electric vehicles on the rise, the demand for fossil diesel fuel by the remaining diesel vehicles is likely to decrease in the future.

Chapter 6

Summary, conclusions, and future perspectives

In this final chapter, the thesis is summarized and the main conclusions are drawn in Section 6.1, followed by Section 6.2 outlining perspectives for future research.

6.1 Summary and conclusions

One of today's major challenges in mitigating climate change is the transition towards clean transportation. Direct electrification of transportation is most efficient and should therefore be prioritized wherever possible. However, hard-to-electrify transport subsectors are projected to remain partly reliant on liquid energy carriers. In these subsectors, synthetic fuels produced from renewable electricity and alternative carbon feedstocks can contribute to climate change mitigation as complements for direct electrification.

The current practice of environmental assessment and model-based design of synthetic fuels revealed major scientific gaps regarding their *screening*, *filtering*, and *distribution* (Chapter 2). For the *screening* of synthetic fuels via model-based fuel design, the identification of key environmental objectives is desirable to design synthetic fuels holistically but with manageable computational cost. However, these key environmental objectives have not yet been identified. Furthermore, only those synthetic fuels from *screening* should be *filtered* out for more detailed analyses that address the four key challenges of current synthetic fuels. Yet, so far, synthetic fuels fulfilling all key challenges simultaneously are lacking. From an environmental perspective, it is also unclear whether limited amounts of synthetic fuels should be *distributed* as pure fuel to only few vehicles or as blend with fossil fuel to all vehicles of a fleet. This

thesis intends to narrow these scientific gaps with a three-stage fuel design procedure, guiding decision-making in *screening*, *filtering*, and *distribution* of synthetic fuels.

In the *screening* stage, a wide range of synthetic fuel candidates is screened in an early development stage to find potential substitutes for fossil fuels. To design synthetic fuels holistically, we extend the objective space of the integrated process and fuel design framework by König et al. (2021), by including 15 objectives of the LCA methodology in addition to the current objectives production cost and GWI (Chapter 3). However, multi-objective optimization with 17 objectives is computationally expensive. We therefore identify those environmental objectives that cover the key trade-offs of the optimization problem to keep the computational cost minimal. For this purpose, we apply the dominance-based optimization approach by Guillén-Gosálbez (2011) to identify key objective subsets that induce minimal changes to the problem's dominance structure.

Our findings suggest that considering few environmental objectives is sufficient to capture the major trade-offs in spark-ignition engine fuel design. Among all objectives, "land use" and "resource use of minerals and metals" stand out as key objectives in addition to "production cost." These key objectives hold for both current and future technologies for feedstock and utility supply. Notable, the suggested key environmental objectives should be verified if major changes are applied to the fuel design framework, the case study, or the considered LCIA methods. Our integrated process and fuel design with these three objectives highlights that the obtained bio-hybrid fuels can balance the benefits and drawbacks of pure bio- and e-fuels.

The *filtering* stage further narrows the group of synthetic fuels obtained from *screening*. For this purpose, only those synthetic fuels are filtered out for further analyses that can address the four key challenges of current synthetic fuels: (1) technological maturity for timely production at scale, (2) compatibility with fuel standards and sealing materials, (3) reducing urban air pollutants, and (4) enabling net-zero GHG emissions. Our multi-disciplinary study on hydroformylated Fischer-Tropsch (HyFiT) fuels demonstrates that HyFiT-fuels can be tailored to address all key challenges simultaneously (Chapter 4).

The proposed HyFiT-fuel production concept enables to close the carbon cycle flexibly by employing either biomass, CO_2, or combinations thereof as feedstock. Furthermore, the process concept is scalable due to the use of the well-established technologies FT synthesis and hydroformylation. Our experiments demonstrate that HyFiT-fuels can be tailored for compliance with global fuel standards and compatibility with two standard sealing materials, which enable retrofitting today's vehicle fleets. Combustion-induced PM and NO_x emissions can also be reduced substantially com-

pared to fossil diesel. The comprehensive well-to-wheel LCA finds that, in particular, bio-based HyFiT-fuels can aid the transition towards net-zero GHG emissions. Bio-based HyFiT-fuels are shown to yield GHG emissions well below those of fossil diesel and competitive to BEVs even with the EU's present electricity grid mix. Overall, bio-based HyFiT-fuels are promising complements to electrified powertrains especially in long-haul applications: they show lower environmental impacts than BEVs in ten to twelve of 16 impact categories if driving ranges greater than 550 km are required. Notable, land use is large for bio-based HyFiT-fuels and needs to be carefully assessed regionally for a large-scale deployment.

In the *distribution* stage, the optimal distribution of limited amounts of synthetic fuels in vehicle fleets is determined from an environmental perspective. Since the feedstocks of synthetic fuels are likely to remain limited in the future, the production volume of synthetic fuels can be expected to be limited as well. Therefore, limited amounts of synthetic fuels could be either distributed as pure fuels for only few vehicles or as blends with fossil fuel, e.g., diesel, for all vehicles in a fleet.

We analyze the optimal distribution of synthetic fuels for minimal environmental impacts using LCA (Chapter 5). For this purpose, we choose electricity-based $OME_{3\text{-}5}$ as an exemplary synthetic fuel since a comprehensive well-to-wheel LCA is missing that considers all major electricity-based $OME_{3\text{-}5}$ production routes and includes measured combustion emissions. In this analysis, the blending ratio of $OME_{3\text{-}5}$ in diesel is treated as an additional degree of freedom. Among all considered routes, aqueous $OME_{3\text{-}5}$ production is shown to be preferable: Our well-to-wheel LCA highlights that blends of $OME_{3\text{-}5}$ in diesel can reduce all considered impacts compared to fossil diesel. However, the environmental impacts of electricity supply and the blending ratio are decisive for the reduction potentials of diesel-$OME_{3\text{-}5}$ blends. With our fleet analysis, we demonstrate that the environmentally optimal distribution of synthetic fuels depends on how the fuel's combustion-induced emissions develop with increasing blending ratios. If combustion-induced emissions reduce disproportionately strong with increasing blending ratios, as shown for $OME_{3\text{-}5}$, distribution as a blend is optimal. In contrast, distribution as pure fuel would be optimal if combustion-induced emissions increase disproportionately strong with increasing blending ratios.

In conclusion, this thesis contributes to narrow major scientific gaps in the assessment and model-based design of synthetic fuels. Based on the methodology of LCA, the herein proposed fuel design procedure aims to guide decision-making regarding the *screening*, *filtering*, and *distribution* of synthetic fuels. However, other scientific gaps are still to be addressed and provide perspectives for future research, as discussed in the proceeding section.

6.2 Future perspectives

In the following, we discuss perspectives for future research in the assessment and model-based design of synthetic fuels, based on the contributions outlined in this thesis.

Enhance the use-phase model of integrated process and fuel design: The accuracy of early-stage synthetic fuel screening by integrated process and fuel design could be enhanced by developing a sophisticated use-phase model. The current use-phase model considers only CO_2 emissions but neglects combustion-induced pollutants such as PM, NO_x, and CO. Estimating these pollutants accurately can, however, influence environmental impacts of synthetic fuels drastically, as demonstrated with our work on $OME_{3\text{-}5}$ in Chapter 5. In this regard, engine-out PM emissions of non-oxygenated hydrocarbons may be predicted with the particulate matter index by Aikawa et al. (2010), whereas the yield sooting index by Das et al. (2018) may serve as a starting point to predict engine-out PM emissions also for oxygenated hydrocarbons. In contrast, pollutants such as NO_x depend strongly on the engine operation, which may render their estimation challenging at an early stage.

Include social objectives: The design of sustainable synthetic fuels requires considering all three dimensions of sustainability: the economic, environmental, and social dimension. While economic and environmental objectives are usually considered, e.g., in this thesis, the social dimension is often overlooked. For decision-making, social aspects such as public acceptance are of equal importance to design sustainable synthetic fuels. For instance, Linzenich et al. (2019) found that predominantly fuel costs drive the social acceptance of synthetic fuels. However, considering social acceptance as objective for fuel design requires a mathematical equation that can be optimized for. For the optimization of fuel production networks, Becker et al. (2024) recently derived such a social acceptance objective function. Based on their work, social acceptance could be also included as additional objective in the integrated process and fuel design framework.

Consider scaling effects in integrated process and fuel design: Depending on the production scale, prices and environmental impacts of feedstocks and auxiliaries for fuel production might change. For instance, feedstock and auxiliary prices are influenced by market effects such as the price elasticity of demand. Moreover, the development of new land for biomass cultivation or wind parks might induce land-use change emissions. These scaling effects of fuel production are currently not considered in the integrated process and fuel design framework. One option would be to capture these scaling effects endogenously by incorporating integrated assessment models into

the fuel design framework, e.g., the SecMOD framework by Baumgärtner et al. (2021) and Reinert et al. (2022). However, solving an integrated assessment model would likely increase the computational cost of integrated process and fuel design substantially. Alternatively, scaling effects could be specified exogenously, e.g., by defining constant price elasticity functions as applied for energy service demands in the TIMES integrated assessment model (Loulou and Labriet, 2008; Loulou, 2008).

Explore the near-optimal solution space: In this thesis, we explored the Pareto-optimal solution space of integrated process and fuel design (Chapter 3) and climate-change-optimal supply chains of HyFiT-fuels (Chapter 4) and $OME_{3\text{-}5}$ (Chapter 5). These optimizations revealed burden-shifting between environmental impact categories and, in case of integrated process and fuel design, production cost. However, near-optimal process and fuel designs as well as supply chain designs might exist that can leverage a small increase in few objectives to gain substantial reductions in many other objectives. Therefore, it might be worth exploring the near-optimal solution space with methods such as Modeling to Generate Alternatives (MGA) by Brill et al. (1982, 1990) and Modeling All Alternatives (MAA) by Pedersen et al. (2021).

Consider model-based fuel design for other propulsion technologies: The integrated process and fuel design framework could be also adapted to design synthetic fuels for other propulsion technologies than internal combustion engines. For instance, synthetic fuels for fuel cells and gas turbines have not yet been in focus of early-stage fuel screening. Nonetheless, model-based fuel design for these technologies would enable to broaden the scope towards the transport subsectors shipping and aviation. Synthetic fuels for these transport subsectors would, however, likely require adjustments to both the pathway and fuel property model of the fuel design framework. Fuel cells and gas turbines likely have other fuel specifications than internal combustion engines, which may require producing and blending new fuel components in the pathway model. In addition, other fuel specifications may also include fuel properties for whose prediction no model-based approaches exist yet.

Test and develop HyFiT-fuels further: While this thesis establishes the potential of HyFiT-fuels, we also identify target areas for future development. On the process level, research should address the gas loop design and the removal of aromatics and oxygenates. Furthermore, the benefits of the recently demonstrated one-pot reactors for tandem integration of FT synthesis and hydroformylation could be exploited (Jeske et al., 2022). Although we are confident that our process concept can be scaled up successfully because all its elements have been, future studies should also consider the scale-up of HyFiT-fuels and its implications on environmental impacts. On the system level, the use of by-products of fuel production should be explored, e.g.,

the aromatic compounds assumed to be incinerated are key platform chemicals. By-product use may give rise to environmental credits for by-products, so-called avoided burdens, improving the LCA results further.

For fuel usage, further studies could go beyond the elastomers investigated and examine static and dynamic technical seals. Regarding fuel storage and handling, studies on n-octanol and n-decanol found low hygroscopicity (Wang et al., 2021; El-Seesy et al., 2021), suggesting that long-chain alcohols are promising alternative fuels and do not suffer from water uptake. Still, further experiments should analyze the fuels' hygroscopicity as well as electrical conductivity, microbial infestation, flash point, and toxicity. Combustion may further leverage the potential of HyFiT-fuels to reduce NO_x emissions by experimentally testing the optimized calibration of the exhaust gas recirculation.

Consider the Earth's planetary boundaries: The environmental impacts of synthetic fuels could be put into perspective by including the Earth's planetary boundaries into the assessment and model-based design of synthetic fuels. In such a planetary boundary analysis, it would be desirable to include also electrified powertrains, i.e., FCEVs and BEVs. Therefore, the transgression of the Earth's so-called safe operating space could be compared for different propulsion technologies. Notable, the safe operating space would have to be scaled down, as synthetic fuels account only for a fraction of all human activities. For downscaling, different principles could be applied, which have to be classified regarding their suitability (Bachmann et al., 2023b).

Appendices

Appendix A

Supporting information to Chapter 3

Here, we provide further details for Chapter 3. In Section A.1, we review recent studies applying objective reduction methods on environmental objectives. Additional information on applied methods and generated results are presented in Section A.2 and Section A.3, respectively.

A.1 Introduction

In Table A.1, we give an overview on recent applications of objective reduction methods on environmental objectives. Approximately 70 % of the case studies use the dominance-based objective reduction method by Guillén-Gosálbez (2011) that is based on the work of Brockhoff and Zitzler (2006). Correlation-based PCA is used by 33 %, whereas 6 % rely on other methods for objective reduction.

Table A.1: Recent studies that applied objective reduction methods on environmental objectives. PCA: principal component analysis.

Author	**Year**	**Objective reduction method**			**Application**
		Dominance	PCA	Other	
Qin et al.	2020		✓		Energy systems
Chu et al.	2018		✓		Tidal flat reclamation
Perez-Gallardo et al.	2018		✓		Photovoltaic grid-connected systems
Vázquez et al.	2018b	✓	✓		Chemical supply chains
Vázquez et al.	2018b	✓	✓		Construction of a building
Vázquez et al.	2018c	✓	✓		Safety of a distillation train
Vázquez et al.	2018a	✓			Chemical supply chains
Vázquez et al.	2018a	✓			Construction of a building
Hennen et al.	2017	✓			Energy system

Continued on next page.

Continued from previous page.

Author	Year	Objective reduction method			Application
		Dominance	PCA	Other	
Wheeler et al.	2017			✓	Bioethanol supply chains
Carreras et al.	2016	✓			Construction of a building
Copado-Méndez et al.	2016	✓			Bioethanol supply chains
Copado-Méndez et al.	2016	✓			Hydrogen supply chains
Steinmann et al.	2016		✓		Product life cycles
Kostin et al.	2015	✓			Bioethanol supply chains
Kostin et al.	2015	✓			Hydrogen supply chains
Postels et al.	2015	✓			Energy system
Copado-Méndez et al.	2014	✓			Hydrogen supply chains
Copado-Méndez et al.	2014	✓			Metabolic networks
Čuček et al.	2014			✓	Biomass and bioenergy supply chains
Vaskan et al.	2014	✓			Utility plants
Antipova et al.	2013	✓			Reverse osmosis desalination plant
Oliva et al.	2013	✓			Chemical supply chains
Oliva et al.	2013	✓			Bioethanol supply chains
Oliva et al.	2013	✓			Hydrogen supply chains
Brunet et al.	2012		✓		L-lysine production
Kostin et al.	2012	✓			Bioethanol supply chains
Pozo et al.	2012		✓		Chemical supply chains
Sabio et al.	2012		✓		Hydrogen supply chains
Vaskan et al.	2012	✓			Heat exchanger
Guillén-Gosálbez	2011	✓			Heat exchanger
Guillén-Gosálbez	2011	✓			Chemical supply chains
Gutiérrez et al.	2010		✓		Domestic appliances

A.2 Methods

This section presents details on the LCA (Section A.2.1), integrated process and fuel design (Section A.2.2), and objective reduction (Section A.2.3).

A.2.1 Life cycle assessment

The used LCA inventory datasets are listed for all feedstocks, utilities, solvents, and others in Table A.2. Note that the LCA database ecoinvent does not provide inventory data for each solvent. We thus list only those solvents for which datasets are available.

Table A.2: LCA datasets of the life cycle inventory.

Flow	Unit	Dataset[a]	Reference
Feedstocks			
Carbon dioxide	kg	Capture at steel plant	von der Assen et al. (2016)
		Direct air capture[b]	Deutz and Bardow (2021)
Biomass	kg	DE: hardwood forestry, beech, sustainable forest management	Wernet et al. (2016)
Hydrogen	kg	Water electrolysis, polymer electrolyte membrane	Reuß et al. (2017)
Utilities			
Electricity	MJ	DE: market for electricity, medium voltage	Wernet et al. (2016)
		DE: electricity production, wind, 1-3MW turbine, onshore	Wernet et al. (2016)
Heat	MJ	RER: steam production, as energy carrier, in chemical industry	Wernet et al. (2016)
		Electrode vessel with a power-to-heat efficiency of 95 %	Müller et al. (2020a)
Cooling water	kg	DE: market for water, decarbonised	Wernet et al. (2016)
Refrigeration	MJ	Cryogenic cooler	Ladner (2011)
Solvents[c] and others			
Dimethyl sulfoxide	kg	RER: dimethyl sulfoxide production	Wernet et al. (2016)
γ-butyrolactone	kg	RER: dehydrogenation of butan-1,4-diol	Wernet et al. (2016)
1,4-dioxane	kg	RER: dioxane production	Wernet et al. (2016)
Helium	kg	GLO: helium purification	Wernet et al. (2016)
Benzene	kg	RER: benzene production	Wernet et al. (2016)
1,2-dichloroethane	kg	RER: ethylene dichloride production	Wernet et al. (2016)
Chlorobenzene	kg	RER: benzene chlorination	Wernet et al. (2016)
Dichloromethane	kg	RER: dichloromethane production	Wernet et al. (2016)
Chloroform	kg	RER: trichloromethane production	Wernet et al. (2016)
Cyclohexane	kg	RER: cyclohexane production	Wernet et al. (2016)
Gasoline	kg	RER: petrol production, low-sulfur[d]	Wernet et al. (2016)

[a] Abbreviations in ecoinvent dataset names: DE: Germany; RER: Europe; GLO: global.

[b] Energy requirements are taken from the predicted energy targets for a TSA DAC system by Deutz and Bardow (2021). Heat is provided by heat pumps with a COP of 3.28. The COP is averaged from heat pumps built since 2006 with condenser temperatures of about 90 °C and evaporator temperatures between $\in [9, 15]$ °C, according to David et al. (2017).

[c] Solvents without available ecoinvent datasets are excluded from this list.

[d] For gasoline, we assume a carbon content of 0.83 kg of carbon and a lower heating value of 41.3 MJ kg^{-1} to model combustion-induced CO_2 emissions.

A.2.2 Integrated process and fuel design

In the following, we describe the integrated process and fuel design model (Section A.2.2.1) and analyze the consistency of our 'today' scenario with the scenario of previous studies (Section A.2.2.2).

A.2.2.1 Model description

Here, we briefly summarize the environmental and economical objective functions of König et al. (2020, 2021). In contrast to König et al. (2020, 2021), we write the environmental objective in a generalized form for an environmental impact (EI) instead of specifically for global warming impact. The mth specific environmental impact EI_m is calculated by dividing the total environmental impact $EI_{\text{total},m}$ by a fixed annual fuel production of $\beta = 2.77 \cdot 10^{12}\,\text{kJ}\,\text{a}^{-1}$. This annual fuel production relates to the energy content of 100,000 tons of ethanol per year, in line with previous studies (Ulonska et al., 2016; König et al., 2020, 2021).

$$EI_m = \frac{EI_{\text{total},m}}{\beta} \tag{A.1}$$

The total environmental impact $EI_{\text{total},m}$ comprises the impacts due to the supply of utilities $EI_{\text{util},m}$ and feedstocks $EI_{\text{feedstock},m}$:

$$EI_{\text{total},m} = EI_{\text{util},m} + EI_{\text{feedstock},m}. \tag{A.2}$$

Environmental impacts due to utility supply $EI_{\text{util},m}$ are calculated by multiplying the energy demands of reactions $E_{\text{reac},i}$ and separation sequences $E_{\text{sep},i}$ with the specific environmental impact factor $ei_{i,m}$ of the ith utility. Considered utilities are electricity, process heat, cooling, and refrigeration.

$$EI_{\text{util},m} = \sum_{i \in N_{\text{utils}}} (E_{\text{reac},i} + E_{\text{sep},i}) \cdot ei_{i,m} \tag{A.3}$$

Environmental impacts induced by feedstock supply $EI_{\text{feedstock},m}$ are calculated as the product of the feedstock fluxes f_j, their molar masses M_j, and the specific environ-

mental impact factor $ei_{j,m}$ of the jth feedstock. As feedstocks, we consider biomass, carbon dioxide, and hydrogen but also solvents (see Table A.2).

$$EI_{\text{feedstock},m} = \sum_{j \in N_{\text{feedstock}}} f_j M_j ei_{j,m} \tag{A.4}$$

As economical objective, the specific production cost C is evaluated by dividing the total annualized production cost C_{total} by the fixed annual fuel production β:

$$C = \frac{C_{\text{total}}}{\beta}. \tag{A.5}$$

The total annualized production cost C_{total} is determined by summing up the annualized costs due to investments C_{invest}, utilities C_{util}, feedstocks $C_{\text{feedstock}}$, and wastes C_{waste}:

$$C_{\text{total}} = C_{\text{invest}} + C_{\text{util}} + C_{\text{feedstock}} + C_{\text{waste}}. \tag{A.6}$$

Annualized investment costs C_{invest} are calculated from the investment costs IC, the interest rate ir, and the project lifetime a:

$$C_{\text{invest}} = \frac{ir}{1 - (1 + ir)^{-a}} \cdot IC. \tag{A.7}$$

The investment costs IC are derived from the amount of transferred energy in reactions $E_{\text{reac,transfer},i}$ and separation sequences $E_{\text{sep,transfer},i}$ as well as the chemical engineering plant cost index (CEPCI) of the years 1993 and 2016, according to an empirical investment cost correlation.

$$IC = \frac{\text{CEPCI}_{2016}}{\text{CEPCI}_{1993}} \cdot 2.9 \cdot \left(E_{\text{transfer duty}}\right)^{0.55} \tag{A.8}$$

$$E_{\text{transfer duty}} = \sum_i \left(E_{\text{reac,transfer},i} + E_{\text{sep,transfer},i}\right) \tag{A.9}$$

Utility costs C_{util} are determined by multiplying the energy demands of reactions $E_{\text{reac},i}$ and separation sequences $E_{\text{sep},i}$ with the specific utility price parameter PR_i:

$$C_{\text{util}} = \sum_{i \in N_{\text{utils}}} (E_{\text{reac},i} + E_{\text{sep},i}) \cdot PR_i. \tag{A.10}$$

Feedstock costs $C_{\text{feedstock}}$ are the product of the feedstock fluxes f_j, their molar masses M_j, and the specific feedstock price parameter PR_j:

$$C_{\text{feedstock}} = \sum_{j \in N_{\text{feedstock}}} f_j M_j PR_j. \tag{A.11}$$

Waste costs C_{waste} are estimated by multiplying the fluxes of wastes r_k and byproducts b_k with their molar masses M_k and a generic waste price PR_{waste} for liquid and solid wastes:

$$C_{\text{waste}} = \sum_{k \in N_{\text{waste}}} (r_k + b_k)\, M_k PR_{\text{waste}}. \tag{A.12}$$

A.2.2.2 Comparison with previous fuel design studies

In this study, we partly adjust the economic and environmental input data of utilities and feedstocks based on the study of König et al. (2021). To analyze the implications of these adjustments, we compare the Pareto fronts for GWI and production cost using the input data of König et al. (2021) with using the input data of our 'today' scenario (Figure A.1).

Overall, we find similar trends using the input data of the 'today' scenario or König et al. (2021). With our 'today' scenario, GWI values are slightly greater while production cost is almost equal except for the GWI-optimal solution: GWI scores increase by 9 to 10 kg CO_2 eq. GJ^{-1}, mainly due to changes in the modeled steam and refrigeration supply. The KEAA blend, a Pareto-optimal solution of König et al. (2021), is a near-optimal solution when evaluated with this study's 'today' scenario (cross, Figure A.1). Noteworthy, the Pareto-optimal solution representing the most-promising compromise of GWI and production cost in the 'today' scenario (circle, Figure A.1) is

also a KEAA blend with the same fuel components but slight changes in composition compared to the KEAA blend identified by König et al. (2021) (Table A.3).

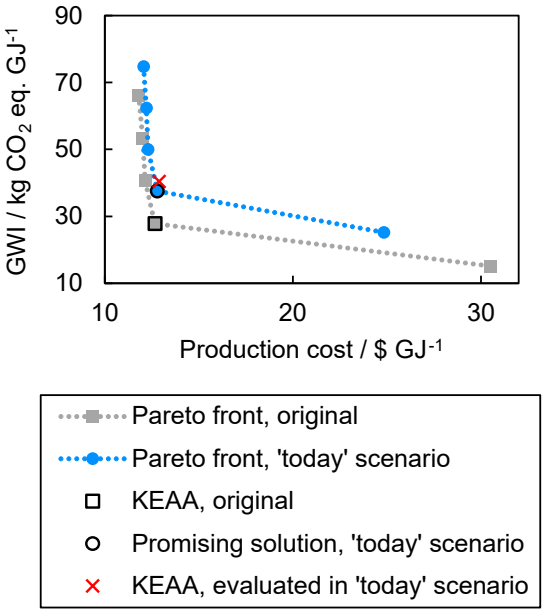

Figure A.1: Comparison of the Pareto fronts generated with feedstock and utility data of König et al. (2021) (grey) or the 'today' scenario of this study (blue). In König et al. (2021), the KEAA blend is a Pareto-optimal solution (square), whereas the KEAA blend is near-optimal when evaluated with this study's 'today' scenario (cross). Noteworthy, the most-promising solution of the 'today' scenario (circle) is also a KEAA blend but with slight changes in fuel composition.

Table A.3: Molar composition of the KEAA blend of König et al. (2021) and the most-promising comprise solution of the 'today' scenario (circle, Figure A.1).

Blend component	**KEAA blend**	**Most promising compromise solution of the 'today' scenario**
Ethanol	0.25	0.24
Methanol	0.02	0.10
Ethyl acetate	0.13	0.12
Methyl isopropyl ketone	0.40	0.38
Methyl acetate	0.16	0.13
Pentane	0.04	0.03

A.2.3 Objective reduction

The exemplary minimization problem of objective reduction has four objectives ($F = (\mathrm{f}_1, \mathrm{f}_2, \mathrm{f}_3, \mathrm{f}_4)^{\mathrm{T}}$) and three Pareto-optimal solutions since no solution is dominated by any of the others (Figure A.2A). If objective f_4 is omitted, all solutions are still non-dominated in the reduced objective space ($F_1' = (\mathrm{f}_1, \mathrm{f}_2, \mathrm{f}_3)^{\mathrm{T}}$), i.e., the Pareto dominance structure is preserved (Figure A.2B). In this case, no error is induced by objective reduction because objective f_4 is redundant. However, if additionally objective f_3 is omitted ($F_2' = (\mathrm{f}_1, \mathrm{f}_2)^{\mathrm{T}}$), solution s2 is dominated by solution s3 (Figure A.2C) although it was not dominated in the full objective space F. Consequently, solution s2 would be lost in F_2' since it is no longer Pareto-optimal. Thus, the Pareto dominance structure of the full objective space is changed due to objective reduction. The so-called δ-error quantifies this change as the maximum amount that has to be subtracted from a solution, which is dominating another solution in a reduced objective space, to render this solution also dominating the other solution in the full objective space. In this exemplary minimization problem, the δ-error is 0.5: The value of solution s3 regarding objective f_3 has to be subtracted by 0.5 such that solution s3 would not only dominate solution s2 in the reduced objective space F_2' but also in the full objective space F.

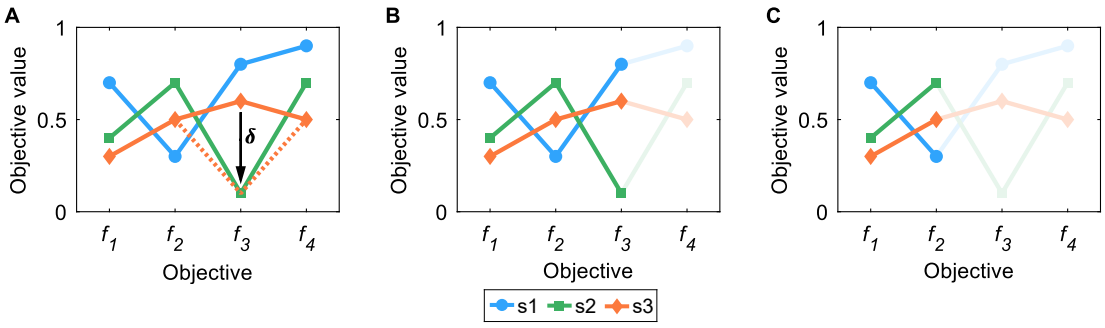

Figure A.2: Exemplary minimization problem of objective reduction. Dominance structures of (A) the full objective set $F = (\mathrm{f}_1, \mathrm{f}_2, \mathrm{f}_3, \mathrm{f}_4)^{\mathrm{T}}$, (B) the reduced objective subset $F_1' = (\mathrm{f}_1, \mathrm{f}_2, \mathrm{f}_3)^{\mathrm{T}}$, and (C) the reduced objective subset $F_2' = (\mathrm{f}_1, \mathrm{f}_2)^{\mathrm{T}}$. In (A) and (B), all solutions are Pareto-optimal while solution s3 dominates solution s2 in (C).

A.3 Results

Here, we give numerical results on the correlation between variables (Section A.3.1), the objective reduction results (Section A.3.2), alternative figures for the Pareto-optimal solutions generated in the reduced objective space (Section A.3.3), and contribution analyses (Section A.3.4).

A.3.1 Correlation between variables

In Table A.4 and Table A.5, we present the correlation matrices of the initial Pareto-optimal solutions $S^{\text{today}}_{\text{filtered}}$ and $S^{\text{future}}_{\text{filtered}}$ for the 'today' and 'future' scenario, respectively. In the 'today' scenario, land use (LU) is most conflicting with all other objectives while production cost (C) and freshwater eutrophication (E_{fw}) show, on average, the weakest correlation with the other objectives. In the 'future' scenario, land use (LU) and freshwater eutrophication (E_{fw}) are both conflicting with the other objectives, whereas production cost (C) shows, again, only a slight correlation. The correlation matrices indicate correlation between all other objectives.

A.3.2 Objective reduction

In Table A.6 and Table A.7, the results of objective reduction are shown for different normalization variants and the 'today' and 'future' scenario, respectively.

Table A.4: Correlation matrix of the 'today' scenario.

	A	GWI	ET	RU_e	E_{fw}	E_m	E_t	HT_c	HT_{nc}	IR	LU	RU_m	OD	PM	POF	WU	C
A	1.00																
GWI	0.97	1.00															
ET	0.84	0.77	1.00														
RU_e	0.98	0.99	0.80	1.00													
E_{fw}	0.70	0.85	0.47	0.78	1.00												
E_m	1.00	0.96	0.83	0.97	0.70	1.00											
E_t	0.99	0.98	0.81	0.98	0.77	0.99	1.00										
HT_c	0.91	0.84	0.81	0.83	0.56	0.93	0.91	1.00									
HT_{nc}	0.95	0.93	0.81	0.91	0.75	0.96	0.96	0.96	1.00								
IR	0.89	0.97	0.68	0.93	0.94	0.89	0.93	0.77	0.90	1.00							
LU	−0.80	−0.89	−0.66	−0.85	−0.88	−0.79	−0.83	−0.73	−0.84	−0.92	1.00						
RU_m	0.89	0.84	0.80	0.82	0.62	0.91	0.89	0.98	0.97	0.80	−0.78	1.00					
OD	0.73	0.66	0.86	0.70	0.37	0.73	0.70	0.69	0.69	0.56	−0.55	0.67	1.00				
PM	0.95	0.84	0.84	0.88	0.44	0.95	0.91	0.93	0.89	0.70	−0.63	0.88	0.75	1.00			
POF	0.90	0.78	0.78	0.83	0.38	0.91	0.87	0.85	0.81	0.64	−0.47	0.78	0.70	0.96	1.00		
WU	0.94	0.84	0.88	0.89	0.49	0.94	0.91	0.92	0.89	0.72	−0.68	0.89	0.80	0.97	0.92	1.00	
C	0.45	0.42	0.47	0.43	0.31	0.47	0.46	0.49	0.49	0.39	−0.35	0.50	0.41	0.45	0.44	0.49	1.00

Table A.5: Correlation matrix of the 'future' scenario.

	A	GWI	ET	RU_e	E_{fw}	E_m	E_t	HT_c	HT_{nc}	IR	LU	RU_m	OD	PM	POF	WU	C
A	1.00																
GWI	1.00	1.00															
ET	0.86	0.87	1.00														
RU_e	0.92	0.95	0.88	1.00													
E_{fw}	−0.76	−0.72	−0.64	−0.60	1.00												
E_m	0.99	0.99	0.84	0.92	−0.71	1.00											
E_t	1.00	0.99	0.84	0.92	−0.72	1.00	1.00										
HT_c	0.99	0.98	0.83	0.88	−0.79	0.99	0.99	1.00									
HT_{nc}	0.99	0.98	0.83	0.88	−0.77	0.99	0.99	1.00	1.00								
IR	0.98	0.98	0.84	0.91	−0.63	0.99	0.99	0.97	0.98	1.00							
LU	−0.97	−0.95	−0.84	−0.85	0.89	−0.94	−0.95	−0.97	−0.97	−0.91	1.00						
RU_m	0.99	0.97	0.82	0.86	−0.81	0.98	0.99	1.00	1.00	0.96	−0.98	1.00					
OD	0.67	0.68	0.77	0.68	−0.35	0.68	0.67	0.65	0.65	0.71	−0.60	0.63	1.00				
PM	1.00	0.99	0.84	0.90	−0.79	0.99	0.99	1.00	1.00	0.97	−0.97	1.00	0.65	1.00			
POF	0.67	0.71	0.54	0.74	−0.06	0.72	0.72	0.63	0.65	0.76	−0.46	0.60	0.58	0.64	1.00		
WU	0.94	0.96	0.89	0.96	−0.61	0.95	0.94	0.91	0.92	0.95	−0.88	0.90	0.70	0.92	0.71	1.00	
C	0.44	0.43	0.45	0.42	−0.42	0.42	0.42	0.43	0.44	0.41	−0.47	0.43	0.33	0.44	0.16	0.44	1.00

Table A.6: Objective reduction results for the 'today' scenario. Normalization variant N3 yields the same results as variant N2 since they differ only by a constant offset of 1. Variant: normalization variant, *OB*: number of omitted objectives, δ: δ-error, ✓: kept objective.

Variant	*OB*	δ	A	GWI	ET	RU_e	E_{fw}	E_m	E_t	HT_c	HT_{nc}	IR	LU	RU_m	OD	PM	POF	WU	C
N1	9	0.00				✓	✓			✓			✓	✓		✓		✓	✓
N1	10	0.15				✓	✓			✓			✓	✓		✓			✓
N1	11	0.76	✓			✓	✓						✓	✓					✓
N1	11	0.76			✓		✓						✓	✓	✓				✓
N1	11	0.76				✓	✓						✓	✓		✓			✓
N1	11	0.76	✓		✓		✓						✓	✓	✓				✓
N1	11	0.76					✓						✓	✓					✓
N1	12	0.80				✓	✓						✓	✓					✓
N1	13	0.96				✓	✓						✓	✓					✓
N1	14	1.00															✓	✓	✓
N1	15	1.00																✓	✓
N1	16	1.00																	✓
N2	9	0.00				✓	✓			✓			✓	✓		✓		✓	✓
N2	10	0.14				✓	✓			✓			✓	✓		✓			✓
N2	11	1.55				✓	✓			✓			✓	✓					✓
N2	12	2.46				✓	✓						✓	✓					✓
N2	13	3.34								✓			✓	✓					✓
N2	13	3.34					✓						✓	✓					✓
N2	14	4.42											✓	✓					✓
N2	15	15.45											✓						✓
N2	16	47.79																	✓
N4	9	0.00				✓	✓			✓			✓	✓		✓		✓	✓
N4	10	0.07				✓	✓			✓			✓	✓		✓			✓
N4	11	0.53				✓	✓			✓			✓	✓					✓
N4	11	0.53			✓	✓	✓						✓	✓					✓
N4	12	0.55				✓	✓						✓	✓					✓
N4	13	0.75					✓			✓			✓	✓					✓
N4	13	0.75					✓						✓	✓					✓
N4	14	0.79											✓	✓					✓
N4	15	0.94											✓						✓
N4	16	0.98																	✓

Table A.7: Objective reduction results for the 'future' scenario. Normalization variant N3 yields the same results as variant N2 since they differ only by a constant offset of 1. Variant: normalization variant, OB: number of omitted objectives, δ: δ-error, ✓: kept objective.

Variant	OB	δ	**A**	**GWI**	**ET**	**RU$_e$**	**E$_{fw}$**	**E$_m$**	**E$_t$**	**HT$_c$**	**HT$_{nc}$**	**IR**	**LU**	**RU$_m$**	**OD**	**PM**	**POF**	**WU**	**C**
N1	10	0.00			✓	✓					✓		✓	✓				✓	✓
N1	10	0.00			✓	✓						✓	✓	✓				✓	✓
N1	11	0.24				✓					✓		✓	✓				✓	✓
N1	11	0.24				✓						✓	✓	✓				✓	✓
N1	12	0.38				✓					✓		✓	✓					✓
N1	12	0.38				✓						✓	✓	✓					✓
N1	13	0.90									✓		✓	✓					✓
N1	13	0.90										✓	✓	✓					✓
N1	14	0.99											✓	✓					✓
N1	15	1.00												✓					✓
N1	16	1.00																	✓
N2	10	0.00			✓	✓						✓	✓	✓				✓	✓
N2	10	0.00			✓	✓					✓		✓	✓				✓	✓
N2	11	0.58			✓	✓					✓		✓	✓					✓
N2	11	0.58			✓	✓						✓	✓	✓					✓
N2	12	0.65			✓	✓							✓	✓					✓
N2	13	1.01				✓							✓	✓					✓
N2	14	2.17											✓	✓					✓
N2	15	8.62											✓						✓
N2	16	36.87																	✓
N4	10	0.00			✓	✓					✓		✓	✓				✓	✓
N4	10	0.00			✓	✓						✓	✓	✓				✓	✓
N4	11	0.11			✓	✓					✓		✓	✓					✓
N4	12	0.20				✓						✓	✓	✓					✓
N4	12	0.20				✓					✓		✓	✓					✓
N4	13	0.28				✓							✓	✓					✓
N4	14	0.61											✓	✓					✓
N4	15	0.90											✓						✓
N4	16	0.97																	✓

A.3.3 Optimal fuel designs for the reduced objective space

In Figure A.3, we present the single-objective minima of the Pareto-optimal solutions generated with the reduced objective subsets. Figure A.4 presents Pareto-optimal process and fuel designs of bio-fuels generated in the 'future' scenario that yield lower scores in all objectives than the benchmark KEAA.

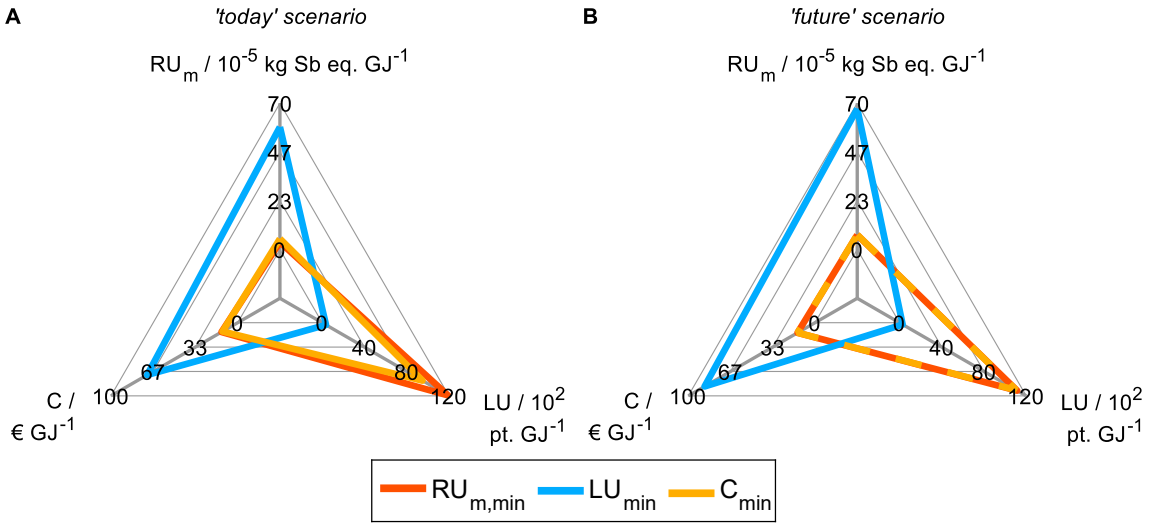

Figure A.3: Pareto-optimal process and fuel designs regarding the reduced objective space of the (A) 'today' and (B) 'future' scenario. For each of these objectives, the optimum is shown, i.e., the design with minimum production cost (C), resource use of minerals and metals (RU_m), and land use (LU).

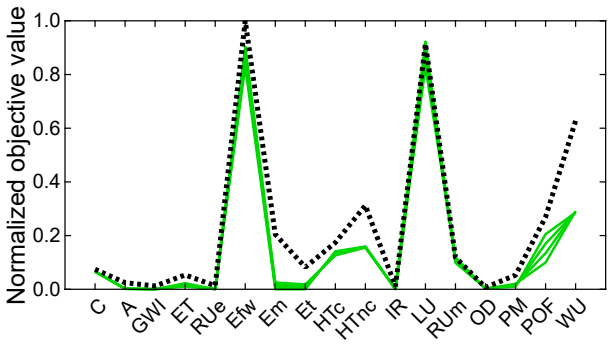

Figure A.4: Pareto-optimal process and fuel designs of bio-fuels (green) generated for the 'future' scenario and evaluated in the full objective space. All of the depicted bio-fuels yield lower scores than the KEAA benchmark (dotted) in all objectives. Each objective is normalized according to normalization variant N1. Note that, for consistency, we recalculated the results of the KEAA blend of previous studies with our 'future' scenario.

A.3.4 Contribution analyses

In Figure A.5–A.21, we present violin plots for relative contribution analyses regarding all 17 objectives. For these contribution analyses, we clustered the generated Pareto-optimal solutions of the reduced objective subsets by fuel type (bio-, e-, and bio-hybrid-fuel) for each scenario.

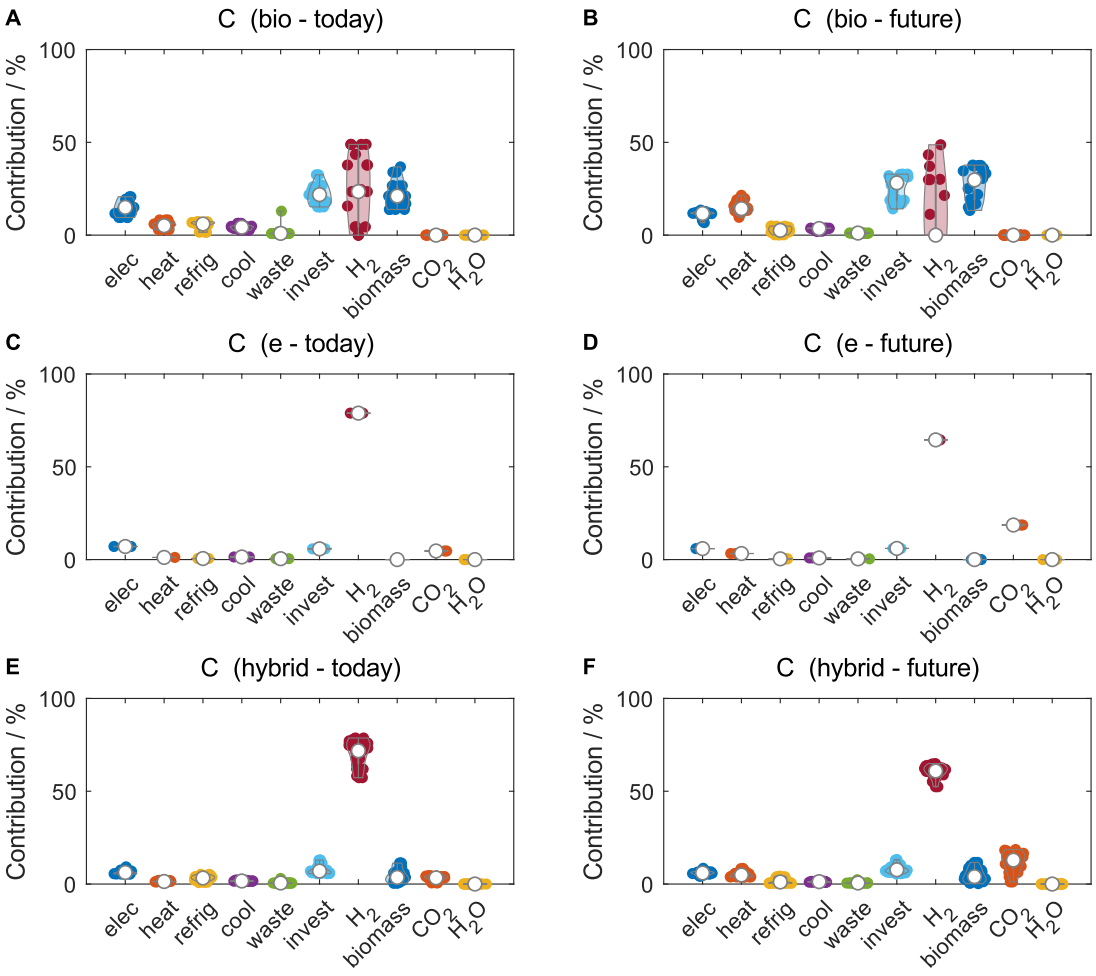

Figure A.5: Violin plot for the relative contribution analysis regarding production cost of bio-, e-, and bio-hybrid fuels in the 'today' and 'future' scenario. For each subfigure, all Pareto-optimal solutions of the corresponding fuel type and scenario are considered that have been generated for the reduced objective subset.

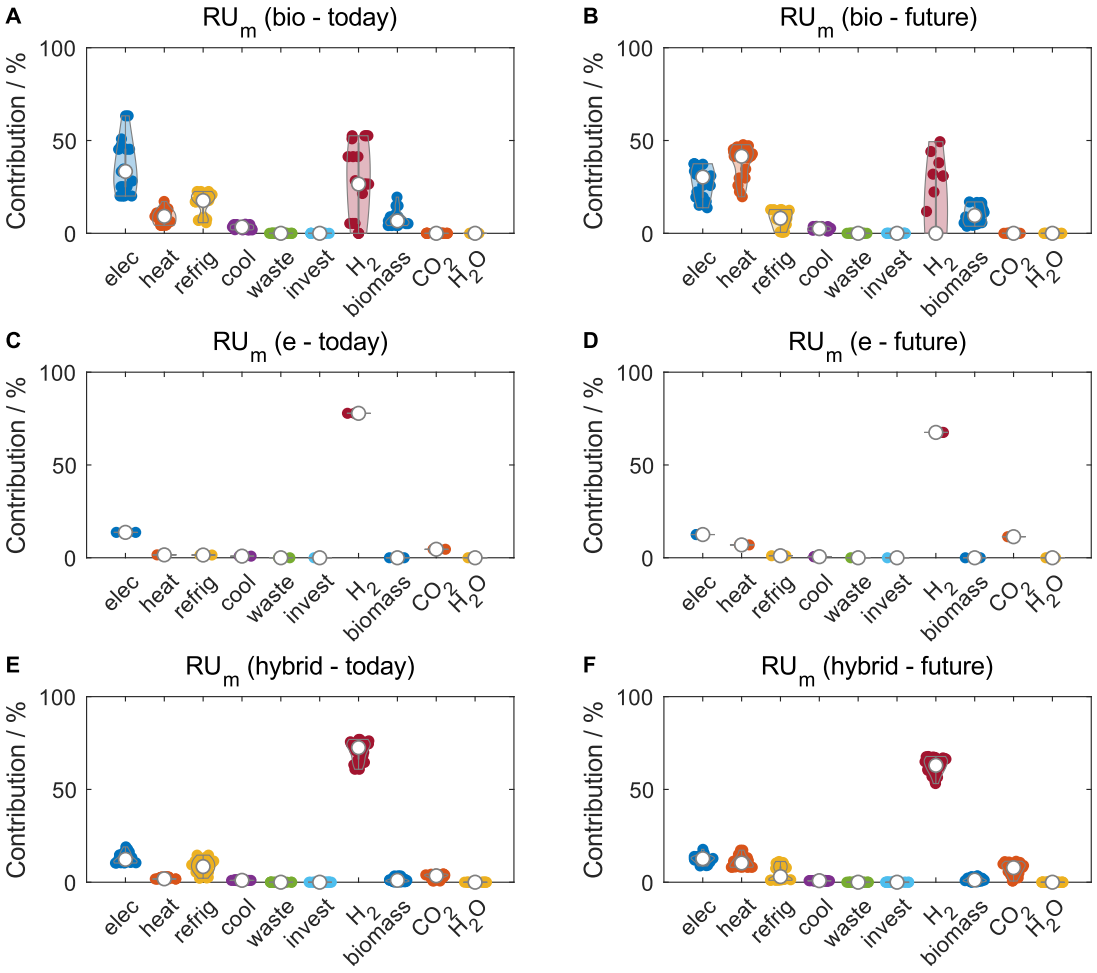

Figure A.6: Violin plot for the relative contribution analysis regarding resource use of minerals and metals of bio-, e-, and bio-hybrid fuels in the 'today' and 'future' scenario. For each subfigure, all Pareto-optimal solutions of the corresponding fuel type and scenario are considered that have been generated for the reduced objective subset.

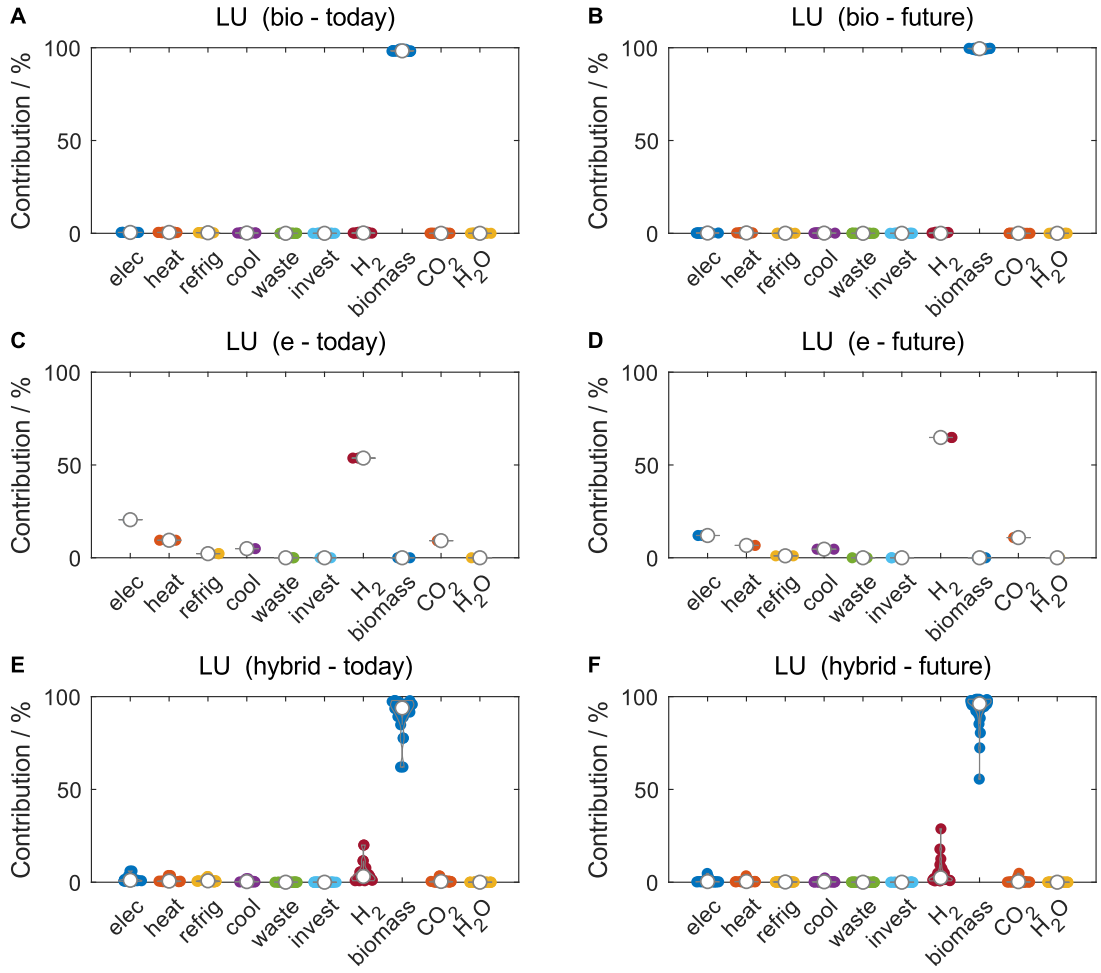

Figure A.7: Violin plot for the relative contribution analysis regarding land use of bio-, e-, and bio-hybrid fuels in the 'today' and 'future' scenario. For each subfigure, all Pareto-optimal solutions of the corresponding fuel type and scenario are considered that have been generated for the reduced objective subset.

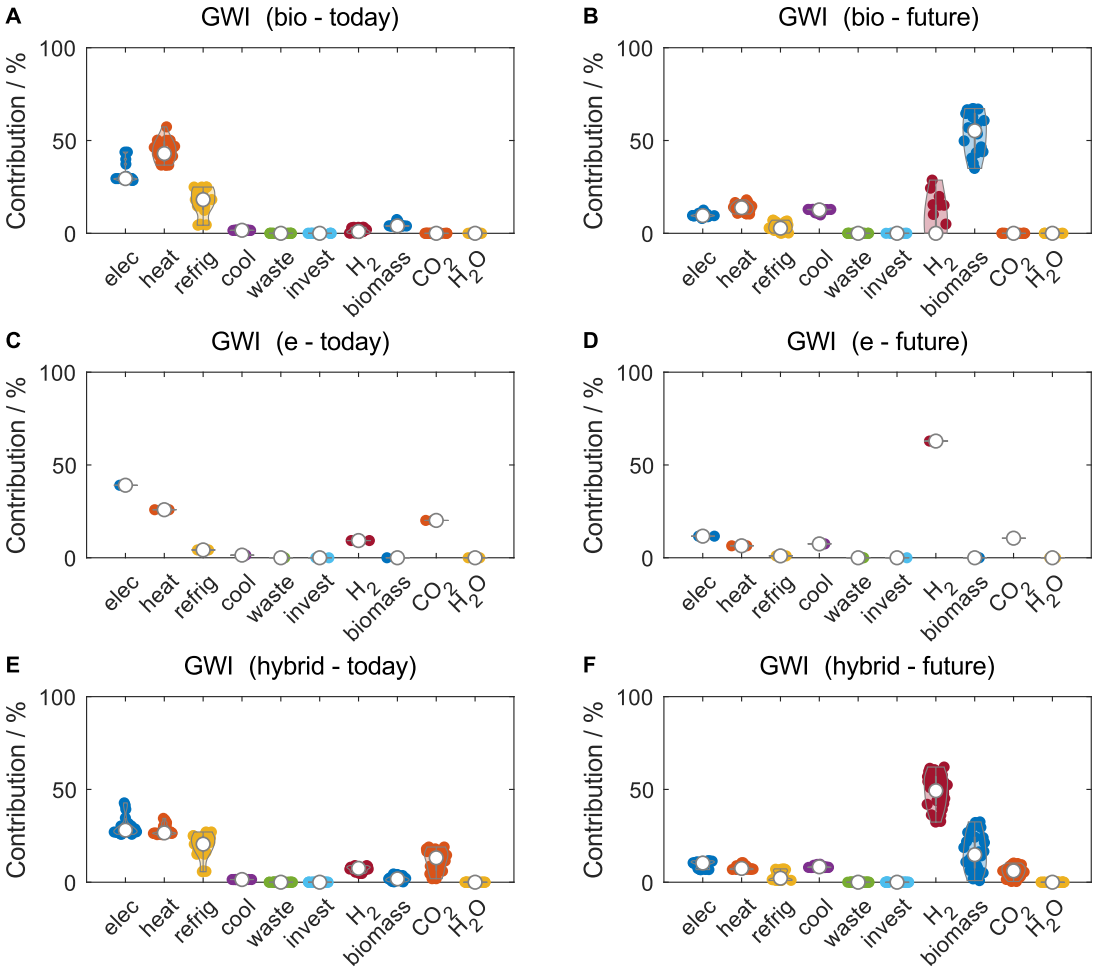

Figure A.8: Violin plot for the relative contribution analysis regarding global warming impact of bio-, e-, and bio-hybrid fuels in the 'today' and 'future' scenario. For each subfigure, all Pareto-optimal solutions of the corresponding fuel type and scenario are considered that have been generated for the reduced objective subset.

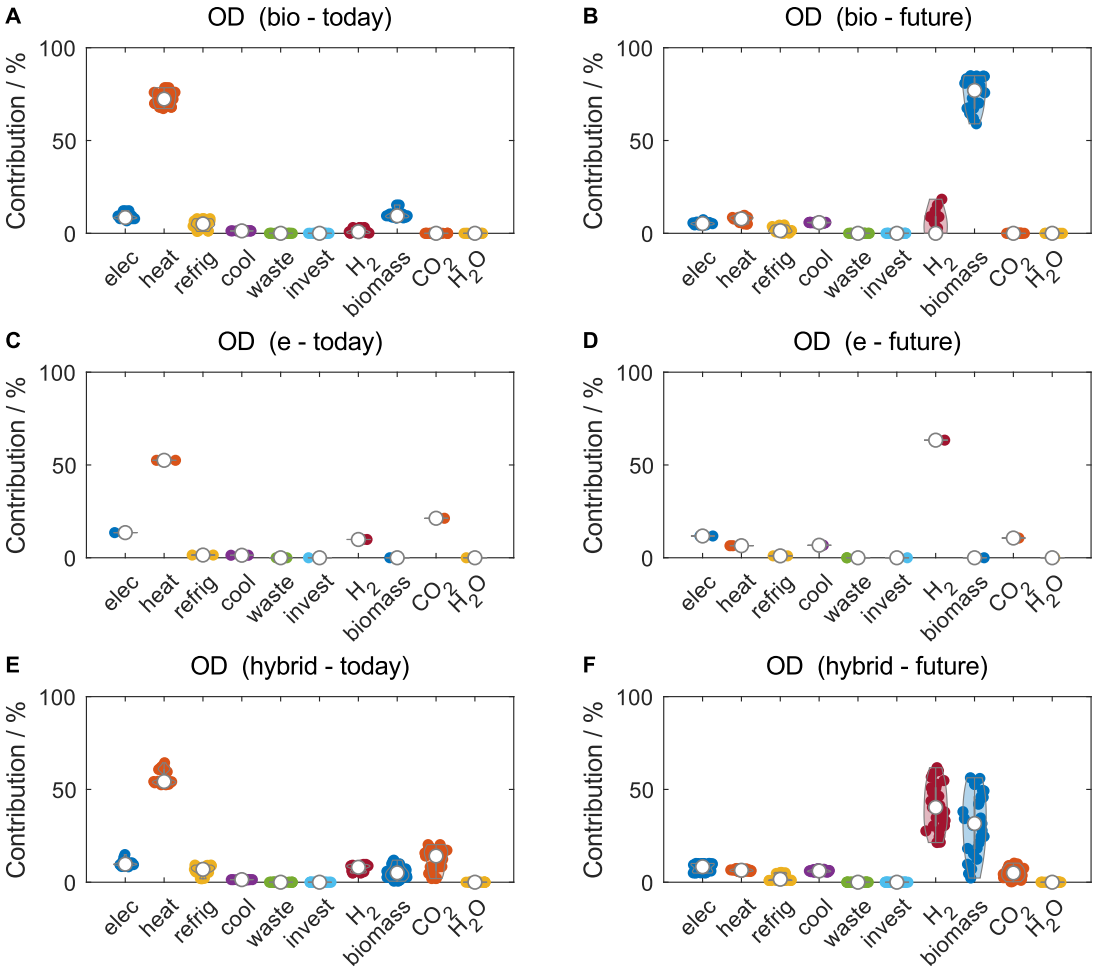

Figure A.9: Violin plot for the relative contribution analysis regarding ozone depletion of bio-, e-, and bio-hybrid fuels in the 'today' and 'future' scenario. For each subfigure, all Pareto-optimal solutions of the corresponding fuel type and scenario are considered that have been generated for the reduced objective subset.

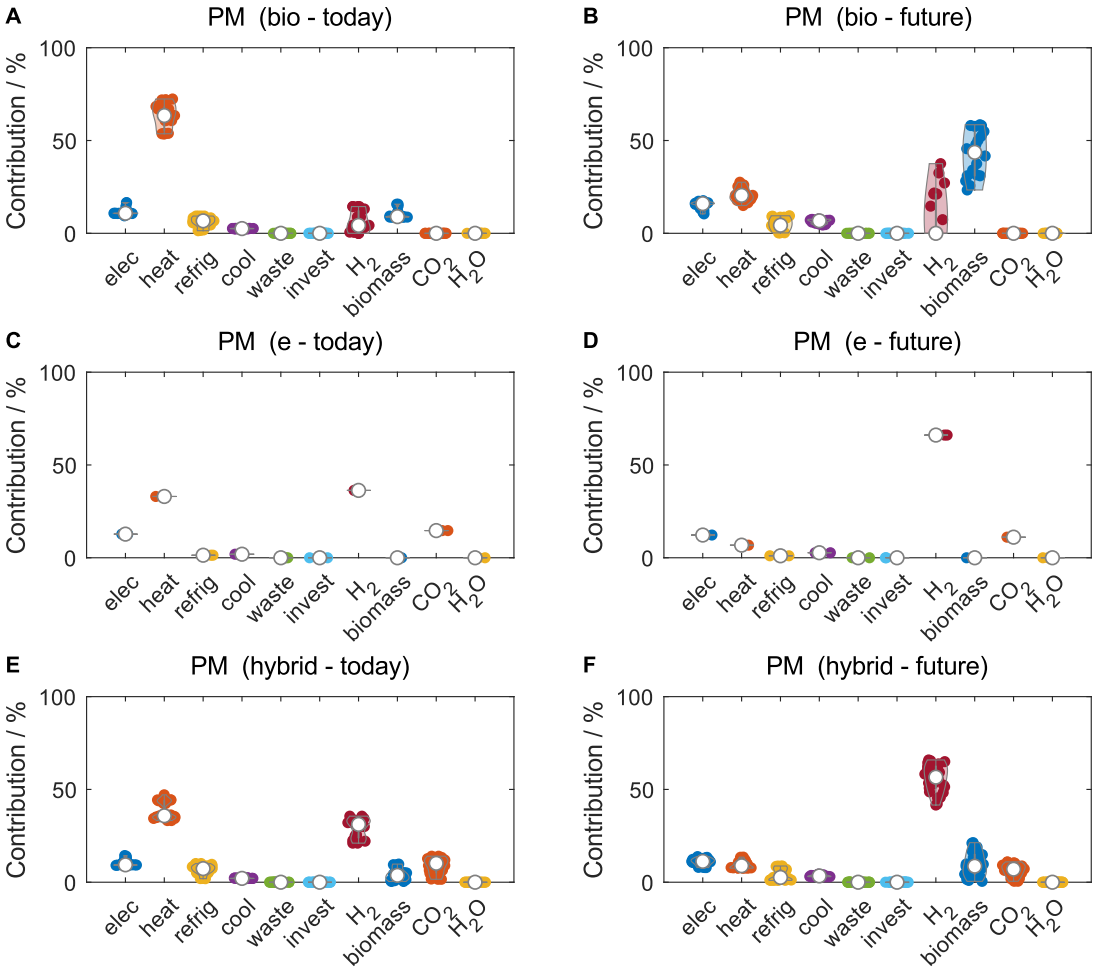

Figure A.10: Violin plot for the relative contribution analysis regarding particulate matter of bio-, e-, and bio-hybrid fuels in the 'today' and 'future' scenario. For each subfigure, all Pareto-optimal solutions of the corresponding fuel type and scenario are considered that have been generated for the reduced objective subset.

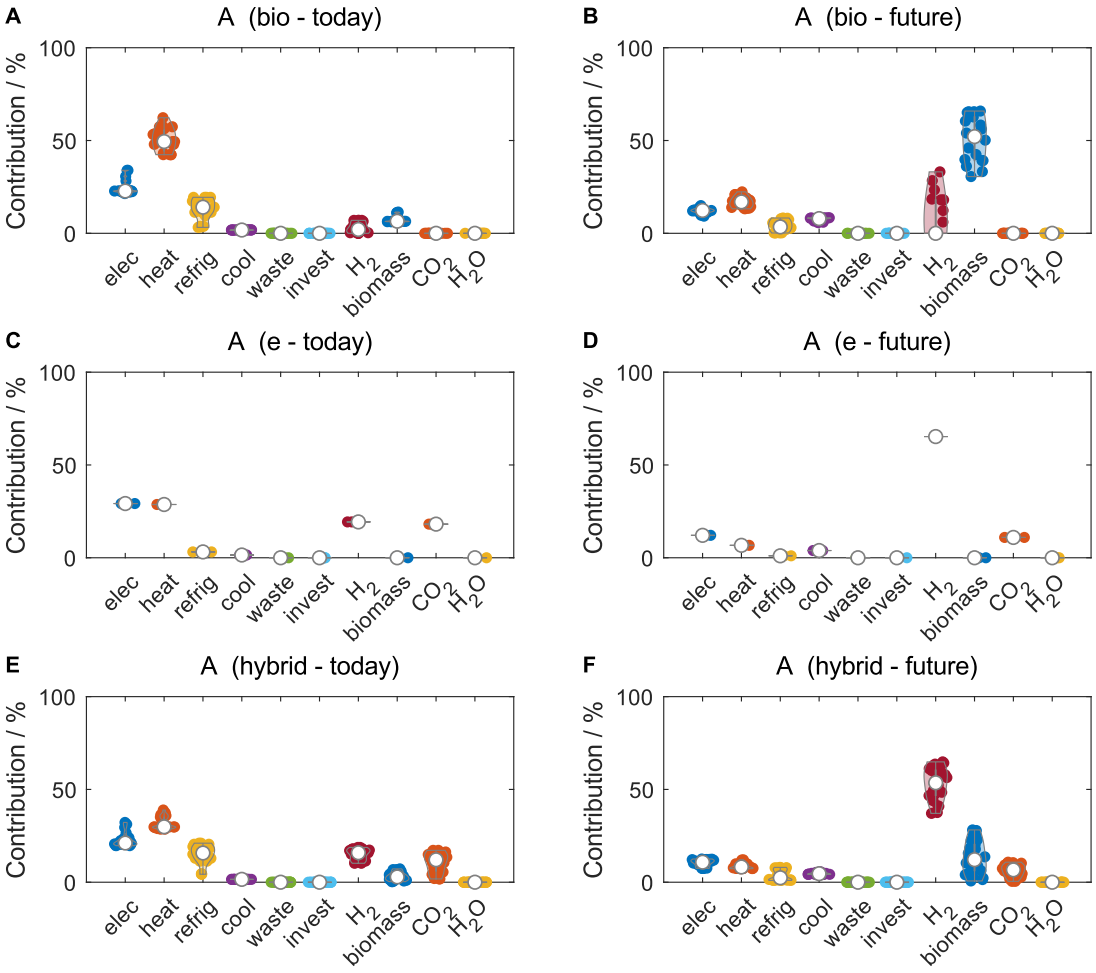

Figure A.11: Violin plot for the relative contribution analysis regarding acidification of bio-, e-, and bio-hybrid fuels in the 'today' and 'future' scenario. For each subfigure, all Pareto-optimal solutions of the corresponding fuel type and scenario are considered that have been generated for the reduced objective subset.

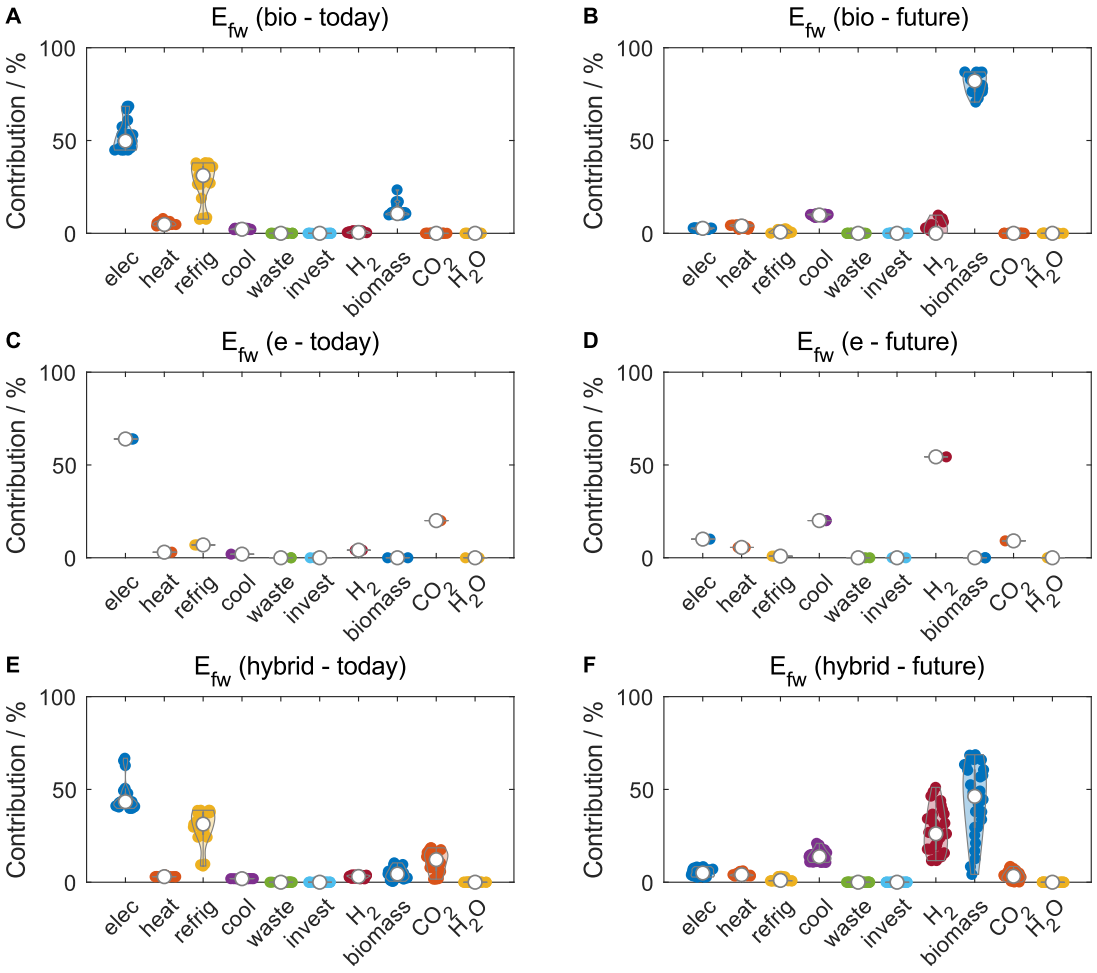

Figure A.12: Violin plot for the relative contribution analysis regarding freshwater eutrophication of bio-, e-, and bio-hybrid fuels in the 'today' and 'future' scenario. For each subfigure, all Pareto-optimal solutions of the corresponding fuel type and scenario are considered that have been generated for the reduced objective subset.

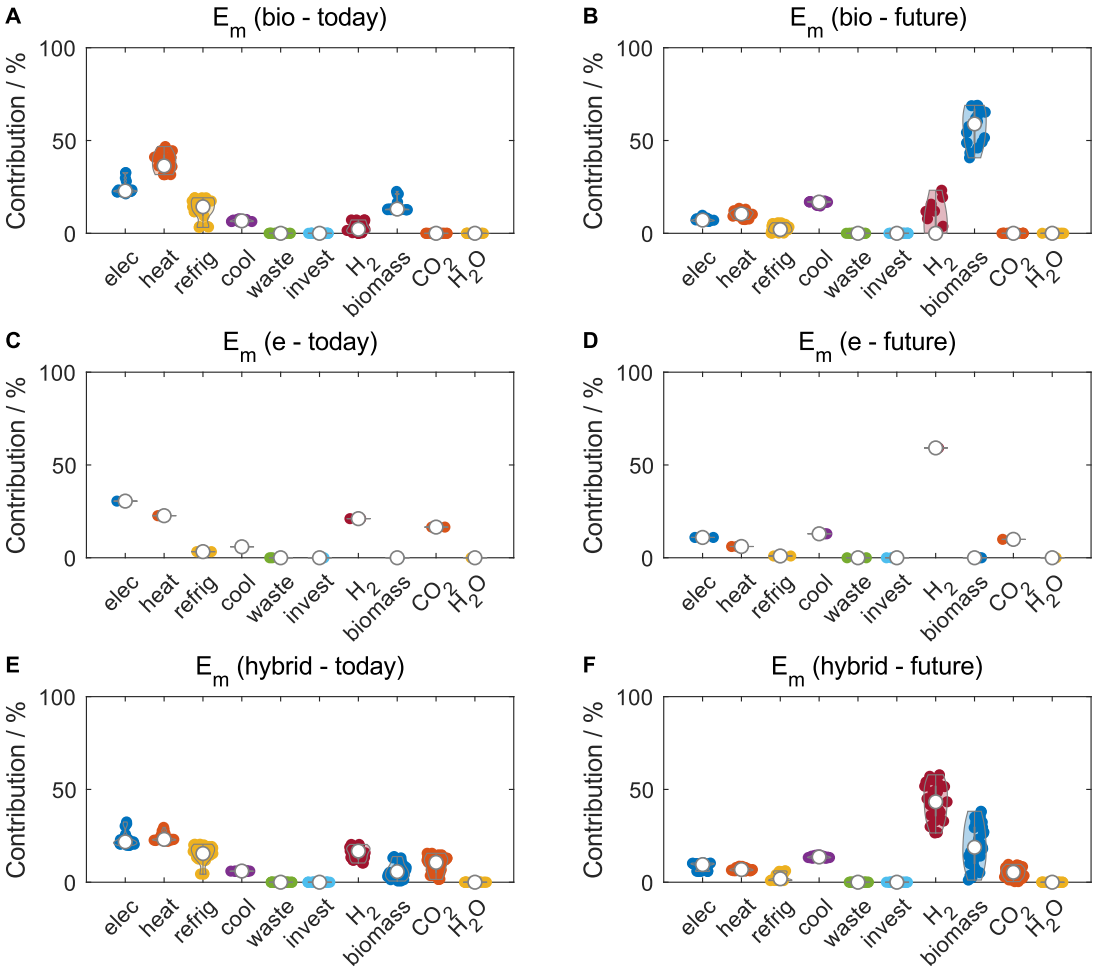

Figure A.13: Violin plot for the relative contribution analysis regarding marine eutrophication of bio-, e-, and bio-hybrid fuels in the 'today' and 'future' scenario. For each subfigure, all Pareto-optimal solutions of the corresponding fuel type and scenario are considered that have been generated for the reduced objective subset.

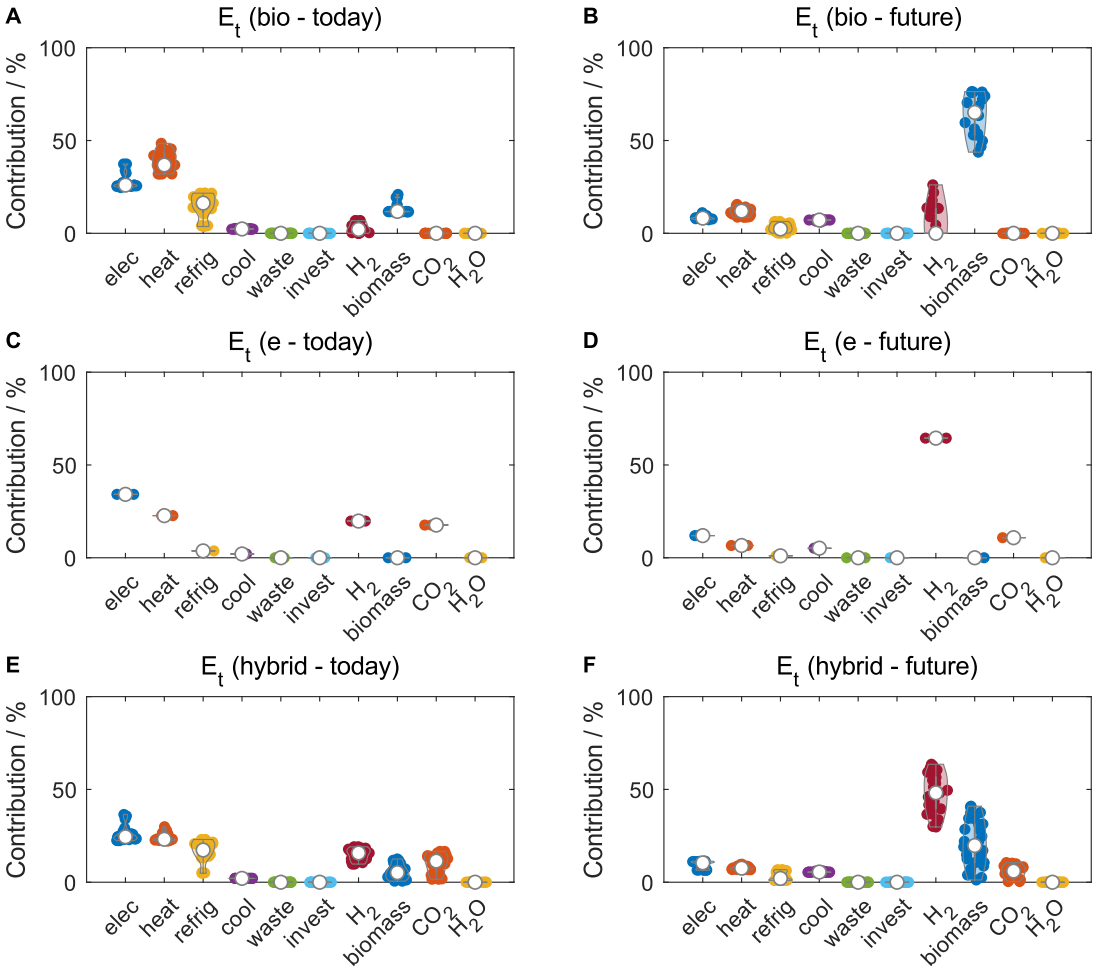

Figure A.14: Violin plot for the relative contribution analysis regarding terrestrial eutrophication of bio-, e-, and bio-hybrid fuels in the 'today' and 'future' scenario. For each subfigure, all Pareto-optimal solutions of the corresponding fuel type and scenario are considered that have been generated for the reduced objective subset.

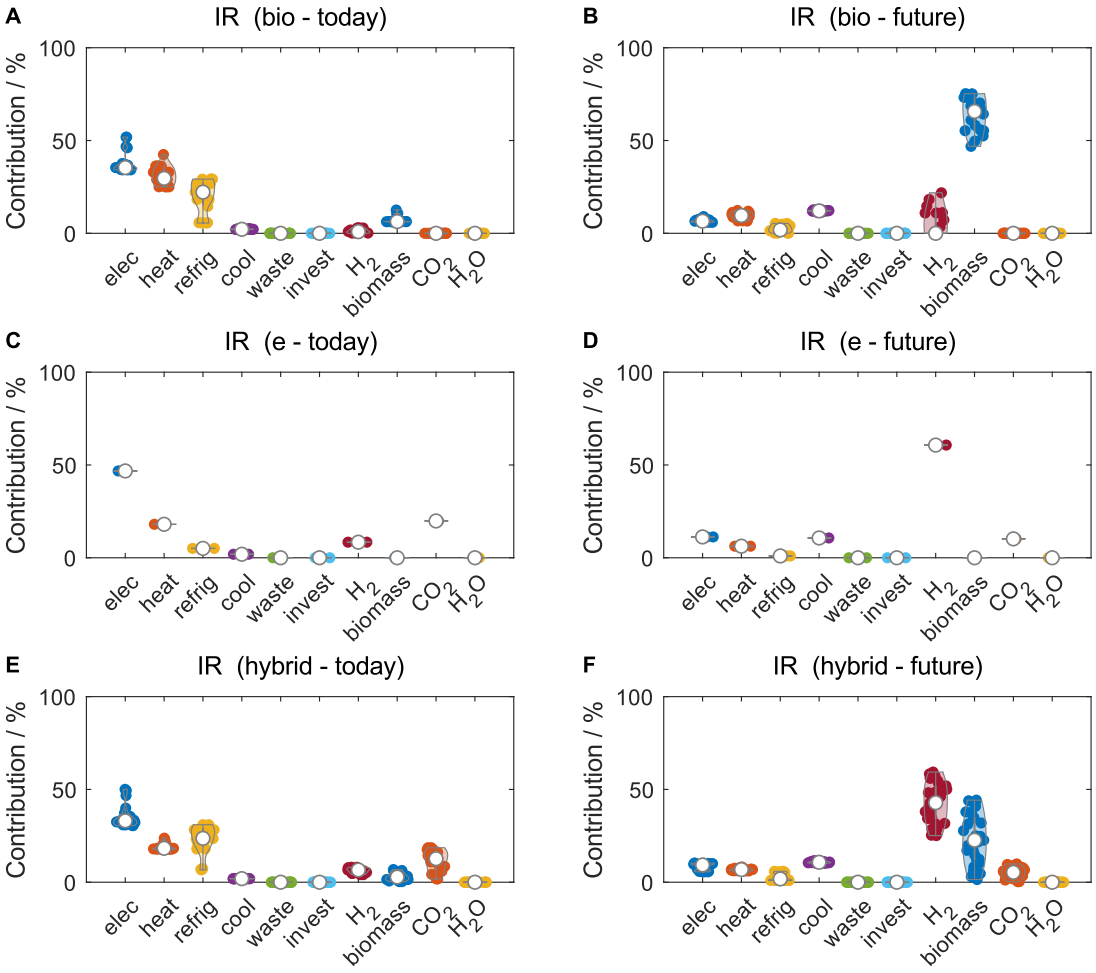

Figure A.15: Violin plot for the relative contribution analysis regarding ionizing radiation of bio-, e-, and bio-hybrid fuels in the 'today' and 'future' scenario. For each subfigure, all Pareto-optimal solutions of the corresponding fuel type and scenario are considered that have been generated for the reduced objective subset.

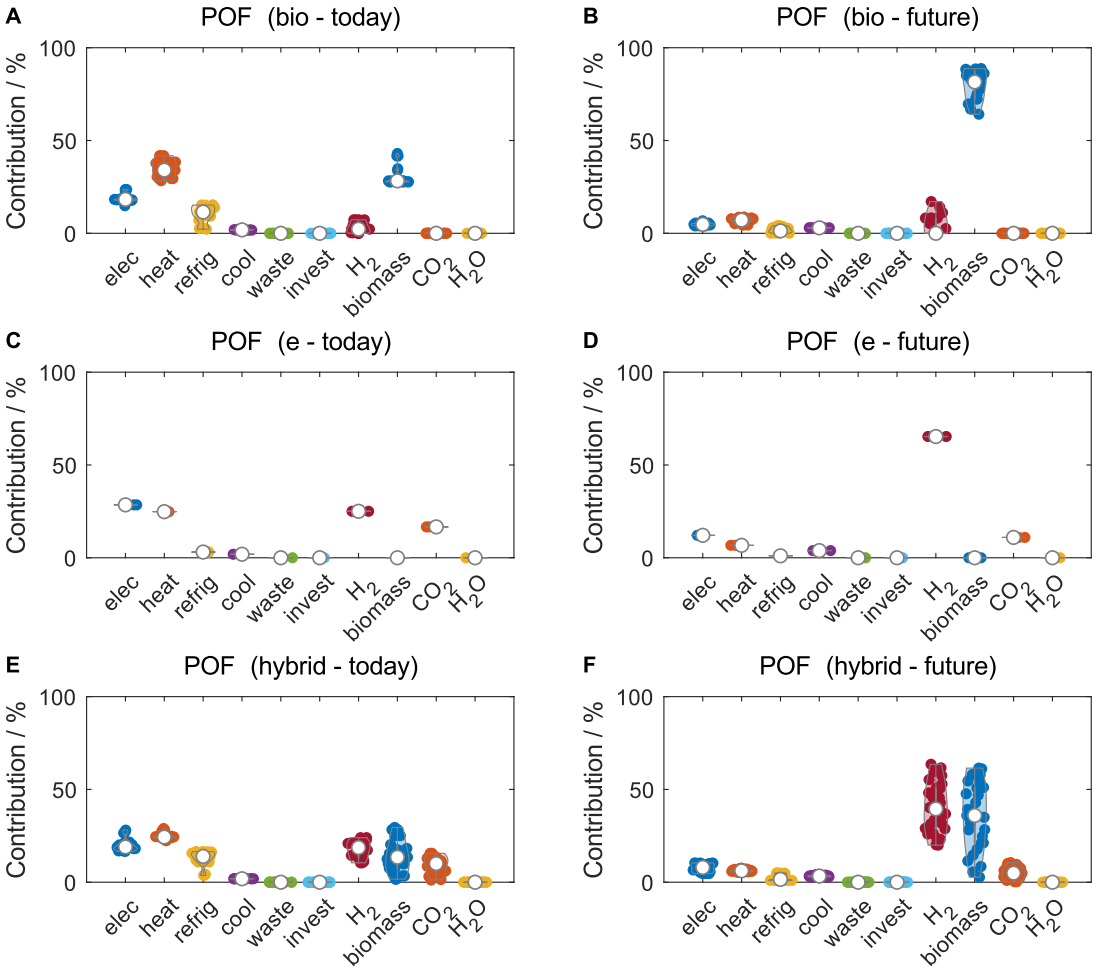

Figure A.16: Violin plot for the relative contribution analysis regarding photochemical ozone formation of bio-, e-, and bio-hybrid fuels in the 'today' and 'future' scenario. For each subfigure, all Pareto-optimal solutions of the corresponding fuel type and scenario are considered that have been generated for the reduced objective subset.

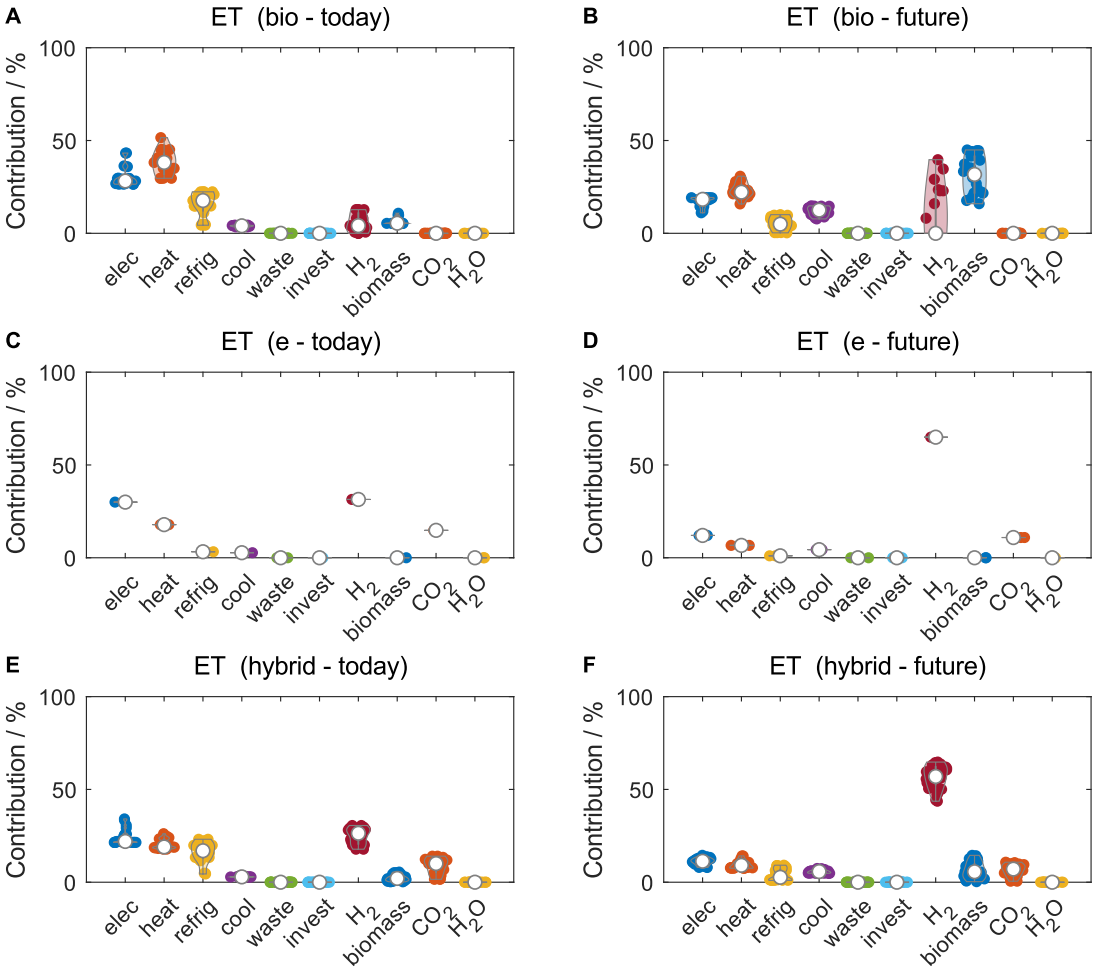

Figure A.17: Violin plot for the relative contribution analysis regarding ecotoxicity of bio-, e-, and bio-hybrid fuels in the 'today' and 'future' scenario. For each subfigure, all Pareto-optimal solutions of the corresponding fuel type and scenario are considered that have been generated for the reduced objective subset.

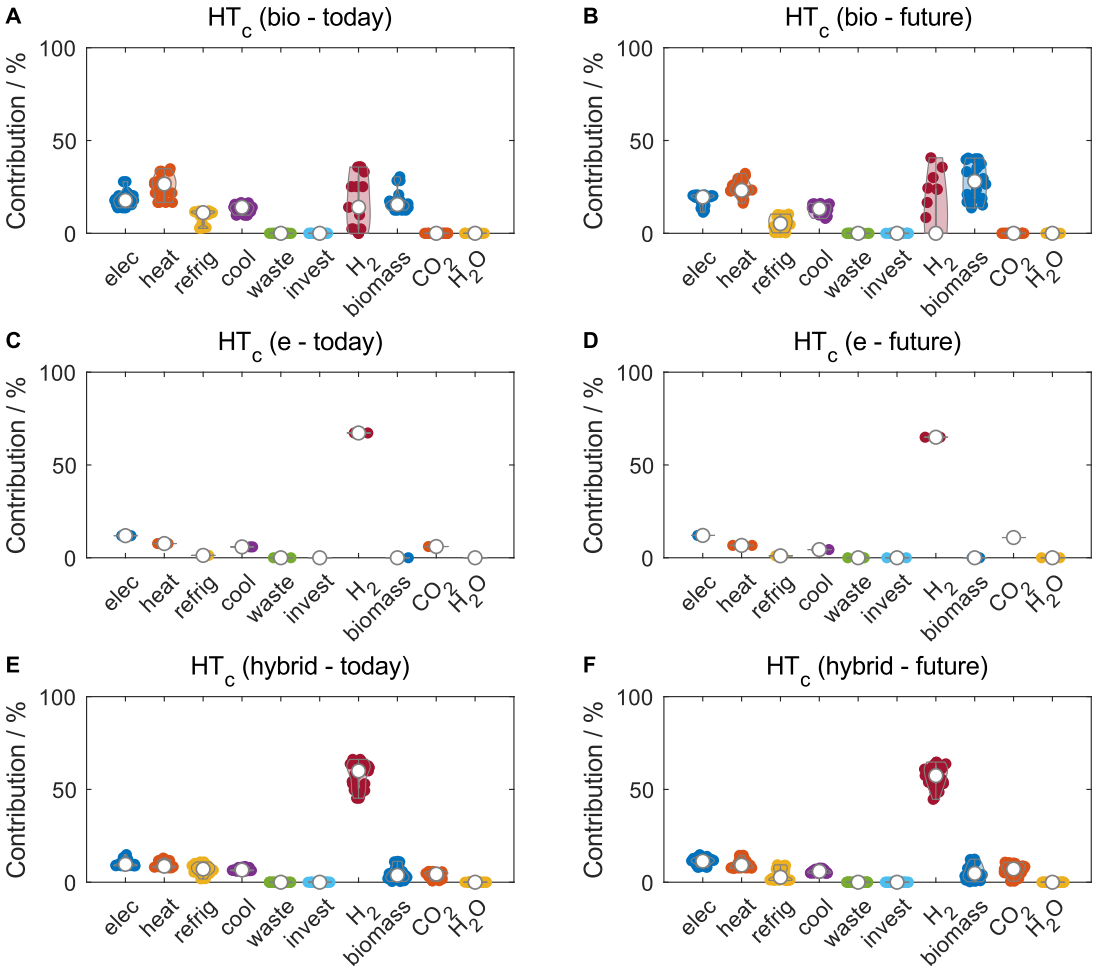

Figure A.18: Violin plot for the relative contribution analysis regarding carcinogenic human toxicity of bio-, e-, and bio-hybrid fuels in the 'today' and 'future' scenario. For each subfigure, all Pareto-optimal solutions of the corresponding fuel type and scenario are considered that have been generated for the reduced objective subset.

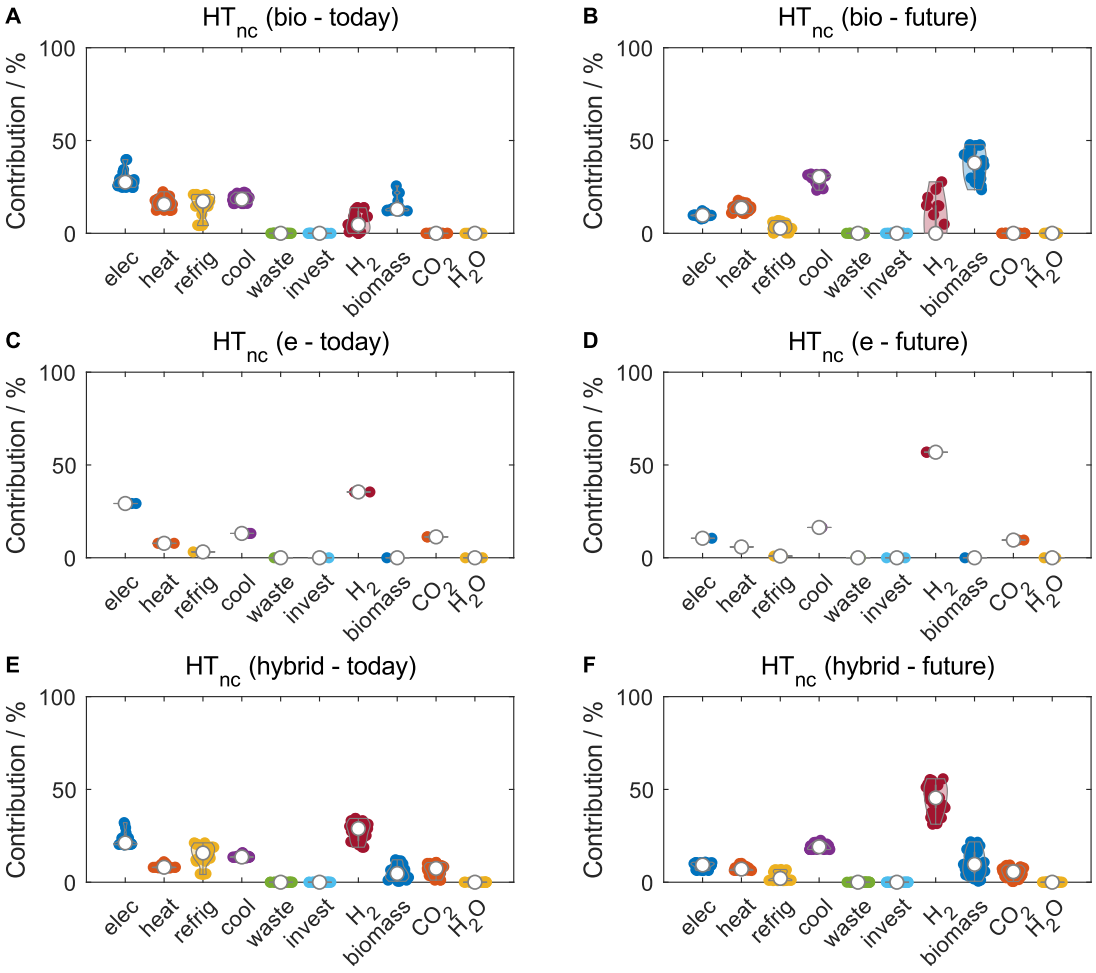

Figure A.19: Violin plot for the relative contribution analysis regarding non-carcinogenic human toxicity of bio-, e-, and bio-hybrid fuels in the 'today' and 'future' scenario. For each subfigure, all Pareto-optimal solutions of the corresponding fuel type and scenario are considered that have been generated for the reduced objective subset.

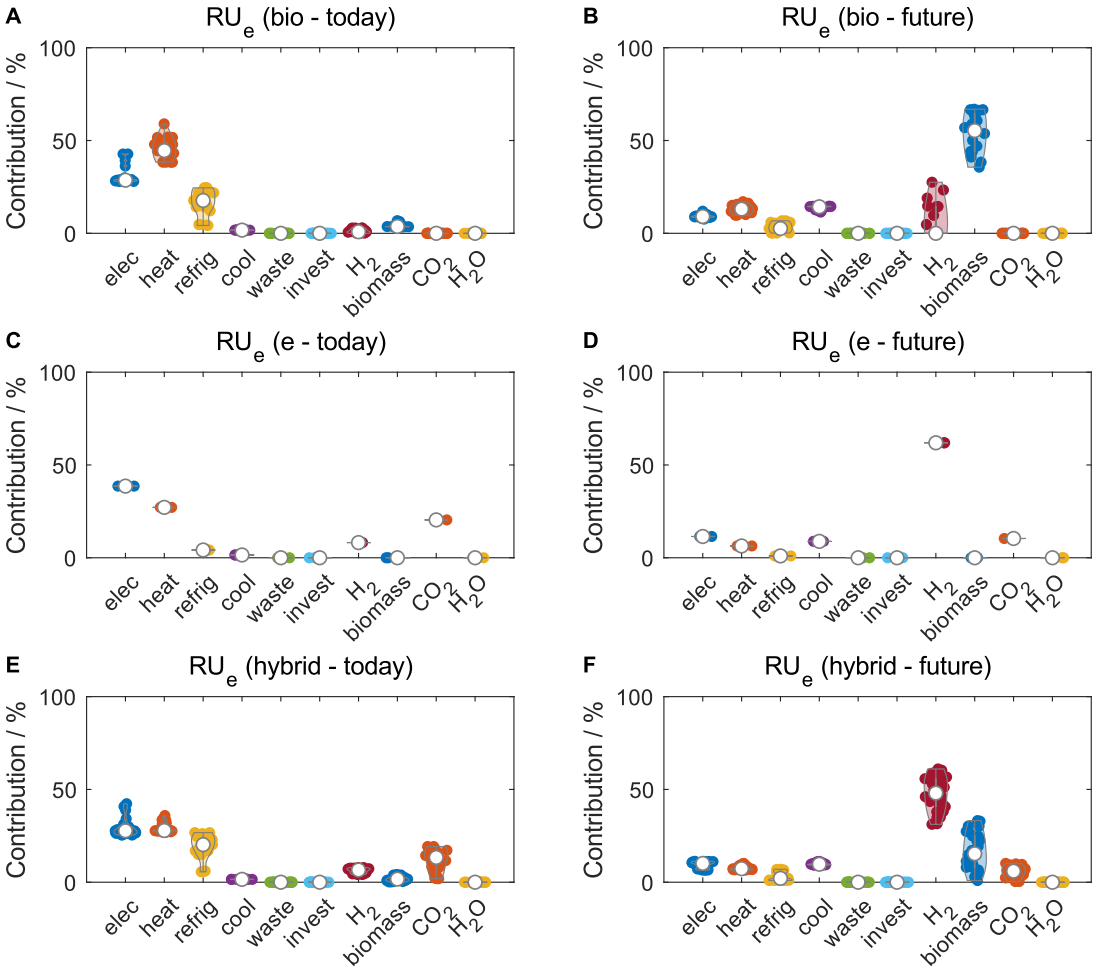

Figure A.20: Violin plot for the relative contribution analysis regarding resource use of energy carriers of bio-, e-, and bio-hybrid fuels in the 'today' and 'future' scenario. For each subfigure, all Pareto-optimal solutions of the corresponding fuel type and scenario are considered that have been generated for the reduced objective subset.

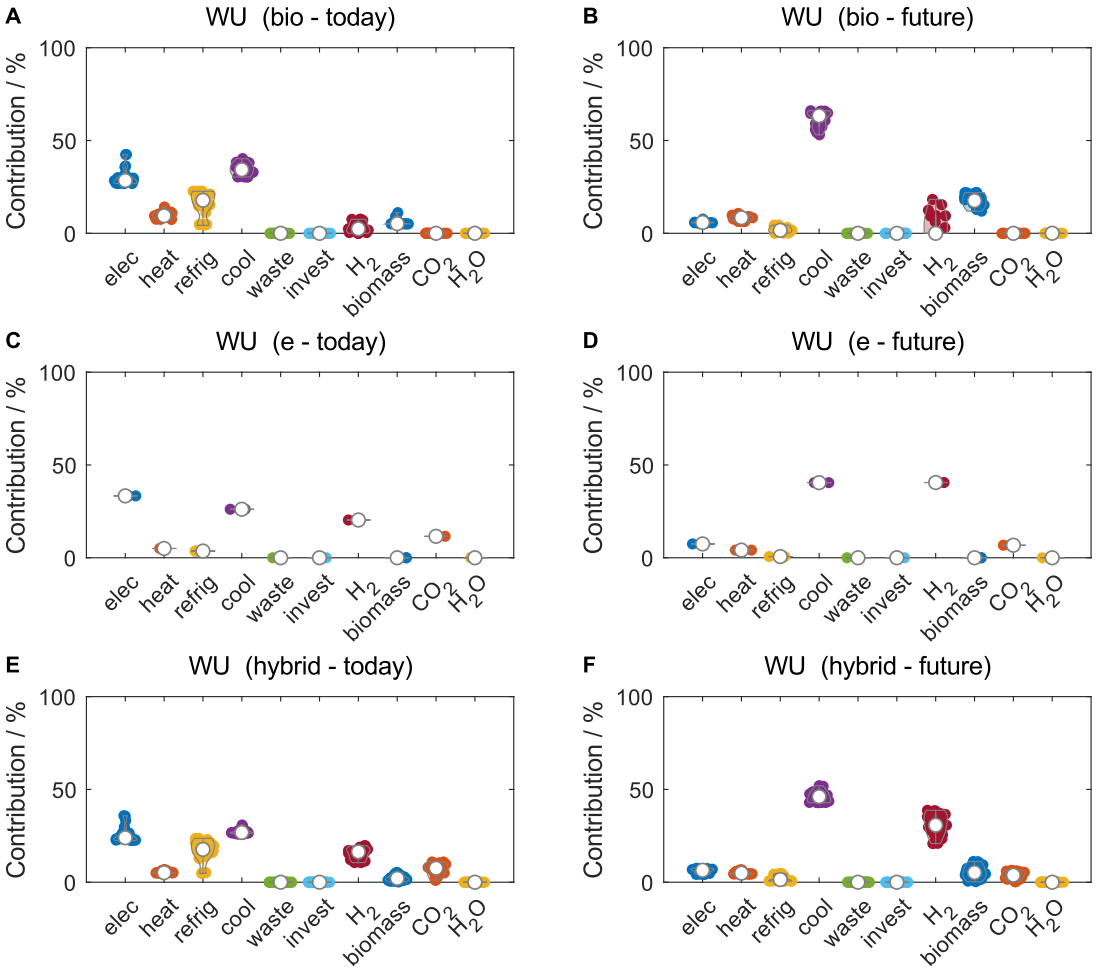

Figure A.21: Violin plot for the relative contribution analysis regarding water use of bio-, e-, and bio-hybrid fuels in the 'today' and 'future' scenario. For each subfigure, all Pareto-optimal solutions of the corresponding fuel type and scenario are considered that have been generated for the reduced objective subset.

A.3.5 Composition of Pareto-optimal bio-hybrid fuels

In Figure A.22, we show the molar fuel composition of all generated Pareto-optimal bio-hybrid fuels as violin plot. For comparison, we also present the molar composition of the KEAA blend of previous studies (König et al., 2021).

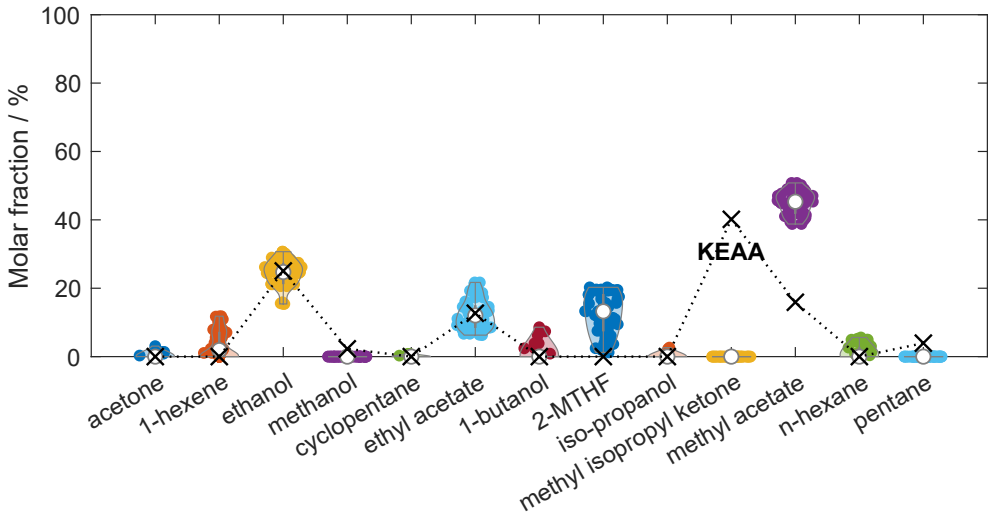

Figure A.22: Violin plot for the molar composition of all generated Pareto-optimal bio-hybrid fuels. For comparison, the molar composition of the KEAA blend of previous studies is shown as crosses (König et al., 2021). MTHF: methyltetrahydrofuran.

Appendix B

Supporting information to Chapter 4

This appendix provides additional information for Chapter 4. Recent studies on LCAs, TEAs, and reviews of Fischer-Tropsch fuels are listed in Section B.1. Further details on applied methods are presented in Section B.2. HyFiT-fuel production is described in Section B.3. Additional information on fuel usage and the life cycle impact assessment is presented in Section B.4 and Section B.5, respectively.

B.1 Introduction

In Table B.1, we present an overview on recent LCAs, TEAs, and reviews for FT fuels for further reading. While most assessments consider either biomass or CO_2 as feedstock, only five studies include both. About twice as many studies focus on road as on aviation applications. Approximately 80% of the studies conduct TEAs and less than 50% perform LCAs.

Table B.1: Recent literature on life cycle assessments (LCAs), techno-economic assessments (TEAs), and reviews for Fischer-Tropsch fuels.

Author	**Year**	**Feedstock**			**Application**		**Assessment**		
		Biomass	CO_2	Fossil	Road	Aviation	LCA	TEA	Review
Colelli et al.	2023		✓			✓		✓	
Delgado et al.	2023		✓		unspecified		✓	✓	
Hong et al.	2023		✓		unspecified			✓	
Jacobsen et al.	2023		✓			✓		✓	
Katiyo et al.	2023	✓			✓			✓	
Okolie et al.	2023	✓				✓			✓
van den Oever et al.	2023	✓			✓		✓		
Weyand et al.	2023	✓	✓		unspecified		✓	✓	

Continued on next page.

Continued from previous page.

Author	**Year**	**Feedstock**			**Application**		**Assessment**		
		Biomass	CO_2	Fossil	Road	Aviation	LCA	TEA	Review
Gao et al.	2022		✓		unspecified			✓	
Medrano-García et al.	2022		✓		✓		✓	✓	
Peters et al.	2022		✓		✓	✓		✓	
Gao et al.	2021		✓		unspecified			✓	
Herz et al.	2021		✓		unspecified			✓	
Marchese et al.	2021		✓		unspecified			✓	
Freire Ordóñez et al.	2021		✓		✓		✓	✓	
Zang et al.	2021a		✓		✓	✓	✓		
Zang et al.	2021b		✓		✓	✓		✓	
Zang et al.	2021c		✓		✓		✓	✓	
Borugadda et al.	2020	✓			✓		✓	✓	
Dieterich et al.	2020	✓	✓	✓	✓			✓	✓
Drünert et al.	2020		✓			✓		✓	
Liu et al.	2020		✓		✓		✓		
Lundberg et al.	2020	✓				✓	✓		
Okeke et al.	2020	✓			✓		✓		
Alhyari et al.	2019		✓		✓		✓		
Cuéllar-Franca et al.	2019		✓		✓		✓	✓	
Decker et al.	2019		✓		✓			✓	
Hombach et al.	2019		✓		✓		✓	✓	
Navas-Anguita et al.	2019	✓			✓		✓		
Schemme et al.	2019		✓		✓	✓		✓	
Tsongidis et al.	2019		✓		unspecified			✓	
Blanco et al.	2018	✓			✓	✓		✓	
Brynolf et al.	2018		✓		✓			✓	✓
Dietrich et al.	2018	✓	✓			✓		✓	
Dimitriou et al.	2018	✓			✓	✓		✓	
Hernandez and Martin	2018	✓			✓			✓	
Herz et al.	2018		✓		unspecified			✓	
Neuling and Kaltschmitt	2018	✓				✓	✓	✓	
Samavati et al.	2018	✓	✓		✓		✓	✓	
Vázquez et al.	2018d		✓		unspecified				
Zhang et al.	2018b	✓		✓	✓	✓	✓	✓	
Albrecht et al.	2017	✓	✓		✓	✓		✓	
de Jong et al.	2017	✓				✓	✓		
Herz et al.	2017	✓			unspecified			✓	
Liu et al.	2017	✓		✓	✓		✓	✓	
Okeke and Mani	2017	✓			✓			✓	
Rafati et al.	2017	✓			unspecified			✓	
Snehesh et al.	2017	✓			unspecified			✓	
Tsalidis et al.	2017	✓			✓		✓		
Zhou et al.	2017	✓		✓	✓		✓	✓	
Ail and Dasappa	2016	✓			✓		✓	✓	✓
König et al.	2015a		✓		✓	✓		✓	
König et al.	2015b		✓		unspecified			✓	

B.2 Methods

In this section, we present additional information regarding fuel properties, material compatibility, combustion emissions, and environmental impacts.

B.2.1 Fuel properties and material compatibility

Common global fuel standards and their limits are listed in Table B.2. Numerical values of the investigated fuel properties are presented in Table B.12.

B.2.1.1 Fuel properties

Lower heating value. The LHV of HyFiT-fuels is calculated as the sum of each fuel component's product of LHV and mass fraction y in the HyFiT-fuel:

$$LHV_{\mathrm{HyFiT}} = \sum_{i}^{n} LHV_{i,\mathrm{HyFiT}} \cdot y_{i,\mathrm{HyFiT}}. \tag{B.1}$$

LHVs of all fuel components are listed in Table B.3. The mass fractions of alcohols and alkanes in the fuel depend on the targeted alcohol-alkane ratio of the HyFiT-fuel, i.e., on the combination of low-temperature (LT) and high-temperature (HT) FT synthesis. The composition of HyFiT-fuels is presented in Section B.3.3.

Density. The density was measured with a tension scale (Tensiometer TD4) in buoyancy tests using the Archimedes principle. The measurement resolution of the scale and the temperature accuracy of the thermostat were 0.01 mg and 0.1 K, respectively, and measurements were carried out at 15 °C. During the measurements, the volume and mass of the displacement body (DB) were known (Figure B.1). For the calibration of the scale, the displacement body was placed outside of the sample liquid at first. After calibration, the displacement body was immersed into the sample liquid to measure its mass. The liquid density was subsequently calculated by

$$m_{\mathrm{meas}} \cdot g = \sum_{i} \mathrm{F}_i = m_{\mathrm{DB}} \cdot g - V_{\mathrm{DB}} \cdot \rho_{\mathrm{L}} \cdot g \tag{B.2}$$

$$\rho_{\mathrm{L}} = \frac{m_{\mathrm{DB}} - m_{\mathrm{meas}}}{V_{\mathrm{DB}}}. \tag{B.3}$$

For the evaluation of the results, each measurement was repeated ten times.

Table B.2: Fuel standards for diesel, paraffinic diesel, and biodiesel with their respective limits for the derived cetane number (DCN), viscosity, density, and lubricity.

Standard	**Region**	**Fuel**	**DCN**	**Viscosity**		**Density**		**Lubricity**
			–	$mm^2\,s^{-1}$		$kg\,m^{-3}$		μm
			min	min	max	min	max	max
EN 590 (summer)	EU	Diesel	51	2.0	4.5	820	845	460
EN 590 (winter)	EU	Diesel	49	2.0	4.5	820	860	–
EN 15940	EU	Paraffinic diesel	70	2.0	4.5	765	800	460
EN 14214	EU	Biodiesel	51	3.5	5.0	860	900	–
ASTM D975	USA	Paraffinic diesel	40	1.9	4.1	–	–	520
ASTM D7467	USA	Diesel	40	1.9	4.1	–	–	520
ASTM D6751	USA	Biodiesel	47	1.9	6.0	–	–	–
GOST 305-82 (summer)	Russia	Diesel	45	3.0	6.0	–	860	–
GOST 305-82 (winter)	Russia	Diesel	45	1.8	5.0	–	840	–
CAN/CGSB-3.524	Canada	Biodiesel	–	1.9	6.0	–	–	–
CAN/CGSB-3.522	Canada	Diesel	40	1.7	4.1	–	–	–
CAN/CGSB-3.520	Canada	Diesel	40	1.3	4.1	–	–	–
GB 19147-2016 (China VI)	China	Diesel	51	3.0	8.0	810	850	460
GB 25199-2017	China	Diesel	49	1.9	6.0	820	900	–
GB/T 20828	China	Biodiesel	49	1.9	6.0	820	900	–
JIS K 2204 (No. 2)	Japan	Diesel	50	2.5	–	–	860	–
JIS K 2204 (No. 3, winter)	Japan	Diesel	50	1.7	–	–	860	–
JIS K 2390	Japan	Biodiesel	51	3.5	5.0	860	900	–
IS 15607: 2005	India	Biodiesel	48	2.5	6.0	860	900	–
SANS 1935	South Africa	Biodiesel	51	3.5	5.0	860	900	–

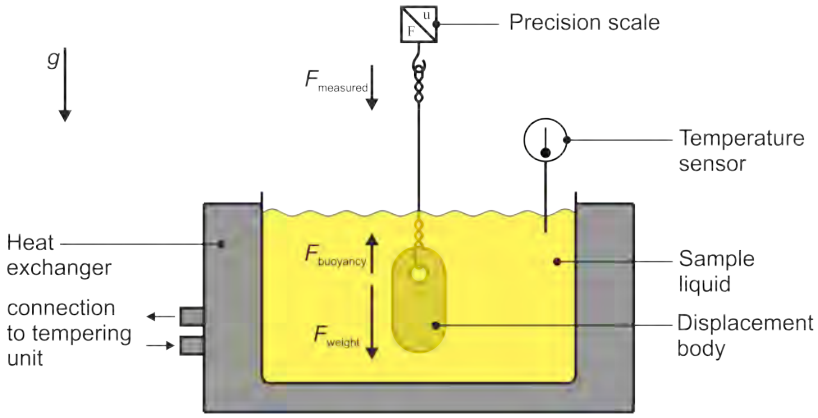

Figure B.1: Measurement of the liquid density with a precision scale.

Viscosity. An Ubbelohde viscometer, according to DIN 51562, and a thermostat with a temperature constancy of 0.01 K were used to determine the viscosity. Measurements were carried out at a temperature of 40 °C. Before each measurement, the viscometer was filled with the test liquid and placed in the thermostat. After filling the viscometer with the sample liquid, the viscometer was tempered for 30 min to ensure a constant temperature level of sample and viscometer. For the evaluation of the results, each measurement was repeated five times and the mean value was calculated.

Table B.3: Lower heating values (LHVs) of alcohols and alkanes present in HyFiT-fuels. For each alcohol and alkane, the LHV is calculated from the enthalpy of reaction of stoichiometric combustion with oxygen. Required standard enthalpies of formation of each reactant and product are taken from the NIST Chemistry WebBook.

Carbon atoms	**LHV**	
–	$MJ\,kg^{-1}$	
	Alcohol	Alkane
5	–	44.98
6	35.98	44.74
7	36.88	44.56
8	37.61	44.42
9	38.17	44.33
10	38.65	44.24
11	39.03	44.17
12	–	44.11
13	–	44.06
14	–	44.02
15	–	43.99
16	–	43.95
17	–	43.93

Lubricity. For lubricity, the high frequency reciprocating rig (HFRR) value and friction coefficient were measured (Figure B.2). The HFRR tests were conducted according to ISO 12156-1:2018. For each sample liquid, the test procedure was conducted five times with and without additive. The HFRR value is derived from the wear scar diameter (WSD), whereas the friction coefficient μ is calculated by the ratio of gravitational and tangential force:

$$WSD = \frac{\mathrm{dx} + \mathrm{dy}}{2} \tag{B.4}$$

$$\mu = \frac{F_{\mathrm{grav}}}{F_{\mathrm{tan}}}. \tag{B.5}$$

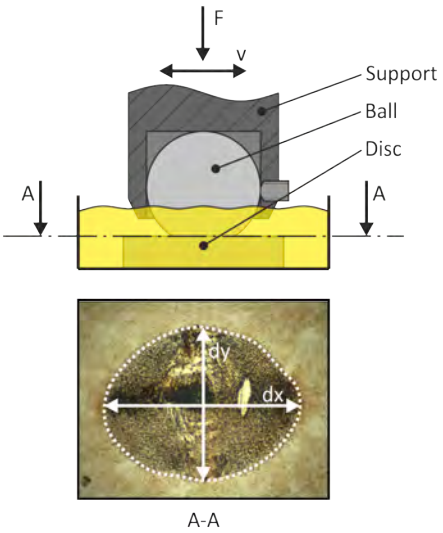

Figure B.2: Measurement of the high frequency reciprocating rig (HFRR) value and friction coefficient.

B.2.1.2 Material compatibility

Material compatibility tests were carried out according to DIN ISO 1817. As sealing materials, the reference elastomers FKM, NBR, and HNBR were considered, following DIN ISO 13226. For each elastomer, three samples were measured. At the beginning of one test series, the reference materials were placed in the sample liquids. Immediately before and at defined time intervals within the experiment (Table B.4), the material properties mass, volume, and hardness were determined. Since the largest changes in sealing and liquid properties are to be expected at the beginning of a measurement series, the individual measurements initially take place within short time intervals that become longer as the measurement series progresses. The intervals listed are based on empirical values from previous experiments and represent a reasonable compromise between acceptable measurement effort and sufficient data volume. All measurements to determine the material compatibility were carried out in air-conditioned rooms at 23±2 °C, according to the laboratory conditions in DIN ISO 23529. To ensure a constant temperature of liquids and elastomers between two measuring points, the samples were stored in a climate chamber at 23 °C. The local temperature constancy of the chamber is specified by the manufacturer as ±0.2 °C, while the temporal constancy is ±0.5 °C. Each test series ended after 672 h.

Table B.4: Timing of measurements for material compatibility tests.

Measurement point	**Time since start of the test series**	
–	h	
1	0	Sealing
2	6	Sealing plus liquid
3	16	
4	24	
5	72	
6	168	
7	336	
8	504	
9	672	

Change of mass. The mass change was measured with a precision scale (Sartorius Research R 160 P) that has a measurement resolution of 0.01 mg and standard deviation of 0.02 mg. For the measurement process, the scale was calibrated at first. Elastomers were taken from the sample vessel and carefully cleaned with lint-free pa-

per so that the liquid on the elastomer surface is removed. Next, the elastomer was put on the scale and, after the balance had settled in, the mass change was measured. Note that, in case of high vapor pressures, the measurement process may be influenced by evaporation of the sample liquid (Figure B.3), but the influence of evaporation played only a minor role for all HyFiT-fuels: HyFiT-fuels showed comparable behavior to diesel. All samples were measured once and each measurement process took less than 10 s.

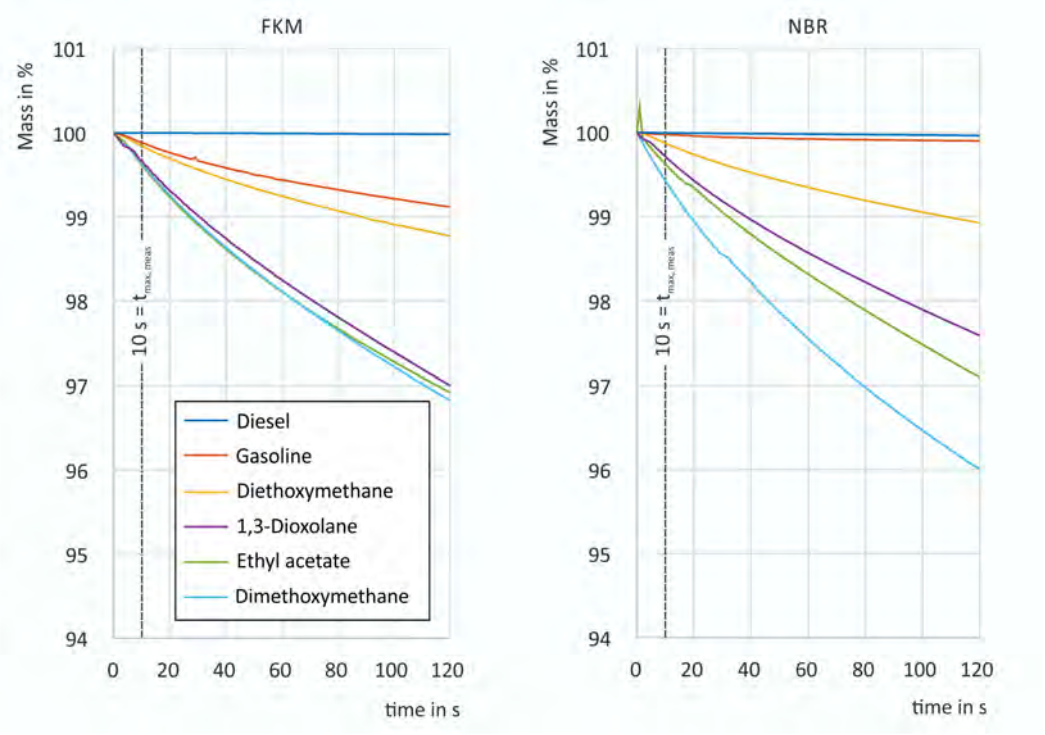

Figure B.3: Mass change over time due to evaporation during the measurement process of various fuels.

Change of volume. The volume change was measured with a tension scale (Tensiometer TD4, see Figure B.1) that has a measurement resolution of 0.01 mg and temperature accuracy of 0.02 K. As prerequisites, the density of the reference liquid and the mass of the displacement body are known. The measurement process follows the description of the density measurement above. Each measurement was repeated three times with a measurement temperature of 20 °C. The sample volume V_S is calculated as follows:

$$m_{\text{meas}} \cdot g = \sum_i \mathrm{F}_i = m_{\text{DB}} \cdot g - V_S \cdot \rho_L \cdot g \tag{B.6}$$

$$V_S = \frac{m_{DB} - m_{meas}}{\rho_L}. \tag{B.7}$$

Change of hardness. The hardness change was measured with a hardness test device, according to DIN ISO 48. The measurement process was repeated six times for each elastomer sample.

B.2.2 Fuel combustion

The diesel engine features two-stage turbocharging and cooled EGR. The exhaust gas aftertreatment system of the vehicle consists of a diesel-oxidation catalyst and a diesel-particulate filter with a selective catalytic reduction (SCR) coating followed by an ammonia-slip catalyst. The hybrid strategy is calibrated to minimize tailpipe NO_x emissions (Schaub et al., 2020b). Thereby, the current Euro 6d final emissions standards and the requirements for the upcoming Euro 7 are already met in the investigated cycle, using regular diesel. In the following, we present the powertrain layout of the P0P2 plug-in hybrid vehicle (Figure B.4) and describe how we corrected the deviation of the battery SOC.

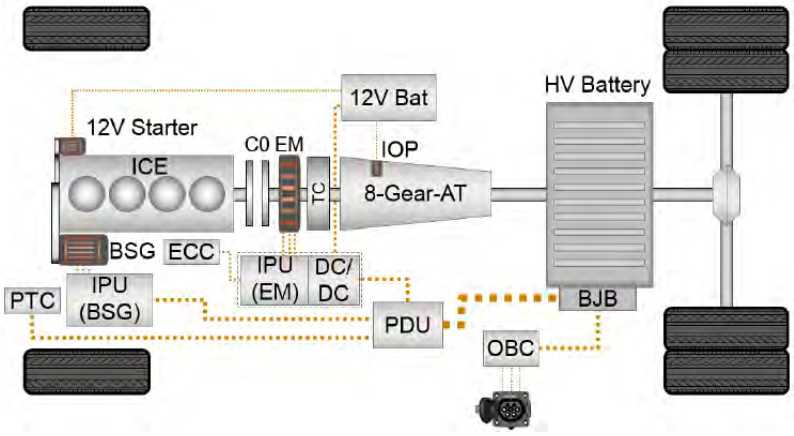

Figure B.4: Powertrain layout of the P0P2 plug-in hybrid vehicle.

For plug-in hybrid vehicles, the test procedure of the WLTP provides for a charge sustain mode, which means that the battery must have the same SOC at the end of the cycle as at the beginning, with a tolerance of 1 %. No adjustments were made to the vehicle calibration for the tests. In combination with the different lower heating values of the HyFiT-fuels (see Figure 4.5A), deviations of the SOC of −2.2 % for HyFiT-20% and −2.5 % for HyFiT-40% occur (Figure B.5). The diesel base measurement also shows a SOC deviation of −1.2 %.

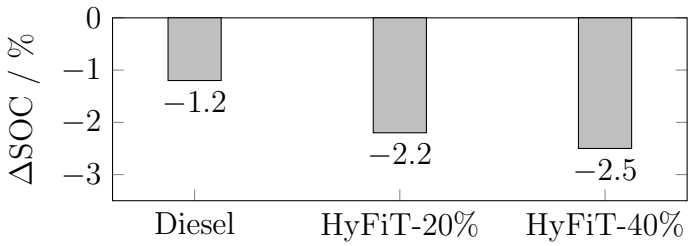

Figure B.5: Comparison of the deviation in battery state of charge (ΔSOC) of diesel, HyFiT-20%, and HyFit-40%.

To enable a comparison of the tests with different fuels, the fuel consumption as well as CO_2, NO_x, and PM emissions are corrected according to the SOC deviation. The corrected fuel consumption FC_{SOC} is calculated by converting the electrical energy required to charge the battery ($\Delta SOC \cdot cap_{\mathrm{Batt}}$) into the corresponding fuel quantity with the fuel's lower heating value (H_{u}) and density (ρ), the average efficiency of the combustion engine ($\bar{\eta}_{\mathrm{ICE}} = 35\ \%$), the conversion efficiencies for battery charging/discharging ($\bar{\eta}_{\mathrm{Ch/Dch}} = 90\ \%$) determined from experimental investigations, and the driven cycle distance (s_{cycle}):

$$FC_{\mathrm{SOC}} = FC - \frac{\Delta SOC \cdot cap_{\mathrm{Batt}}}{H_{\mathrm{u}} \cdot \rho \cdot \bar{\eta}_{\mathrm{ICE}} \cdot \bar{\eta}_{\mathrm{Ch/Dch}} \cdot s_{\mathrm{cycle}}}. \tag{B.8}$$

The corrected CO_2 emissions $m_{\mathrm{CO_2,SOC}}$ are calculated based on the corrected fuel consumption FC_{SOC}, the fuel's carbon mass fraction $Y_{\mathrm{C,Fuel}}$ and density ρ, and the molar masses M of CO_2 and carbon:

$$m_{\mathrm{CO_2,SOC}} = FC_{\mathrm{SOC}} \cdot Y_{\mathrm{C,Fuel}} \cdot \rho \cdot \frac{M_{\mathrm{CO_2}}}{M_{\mathrm{C}}}. \tag{B.9}$$

For the example of diesel, this results in

$$\begin{aligned} FC_{\mathrm{SOC,Diesel}} &= 9.74\,\frac{\mathrm{L}}{100\,\mathrm{km}} - \frac{-1.15\ \% \cdot 13.5\,\mathrm{kW} \cdot 3600\,\mathrm{s}}{42{,}800\,\frac{\mathrm{kJ}}{\mathrm{kg}} \cdot 0.833\,\frac{\mathrm{kg}}{\mathrm{L}} \cdot 0.35 \cdot 0.9 \cdot 23.1\,\mathrm{km}} \cdot 100 \\ &= 9.96\,\frac{\mathrm{L}}{100\,\mathrm{km}} \end{aligned} \tag{B.10}$$

$$m_{\mathrm{CO_2,SOC,Diesel}} = 9.96\,\frac{\mathrm{L}}{100\,\mathrm{km}} \cdot 0.86 \cdot 833\,\frac{\mathrm{g}}{\mathrm{L}} \cdot \frac{44\,\frac{\mathrm{g}}{\mathrm{mol}}}{12\,\frac{\mathrm{g}}{\mathrm{mol}}} = 262\,\frac{\mathrm{g}}{\mathrm{km}}. \tag{B.11}$$

The correction of NO_x and PM emissions is carried out analogously via the brake-specific engine-out emissions, taking into account the average conversion efficiency of the exhaust gas aftertreatment system (EATS) for the tailpipe emissions (NO_x: $\bar{\eta}_{EATS,NO_x,Diesel} = 93\ \%$, $\bar{\eta}_{EATS,NO_x,HyFiT\text{-}20\%} = 91\ \%$, $\bar{\eta}_{EATS,NO_x,HyFiT\text{-}40\%} = 90\ \%$; PM: $\bar{\eta}_{EATS,PM,Diesel} = 99\ \%$, $\bar{\eta}_{EATS,PM,HyFiT\text{-}20\%} = 99\ \%$, $\bar{\eta}_{EATS,PM,HyFiT\text{-}40\%} = 98\ \%$). Due to the lower exhaust gas temperatures, the conversion efficiency of the NO_x exhaust gas aftertreatment system is on average lower for the HyFiT-fuels than for conventional diesel fuel.

As HyFiT-fuels greatly reduce PM emissions (see Figure 4.6), NO_x emissions may be reduced by increasing the EGR rate. Since the calibration of the test vehicle cannot be changed, we estimate the NO_x reduction potential based on previously measured FT fuels with comparable oxygen contents on a single cylinder research engine (Table B.5) (Neumann et al., 2018). These measurements provide detailed information on the PM-NO_x trade-off, which we apply to the HyFiT-fuel vehicle measurements for two cases.

In the first case, the EGR rate is increased iteratively until the NO_x tailpipe emissions of the HyFiT operation correspond to those of the diesel operation, i.e., the NO_x reduction potential is not fully utilized in favor of PM and CO_2 emissions. In the second case, the EGR rate is increased until the engine-out PM emissions of the HyFiT operation correspond to those of the diesel operation. Thereby, NO_x is reduced more than in the first case, but CO_2 emissions are also increased, resulting from higher mass flows associated with the increased EGR rate and faster loading of the particulate filter. Single cylinder measurements with conventional diesel show that increasing the EGR rate to reduce NO_x emissions by 0.1 g/kWh increases CO_2 emissions by 0.083 % (Omari et al., 2017b, 2019). Since this effect occurs mainly due to losses in the air path, these values can also be applied to HyFiT-fuel operation to estimate the impact of an increased EGR rate on CO_2 emissions. In both cases, we expect no significant impact of the measures on the conversion efficiency of the SCR system.

When HyFiT-fuels are used instead of diesel, exhaust gas temperatures are, on average, lower, whereby the warm-up of the SCR system is slower. As long as the SCR system has not yet reached its operating temperature of approx. 200 °C, the SCR system operates at lower conversion rates, resulting in increased tailpipe NO_x emissions. When the operating temperature is reached, NO_x emissions are almost completely converted. In order to minimize disadvantages with regard to CO_2 emissions resulting from an increased EGR rate, we adjust the EGR rate only if the SCR system has not yet reached the stated operating temperature. In the WLTC tests considered herein, the SCR system reaches operating temperature after 825 s.

Table B.5: Comparison of FT fuel compositions from Neumann et al. (2018) (FT low-oxygen, FT high-oxygen) and this study (HyFiT-20%, HyFiT-40%).

Fuel	**Weight fraction**			
	C	H	O	S
FT low-oxygen[a]	0.84	0.15	0.01	0.00
HyFiT-20%[b]	0.82	0.15	0.02	0.00
FT high-oxygen[a]	0.79	0.15	0.06	0.00
HyFiT-40%[b]	0.80	0.15	0.05	0.00

[a] Adopted from Neumann et al. (2018).
[b] This study.

B.2.3 Life cycle assessment

In Table B.6 and Table B.7, we list the considered environmental impact categories of the "Environmental Footprint 3.0" framework (European Commission, 2018b) and LCA datasets of the life cycle inventory, respectively.

Table B.6: List of considered environmental impact categories of the "Environmental Footprint 3.0" framework (European Commission, 2018b).

Abbreviation	**Impact category**	**Unit**	**Level of recommendation**[a]
CF	Carbon footprint	kg CO_2 eq.	I
OD	Ozone depletion	kg CFC-11 eq.	I
PM	Particulate matter	disease incidence	I
A	Acidification	mol H^+ eq.	II
E_{fw}	Eutrophication, freshwater	kg P eq.	II
E_m	Eutrophication, marine	kg N eq.	II
E_t	Eutrophication, terrestrial	mol N eq.	II
IR	Ionizing radiation, human health	kBq U^{235} eq.	II
POF	Photochemical ozone formation	NMVOC eq.	II
ET	Ecotoxicity, freshwater	CTUe	III
HT_c	Human toxicity, carcinogenic	CTUh	III
HT_{nc}	Human toxicity, non-carcinogenic	CTUh	III
LU	Land use	points	III
RU_e	Resource use, energy carriers	MJ	III
RU_m	Resource use, minerals and metals	kg Sb eq.	III
WU	Water use	m^3 world eq.	III

[a] "Level I" is recommended and satisfactory, "Level II" is recommended but needs some improvements, and "Level III" is recommended but has to be applied with caution (European Commission, 2018b).

Table B.7: LCA datasets of the life cycle inventory of HyFiT-fuels (continued on next page).

Flow	Unit	Dataset[a]	Reference
Energy			
Electricity	MJ	Grid mix of the European Union in 2030[b]	Reinert et al. (2020)
		RoW: electricity production, wind, 1-3MW turbine, onshore	Wernet et al. (2016)
Heat, below 100 °C	MJ	RER: steam production, as energy carrier, in chemical industry	Wernet et al. (2016)
		Heat pump with a coefficient of performance of 3.28[c]	David et al. (2017)
Heat, 100-250 °C	MJ	RER: steam production, as energy carrier, in chemical industry	Wernet et al. (2016)
		Electrode vessel with a power-to-heat efficiency of 95 %	Müller et al. (2020a)
Heat, above 250 °C	MJ	RoW: heat production, natural gas, at boiler modulating >100kW	Wernet et al. (2016)
		Electrode vessel with a power-to-heat efficiency of 95 %	Müller et al. (2020a)
		Incineration of excess hydrogen[d]	
		Incineration of by-products and unconverted syngas	
Refrigeration	MJ	Cryogenic cooler	Ladner (2011)
Feedstocks			
Carbon dioxide	kg	DAC system based on temperature swing adsorption[e]	Deutz and Bardow (2021)
Miscanthus	kg	GLO: market for miscanthus, chopped	Wernet et al. (2016)
Natural gas	kg	RoW: market for natural gas, high pressure	Wernet et al. (2016)
Intermediates			
Carbon monoxide	kg	Dry reforming of methane[d]	Sternberg and Bardow (2016)
		Reverse water-gas shift[d]	Sternberg and Bardow (2016)
Hydrogen	kg	Water electrolysis, polymer electrolyte membrane	Bareiß et al. (2019)
		Steam methane reforming[d]	IHS Markit (2018)
		Dry reforming of methane, by-product[d]	Sternberg and Bardow (2016)
Methane	kg	Sabatier process[d]	Agora Verkehrswende (2018)
		RoW: market for natural gas, high pressure	Wernet et al. (2016)
Synthesis gas, 2:1	kg	Partial oxidation of methane[d]	IHS Markit (2018)
		Steam methane reforming with H_2 skimming[d]	IHS Markit (2018)
		Steam methane reforming with CO_2 import[d]	IHS Markit (2018)
		Circulating fluidized bed gasifier[d]	Bachmann et al. (2021)
		Dual fluidized bed gasifier[d]	Bachmann et al. (2021)

[a] Abbreviations in ecoinvent dataset names: RER: Europe; GLO: global; RoW: Rest-of-the-World.
[b] Systemic changes in the underlying electricity grid are captured following the approach of Reinert et al. (2020), based on the "2 °C scenario" of the International Energy Agency (2017) and process data from ecoinvent 3.5, cut-off (Wernet et al., 2016).
[c] The coefficient of performance is averaged from heat pumps built since 2006 with condenser temperatures of about 90 °C and evaporator temperatures between $\in [9, 15]$ °C, according to David et al. (2017).
[d] Adopted from Bachmann et al. (2023a).
[e] Energy requirements are taken from the predicted energy targets by Deutz and Bardow (2021).

Table B.7: LCA datasets of the life cycle inventory of HyFiT-fuels (continued from previous page).

Flow	Unit	Dataset[a]	Reference
Driving			
Transportation	km	Battery-electric van (2030, 3.3 t driving mass, 153 kWh battery capacity)	Sacchi et al. (2022)
Battery	piece	Battery for battery-electric van (2030, 153 kWh battery capacity)	Sacchi et al. (2022)
		Battery for hybrid van (2030, 14 kWh battery capacity)	Sacchi et al. (2022)
Other			
Ash	kg	RoW: Treatment of wood ash mixture, pure, sanitary landfill	Wernet et al. (2016)
Cooling water	kg	GLO: market for water, decarbonised, at user	Wernet et al. (2016)
Diesel	kg	RoW: diesel production, low-sulfur	Wernet et al. (2016)
Monoethanolamine	kg	GLO: market for monoethanolamine	Wernet et al. (2016)
Oxygen	kg	Oxygen vapor via cryogenic air separation	IHS Markit (2018)
Process water	kg	GLO: market for water, decarbonised, at user	Wernet et al. (2016)
Steam	kg	Packaged gas boiler, from "Heat, above 250 °C" or "Heat, 90-250 °C"[d]	IHS Markit (2018)
Vegetable oil methyl ester	kg	GLO: market for vegetable oil methyl ester	Wernet et al. (2016)

[a] Abbreviations in ecoinvent dataset names: RER: Europe; GLO: global; RoW: Rest-of-the-World.
[b] Systemic changes in the underlying electricity grid are captured following the approach of Reinert et al. (2020), based on the "2 °C scenario" of the International Energy Agency (2017) and process data from ecoinvent 3.5, cut-off (Wernet et al., 2016).
[c] The coefficient of performance is averaged from heat pumps built since 2006 with condenser temperatures of about 90 °C and evaporator temperatures between $\in [9, 15]$ °C, according to David et al. (2017).
[d] Adopted from Bachmann et al. (2023a).
[e] Energy requirements are taken from the predicted energy targets by Deutz and Bardow (2021).

B.3 Fuel production

The following section describes our model for HyFiT-fuel production in detail. For the HyFiT-fuel concept, we combine the well-established technologies FT synthesis and hydroformylation and assume a green-field approach, i.e., a facility with at dedicated production site. First, we describe involved process steps depicted in Figure 4.3 (Section B.3.1). Process flowsheets are shown subsequently (Section B.3.2), followed by the modeled fuel composition (Section B.3.3).

B.3.1 Process steps

Processes simulated in AspenPlus use the non-random two-liquid (NRTL) or Peng-Robinson property model for pressures below or greater 10 bar, respectively. In mass and energy balances, alkanes, olefins, aromatics, and oxygenates (i.e., 1-alkanols) are modeled with the chemical formulas $C_nH_{2(n+1)}$, C_nH_{2n}, C_nH_n, and $C_nH_{2n+1}OH$. If property data is missing in AspenPlus for a component of certain chain length, we rely on property data of the next shorter chain length for which complete property data is available. If no aromatic compound exists in AspenPlus with the modeled C:H ratio, an aromatic compound with the closest number of hydrogen atoms is considered for the corresponding number of carbon atoms. For all process steps, we assume 20 °C and 1 bar as ambient conditions. Hydrogen and syngas enter the process at ambient temperature and 30 bar, corresponding to their pressure level of supply; both are heated up and compressed or expanded if required for the following process steps. For compressors, we assume isentropic and mechanical efficiencies of 80 % and 90 %. Pumps are modeled with an efficiency of 80 %.

FT synthesis. In the FT reactor, CO and hydrogen (syngas) are converted in the presence of a metal catalyst to hydrocarbons of various chain lengths, i.e., alkanes, olefins, with small amounts of aromatics and oxygenates as side products. The product of FT synthesis is commonly referred to as so-called syncrude in analogy to the similar composition of crude oil in petrochemical refineries. In literature, FT synthesis is usually divided into low-temperature (LT) and high-temperature (HT) FT synthesis, depending on the reaction temperature. LT-FT synthesis uses cobalt-based catalysts which yield a syncrude of mostly long-chain alkanes, only few oxygenates, and almost no aromatics. Iron-based catalysts are usually used for HT-FT synthesis and are less hydrogenation-active compared to cobalt-based catalysts. Thus, the syncrude of HT-FT synthesis contains much more short-chain olefins in addition to alkanes. We model the inputs (syngas), outputs (syncrude, unconverted syngas, CO_2, water), and heat

releases of a HT-FT and LT-FT synthesis. Syncrude compositions are modeled with the commonly used Anderson-Schulz-Flory (ASF) distribution (Klerk, 2011). According to the ASF distribution, the mole fraction x_n of syncrude compounds containing n carbon atoms is a function of the chain growth probability α:

$$x_n = (1 - \alpha) \cdot \alpha^{n-1}. \tag{B.12}$$

The chain growth probability α can be determined experimentally for a given reactor setup and is influenced by several factors such as reactor operation conditions, catalyst, and H_2:CO ratio of the syngas. Typical α-values are in the range of $0.70 < \alpha < 0.75$ for HT-FT synthesis and $0.85 < \alpha < 0.95$ for LT-FT synthesis (van de Loosdrecht et al., 2013), with single-pass CO conversions of 80-90 % and 40-60 %, respectively (Klerk, 2003). In our model, we select an α-value of 0.74 and a CO conversion of 88 % for the HT-FT synthesis, as reported by Tu et al. (2015) for an iron-based catalyst. Tu et al. (2015) mention a selectivity towards undesired CO_2 of 35 %, reaction conditions of 280 °C and 20 bar, and an H_2:CO ratio of 1:1. For the LT-FT synthesis, we choose the cobalt-based catalyst with an α value of 0.88 and CO conversion of 57 % by Tsubaki et al. (2001). The authors report a selectivity towards undesired CO_2 of 2 %, reaction conditions of 240 °C and 10 bar, and an H_2:CO ratio of 2:1.

Next, we subdivide the modeled syncrude distribution of the LT-FT and HT-FT synthesis into the compound classes alkanes, olefins, aromatics, and oxygenates. For this purpose, we apply the typical generic syncrude compositions of cobalt-based LT-FT and iron-based HT-FT synthesis reported by Klerk (2011) (Table B.8 and Figure B.6). Note that we only consider hydrocarbons up to a chain length of 40 carbon atoms. We further model all oxygenates as 1-alkanols since 1-alkanols represent the largest fraction of oxygenated compounds in the syncrude (Maitlis and Klerk, 2013). Consequently, we do not consider other oxygenated compounds such as aldehydes, ketones, and carboxylic acids. The resulting syncrude compositions are presented in Figure B.6. Note that discontinuities in the shown syncrude compositions, e.g., between chain length four and five, result from the generic syncrude compositions reported by Klerk (2011) that cluster product fractions into discrete carbon ranges (Table B.8). In reality, syncrude compositions can be expected to be more continuous. Subsequently, we calculate the amount of water-gas shift compounds, i.e., CO, H_2, CO_2, and water, which are present in both reactor outlet streams besides the syncrude. For the calculation, we use the modeled syncrude compositions and reported CO conversions and CO_2 selectivities.

The FT synthesis is highly exothermic, releasing large amounts of excess heat (van de Loosdrecht et al., 2013). This excess heat can be used for heat integration or has to be cooled if heat integration is not possible. We calculate the heat release of both FT syntheses as enthalpy difference over the reactor at 280 °C and 20 bar for HT-FT synthesis as well as 240 °C and 10 bar for LT-FT synthesis with isothermal *RYield* reactor models in AspenPlus v11.

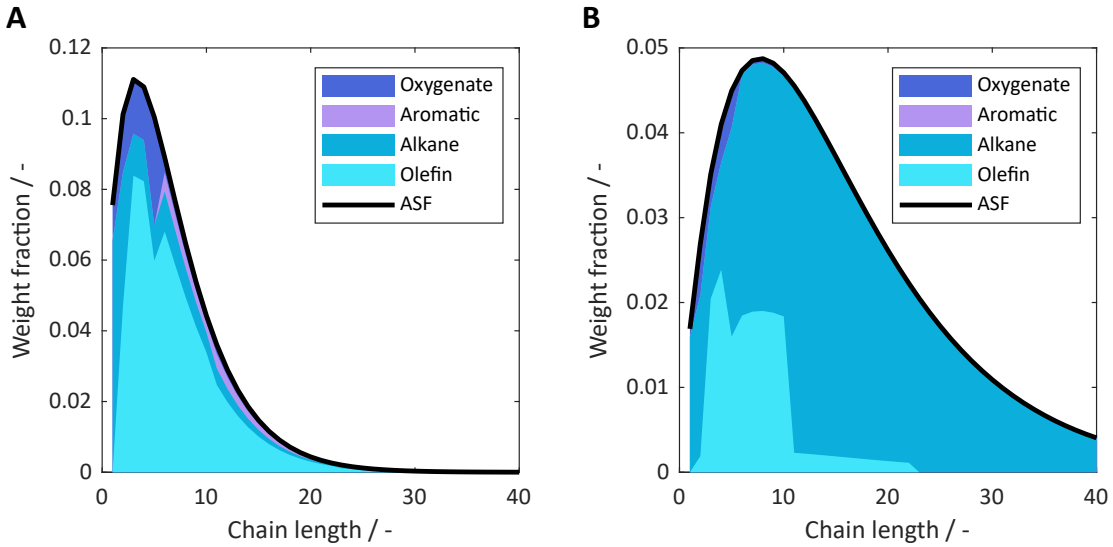

Figure B.6: Weight fractions of the modeled syncrude composition for (A) HT-FT with a chain growth probability α of 0.74 and (B) LT-FT synthesis with an α-value of 0.88 without water-gas shift compounds (CO, H_2, CO_2, and water). The distribution of the compound classes oxygenates, aromatics, alkanes, and olefins is adopted from Klerk (2011) (see Table B.8) and represents typical syncrude compositions for HT-FT and LT-FT syntheses. The black bold curve represents the Anderson-Schulz-Flory (ASF) distribution.

Table B.8: Generic syncrude compositions of iron-based high-temperature FT (Fe HT-FT) and cobalt-based low-temperature FT (Co LT-FT) syntheses, adopted from Klerk (2011).

Product fraction	**Carbon range**	**Compound class**	**Syncrude composition**[a] wt%	
			Fe HT-FT	Co LT-FT
Tail gas	C_1	Alkane	12.7	5.6
	C_2	Alkene	5.6	0.1
		Alkane	4.5	1.0
LPG	C_3-C_4	Alkene	21.2	3.4
		Alkane	3.0	1.8
Naphtha	C_5-C_{10}	Alkene	25.8	7.8
		Alkane	4.3	12.0
		Aromatic	1.7	0.0
		Oxygenate	1.6	0.2
Distillate	C_{11}-C_{22}	Alkene	4.8	1.1
		Alkane	0.9	20.8
		Aromatic	0.8	0.0
		Oxygenate	0.5	0.0
Residue/wax	C_{22+}	Alkene	1.6	0.0
		Alkane	0.4	44.6
		Aromatic	0.7	0.0
		Oxygenate	0.2	0.0
Aqueous product	C_1-C_5	Alcohol	4.5	1.4
		Carbonyl	3.9	0.0
		Carboxylic acid	1.3	0.2

[a] Excluding inert gases (nitrogen, argon) and water-gas shift products (water, carbon monoxide, carbon dioxide, hydrogen).

Syncrude recovery. To recover the syncrude from the water-gas shift compounds, industrial FT plants use stepwise cooling and phase separation during the so-called syncrude recovery. Syncrude recovery is followed by refining steps of targeted products (Rodríguez Vallejo and Klerk, 2013; Klerk and Furimsky, 2010). The recovered syncrude is thereby pre-fractionated into a tail gas (C_1-C_4), naphtha (C_5-C_{10}), and distillate (C_{11+}) cut. The tail gas cut is further treated in the so-called gas loop, whereas the naphtha and distillate cut are fractionated in the atmospheric distillation unit. In the tail gas cut, water-gas shift compounds are also present in addition to hydrocarbons, with substantial amounts of unconverted CO in the case of LT-FT synthesis due to its low CO conversion. We model this process sequence based on

the work of Rodríguez Vallejo and Klerk (2013). For simplicity, we assume sharp splits for mass balances of separation units. We estimate the separation units' energy consumptions with AspenPlus models.

The product of LT-FT synthesis has a liquid and gaseous phase that are separated with a *Flash2* block at reactor conditions. In contrast, the HT-FT product is solely gaseous. The gaseous phases of LT-FT and HT-FT syntheses are separated into an organic gaseous, organic liquid, and aqueous liquid stream in two three-phase separators. The organic gaseous stream, called tail gas, contains C_1-C_4 hydrocarbons and water-gas shift compounds and is led to the gas loop. The organic liquid stream contains the naphtha cut of C_5-C_{10} and the distillate cut of C_{11+} hydrocarbons and is sent to the atmospheric distillation unit. The aqueous liquid stream contains water and oxygenated compounds and is treated as wastewater. Both three-phase separators are modeled with *Flash3* blocks in AspenPlus. The three-phase separators are modeled with a pressure of 10 bar for LT-FT and 20 bar for HT-FT synthesis and temperatures of 150 °C and 40 °C for the first and second separator, respectively.

Gas loop. The overall carbon efficiency of the process concept is strongly affected by the fate of unconverted CO in the gas loop (Klerk, 2011). Gas loop designs among industrial FT facilities differ greatly (Klerk, 2011), and finding the optimal gas loop is a complex design problem that is beyond the scope of this study. However, all gas loop designs are in-between two extremes considered in this study: an open-loop and a closed-loop design (Dry and Steynberg, 2006). In both gas loop designs, purge gases and by-products can be incinerated for heat recovery followed by optional CO_2 capture or flared (see Figure B.11). In our open-loop design, no tail gas is recycled, resulting in a simple process concept at the cost of low carbon efficiency. In this case, the entire tail gas stream is purged without any CO recovery.

In contrast, our closed-loop design aims for maximum recovery of CO and H_2 that are recycled to the FT reactor inlet. The closed-loop design improves the carbon efficiency, however, at the cost of a complex process sequence that includes cryogenic separation of C_1-C_2 hydrocarbons, resulting in additional utility consumption (Klerk, 2011). To prevent inert gas build-up (Dry and Steynberg, 2006), 5 % of the tail gas is purged. The remaining tail gas is cooled to 25 °C and fed to a Benfield unit, where CO_2 is separated. The Benfield unit's energy consumption is modeled with 1.56 MJ of heat and 0.05 MJ of electricity per kg of CO_2, based on Bartoo (1984). The temperature of the CO_2-free tail gas stream is assumed to be 101 °C, following Kohl and Nielsen (1997). Before separation in a three-phase separator at reactor pressure, the tail gas stream is cooled to 5 °C.

The three-phase separator is modeled as *Flash3* block in AspenPlus, and the top gaseous stream is sent to a rectification column modeled with a rigorous *RadFrac* block with a partial-vapor condenser. Note that separating CO and H_2 from short-chain hydrocarbons requires cryogenic operating temperatures of approximately $-170\,°C$ in the condenser. Targeted recovery rates are set to over 99 % for CO and H_2 in the top and all other compounds in the bottom stream. For HT-FT synthesis, the optimized rectification column has 8 stages with the feed entering at the 7th stage, a reflux ratio of 2.65, and a top-to-feed ratio of 0.74. In contrast, for the LT-FT synthesis, the optimized rectification column has 6 stages with the feed entering at the 5th stage, a reflux ratio of 1.09, and a top-to-feed ratio of 0.97. Next, the top stream is heated to $20\,°C$ and is assumed to consist of purely CO and H_2 for simplicity.

Atmospheric distillation unit. In the ADU, the organic liquid stream is separated into a naphtha and distillate cut at 1 bar. The rectification column is modeled with a rigorous *RadFrac* block in AspenPlus with a total condenser. Targeted recovery rates are set to 99 % for decane in the top and undecane in the bottom stream. For HT-FT synthesis, the optimized ADU has 38 stages with the feed entering at the 18th stage, a reflux ratio of 0.23, and a top-to-feed ratio of 0.80. In contrast, for the LT-FT synthesis, the optimized ADU has 46 stages with the feed entering at the 24th stage, a reflux ratio of 0.35, and a top-to-feed ratio of 0.53.

Removal of aromatics and oxygenates. After the atmospheric distillation unit, the naphtha and distillate cuts still contain aromatics and oxygenates, which are undesirable in the HyFiT-fuel. Their removal is thus necessary to obtain a mixture consisting solely of olefins and alkanes. To the authors' knowledge, industrial applications for the selective removal of aromatics and oxygenates from entire naphtha and distillate cuts are not documented in open-access literature. We, therefore, estimate the utility requirements for this separation sequence with proxy data of the "UOP Sulfolane process," which is industrially used for high-purity recovery of aromatics from hydrocarbon mixtures (Meyers, 2004). The "UOP Sulfolane process" is named after the used solvent and combines liquid-liquid extraction with extractive distillation.

Note that oxygenates in the C_5-C_{10} and C_{11+} cuts contain alcohols that could be also used as components in HyFiT-fuels. However, the C_5-C_{10} and C_{11+} cuts contain much less oxygenates compared to, in particular, olefins that can be hydroformylated and hydrogenated to alcohols in much greater amounts (see Table B.8). Additionally, these alcohols in the C_5-C_{10} and C_{11+} cuts would have to be separated from other oxygenated compounds such as carboxylic acids, carbonyls, and ketones that are undesirable components in HyFiT-fuels. Such a separation sequence would increase the utility consumption which would have to be weighed against the benefit

of a slightly increased carbon efficiency. Consequently, in this study, we decided to remove the small amounts of oxygenates entirely in this initial process concept in favor of a simpler process design. Still, the potential of using the alcohols of the C_5-C_{10} and C_{11+} cuts should be considered for proceeding process optimization of HyFiT-fuel production.

In this estimation, we assume a sharp split into a product stream consisting of alkanes and olefins and a by-product stream consisting of aromatics and oxygenates. The process operates at 1 bar, and inputs are heated to 116 °C before entering (Ullmann, 2000). Utility requirements are determined to 1.39 MJ of heat, 0.03 MJ of electricity, and 5.03 kg of cooling water per kg of process input, according to Meyers (2004). For heat consumption, we assume a temperature level of 300 °C since sulfolane, with a boiling temperature of 287 °C at 1 bar, needs to be vaporized (Ullmann, 2000). The temperature of the product stream is estimated to 100 °C, corresponding to documented extractor top temperatures (Ullmann, 2000). The separated aromatics and oxygenates can be either incinerated for heat recovery followed by optional CO_2 capture or flared (see Figure B.11).

Since using proxy data for such an essential separation sequence may induce large uncertainty to the calculated environmental impacts of the HyFiT-fuel, we perform a sensitivity analysis (see Section B.5.4.3). In this sensitivity analysis, we find that the carbon footprint of HyFiT-fuels is only slightly sensitive towards the quantity and temperature level of heat consumption of the proxy process. Future studies on the HyFiT-fuel concept should focus on designing a suitable separation sequence.

Hydroformylation and hydrogenation. After removing aromatics and oxygenates, the naphtha cut consists of C_5-C_{10} olefins and alkanes. The naphtha cut is treated next by a hydroformylation and hydrogenation sequence to increase the amount of alcohols as oxygen carriers in the HyFiT-fuel. During hydroformylation, alkanes remain inert (Püschel et al., 2021) while olefins are converted with equimolar syngas to aldehydes (Equation B.13) by adding hydrogen and a formyl group (CHO) to the olefin's carbon-carbon double bond (Cornils et al., 2018). The aldehydes are subsequently hydrogenated to alcohols. The hydroformylation reactor is modeled as isothermal *RStoic* block in AspenPlus at reaction conditions of 90 °C and 15 bar, reported by Shaharun et al. (2010). These reported reaction conditions are in the range of industrial hydroformylation processes (Cornils et al., 2013). For all olefins, the hydroformylation is modeled with the reported 1-octene conversion of 97 % and n-nonanal yield of 95 % (Shaharun et al., 2010). The amount of required syngas is calculated by closing elemental balances and assuming complete syngas conversion (Börner and Franke, 2016). As demonstrated by Warmeling et al. (2017a,b), olefin

isomers are the only by-products of aldehydes during hydroformylation. Pressure and temperature of the reactants, olefins and syngas, are adjusted by compression, expansion, and heating to match reaction conditions. To ensure that all olefins are liquid before compression, the naphtha cut is cooled to 60 °C after the removal of aromatics and oxygenates.

$$C_nH_{2n} + CO + H_2 \longrightarrow C_{n+1}H_{2(n+1)}O \tag{B.13}$$

During hydrogenation, aldehydes are converted with H_2 to alcohols, whereas unconverted and isomerized olefins are saturated to their corresponding alkanes (Equations B.14 and B.15) (Püschel et al., 2021). For simplicity, we assume a yield of 100 % since Redina et al. (2019) report yields greater than 99 % for most hydrogenation reactions of C_6-C_{11} aldehydes at ambient conditions of 20 °C and 1 bar. The hydrogenation reactor is modeled as isothermal *RStoic* block in AspenPlus, and the amount of required H_2 is calculated by closing elemental balances. The reactants are expanded and cooled to reaction conditions before entering the reactor. Heat releases of both reactors are calculated as enthalpy differences over each reactor in AspenPlus. After hydroformylation and hydrogenation, the product mixture consists of the targeted C_6-C_{11} alcohols and C_5-C_{10} alkanes.

$$C_nH_{2n}O + H_2 \longrightarrow C_nH_{2n+1}OH \tag{B.14}$$

$$C_nH_{2n} + H_2 \longrightarrow C_nH_{2(n+1)} \tag{B.15}$$

Hydrocracking. After the removal of aromatics and oxygenates, the distillate cut of C_{11+} olefins and alkanes is sent to the hydrocracking process. In our hydrocracker model, olefins are saturated to their corresponding alkanes (Equation B.15) and long-chain C_{17+} alkanes are cracked to chain lengths of C_9-C_{17}. We model the cracking by splitting each C_{17+} alkane into two alkanes of equal carbon chain length until all alkanes are in the range of C_9-C_{17} (Equation B.16). Consequently, the product mixture of the hydrocracker outlet stream consists solely of C_9-C_{17} alkanes. The amount of required H_2 for hydrocracking is calculated by closing elemental balances.

$$\mathrm{C}_n\mathrm{H}_{2(n+1)} + \mathrm{H}_2 \longrightarrow \begin{cases} 2\ \mathrm{C}_{\frac{n}{2}}\mathrm{H}_{n+2} & \text{for even } n > 17 \\ \mathrm{C}_{\frac{n-1}{2}}\mathrm{H}_{n+1} + \mathrm{C}_{\frac{n+1}{2}}\mathrm{H}_{n+3} & \text{for odd } n > 17 \end{cases} \tag{B.16}$$

For the utility requirements of hydrocracking, we consider 0.89 MJ of heat, 0.10 MJ of medium-pressure steam, 0.27 MJ of electricity, and 12.36 kg of cooling water per kg of process input. The utility requirements are derived from typical energy requirements of the "Chevron Lummus Global Isocracking process" in its two-stage configuration (Meyers, 2004). The "Isocracking" technology can be adapted to produce almost any desired product distribution and has been widely used in industry for decades (Meyers, 2004), e.g., in the wax hydrocracker of the Oryx gas-to-liquids FT facility (Klerk, 2011). We assume medium-pressure steam to be saturated at 184 °C, corresponding to the reported pressure level of 11 bar (Hydrocarbon Processing, 2008). For the reactants, we consider compression and heating of the liquid C_{11+} cut to 3.6 bar and 200 °C and of H_2 to 46 bar and 50 °C (Rudin, 2018). H_2 compression is modeled by an isentropic two-stage *MCompr* block, using the ASME method. H_2 is compressed from 30 bar to 40 bar in the first stage, subsequently cooled to 50 °C, and compressed from 40 bar to 46 bar in the second stage.

Membrane separation. The LT-FT synthesis requires syngas with an H_2:CO ratio of 2:1, as the syngas is supplied by the production network by Bachmann et al. (2023a). In contrast, the HT-FT synthesis and hydroformylation require syngas with an H_2:CO ratio of 1:1. To adjust the syngas ratio from 2:1 to 1:1, we model a membrane separation unit in which excess H_2 is separated by membrane permeation. For ceramic membranes, Prabhu and Oyama (2000) report separation factors of 87,000 for H_2:CO mixtures. No CO permeation through the membrane was observed, which corresponds to a selectivity towards H_2 of 100 %. We assume that a pressure difference of 29 bar between the feed (30 bar) and permeate side (1 bar) is sufficiently high as driving force for the proposed membrane separation. The product, i.e., syngas with H_2:CO ratio of 1:1 at the retentate side, is modeled with the same pressure level as the feed (30 bar). In contrast, at the permeate side, the separated H_2 is compressed back to 30 bar, modeling an isentropic three-stage *MCompr* block with the ASME method. H_2 is compressed from 1 bar to 10 bar in the first stage, 10 bar to 20 bar in the second stage, and 20 bar to 30 bar in the third stage. After each stage, H_2 is cooled back to 20 °C.

By-product treatment. Depending on the supply chain optimization, purge gases and by-products are either incinerated for energy recovery followed by optional CO_2

capture or flared (see Figure B.11). For energy recovery, we consider the lower heating values of the incinerated by-products for the heat releases. For optional CO_2 capture from the flue gas, we adapt energy requirements of 2.75 MJ of heat per kg of captured CO_2 at 154 °C, 0.02 MJ of electricity per kg of captured CO_2 and a CO_2 absorption rate of 90 % from Dubois and Thomas (2018). Before CO_2 capture, the flue gas is cooled to 40 °C (Dubois and Thomas, 2018).

B.3.2 Process flowsheets

In the following, we present detailed flowsheets of the HyFiT process concept with HT-FT or LT-FT synthesis and either open-gas-loop or closed-gas-loop design. Additionally, we show a process flowsheet of the by-product treatment.

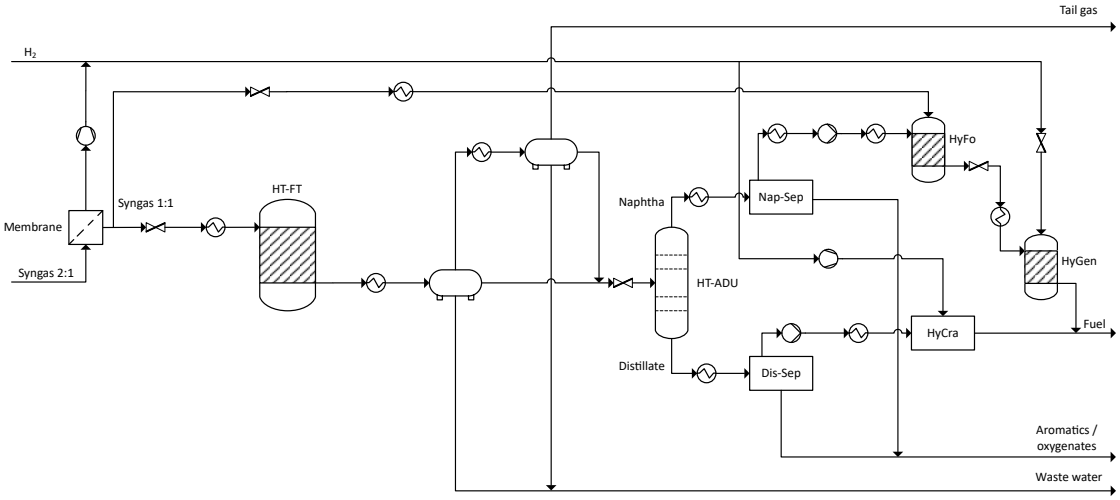

Figure B.7: Flowsheet of the HyFiT process concept for the HT-FT synthesis and the open-gas-loop design. ADU: atmospheric distillation unit, Nap-Sep: naphtha separation, Dis-Sep: distillate separation, HyFo: hydroformylation, HyGen: hydrogenation, HyCra: hydrocracking.

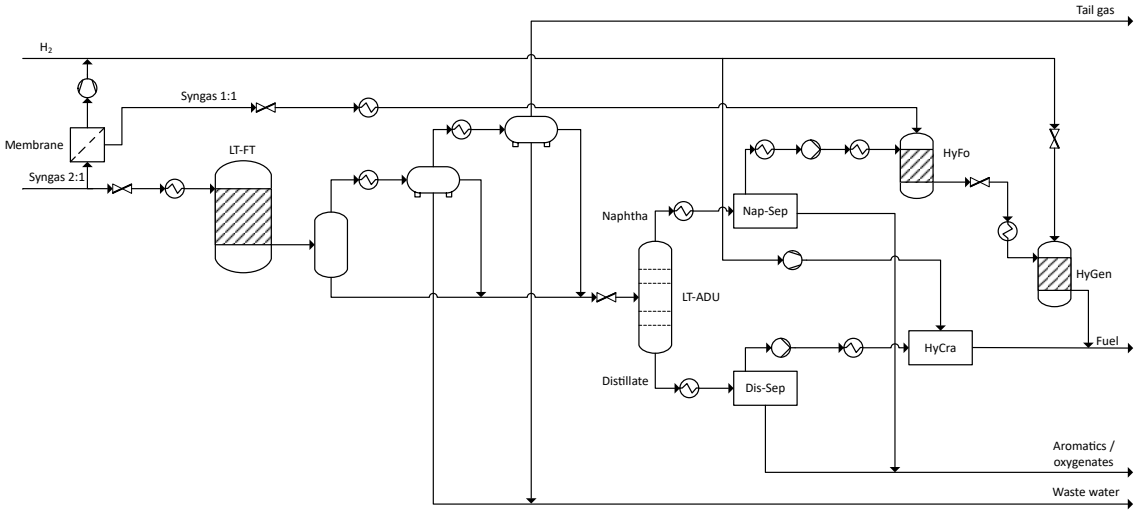

Figure B.8: Flowsheet of the HyFiT process concept for the LT-FT synthesis and the open-gas-loop design. ADU: atmospheric distillation unit, Nap-Sep: naphtha separation, Dis-Sep: distillate separation, HyFo: hydroformylation, HyGen: hydrogenation, HyCra: hydrocracking.

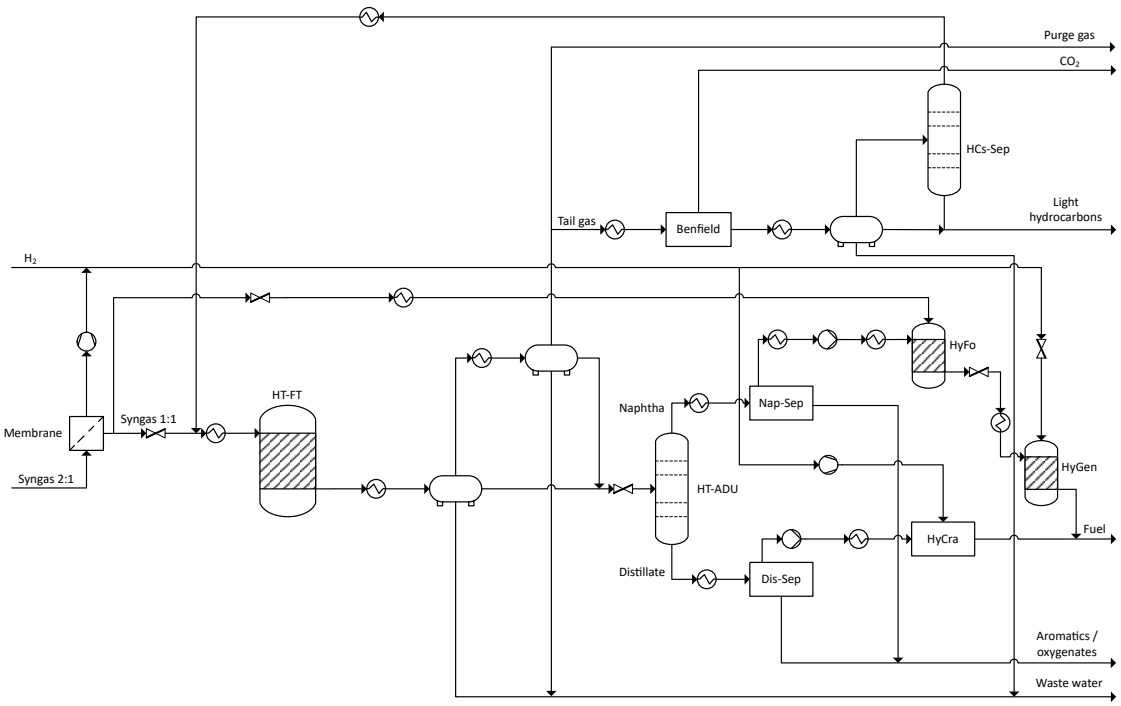

Figure B.9: Flowsheet of the HyFiT process concept for the HT-FT synthesis and the closed-gas-loop design. ADU: atmospheric distillation unit, Nap-Sep: naphtha separation, Dis-Sep: distillate separation, HyFo: hydroformylation, HyGen: hydrogenation, HyCra: hydrocracking, HCs-Sep: hydrocarbons separation.

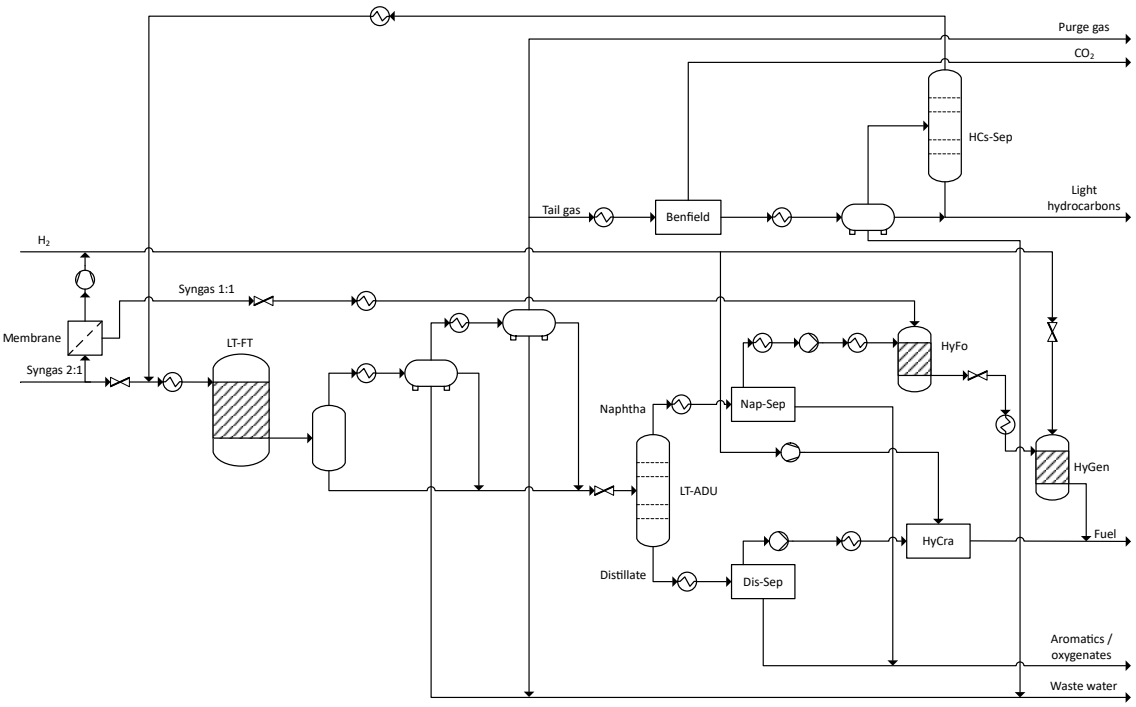

Figure B.10: Flowsheet of the HyFiT process concept for the LT-FT synthesis and the closed-gas-loop design. ADU: atmospheric distillation unit, Nap-Sep: naphtha separation, Dis-Sep: distillate separation, HyFo: hydroformylation, HyGen: hydrogenation, HyCra: hydrocracking, HCs-Sep: hydrocarbons separation.

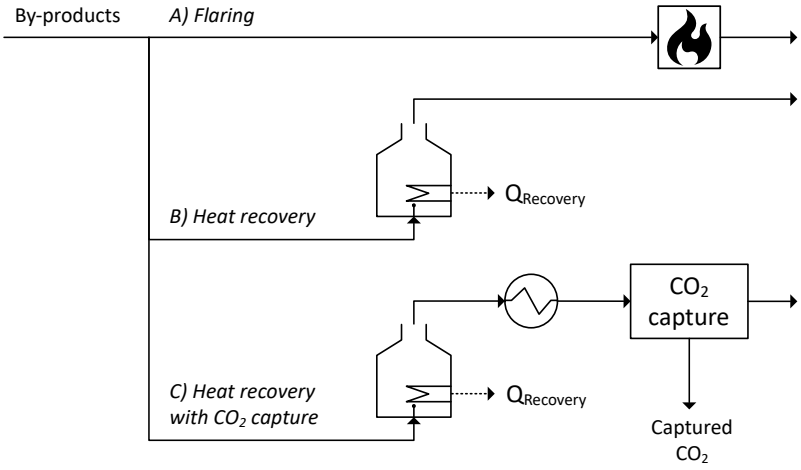

Figure B.11: Flowsheet of by-product treatment in the HyFiT process concept. By-products can either be (A) flared, (B) incinerated for heat recovery, or (C) incinerated for heat recovery followed by CO_2 capture of the off-gas.

B.3.3 Fuel composition

In Table B.9, we present the modeled fuel compositions of the HyFiT-fuel production concept that consists of several process units including FT synthesis and hydroformylation (see Figure 4.3). Depending on the FT synthesis used in the HyFiT-fuel production concept, the resulting HyFiT-fuel is either rich in alkanes (LT-FT synthesis) or alcohols (HT-FT synthesis). By combining both LT-FT and HT-FT synthesis, the desired alcohol-alkane ratio of the HyFiT-fuel can be adjusted.

Table B.9: The modeled composition of HyFiT-fuels. Mass fractions of HyFiT-fuel produced via hydroformylation and (A) LT-FT or (B) HT-FT synthesis (see Figure 4.3). Summed values differ slightly due to rounding. (C) By combining HyFiT-fuels produced from both hydroformylation and LT-FT as well as HT-FT synthesis, the desired alcohol-alkane ratio of the HyFiT-fuel can be adjusted. The HyFiT-fuels with 20 wt% (HyFiT-20%) and 40 wt% (HyFiT-40%) alcohol are marked with ([a]) and ([b]), respectively.

A

Carbon atoms	**Mass fraction** wt%	
	Alcohol	Alkane
5	–	3
6	2	3
7	3	3
8	3	3
9	3	10
10	2	10
11	2	10
12	–	9
13	–	8
14	–	7
15	–	7
16	–	6
17	–	5
Σ	**15**	**85**

B

Carbon atoms	**Mass fraction** wt%	
	Alcohol	Alkane
5	–	2
6	14	2
7	15	2
8	12	2
9	10	3
10	8	2
11	7	6
12	–	4
13	–	3
14	–	3
15	–	2
16	–	2
17	–	1
Σ	**65**	**35**

C

Mixing ratio of HyFiT-fuel: LT-FT:HT-FT	wt%	100:0	90:10[a]	80:20	70:30	60:40	50:50[b]	0:100
Alcohol content	wt%	15	20[a]	25	30	35	40[b]	65
Alkane content		85	80[a]	75	70	65	60[b]	35

B.3.4 Conversion, selectivity, and yield

In this section, we describe the calculation of the CO conversion, selectivity, and yield. The CO conversion (*Conv*) is calculated from CO present in the inlet streams ($n_{\mathrm{CO,input}}$) of FT synthesis and hydroformylation as well as CO present in the outlet streams ($n_{\mathrm{CO,output}}$):

$$Conv = \frac{n_{\mathrm{CO,input}} - n_{\mathrm{CO,output}}}{n_{\mathrm{CO,input}}}. \tag{B.17}$$

The carbon-based selectivity (*Selec*) is calculated from carbon present in the desired product ($n_{\mathrm{C,product}}$) as well as carbon present in all input ($n_{\mathrm{C,input}}$) and output ($n_{\mathrm{C,output}}$) streams. The selectivity is calculated for the entire HyFiT-fuel and the alcohols and alkanes present in HyFiT-fuels.

$$Selec = \frac{n_{\mathrm{C,product}}}{n_{\mathrm{C,input}} - n_{\mathrm{C,output}}} \tag{B.18}$$

The yield (*Yield*) is calculated by multiplying CO conversion and selectivity:

$$Yield = Conv \cdot Selec. \tag{B.19}$$

Calculated conversions, selectivities, and yields are listed in Table B.11.

Table B.11: Conversion, selectivity, and yield of HyFiT-fuels. Conversion and yield are presented for the open and closed gas loop design. Selectivity and yield are shown for the entire fuel as well as the alcohols and alkanes present in the fuel. LT: low-temperature, HT: high-temperature, FT: Fischer-Tropsch.

HyFiT-fuel	**Conversion** *open / closed loop*	**Selectivity**			**Yield** *open / closed loop*		
		Fuel	Alcohols	Alkanes	Fuel	Alcohols	Alkanes
LT-FT	0.57 / 0.96	0.86	0.12	0.75	0.49 / 0.83	0.07 / 0.12	0.43 / 0.72
HT-FT	0.88 / 0.99	0.36	0.22	0.14	0.32 / 0.36	0.19 / 0.22	0.12 / 0.14
HyFiT-20%	0.61 / 0.97	0.77	0.14	0.63	0.47 / 0.74	0.09 / 0.14	0.38 / 0.61
HyFiT-40%	0.75 / 0.98	0.52	0.19	0.33	0.39 / 0.51	0.14 / 0.19	0.25 / 0.32

B.4 Fuel usage

Here, we present numerical results for fuel properties and material compatibility (Section B.4.1) as well as numerical results and alternative figures regarding fuel combustion (Section B.4.2).

B.4.1 Fuel properties and material compatibility

Numerical values of material compatibility results and fuel properties are shown in Table B.12 for HyFiT-fuels with alcohol contents between 15 and 65 wt%.

B.4.2 Fuel combustion

In Figure B.12, the chemical energy is shown that is required from diesel, HyFiT-20%, and HyFiT-40% over the test cycle. Numerical values of measured combustion-related CO_2, NO_x, and PM emissions are presented in Table B.13. Figure B.13 and Figure B.14 show PM and NO_x engine-out emissions as well as alternative figures for PM and NO_x tailpipe emissions.

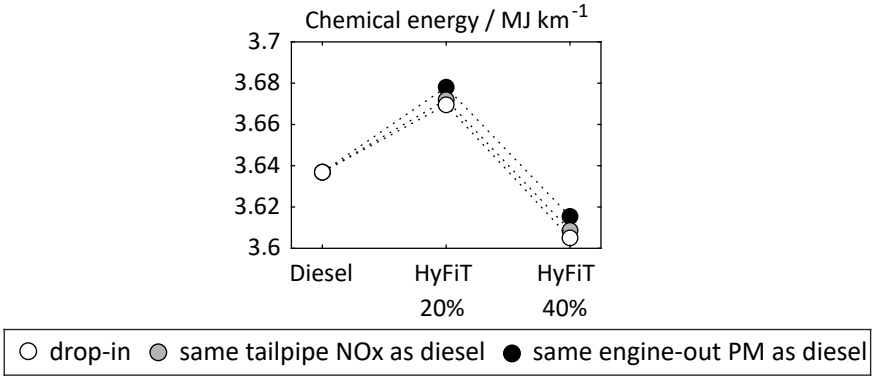

Figure B.12: Chemical energy required from diesel, HyFiT-20%, and HyFiT-40% over the test cycle. Results are shown for three engine calibration cases: measured emissions from vehicle tests with the manufacturer's engine calibration (white circles) and estimated emissions of the HyFiT-fuels with an engine calibration that targets either the same tailpipe NO_x emissions as diesel (grey circles) or the same engine-out PM emissions as diesel (black circles).

Table B.12: Fuel properties and material compatibility results for HyFiT-fuels with alcohol contents between 15 and 65 wt%. The measurements for the change of mass and volume of FKM and 30 wt% alcohol gave inconsistent results. This data point is shown in brackets and not included in the further analysis.

	Unit	Limits		Alcohol content of HyFiT-fuel							
		Lower	Upper	15 %	20 %	25 %	30 %	35 %	40 %	65 %	
Material compatibility[a]											
Change of mass	–	–	–								
FKM				0.2%	0.2%	0.1%	(-1.6%)	0.1%	0.2%	0.1%	
HNBR				6.9%	7.0%	7.6%	7.6%	7.7%	8.5%	8.6%	
NBR				9.7%	9.8%	10.8%	10.9%	10.9%	10.9%	10.7%	
Change of volume	–	-5%	10%								
FKM				0.2%	-0.6%	-0.5%	(-3.2%)	-0.4%	0.1%	-0.6%	
HNBR				10.4%	9.3%	9.6%	9.9%	9.7%	12.6%	10.9%	
NBR				15.4%	13.7%	14.4%	14.9%	15.2%	16.8%	14.8%	
Change of hardness	–	-10%	15%								
FKM				-14.5%	-0.7%	-0.5%	0.0%	-2.0%	-6.6%	-0.6%	
HNBR				-13.5%	-11.0%	-5.5%	-7.4%	-10.1%	-12.6%	-12.0%	
NBR				-2.6%	-17.4%	-19.2%	-14.6%	-18.4%	-12.6%	-13.4%	
Fuel properties[b]											
LHV	$MJ\,kg^{-1}$	–	–	43.2	42.9	42.6	42.2	41.9	41.5	39.8	
DCN	–	51	–	66	64	63	60	59	56	48	
Viscosity	$mm^2\,s^{-1}$	2.0	4.5	1.4	1.5	1.5	1.6	1.7	2.0	2.9	
Density	$kg\,m^{-3}$	820	845	757	766	769	772	777	782	805	
Lubricity											
HFRR[c]	μm	–	460	577[d]	568[d]	571[d]	534[d]	538[d]	546[d]	492[d]	
				417[e]	430[e]	384[e]	432[e]	411[e]	430[e]	429[e]	
Friction coefficient	–	–	–	0.55[d]	0.53[d]	0.53[d]	0.50[d]	0.51[d]	0.48[d]	0.42[d]	
				0.23[e]	0.22[e]	0.24[e]	0.20[e]	0.21[e]	0.20[e]	0.18[e]	

[a] Determined values at the end of each test series. Limits are taken from Richter (2014, 2022).
[b] Limits are taken from the EN 590 diesel fuel standard.
[c] High frequency reciprocating rig.
[d] Measured without additive.
[e] Measured with additive (2000 ppm of R655).

Table B.13: Numerical values for combustion-related CO_2, NO_x, and particulate matter (PM) engine-out (EO) and tailpipe (TP) emissions of diesel, HyFiT-20%, and HyFiT-40%.

	CO_2	**NO_x**		**PM**	
	$g\,km^{-1}$	$mg\,km^{-1}$		$mg\,km^{-1}$	
	TP	EO	TP	EO	TP
Diesel					
drop-in	267	318	24	51	0.34
HyFiT-20%					
drop-in	258	343	29	23	0.16
same tailpipe NO_x as diesel	258	333	22	24	0.17
same engine-out PM as diesel	259	323	16	28	0.20
HyFiT-40%					
drop-in	255	346	35	15	0.33
same tailpipe NO_x as diesel	255	331	23	17	0.38
same engine-out PM as diesel	256	320	15	21	0.47

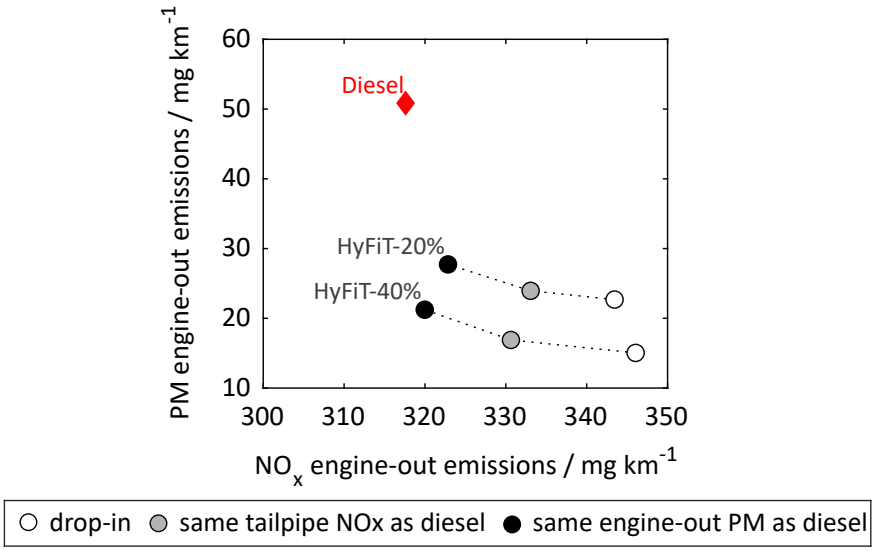

Figure B.13: PM over NO_x engine-out emissions from the combustion of diesel, HyFiT-20%, and HyFiT-40%. Results are shown for three engine calibration cases: measured emissions from vehicle tests with the manufacturer's engine calibration, denoted as "drop-in," (white circles) and estimated emissions of HyFiT-fuels with an engine calibration that targets either the same tailpipe NO_x emissions (grey circles) or engine-out PM emissions as diesel (black circles). Note that, for the estimated emissions of HyFiT-fuels, the EGR rate is solely adjusted to lower NO_x emissions if the SCR system has not yet reached its operating temperature, i.e., for the first 825 seconds of the test cycle (see Section B.2.2). In the remaining test cycle time, the SCR system reduces NO_x emissions since it has reached its operating temperature; thus, no adjustment of the EGR rate is required. Consequently, overall PM engine-out emissions of HyFiT-fuels are lower than those of diesel for the "same engine-out PM as diesel" calibration. Numerical values of emissions are presented in Table B.13.

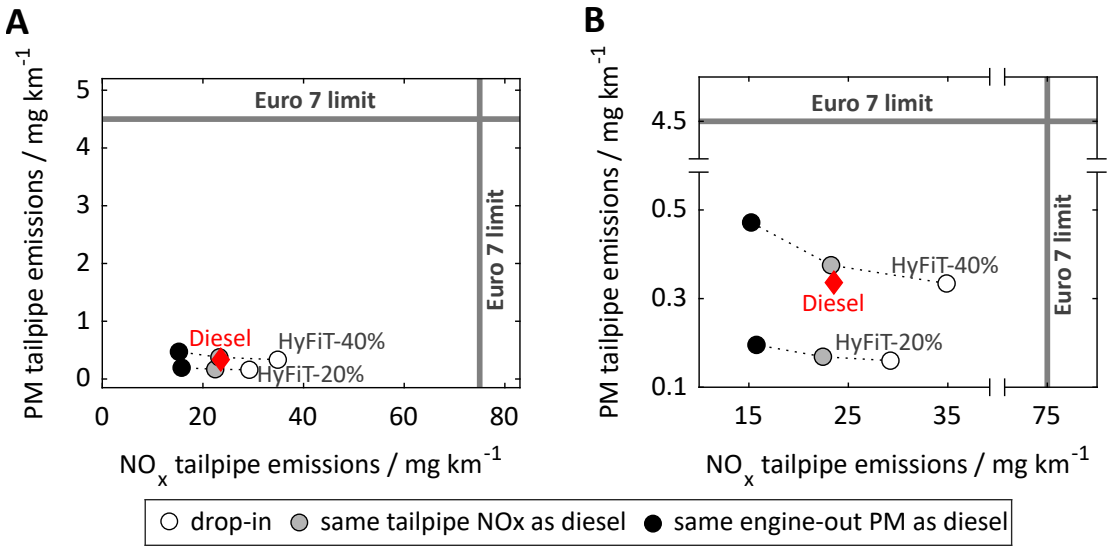

Figure B.14: (A) PM over NO_x tailpipe emissions from the combustion of diesel, HyFiT-20%, and HyFiT-40%. In (B), emissions have a higher resolution due to the axes breaks. Results are shown for three engine calibration cases: measured emissions from vehicle tests with the manufacturer's engine calibration, denoted as "drop-in," (white circles) and estimated emissions of HyFiT-fuels with an engine calibration that targets either the same tailpipe NO_x emissions (grey circles) or engine-out PM emissions as diesel (black circles). Numerical values of emissions are presented in Table B.13.

B.5 Life cycle impact assessment

This section presents further details regarding the carbon footprint minimization (Section B.5.1), limited feedstock availability (Section B.5.2), contribution and sensitivity analyses (Section B.5.3–B.5.4), and carbon efficiency (Section B.5.5).

B.5.1 Carbon footprint minimization

In the following, we present the carbon footprints of HyFiT-20% with closed-gas-loop design and HyFiT-40% with both open- and closed-gas-loop design (Figure B.15).

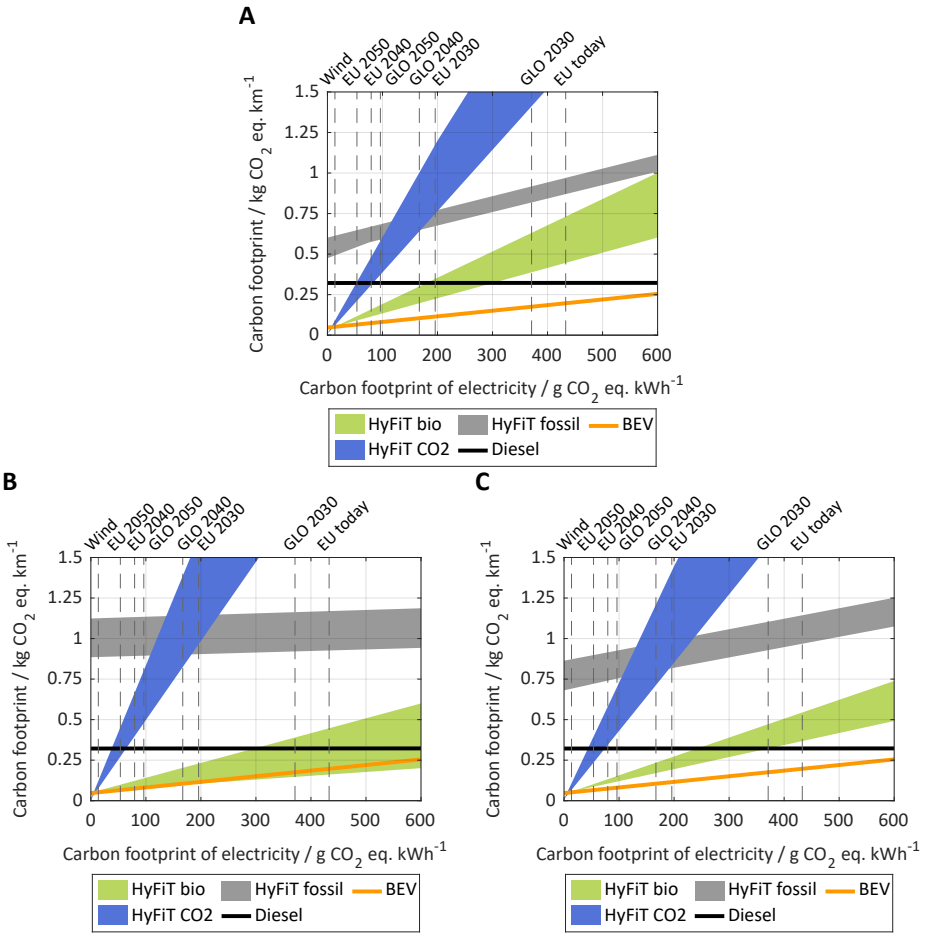

Figure B.15: The well-to-wheel carbon footprint of the van powered by bio-, CO_2-, or fossil-based HyFiT-fuel as function of the carbon footprint of electricity. Since there are multiple production routes for each feedstock (see Section 4.1.3), we show colored ranges for the feedstock-specific carbon footprints. The lower and upper margin of each range represents the supply chain with the lowest and highest carbon footprint. Benchmark results of diesel and the BEV are additionally shown. At the top, exemplary carbon footprints are shown for various electricity supplies. Results are shown for (A) HyFiT-20% with closed-gas-loop design, (B) HyFiT-40% with open-gas-loop design, and (C) HyFiT-40% with closed-gas-loop design. As engine calibration, "same engine-out PM as diesel" is considered (see Figure 4.6). EU: European Union, GLO: global.

B.5.2 Limited feedstock availability

In Figure B.16, we compare biomass consumption of bio-based HyFiT-fuel with recent studies on bio-based FT fuels and bioethanol. Numerical values of considered studies are listed in Table B.14.

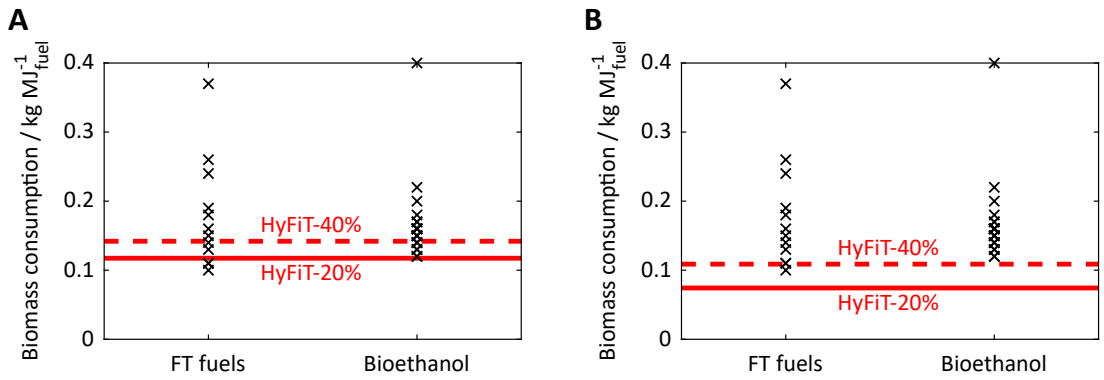

Figure B.16: Biomass consumption of bio-based HyFiT-20% (solid, red line) and HyFiT-40% (dashed, red line) compared to studies on FT fuels and bioethanol (X). HyFiT-fuel is produced with (A) open or (B) closed gas loop. For numerical values of biomass consumptions of FT fuels and bioethanol, see Table B.14.

Table B.14: Biomass consumption per MJ of fuel of HyFiT-fuels and derived from studies on FT fuels and bioethanol.

Fuel	**Biomass consumption** $kg_{Biomass}\,MJ^{-1}_{Fuel}$	**Author**
HyFiT-20%		
Open gas loop	0.12	This study
Closed gas loop	0.07	This study
HyFiT-40%		
Open gas loop	0.14	This study
Closed gas loop	0.11	This study
FT fuel	0.37	Lundberg et al. (2020)
	0.26	Okeke et al. (2020)
	0.11	Dimitriou et al. (2018)
	0.24	Neuling and Kaltschmitt (2018)
	0.18	Neuling and Kaltschmitt (2018)
	0.15	Zhang et al. (2018b)
	0.16	Albrecht et al. (2017)
	0.13	Rafati et al. (2017)
	0.14	Rafati et al. (2017)
	0.10	Snehesh et al. (2017)
	0.19	Snehesh et al. (2017)
	0.11	Zhou et al. (2017)
Bioethanol	0.17	Wang et al. (2013)
	0.15	Wang et al. (2013)
	0.16	Wang et al. (2013)
	0.18	Wang et al. (2013)
	0.16	Daylan and Ciliz (2016)
	0.16	González-García et al. (2010)
	0.15	González-García et al. (2010)
	0.12	González-García et al. (2010)
	0.13	González-García et al. (2012)
	0.14	Borrion et al. (2012)
	0.40	Papong and Malakul (2010)
	0.16	Sims et al. (2010)
	0.20	Sassner et al. (2008)
	0.22	Sassner et al. (2008)
	0.16	Sassner et al. (2008)
	0.15	Piccolo and Bezzo (2009)
	0.16	da Silva et al. (2016)
	0.14	Gnansounou and Dauriat (2010)
	0.15	Gnansounou and Dauriat (2010)

B.5.3 Contribution analyses

In the following, contribution analyses of HyFiT-20% and HyFiT-40% are presented for electricity from either wind power or the grid.

B.5.3.1 HyFiT-20% with electricity from wind power

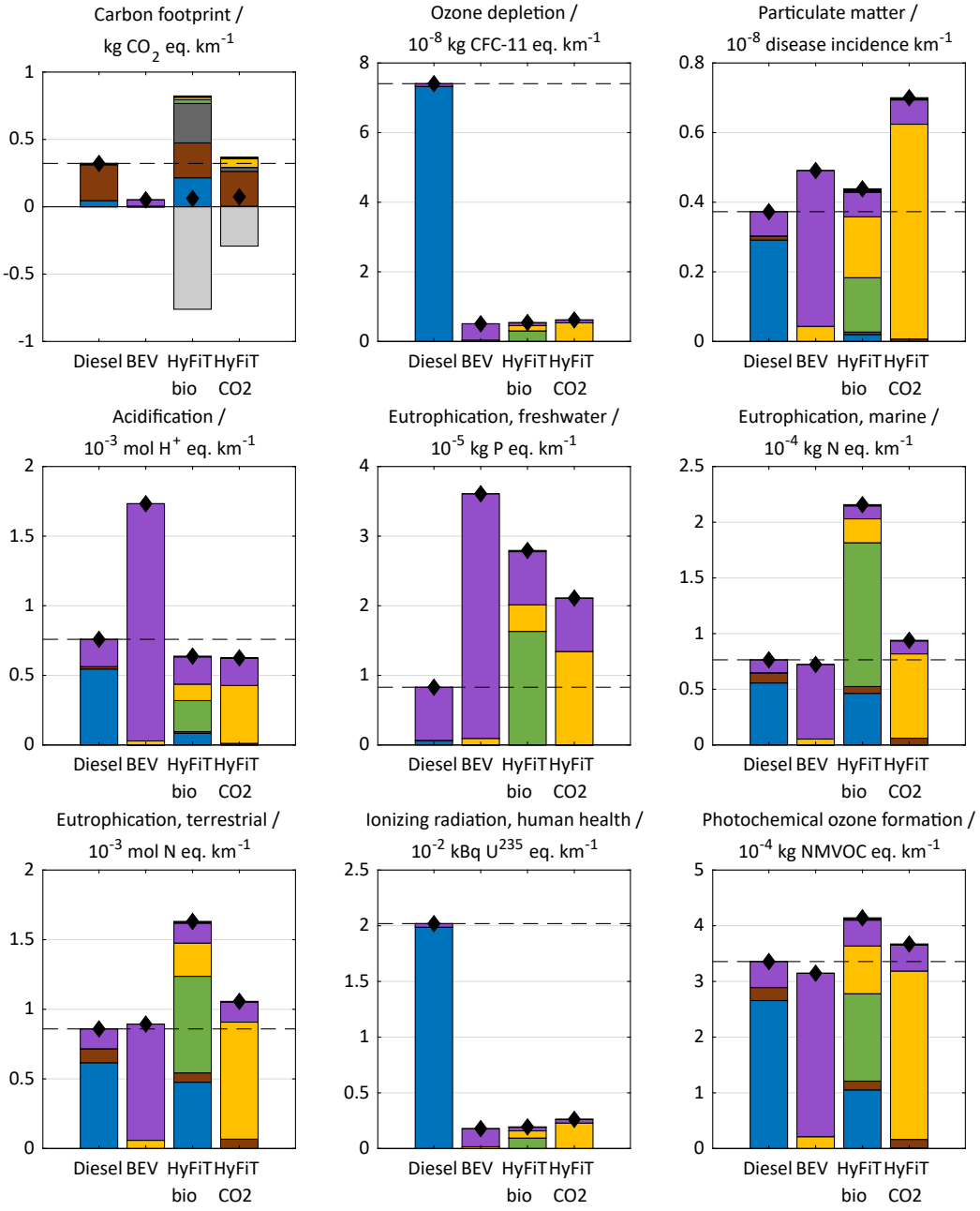

Figure B.17: Contribution analyses for the well-to-wheel environmental impacts of the benchmarks diesel and BEV as well as bio- and CO_2-based HyFiT-20%. The results are shown for the feedstock-specific optimal supply chain with electricity from wind power, open-gas-loop design, and the engine calibration "same engine-out PM as diesel." For the ease of comparison, the dashed, horizontal line indicates the environmental impact of diesel, and the net impact is shown as black diamond.

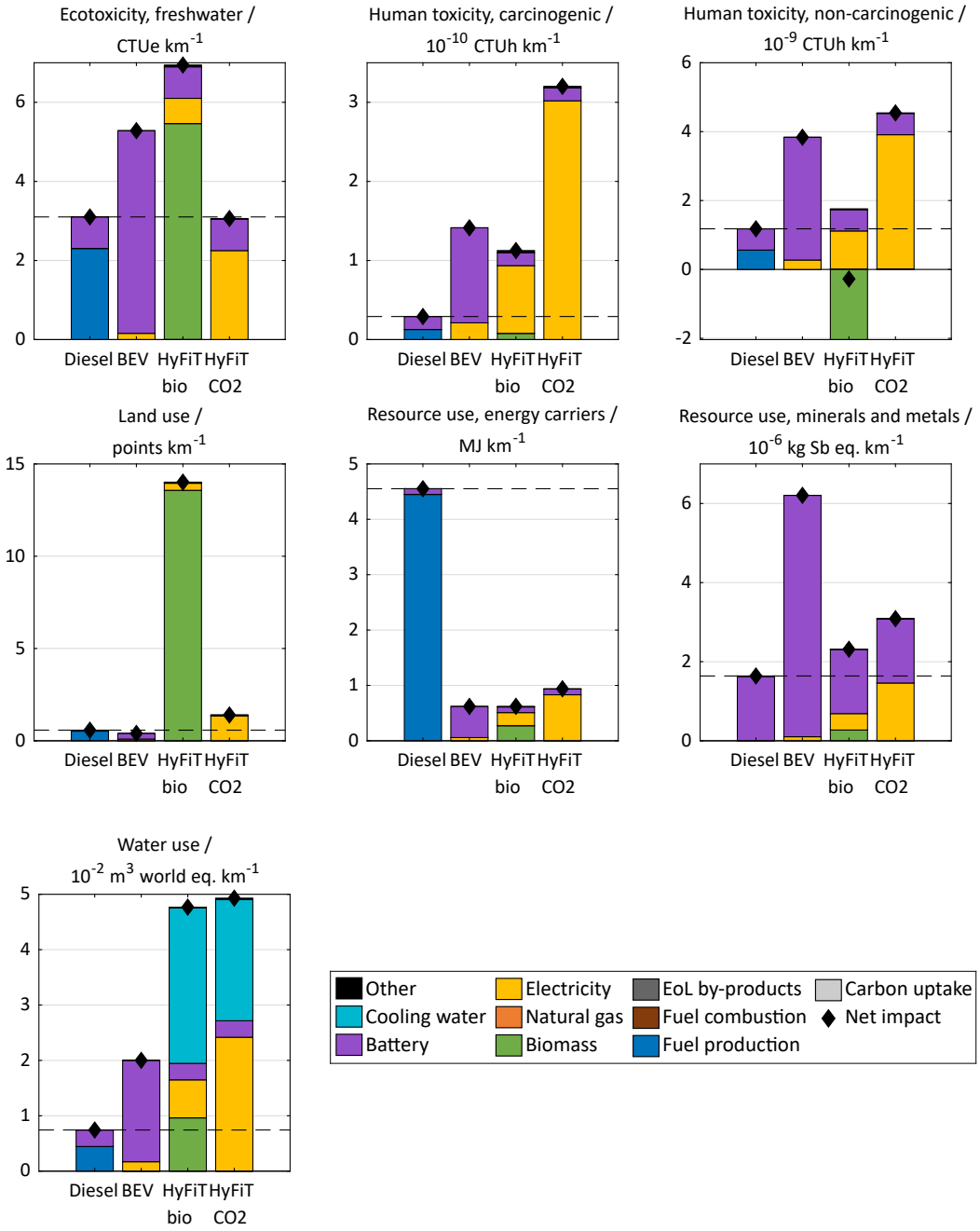

Figure B.17: Continued.

B.5.3.2 HyFiT-20% with electricity from the grid

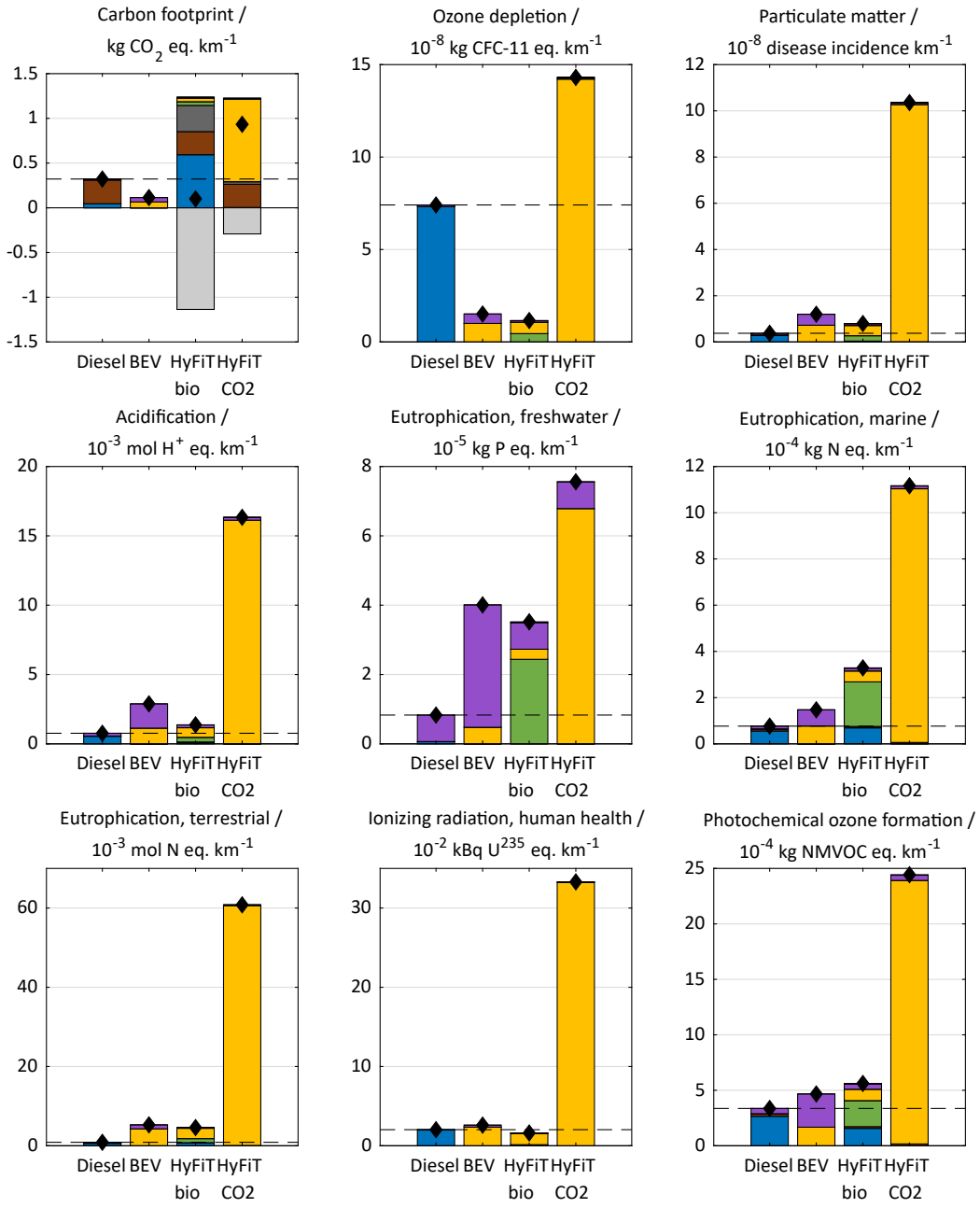

Figure B.18: Contribution analyses for the well-to-wheel environmental impacts of the benchmarks diesel and BEV as well as bio- and CO_2-based HyFiT-20%. The results are shown for the feedstock-specific optimal supply chain with electricity from the grid, open-gas-loop design, and the engine calibration "same engine-out PM as diesel." For the ease of comparison, the dashed, horizontal line indicates the environmental impact of diesel, and the net impact is shown as black diamond.

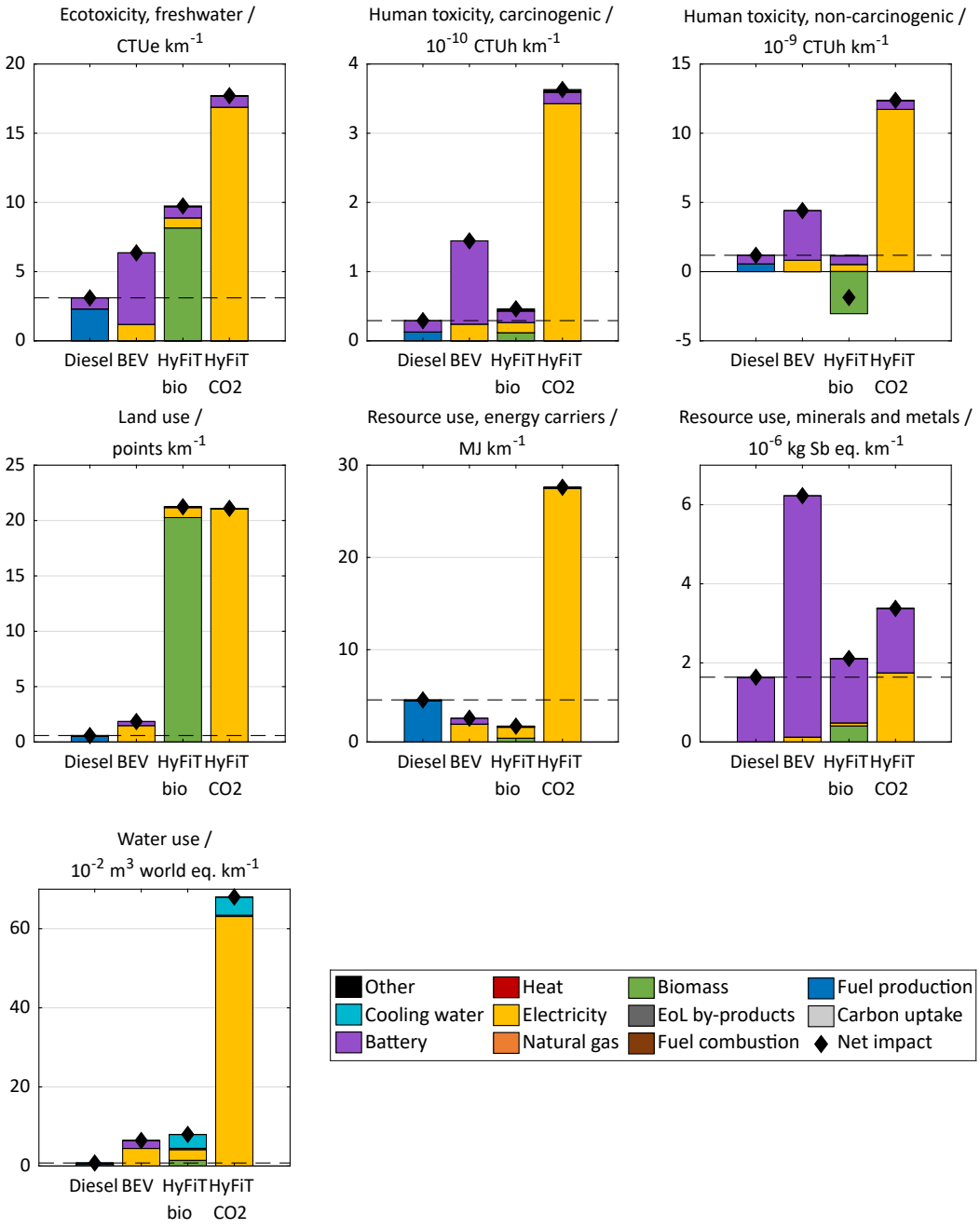

Figure B.18: Continued.

B.5.3.3 HyFiT-40% with electricity from wind power

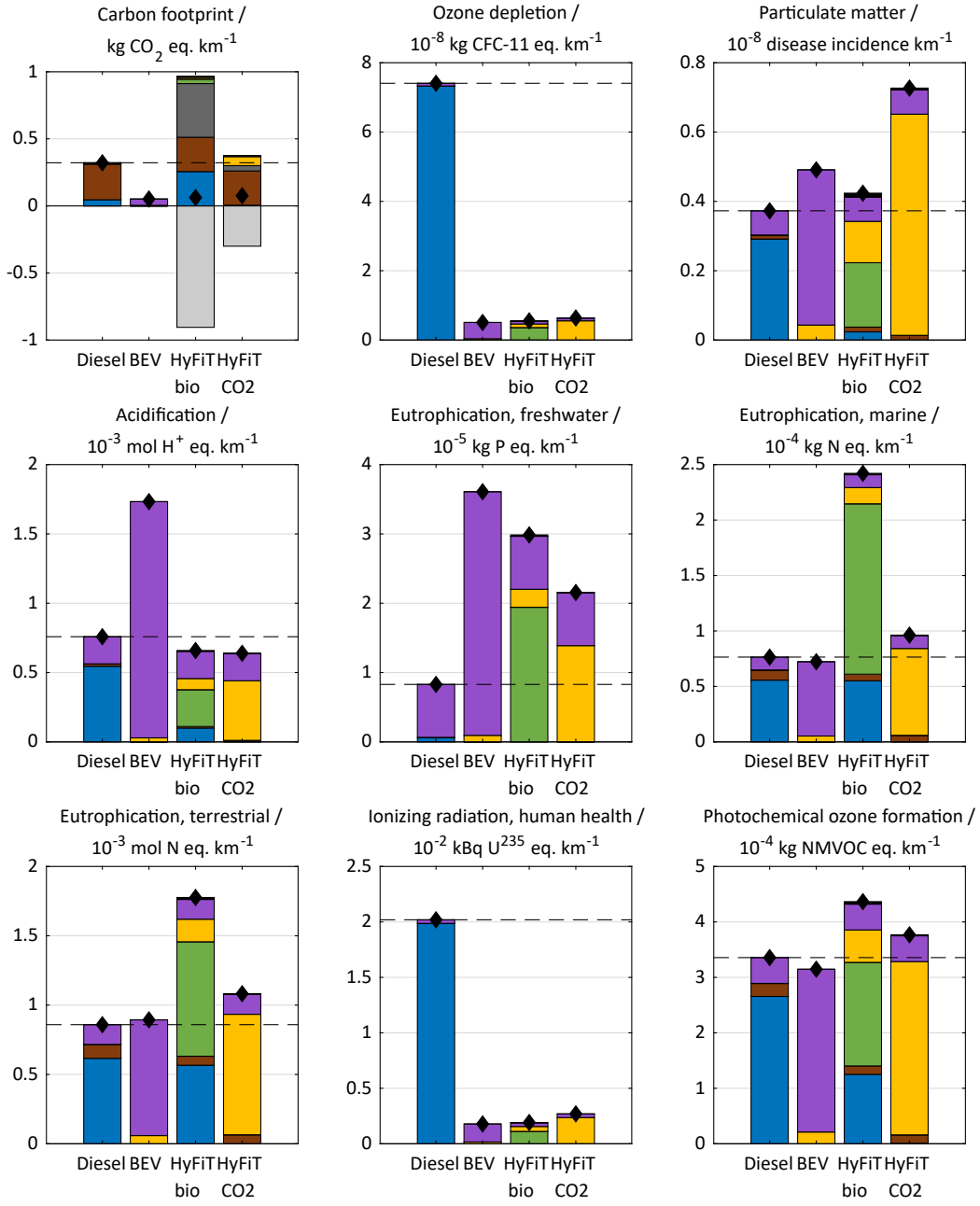

Figure B.19: Contribution analyses for the well-to-wheel environmental impacts of the benchmarks diesel and BEV as well as bio- and CO_2-based HyFiT-40%. The results are shown for the feedstock-specific optimal supply chain with electricity from wind power, open-gas-loop design, and the engine calibration "same engine-out PM as diesel." For the ease of comparison, the dashed, horizontal line indicates the environmental impact of diesel, and the net impact is shown as black diamond.

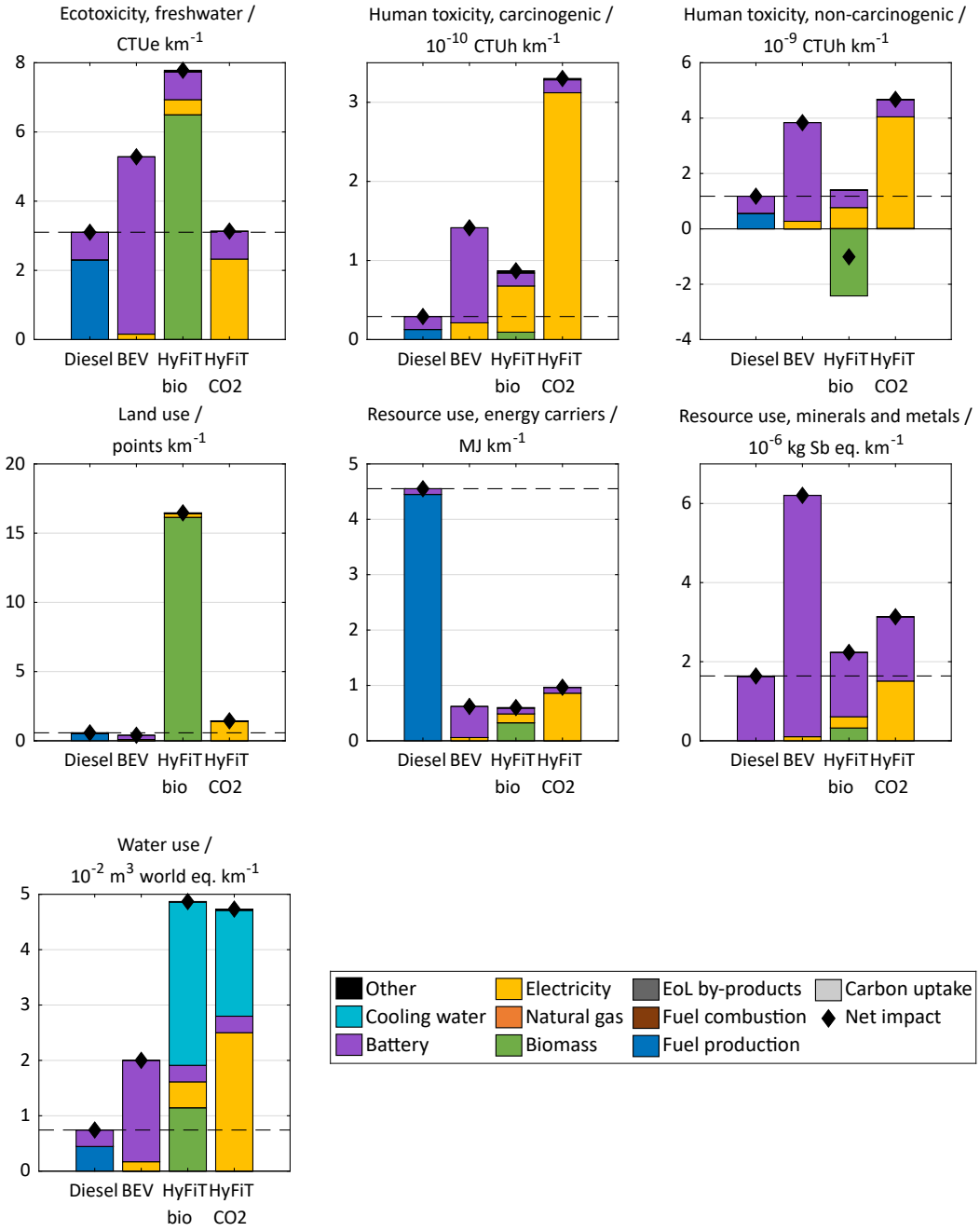

Figure B.19: Continued.

B.5.3.4 HyFiT-40% with electricity from the grid

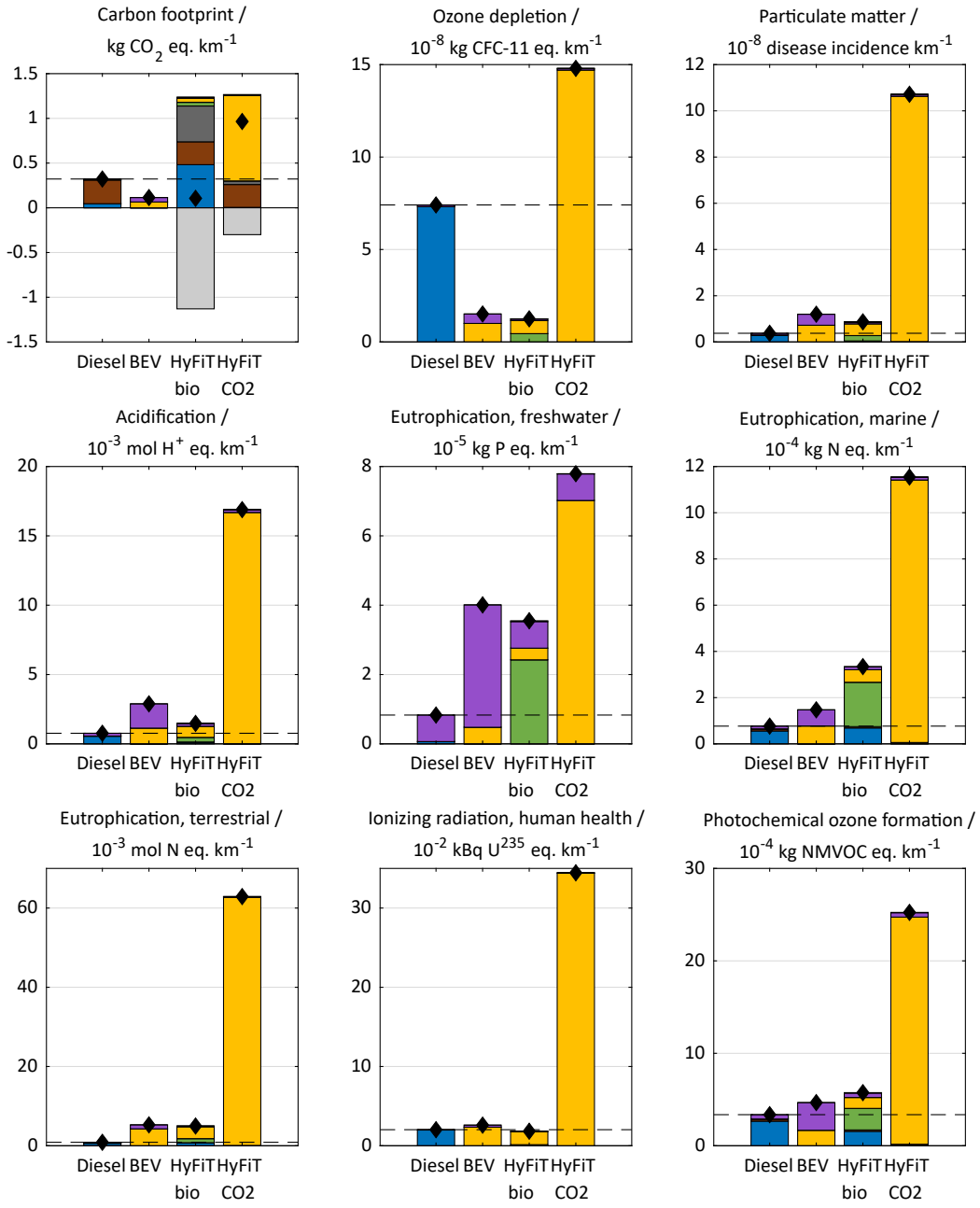

Figure B.20: Contribution analyses for the well-to-wheel environmental impacts of the benchmarks diesel and BEV as well as bio- and CO_2-based HyFiT-40%. The results are shown for the feedstock-specific optimal supply chain with electricity from the grid, open-gas-loop design, and the engine calibration "same engine-out PM as diesel." For the ease of comparison, the dashed, horizontal line indicates the environmental impact of diesel, and the net impact is shown as black diamond.

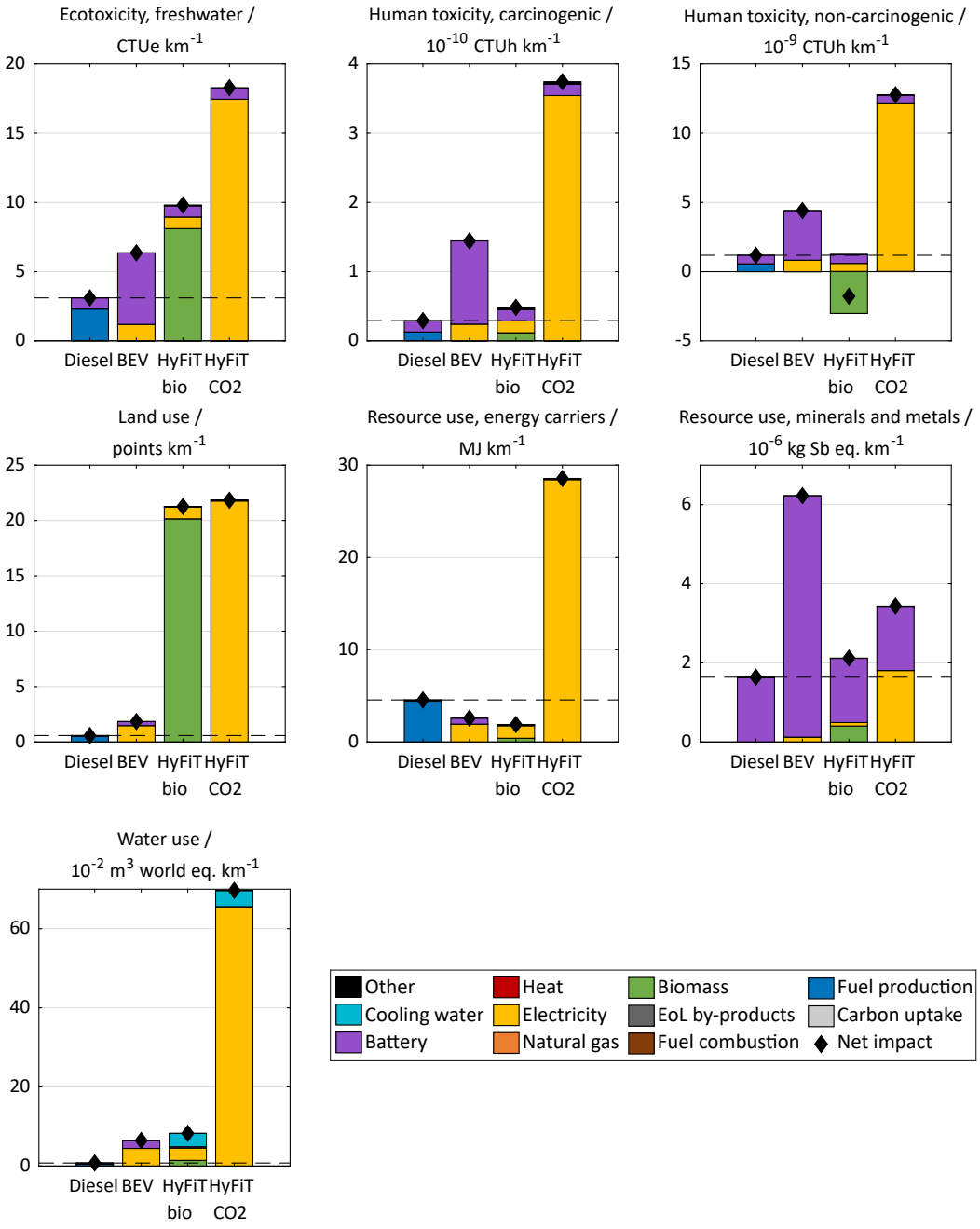

Figure B.20: Continued.

B.5.4 Sensitivity analyses

Here, we present sensitivity analyses for the BEV, LUC emissions, and the removal of aromatics and oxygenates.

B.5.4.1 Battery-electric van

For the BEV, we vary the battery lifetime and capacity in Figure B.21 to assess the sensitivity of the BEV's carbon footprint towards both parameters. In this sensitivity analysis, battery lifetime is reduced from 200,000 km (default) to 100,000 km and 50,000 km, requiring two to four batteries instead of one battery per vehicle lifetime of 200,000 km (default). Separately, battery capacity is increased from 153 kWh (default) to 200 kWh and 300 kWh, accounting for higher driving ranges of 562 km to 843 km instead of 430 km (default). With increases of 0.04-0.07 kg CO_2 eq. km^{-1}, both parameters have only minor influence on the carbon footprint of the BEV. However, the BEV's carbon footprint increases substantially by 0.14-0.19 kg CO_2 eq. km^{-1} if a battery lifetime of 50,000 km and battery capacity of 300 kWh are considered simultaneously.

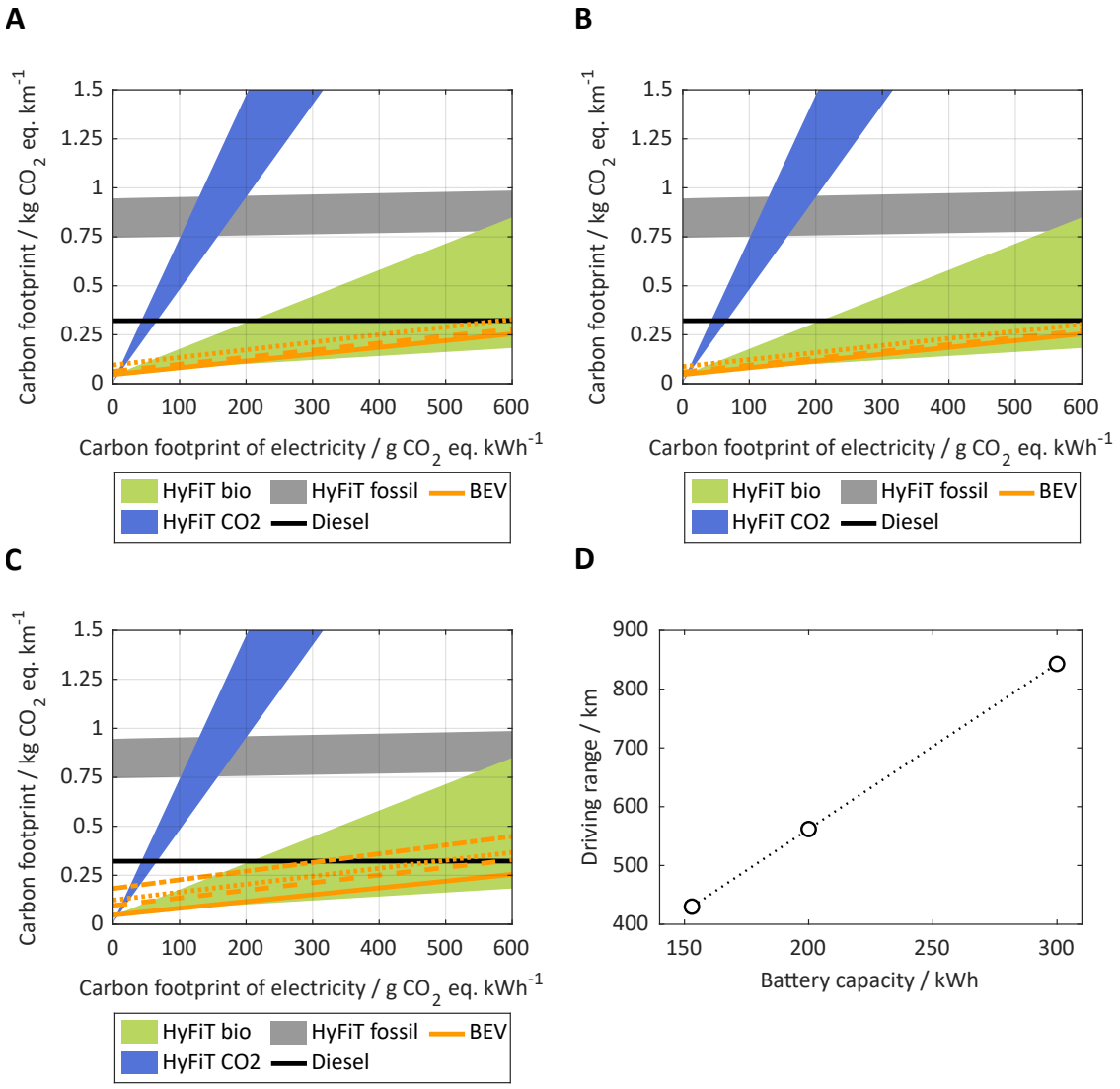

Figure B.21: Sensitivity analysis of the well-to-wheel carbon footprint of the BEV as function of the carbon footprint of electricity. In all sensitivity analyses, the total BEV driving mass of 3.3 t is maintained for consistency with the testing vehicle. The default BEV (battery lifetime of 200,000 km, battery capacity of 153 kWh) is shown as solid yellow line. (A) Battery lifetime is varied to 100,000 km (dashed) and 50,000 km (dotted), with default battery capacity. (B) Battery capacity is varied to 200 kWh (dashed) and 300 kWh (dotted), with default battery lifetime. (C) Battery capacity is varied to 153 kWh (dashed), 200 kWh (dotted), and 300 kWh (dash-dotted), with a battery lifetime of 50,000 km. (D) Driving range of the BEV as function of the battery capacity.

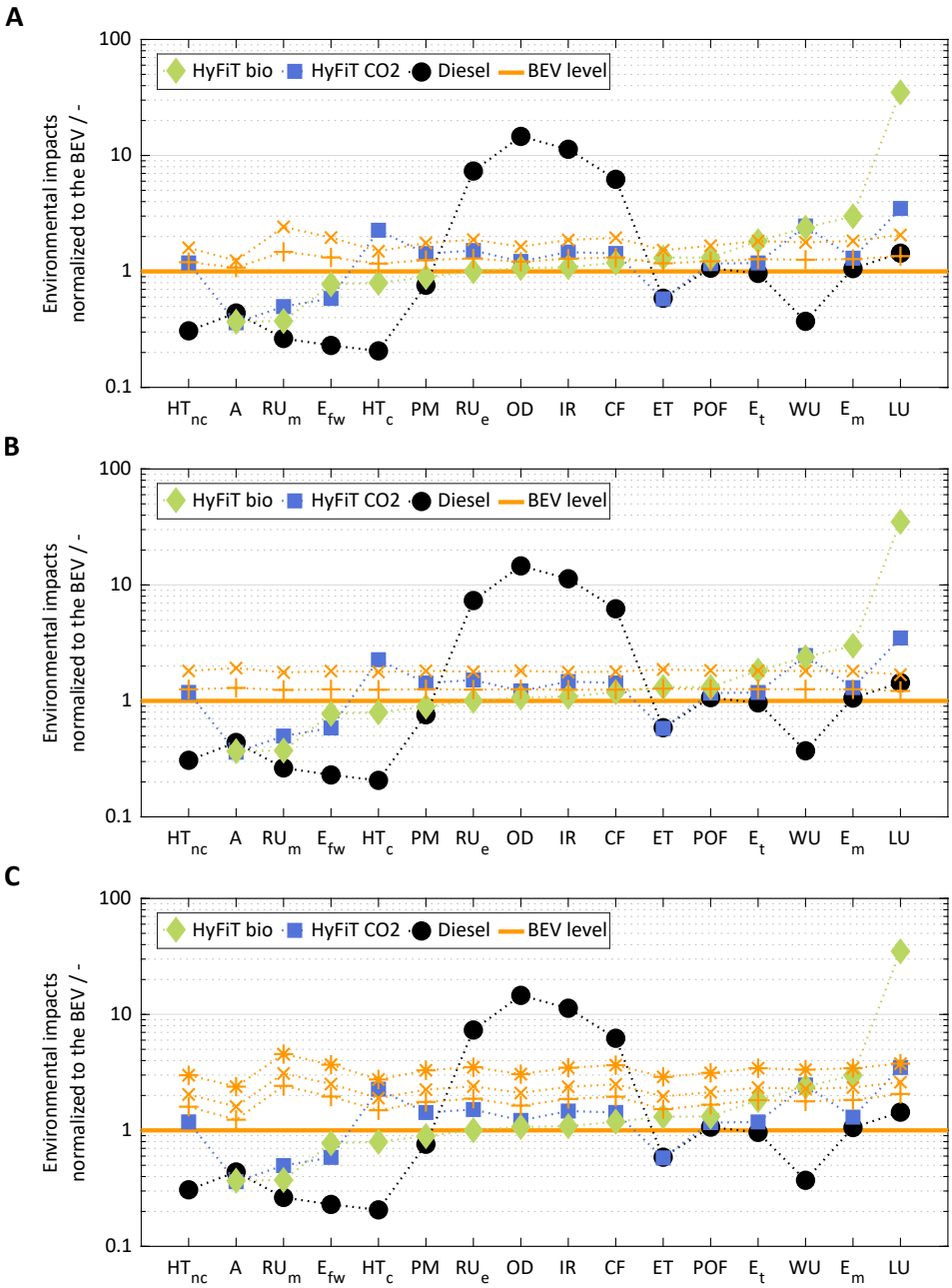

Figure B.22: Sensitivity analysis of the well-to-wheel environmental impacts of the BEV normalized to the environmental impacts of the default BEV. Results are shown for electricity from wind power. In all sensitivity analyses, the total BEV driving mass of 3.3 t is maintained for consistency with the testing vehicle. The default BEV (battery lifetime of 200,000 km, battery capacity of 153 kWh) is shown as solid yellow line. (A) Battery lifetime is varied to 100,000 km (plus) and 50,000 km (x), with default battery capacity. (B) Battery capacity is varied to 200 kWh (plus) and 300 kWh (x), with default battery lifetime. (C) Battery capacity is varied to 153 kWh (plus), 200 kWh (x), and 300 kWh (asterisk), with a battery lifetime of 50,000 km.

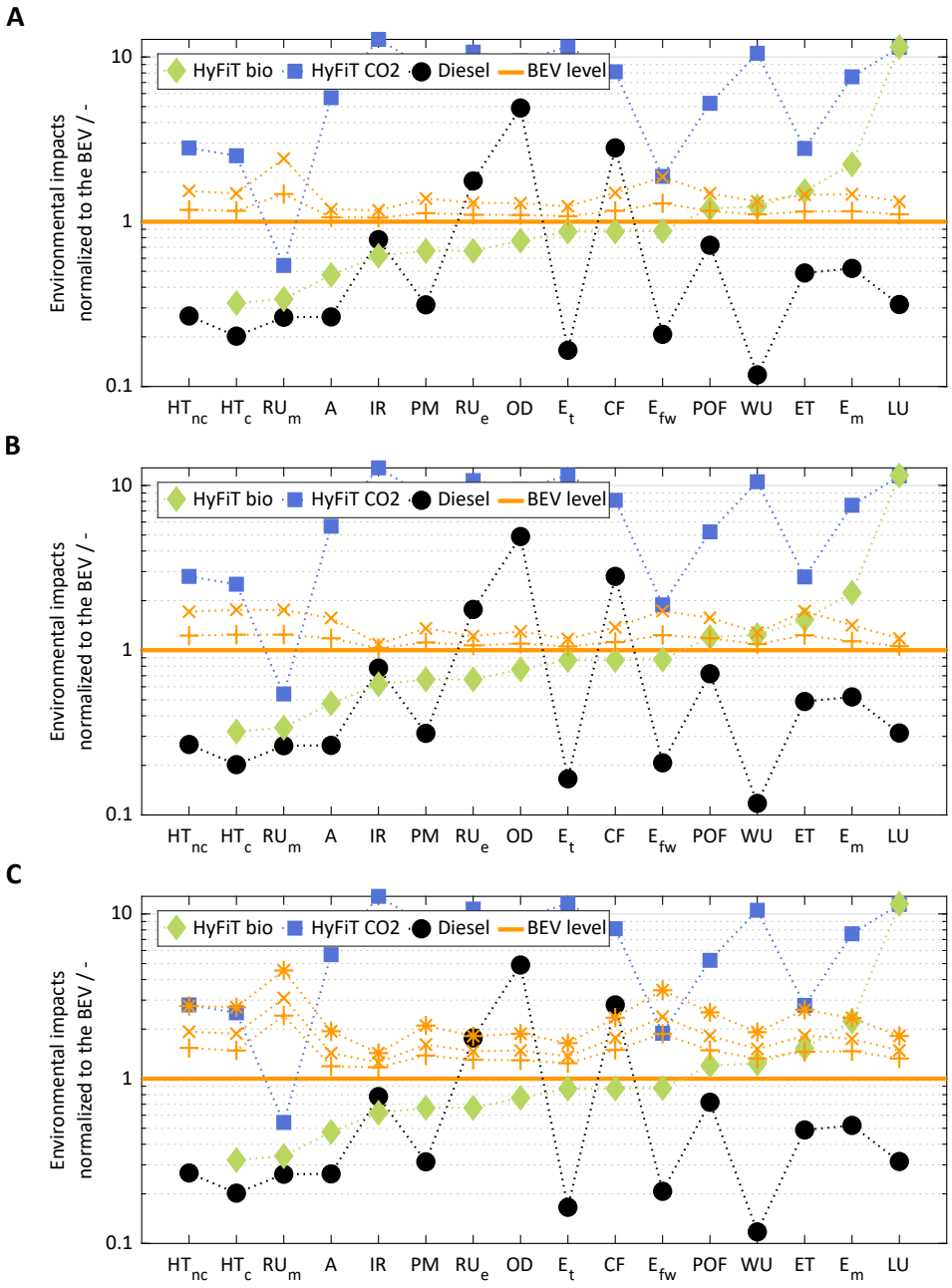

Figure B.23: Sensitivity analysis of the well-to-wheel environmental impacts of the BEV normalized to the environmental impacts of the default BEV. Results are shown for electricity from the grid. In all sensitivity analyses, the total BEV driving mass of 3.3 t is maintained for consistency with the testing vehicle. The default BEV (battery lifetime of 200,000 km, battery capacity of 153 kWh) is shown as solid yellow line. (A) Battery lifetime is varied to 100,000 km (plus) and 50,000 km (x), with default battery capacity. (B) Battery capacity is varied to 200 kWh (plus) and 300 kWh (x), with default battery lifetime. (C) Battery capacity is varied to 153 kWh (plus), 200 kWh (x), and 300 kWh (asterisk), with a battery lifetime of 50,000 km.

B.5.4.2 Land-use change emissions

Here, we present the sensitivity analysis for LUC emissions of biomass. In this sensitivity analysis, we vary LUC emissions from −0.15 to 0.10 kg CO_2 eq. per kg of biomass. We derived this range from the carbon calculator for LUC from biofuels production that is part of the GREET model by the Argonne National Laboratory (Kwon et al., 2021). Overall, LUC emissions have only minor influence on the carbon footprint of bio-based HyFiT-fuel: LUC emissions add GHG emissions in the range of −0.07 to 0.04 kg CO_2 eq. km^{-1} to the overall carbon footprint. Thus, the overall carbon footprint of bio-based HyFiT-fuel is still in the range of the BEV and can even become negative for clean electricity supplies and negative LUC emissions. Note though that LUC emissions are subject to uncertainty.

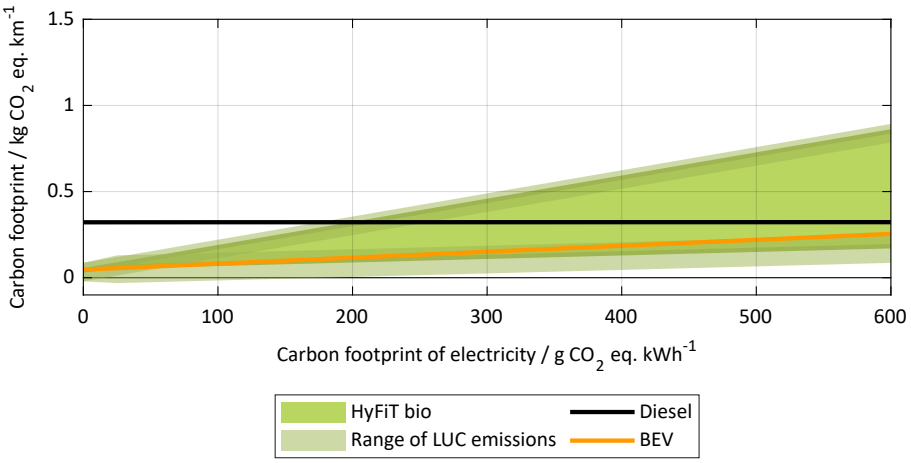

Figure B.24: The well-to-wheel carbon footprint with LUC emissions of bio-based HyFiT-fuel as function of the carbon footprint of electricity. Benchmark results of diesel and the BEV are additionally shown. The range of varied LUC emissions of biomass is depicted in light green.

B.5.4.3 Removal of aromatics and oxygenates

Since we estimate the removal of aromatics and oxygenates during HyFiT-fuel production with proxy process data, we quantify the degree of uncertainty that our estimation implies on the carbon footprint of HyFiT-fuels by varying the quantity and temperature level of heat consumption of the proxy process. For all variations of quantity and temperature level of heat consumption, the feedstock-specific supply chain is again optimized for minimal carbon footprint, followed by pinch-based heat integration. The carbon footprints of the supply chain optimizations with varied parameters are presented as heatmap and relative to the carbon footprint of the base case. For reference, we also present the average and the maximum heat consumption of EU refineries (European Commission, 2015) and the boiling temperature range of VGO (Riazi et al., 2013) as dashed vertical and horizontal lines, respectively.

The sensitivity analysis shows that the carbon footprint of HyFiT-fuels is only slightly sensitive towards the amount and temperature level of heat consumption of the proxy process. The largest increase is observed for the carbon-footprint-optimal supply chain of bio-based HyFiT-fuel with electricity from the EU 2030 power grid (Figure B.26). In this case, the carbon footprint is increased by 14 % to 0.114 kg CO_2 eq. km^{-1}.

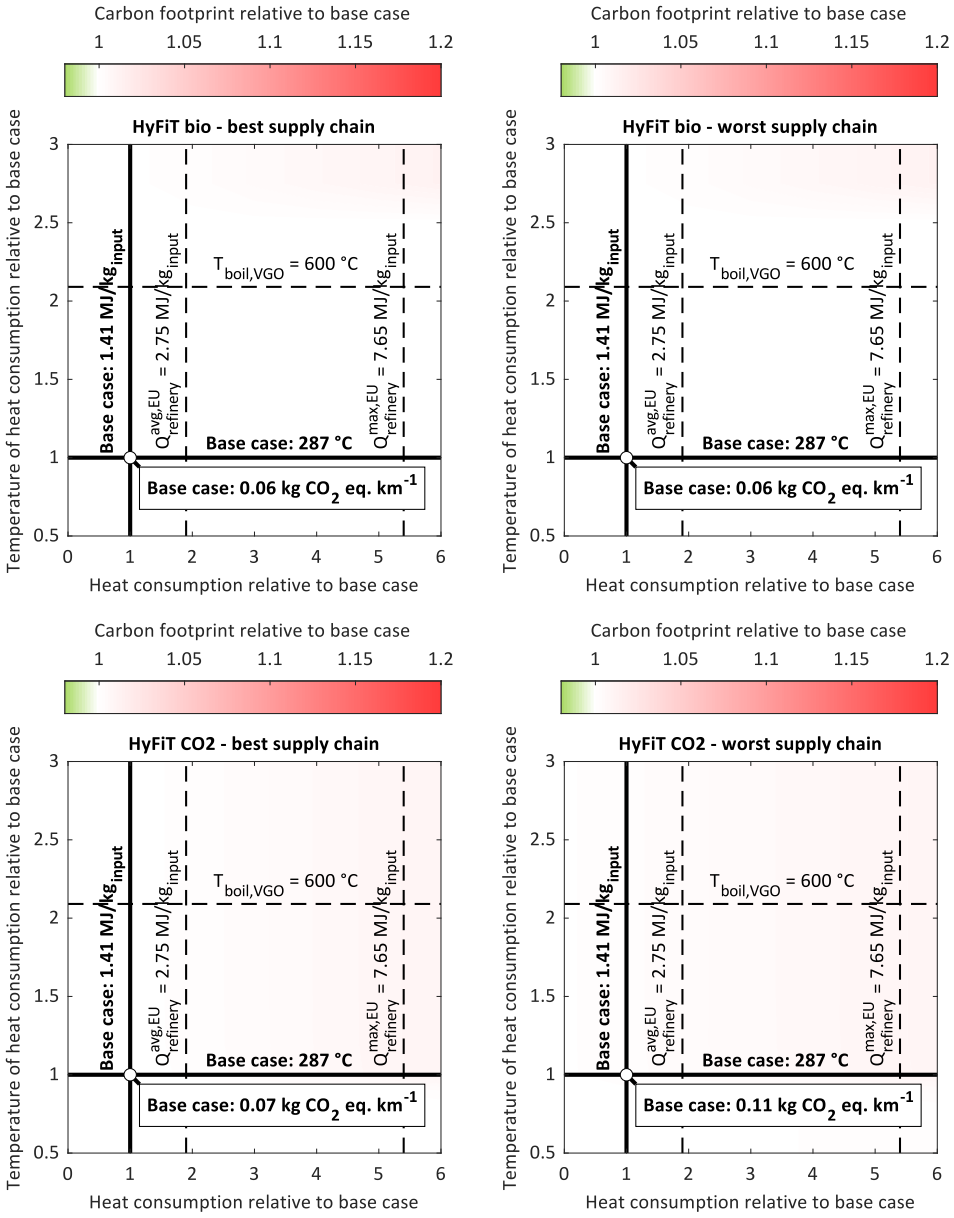

Figure B.25: Sensitivity analysis of the quantity and temperature level of heat consumption for the removal of aromatics and oxygenates. Results are shown for the supply chain design with electricity from wind power, HyFiT-20%, and the open-gas-loop design (see Figure 4.7A). For each data point, a supply chain optimization followed by pinch-based heat integration was performed. The used proxy data based on the utility requirements of the "UOP Sulfolane process" are shown as bold horizontal and vertical line (base case). The carbon footprint of this base case is shown in the rectangular box at the intersection of the bold horizontal and vertical line. For reference, we present the average and the maximum heat consumption of EU refineries (European Commission, 2015) and the boiling temperature range of VGO (Riazi et al., 2013) as dashed vertical and horizontal lines, respectively.

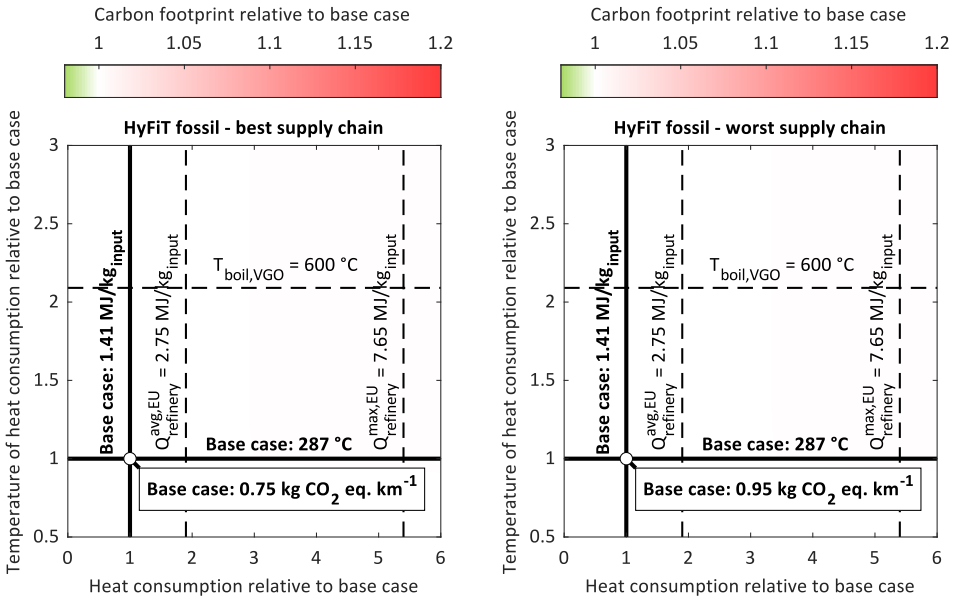

Figure B.25: Continued.

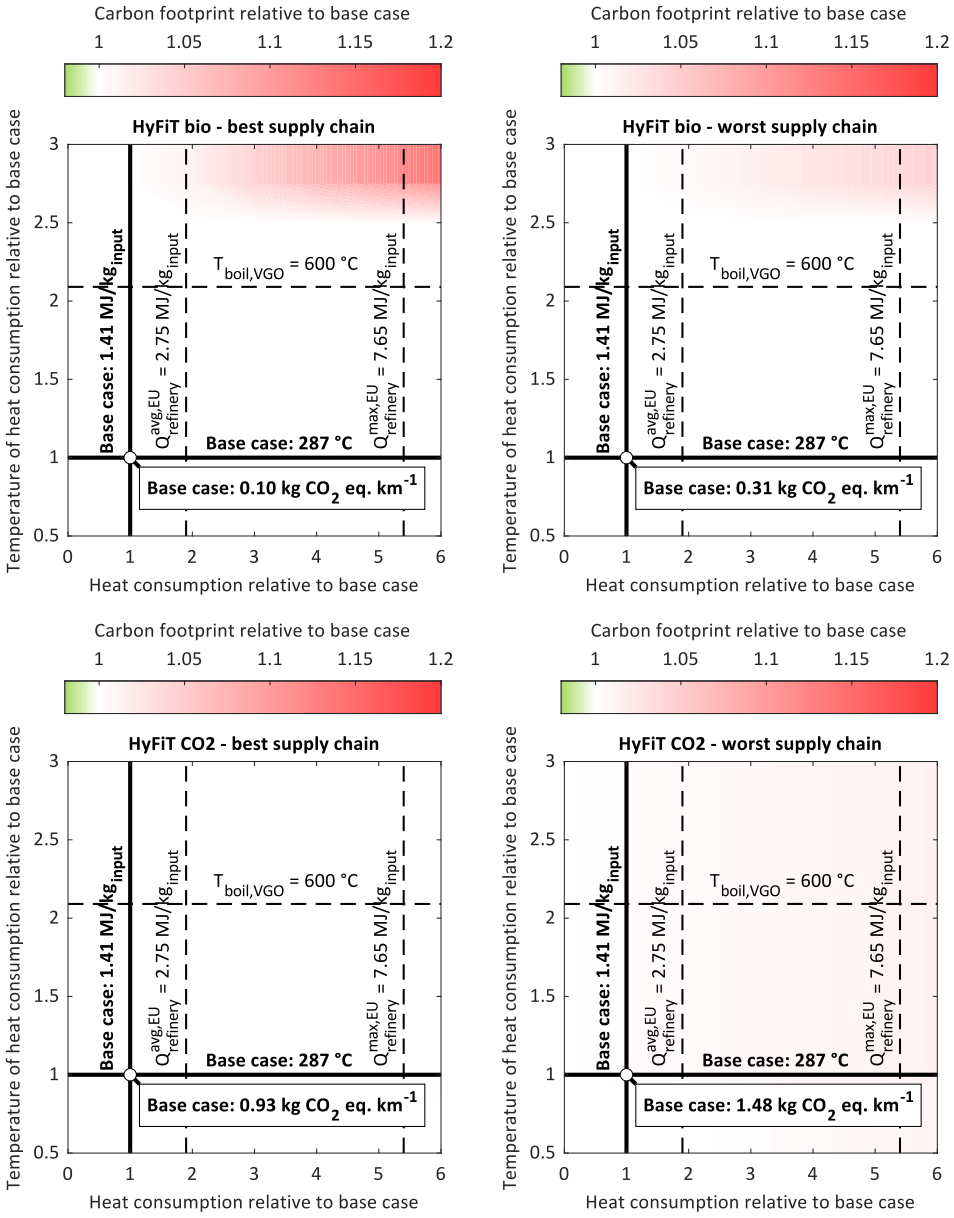

Figure B.26: Sensitivity analysis of the quantity and temperature level of heat consumption for the removal of aromatics and oxygenates. Results are shown for the supply chain design with electricity from the grid, HyFiT-20%, and the open-gas-loop design (see Figure 4.7A). For each data point, a supply chain optimization followed by pinch-based heat integration was performed. The used proxy data based on the utility requirements of the "UOP Sulfolane process" are shown as bold horizontal and vertical line (base case). The carbon footprint of this base case is shown in the rectangular box at the intersection of the bold horizontal and vertical line. For reference, we present the average and the maximum heat consumption of EU refineries (European Commission, 2015) and the boiling temperature range of VGO (Riazi et al., 2013) as dashed vertical and horizontal lines, respectively.

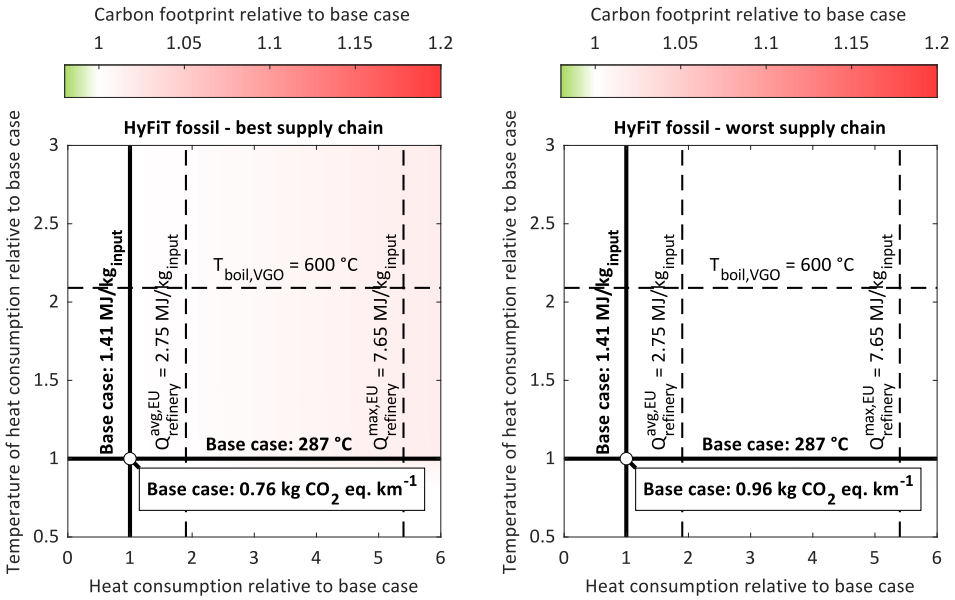

Figure B.26: Continued.

B.5.5 Carbon efficiency

Here, we analyze the carbon efficiency as common key performance indicator (Figure B.27). The carbon efficiency η_C is calculated as the ratio of carbon in the product $n_{C,prod}$, i.e., the HyFiT-fuel, and carbon in the input $n_{C,in}$, i.e., the used feedstock:

$$\eta_C = \frac{n_{C,prod}}{n_{C,in}}. \tag{B.20}$$

Benchmarking ourselves with recent studies on FT-fuels (Figure B.27, crosses), we find that the carbon efficiency is at least on par or even exceeds previous FT-fuels, in particular for the bio-based route. Due to the unexplored potential for process optimization, we expect that even higher efficiencies can be targeted in proceeding studies.

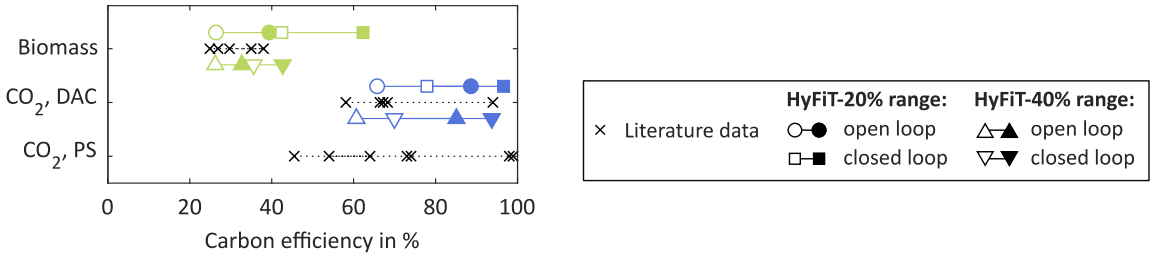

Figure B.27: Carbon efficiency of HyFiT-fuels based on biomass or CO_2 (via DAC), with alcohol contents of 20 wt% or 40 wt% as well as either open or closed gas loop design. DAC: direct air capture, PS: point source. See Table B.15 for an overview of the considered literature studies.

Table B.15: Carbon efficiencies of bio- or CO_2-based FT-fuels from literature.

Feedstock	**Carbon efficiency**	**Author**
Biomass	30	Zhang et al. (2018b)
	35	Neuling and Kaltschmitt (2018)
	38	Neuling and Kaltschmitt (2018)
	25	Albrecht et al. (2017)
	27	Dietrich et al. (2018)
CO_2, direct air capture	58	Marchese et al. (2021)
	68	Marchese et al. (2021)
	67	Marchese et al. (2021)
	66	Marchese et al. (2021)
	94	Vázquez et al. (2018d)
CO_2, point source	46	Zang et al. (2021a)
	64	Herz et al. (2021)
	54	Herz et al. (2021)
	73	König et al. (2015b)
	74	König et al. (2015a)
	98	Albrecht et al. (2017)
	99	Dietrich et al. (2018)

Appendix C

Supporting information to Chapter 5

In the following, we present further details for Chapter 5. In Section C.1, recent LCAs on $OME_{3\text{-}5}$ are described. Additional information on the life cycle inventory of $OME_{3\text{-}5}$ is presented in Section C.2. The calculations of the fleet analysis are explained in Section C.3 while details on the emission measurements are given in Section C.4. Section C.5 concludes with additional results of the life cycle impact assessment.

C.1 Introduction

So far, only few LCA studies have been conducted on $OME_{3\text{-}5}$. While all studies confirm that the well-to-wheel GHG emissions largely depend on the electricity source for e-fuel production, each study focuses on specific phases of the entire $OME_{3\text{-}5}$ life cycle or on selected environmental impact categories. Moreover, only one of the studies considers a blend of $OME_{3\text{-}5}$ and fossil diesel besides pure $OME_{3\text{-}5}$.

Bokinge et al. (2020) have conducted a well-to-tank LCA for the carbon footprint of pure $OME_{3\text{-}5}$ from biomass gasification as well as of an e-fuel route from CO_2 and H_2. Their study focuses solely on fuel production, while any use-phase emissions from fuel combustion remain uninvestigated. Mahbub et al. (2017) have analyzed the well-to-wheel carbon footprint and soot emissions of $OME_{3\text{-}5}$ production from biomass-derived synthesis gas. The study includes the combustion of pure $OME_{3\text{-}5}$ and a blend with 10 vol% of $OME_{3\text{-}5}$ in fossil diesel on the basis of tests on a chassis dynamometer with a Euro-2 diesel passenger car (Pellegrini et al., 2013). Combustion-related NO_x emissions have not been investigated. Mahbub et al. (2017) state that blending 10 vol% of biomass-derived $OME_{3\text{-}5}$ in fossil diesel may reduce GHG and soot emissions by 5 % and 30 %, respectively, in comparison with fossil diesel.

Hank et al. (2019) have conducted a well-to-wheel LCA for pure $OME_{3\text{-}5}$. Their study focuses on $OME_{3\text{-}5}$ production via methanol and FA by dehydrogenation of methanol based on the process concept developed by Ouda et al. (2017, 2018a,b). Hank et al. (2019) evaluate the production phase in detail and show that the electricity supply for H_2 production via electrolysis has a particularly strong influence on the carbon footprint of fuel production. For fuel combustion, proxy data from the LCA database ecoinvent were used (Wernet et al., 2016), neglecting the environmental promises of combustion research that OMEs enable lower NO_x emissions than diesel (Omari et al., 2019, 2017a; Richter and Zellbeck, 2017). The authors' best-case scenario shows that pure $OME_{3\text{-}5}$ can reduce the carbon footprint compared to fossil diesel, while respiratory effects and photochemical ozone formation are the same for both fuels.

Rodríguez-Vallejo et al. (2021) compared $OME_{3\text{-}5}$ production for multiple energy and raw material sources to fossil diesel in an economic and environmental assessment from well-to-wheel. The production of $OME_{3\text{-}5}$ is based on methanol and FA by partial oxidation of methanol. The use phase of $OME_{3\text{-}5}$ is based on the study of Hank et al. (2019), where only pure $OME_{3\text{-}5}$ is analyzed. With these data, Rodríguez-Vallejo et al. (2021) show that $OME_{3\text{-}5}$ can reduce GHG emissions compared to fossil diesel, as expected from previous studies. Contrary to indications from engine measurements (Omari et al., 2019), they assume higher NO_x emissions from fuel combustion for $OME_{3\text{-}5}$ than for fossil diesel and conclude that $OME_{3\text{-}5}$ increases particulate matter and ozone formation compared to fossil diesel. The assumption of higher NO_x emissions from $OME_{3\text{-}5}$ combustion may, however, influence their conclusion strongly, since NO_x emissions contribute not only to photochemical ozone formation but also, as a secondary precursor, to particulate matter formation.

C.2 Life cycle inventory

In this section, the LCI of all $OME_{3\text{-}5}$ production routes and the LCA datasets for the background system are presented. The LCI for $OME_{3\text{-}5}$ production routes is shown as modified for our analyses and as heat-integrated. Heat integration has been performed or recalculated, where necessary due to our modifications (see Section 5.3).

C.2.1 Characteristics of $OME_{3\text{-}5}$ routes

Dependent on whether water coexists in the final process step of $OME_{3\text{-}5}$ formation, $OME_{3\text{-}5}$ routes can be divided into two types: anhydrous and aqueous routes (see Figure 5.2). In the aqueous routes, the production of water during $OME_{3\text{-}5}$ production is disadvantageous. First, it lowers the $OME_{3\text{-}5}$ yield as undesired side products are formed (Maurer, 1986) and equilibrium conversion is shifted towards the reactants (Schmitz et al., 2015b). Second, water complicates product separation due to similar physio-chemical properties between water and OME_2 and the formation of azeotropes (Burger et al., 2010). Promising solutions for water removal, e. g., membranes, are however in investigation (Schmitz et al., 2017). An advantage of the aqueous routes is the direct use of methanol and formaldehyde (FA) for the production of $OME_{3\text{-}5}$. The anhydrous routes are advantageous as water is absent during $OME_{3\text{-}5}$ formation, making both the reaction and the separation of the final product less complicated. However, a water-free FA source, e. g., trioxane or anhydrous FA, is required, whose production is energy-intensive (Reuss et al., 2000).

C.2.2 Consistency of underlying modeling assumptions

Using data from different authors in a comparative study requires thorough consideration of consistency in the underlying modeling assumptions. Given the following model characteristics, we can conclude that the assumptions of the different process models are similar enough for a comparison. For the reactor models, we used detailed kinetic models where available (methanol, formaldehyde via partial oxidation of methanol, OME_1, $OME_{3\text{-}5}$ from trioxane and OME_1, and $OME_{3\text{-}5}$ from methanol and formaldehyde). Where no detailed kinetic models were available, we used either industrial data (trioxane), experimental data (formaldehyde via dehydrogenation of methanol), or equilibrium-based models if the process is experimentally or industrially close to equilibrium (DME, and $OME_{3\text{-}5}$ from trioxane and DME). For distillation columns, tray-to-tray *RadFrac* AspenPlus models were used everywhere. Overall, the thermodynamic models are based on the work of one research group (Maurer, Albert, Hasse, and Burger), which again speaks for a certain consistency among the models. Finally, for all routes, we recalculated or calculated for the first time, where not yet done in literature, pinch-based heat integration to further improve comparability between the routes.

C.2.3 Anhydrous $OME_{3\text{-}5}$ routes

Trioxane is the most common intermediate for anhydrous $OME_{3\text{-}5}$ production. It is commonly produced industrially from aqueous FA with a low FA conversion of approximately 5 % catalyzed by sulfuric acid (Grützner et al., 2007). To achieve a high overall trioxane yield, high recycle streams are necessary, which result in a high energy demand for separation both by pure distillation (Grützner et al., 2007) and by the conventional but more complex extractive distillation (Mahieux, 1969). The capping source for anhydrous $OME_{3\text{-}5}$ production can either be OME_1 or DME (see Figure 5.2).

$OME_{3\text{-}5}$ production via trioxane and OME_1 (TRI+OME_1) is the most well-known anhydrous route (Table C.1–C.5). OME_1 can be produced from methanol and aqueous FA using established process concepts with an acidic catalyst and a reactive pressure-swing distillation (Weidert et al., 2017). In $OME_{3\text{-}5}$ formation, trioxane first decomposes over an acidic catalyst to molecular FA, which is then incorporated into $OME_{n\text{-}1}$ (Burger et al., 2012). An alternative mechanism is the direct incorporation of trioxane into $OME_{n\text{-}3}$. A high selectivity towards $OME_{3\text{-}5}$ of approximately 70 % can be achieved and its purification via rectification requires only little energy (Wang et al., 2014; Wu et al., 2014, 2015, 2016; Lautenschütz et al., 2017).

Table C.1: Life cycle inventory of methanol production (Bongartz et al., 2019) for the anhydrous route via trioxane and OME_1 (TRI+OME_1) with full heat integration per kg of $OME_{3\text{-}5}$.

Flow	**Value**	**Unit**
In		
H_2	−0.249	kg
CO_2	−1.816	kg
Air	−0.676	kg
Electricity	−1.270	MJ
Out		
MeOH	1.272	kg
Exhaust	0.746	kg
thereof CO_2	0.065	kg

Table C.2: Life cycle inventory of formaldehyde production (Bongartz et al., 2019) for the anhydrous route via trioxane and OME_1 (TRI+OME_1) with full heat integration per kg of $OME_{3\text{-}5}$.

Flow	**Value**	**Unit**
In		
MeOH	−0.850	kg
H_2O	−0.318	kg
H_2O, solvent	−0.080	kg
Air	−2.275	kg
Electricity	−0.155	MJ
Out		
FA, aq (50 wt%)	1.446	kg
Exhaust	2.078	kg
thereof CO_2	0.103	kg

Table C.3: Life cycle inventory of OME_1 production (Bongartz et al., 2019) for the anhydrous route via trioxane and OME_1 (TRI+OME_1) with full heat integration per kg of $OME_{3\text{-}5}$.

Flow	**Value**	**Unit**
In		
MeOH	−0.422	kg
FA, aq (50 wt%)	−0.394	kg
Air	−0.338	kg
Electricity	−0.001	MJ
Out		
OME_1	0.484	kg
Wastewater	0.316	kg
Exhaust	0.355	kg
thereof CO_2	0.028	kg

Table C.4: Life cycle inventory of trioxane production (Burre et al., 2019) for the anhydrous route via trioxane and OME_1 (TRI+OME_1) with full heat integration per kg of $OME_{3\text{-}5}$.

Flow	**Value**	**Unit**
In		
FA, aq (50 wt%)	−1.052	kg
Electricity	−1.036	MJ
Heat at 93 °C	−13.265	MJ
Heat at 128 °C	−5.165	MJ
Out		
TRI	0.515	kg
Wastewater	0.536	kg

Table C.5: Life cycle inventory of $OME_{3\text{-}5}$ production (Burre et al., 2019) for the anhydrous route via trioxane and OME_1 (TRI+OME_1) with full heat integration per kg of $OME_{3\text{-}5}$.

Flow	**Value**	**Unit**
In		
OME_1	−0.484	kg
TRI	−0.515	kg
Out		
$OME_{3\text{-}5}$	1.000	kg

The advantage of producing $OME_{3\text{-}5}$ via trioxane and DME (TRI+DME) is the more direct access to DME from H_2 and CO_2 compared to OME_1 (Table C.6–C.10). Thereby, the methanol and FA production plants are only needed for trioxane production and can thus be smaller. DME can be produced directly from H_2 and CO_2 (Azizi et al., 2014) in a one-step process without producing methanol as an intermediate (Shen et al., 2000). For $OME_{3\text{-}5}$ production from trioxane and DME, a higher energy demand is reported compared to $OME_{3\text{-}5}$ production from trioxane and OME_1, while the production of DME is highlighted as cheaper compared to OME_1 (Breitkreuz et al., 2018).

Table C.6: Life cycle inventory of methanol production (Bongartz et al., 2019) for the anhydrous route via trioxane and DME (TRI+DME) with full heat integration per kg of $OME_{3\text{-}5}$.

Flow	**Value**	**Unit**
In		
H_2	−0.169	kg
CO_2	−1.227	kg
Air	−0.457	kg
Electricity	−0.858	MJ
Out		
MeOH	0.860	kg
Exhaust	0.504	kg
thereof CO_2	0.044	kg

Table C.7: Life cycle inventory of formaldehyde production (Bongartz et al., 2019) for the anhydrous route via trioxane and DME (TRI+DME) with full heat integration per kg of $OME_{3\text{-}5}$.

Flow	**Value**	**Unit**
In		
MeOH	−0.860	kg
H_2O	−0.322	kg
H_2O, solvent	−0.081	kg
Air	−2.301	kg
Electricity	−0.157	MJ
Out		
FA, aq (50 wt%)	1.463	kg
Exhaust	2.102	kg
thereof CO_2	0.104	kg

Table C.8: Life cycle inventory of DME production (Bongartz et al., 2018) for the anhydrous route via trioxane and DME (TRI+DME) with full heat integration per kg of $OME_{3\text{-}5}$.

Flow	**Value**	**Unit**
In		
H_2	−0.076	kg
CO_2	−0.552	kg
Air	−0.091	kg
Electricity	−0.409	MJ
Out		
DME	0.284	kg
Wastewater	0.334	kg
Exhaust	0.101	kg
thereof CO_2	0.009	kg

Table C.9: Life cycle inventory of trioxane production (Burre et al., 2019) for the anhydrous route via trioxane and DME (TRI+DME) with full heat integration per kg of $OME_{3\text{-}5}$.

Flow	**Value**	**Unit**
In		
FA, aq (50 wt%)	−1.463	kg
Electricity	−1.440	MJ
Heat at 93 °C	−15.627	MJ
Heat at 128 °C	−9.772	MJ
Out		
TRI	0.716	kg
Wastewater	0.745	kg

Table C.10: Life cycle inventory of $OME_{3\text{-}5}$ production (Breitkreuz et al., 2018) for the anhydrous route via trioxane and DME (TRI+DME) with full heat integration per kg of $OME_{3\text{-}5}$.

Flow	**Value**	**Unit**
In		
DME	−0.284	kg
TRI	−0.716	kg
Out		
$OME_{3\text{-}5}$	1.000	kg

C.2.4 Aqueous $OME_{3\text{-}5}$ routes

In contrast to the anhydrous routes, aqueous routes directly utilize methanol and typically aqueous FA for $OME_{3\text{-}5}$ formation (see Figure 5.2). In addition to the complex oligomerization reactions in methanolic and aqueous FA solutions, which take place without the presence of a catalyst (Hasse et al., 1990), the desired formation of OME_n takes place in the presence of an acidic catalyst accompanied by water formation following etherification reactions (Schmitz et al., 2015a). The alternative chain-growth mechanism of OME_1 towards OME_n is the direct incorporation of FA into $OME_{n\text{-}1}$. Irrespective of the mechanism, water is present in the system. However, the amount of water and thus the type of FA source may have a huge influence on the performance of the $OME_{3\text{-}5}$ production.

Commercial FA production takes place via partial oxidation of methanol (FORMOX process) or combined partial oxidation and dehydrogenation of methanol (BASF process) (Reuss et al., 2000). In the BASF process, co-produced H_2 is burned for power generation since it is diluted in the remaining off-gas. For both processes, the overall reaction stoichiometry is the same and the resulting FA concentration in the aqueous solution is up to 55 wt% (Reuss et al., 2000). To increase the FA concentration, a subsequent falling-film evaporator can be used as it has been applied by Held et al. (2019). Due to a lower heat demand and favorable economics, the BASF process is considered in this study (MeOH POX) (Reuss et al., 2000). Therein, methanol reacts with air completely to FA and small amounts of side products (CO_2, CO, and H_2). Water is added to the reactor to avoid explosive mixture compositions and is further added as a solvent in the subsequent absorber, yielding the desired aqueous FA solution.

Table C.11: Life cycle inventory of methanol production (Held et al., 2019) for the aqueous route via methanol and formaldehyde by partial oxidation of methanol (MeOH POX) with full heat integration per kg of $OME_{3\text{-}5}$.

Flow	**Value**	**Unit**
In		
H_2	−0.250	kg
CO_2	−1.829	kg
Air	−1.018	kg
Electricity	−1.400	MJ
Out		
MeOH	1.252	kg
Wastewater	0.720	kg
Exhaust	1.134	kg
thereof CO_2	0.113	kg

Table C.12: Life cycle inventory of formaldehyde production (Held et al., 2019) for the aqueous route via methanol and formaldehyde by partial oxidation of methanol (MeOH POX) with full heat integration per kg of $OME_{3\text{-}5}$.

Flow	**Value**	**Unit**
In		
MeOH	−0.835	kg
H_2O	−0.241	kg
Air	−1.491	kg
Electricity	−0.043	MJ
Out		
FA, aq (85 wt%)	0.824	kg
Wastewater	0.449	kg
Exhaust	1.294	kg
thereof CO_2	0.121	kg

Table C.13: Life cycle inventory of $OME_{3\text{-}5}$ production (Held et al., 2019) for the aqueous route via methanol and formaldehyde by partial oxidation of methanol (MeOH POX) with full heat integration per kg of $OME_{3\text{-}5}$.

Flow	**Value**	**Unit**
In		
FA, aq (85 wt%)	−0.824	kg
MeOH	−0.417	kg
Heat at 143 °C	−0.597	MJ
Out		
$OME_{3\text{-}5}$	1.000	kg
Wastewater	0.241	kg

The prominent advantage of methanol dehydrogenation (MeOH DEHY) compared to partial oxidation is the significant co-production of H_2 instead of water. This H_2 can be used for the preceding methanol production to lower the overall electricity demand for the entire power-to-fuel process. However, in contrast to the exothermic BASF process, FA production via dehydrogenation of methanol is an endothermic reaction that requires heating at reactor temperatures of 450-900 °C (Shoujin Su et al., 1994). Selective and active catalysts have already been identified resulting in a high single-pass FA yield of over 70 % (Shoujin Su et al., 1994; Usachev et al., 2004). In this study, we assume a copper/zinc/selenium catalyst achieving a methanol conversion of 69 % and FA selectivity of 90 %, resulting in a yield of 62.1 % at 650 °C reactor temperature (Osugi and Uchiyama, 1977). Small amounts of CO and CH_4 are formed as side products. These experimental results have been achieved by methanol dilution with H_2 in the ratio of 1:1 in the reactor feed.

Table C.14: Life cycle inventory of methanol production (Held et al., 2019) for the aqueous route via methanol and formaldehyde by dehydrogenation of methanol (MeOH DEHY) with full heat integration per kg of $OME_{3\text{-}5}$.

Flow	**Value**	**Unit**
In		
H_2	−0.259	kg
CO_2	−1.898	kg
Air	−1.056	kg
Electricity	−1.400	MJ
Out		
MeOH	1.299	kg
Wastewater	0.747	kg
Exhaust	1.176	kg
thereof CO_2	0.118	kg

Table C.15: Life cycle inventory of formaldehyde production (Shoujin Su et al., 1994; Usachev et al., 2004; Osugi and Uchiyama, 1977) for the aqueous route via methanol and formaldehyde by dehydrogenation of methanol (MeOH DEHY) with full heat integration per kg of $OME_{3\text{-}5}$.

Flow	**Value**	**Unit**
In		
MeOH	−1.299	kg
H_2O	−0.152	kg
Air	−2.550	kg
Electricity	−0.637	MJ
Heat at 650 °C	−2.135	MJ
Out		
FA/MeOH/H_2O (56/34/10 wt%)	1.241	kg
H_2	0.055	kg
Exhaust	2.705	kg
thereof CO_2	0.186	kg

Table C.16: Life cycle inventory of $OME_{3\text{-}5}$ production (Held et al., 2019) for the aqueous route via methanol and formaldehyde by dehydrogenation of methanol (MeOH DEHY) with full heat integration per kg of $OME_{3\text{-}5}$.

Flow	**Value**	**Unit**
In		
FA/MeOH/H_2O (56/34/10 wt%)	−1.241	kg
Heat at 197 °C	−3.279	MJ
Out		
$OME_{3\text{-}5}$	1.000	kg
Wastewater	0.241	kg

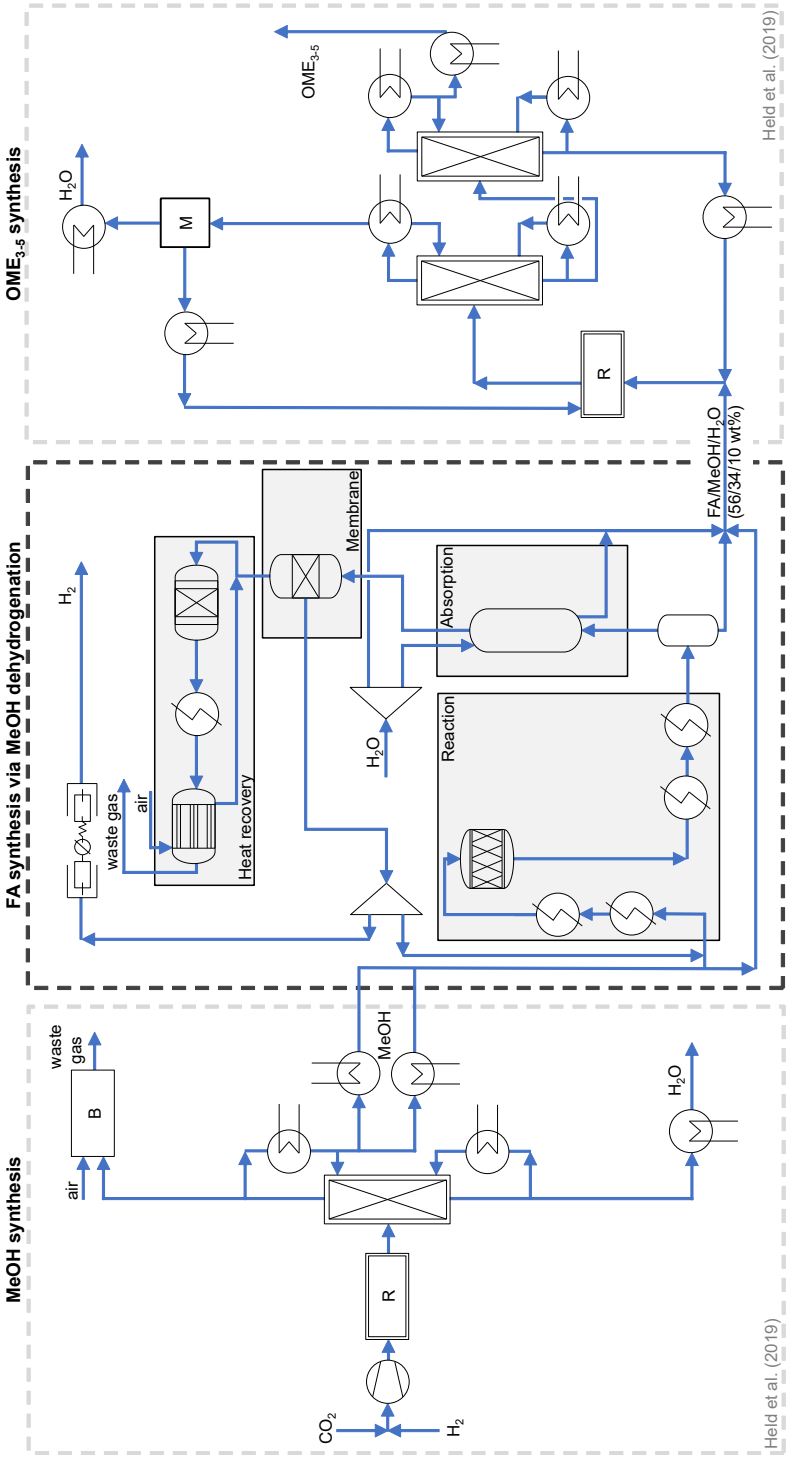

Figure C.1: Flowsheet of the $OME_{3\text{-}5}$ route via methanol and formaldehyde by dehydrogenation of methanol (MeOH DEHY). The simplified process flowsheets for methanol and $OME_{3\text{-}5}$ synthesis are taken from Held et al. (2019) while the formaldehyde synthesis via dehydrogenation of methanol has been developed in this study.

C.2.5 Additional LCA datasets

LCA datasets of the $OME_{3\text{-}5}$ life cycle inventory for the supply of utilities and feedstocks are presented in Table C.17.

Table C.17: LCA datasets of the $OME_{3\text{-}5}$ life cycle inventory.

Flow	Dataset	Region	Reference
Wastewater	treatment of wastewater, average, capacity 1E9l/year	Europe[a]	Wernet et al. (2016)
Water	Water (desalinated; deionised) ts	EU-28	GaBi (2019)
Diesel	Diesel mix at filling station ts	EU-28	GaBi (2019)
Electricity	Electricity grid mix (average power plants) ts[b]	EU-28	GaBi (2019)
	Electricity from wind power ts[c]	EU-28	GaBi (2019)
	Electricity from photovoltaic ts	EU-28	GaBi (2019)
	Electricity from solar thermal ts	EU-28	GaBi (2019)
	Electricity grid mix ts	DE	GaBi (2019)
	Electricity grid mix ts	IT	GaBi (2019)
	Electricity grid mix ts	DK	GaBi (2019)
	Electricity grid mix ts	AT	GaBi (2019)
	Electricity grid mix ts	FI	GaBi (2019)
	Electricity grid mix ts	BE	GaBi (2019)
	Electricity grid mix ts	CH	GaBi (2019)
	Electricity grid mix ts	FR	GaBi (2019)
	Electricity grid mix ts	NO	GaBi (2019)
Heat below 90 °C	steam production, as energy carrier, in chemical industry[b]	Europe	Wernet et al. (2016)
	Heat pump ($COP_{\text{Heat pump}} = 3.28$)[cd]	–	David et al. (2017)
Heat between 90-250 °C	steam production, as energy carrier, in chemical industry[b]	Europe	Wernet et al. (2016)
	Electrode boiler ($\eta_{\text{Boiler}} = 0.95$)[c]	–	Müller et al. (2020a)
Heat above 250 °C	Thermal energy from natural gas ts[b]	EU-28	GaBi (2019)
	Electrode boiler ($\eta_{\text{Boiler}} = 0.95$)[c]	–	Müller et al. (2020a)
H_2	Hydrogen (steam reforming from natural gas) ts[b]	DE	GaBi (2019)
	PEM electrolysis[c]	–	Reuß et al. (2017)
CO_2	CO_2 from direct air capture[b]	–	Deutz and Bardow (2021)
	CO_2 from ammonia plant[ce]	–	von der Assen et al. (2016)

[a] Without Switzerland
[b] Worst-case scenario
[c] Best-case scenario
[d] Averaged COP of heat pumps built after 2006 with $T_{\text{source}} \in [9, 15]$ °C and $T_{\text{operate}} = 90$ °C from David et al. (2017).
[e] Without electricity consumption for compressing CO_2 to 100 bar for transportation. The $OME_{3\text{-}5}$ production routes of this study demand CO_2 at 1 bar and include the CO_2 compression intrinsically in their system boundaries.

C.3 Calculations

Here, further details are given on the calculations for the exergy (Section C.3.1) and fleet (Section C.3.2) analyses.

C.3.1 Exergy analysis

The exergy efficiency is calculated as the share of all exergy output flows divided by all exergy input flows:

$$\eta_{\text{Exergy}} = \frac{\dot{E}_{\text{OME}_{3\text{-}5}}}{\dot{E}_{\text{H}_2} + \dot{E}_{\dot{Q}_{\text{in}}} + P_{\text{el}}}. \tag{C.1}$$

$\dot{E}_{\text{OME}_{3-5}}$, $\dot{E}_{\text{H}_2}$, and $\dot{E}_{\dot{Q}_{\text{in}}}$ denote the exergy flows associated with the flows of $\text{OME}_{3\text{-}5}$, H_2, and the net heat demand $\dot{Q}_{\text{in}}$, while P_{el} represents the electricity consumption of the $\text{OME}_{3\text{-}5}$ production system. The net heat demand $\dot{Q}_{\text{in}}$ is calculated by pinch-based heat integration. Here, CO_2 is not shown as exergy input flow since it brings negligible exergy into the system at 1 bar and 298 K. Using the inventories in Section C.2 and the specific exergies in Table C.18, we can directly compute the exergy flow rates entering and leaving the processes in the considered production routes (Table C.19–C.34). The only point that requires additional attention are the heat flows.

For the LCA as well as for computing the overall exergy efficiency of the production routes, we consider full heat integration along the entire production route. This means that any hot and cold stream from each process step (e. g., methanol production, formaldehyde production, $\text{OME}_{3\text{-}5}$ production) can be matched with any other cold and hot stream, including streams from other process steps. As such, we only get an overall heat demand for each production route. Since we performed heat integration only by pinch analysis, we just know how much external heating and cooling is required for the entire production route, but we do not know how much heat is transferred within each process step and from one process step to another. While this overall heat demand is sufficient to compute the LCA indicators and the overall exergy efficiency, it does not allow us to obtain exergy balances (or, more specifically, the exergy of heat flows) for each individual process step (e. g., methanol production only).

Nevertheless, we still want to be able to calculate approximate exergy balances for each individual process step in order to visualize the main exergy flows and losses. To do so, we derive an estimate for the heat transfer between the individual process steps as follows. We conduct heat integration by pinch analysis individually for each process step, which gives us an estimate for the required external heating and cooling

Table C.18: Specific exergies of mass and heat flows in $OME_{3\text{-}5}$ production. The state of each component is denoted as follows: g for gaseous and l for liquid.

Exergy flow	**State**	**Pressure** bar	**Temperature** K	**Value**
Mass / $MJ_{Exergy}\,kg^{-1}$				
H_2	g	30	298	121.83
CO_2	g	1	298	0.00
MeOH	l	1	298	21.93
FA[a]	l	1	298	8.36
FA[b]	l	1	298	14.35
TRI	l	1	368	17.24
DME	l	10	298	30.21
OME_1	l	1	298	25.01
OME_3	l	1	298	21.42
OME_4	l	1	298	20.78
OME_5	l	1	298	20.23
$OME_{3\text{-}5}$[c]	l	1	298	20.91
$OME_{3\text{-}5}$[d]	l	1	298	20.97
$OME_{3\text{-}5}$[e]	l	1	298	20.80
$FA/MeOH/H_2O$ (56/34/10 wt%)	l	1	368	17.27
Heat / $MJ_{Exergy}\,MJ_{Heat}^{-1}$				
TRI production (93 °C)	–	–	366	0.19
TRI production (128 °C)	–	–	401	0.26
$OME_{3\text{-}5}$ production (143 °C)	–	–	416	0.28
$OME_{3\text{-}5}$ production (197 °C)	–	–	470	0.37
FA production (650 °C)	–	–	923	0.68

[a] 50 wt% aq.
[b] 85 wt% aq.
[c] Burger et al. (2013): 42.88 % OME_3, 33.77 % OME_4, 23.35 % OME_5.
[d] Held et al. (2019): 49.89 % OME_3, 30.69 % OME_4, 19.39 % OME_5.
[e] Breitkreuz et al. (2018): 33.69 % OME_3, 34.30 % OME_4, 32.01 % OME_5.

of each process step as well as the associated temperature levels. We can then approximately match high-enough temperature cooling demand of one process step with lower-temperature heating demand of another process step. This type of heat integration is more restricted than the full heat integration, allowing matches between any two streams considered above. Therefore, it does not yield exactly the same results, but a rough estimate for the heat flows that are exchanged between the process steps.

Anhydrous route via trioxane and OME_1 (TRI+OME_1)

Table C.19: Exergy balance of methanol production (Bongartz et al., 2019) for the anhydrous route via trioxane and OME_1 (TRI+OME_1). Exergy flows are given for 1 kg of $OME_{3\text{-}5}$.

Exergy flow	**Value**	**Unit**
In		
H_2	−30.40	MJ
Electricity	−1.27	MJ
Out		
MeOH	27.89	MJ
Heat export to OME_1 at 155 °C	0.15	MJ
Heat export to $OME_{3\text{-}5}$ at 250/200 °C	1.01	MJ
Loss	2.62	MJ

Table C.20: Exergy balance of formaldehyde production (Bongartz et al., 2019) for the anhydrous route via trioxane and OME_1 (TRI+OME_1). Exergy flows are given for 1 kg of $OME_{3\text{-}5}$.

Exergy flow	**Value**	**Unit**
In		
MeOH	−18.64	MJ
Electricity	−0.16	MJ
Out		
FA, aq (50 wt%)	12.08	MJ
Heat export to OME_1 at 200 °C	0.92	MJ
Heat export to TRI at 200 °C	0.74	MJ
Loss	5.06	MJ

Table C.21: Exergy balance of OME_1 production (Bongartz et al., 2019) for the anhydrous route via trioxane and OME_1 (TRI+OME_1). Exergy flows are given for 1 kg of $OME_{3\text{-}5}$.

Exergy flow	**Value**	**Unit**
In		
MeOH	−9.25	MJ
FA, aq (50 wt%)	−3.29	MJ
Heat import from MeOH at 155 °C	−0.15	MJ
Heat import from FA at 200 °C	−0.92	MJ
Heat import from $OME_{3\text{-}5}$ at 110 °C	−0.24	MJ
Electricity	0.00	MJ
Out		
OME_1	12.11	MJ
Loss	1.74	MJ

Table C.22: Exergy balance of trioxane production (Burre et al., 2019) for the anhydrous route via trioxane and OME_1 (TRI+OME_1). Exergy flows are given for 1 kg of $OME_{3\text{-}5}$.

Exergy flow	**Value**	**Unit**
In		
FA, aq (50 wt%)	−8.79	MJ
Heat import from FA at 200 °C	−0.74	MJ
Heat at 93 °C	−2.46	MJ
Heat at 128 °C	−1.33	MJ
Electricity	−1.04	MJ
Out		
TRI	8.88	MJ
Loss	5.48	MJ

Table C.23: Exergy balance of $OME_{3\text{-}5}$ production (Burre et al., 2019) for the anhydrous route via trioxane and OME_1 (TRI+OME_1). Exergy flows are given for 1 kg of $OME_{3\text{-}5}$.

Exergy flow	**Value**	**Unit**
In		
OME_1	−12.11	MJ
TRI	−8.88	MJ
Heat import from MeOH at 250/200 °C	−1.01	MJ
Out		
$OME_{3\text{-}5}$	20.91	MJ
Heat export to OME_1 at 110 °C	0.24	MJ
Loss	0.85	MJ

Anhydrous route via trioxane and DME (TRI+DME)

Table C.24: Exergy balance of methanol production (Bongartz et al., 2019) for the anhydrous route via trioxane and DME (TRI+DME). Exergy flows are given for 1 kg of $OME_{3\text{-}5}$.

Exergy flow	**Value**	**Unit**
In		
H_2	−20.55	MJ
Electricity	−0.86	MJ
Out		
MeOH	18.86	MJ
Heat export to TRI at 185 °C	0.73	MJ
Loss	1.82	MJ

Table C.25: Exergy balance of formaldehyde production (Bongartz et al., 2019) for the anhydrous route via trioxane and DME (TRI+DME). Exergy flows are given for 1 kg of $OME_{3\text{-}5}$.

Exergy flow	**Value**	**Unit**
In		
MeOH	−18.86	MJ
Electricity	−0.16	MJ
Out		
FA, aq (50 wt%)	12.22	MJ
Heat export to TRI at 200 °C	1.02	MJ
Heat export to $OME_{3\text{-}5}$ at 300 °C	0.85	MJ
Loss	4.93	MJ

Table C.26: Exergy balance of DME production (Bongartz et al., 2018) for the anhydrous route via trioxane and DME (TRI+DME). Exergy flows are given for 1 kg of $OME_{3\text{-}5}$.

Exergy flow	**Value**	**Unit**
In		
H_2	−9.24	MJ
Electricity	−0.41	MJ
Out		
DME	8.58	MJ
Heat export to TRI at 195 °C	0.16	MJ
Loss	0.91	MJ

Table C.27: Exergy balance of trioxane production (Burre et al., 2019) for the anhydrous route via trioxane and DME (TRI+DME). Exergy flows are given for 1 kg of $OME_{3\text{-}5}$.

Exergy flow	**Value**	**Unit**
In		
FA, aq (50 wt%)	−12.22	MJ
Heat import from MeOH at 185 °C	−0.73	MJ
Heat import from FA at 200 °C	−1.02	MJ
Heat import from DME at 195 °C	−0.16	MJ
Heat at 93 °C	−2.90	MJ
Heat at 128 °C	−2.51	MJ
Electricity	−1.44	MJ
Out		
TRI	12.34	MJ
Loss	8.64	MJ

Table C.28: Exergy balance of $OME_{3\text{-}5}$ production (Breitkreuz et al., 2018) for the anhydrous route via trioxane and DME (TRI+DME). Exergy flows are given for 1 kg of $OME_{3\text{-}5}$.

Exergy flow	**Value**	**Unit**
In		
DME	−8.58	MJ
TRI	−12.34	MJ
Heat import from FA at 300 °C	−0.85	MJ
Out		
$OME_{3\text{-}5}$	20.80	MJ
Loss	0.97	MJ

Aqueous route via methanol and formaldehyde by partial oxidation of methanol (MeOH POX)

Table C.29: Exergy balance of methanol production (Held et al., 2019) for the aqueous route via methanol and formaldehyde by partial oxidation of methanol (MeOH POX). Exergy flows are given for 1 kg of $OME_{3\text{-}5}$.

Exergy flow	**Value**	**Unit**
In		
H_2	−30.47	MJ
Electricity	−1.40	MJ
Out		
MeOH	27.45	MJ
Heat export to $OME_{3\text{-}5}$ at 650/230 °C	1.54	MJ
Loss	2.88	MJ

Table C.30: Exergy balance of formaldehyde production (Held et al., 2019) for the aqueous route via methanol and formaldehyde by partial oxidation of methanol (MeOH POX). Exergy flows are given for 1 kg of $OME_{3\text{-}5}$.

Exergy flow	**Value**	**Unit**
In		
MeOH	−18.31	MJ
Electricity	−0.04	MJ
Out		
FA, aq (85 wt%)	11.83	MJ
Heat export to $OME_{3\text{-}5}$ at 650/200 °C	2.79	MJ
Loss	3.73	MJ

Table C.31: Exergy balance of $OME_{3\text{-}5}$ production (Held et al., 2019) for the aqueous route via methanol and formaldehyde by partial oxidation of methanol (MeOH POX). Exergy flows are given for 1 kg of $OME_{3\text{-}5}$.

Exergy flow	**Value**	**Unit**
In		
FA, aq (85 wt%)	−11.83	MJ
MeOH	−9.14	MJ
Heat import from MeOH at 650/230 °C	−1.54	MJ
Heat import from FA at 650/200 °C	−2.79	MJ
Heat at 143 °C	−0.17	MJ
Out		
$OME_{3\text{-}5}$	20.97	MJ
Loss	4.50	MJ

Aqueous route via methanol and formaldehyde by dehydrogenation of methanol (MeOH DEHY)

Table C.32: Exergy balance of methanol production (Held et al., 2019) for the aqueous route via methanol and formaldehyde by dehydrogenation of methanol (MeOH DEHY). Exergy flows are given for 1 kg of $OME_{3\text{-}5}$.

Exergy flow	**Value**	**Unit**
In		
H_2	−24.96	MJ
H_2 recycle from FA	−6.65	MJ
Electricity	−1.40	MJ
Out		
MeOH	28.48	MJ
Heat export to $OME_{3\text{-}5}$ at 650/200 °C	1.93	MJ
Loss	2.60	MJ

Table C.33: Exergy balance of formaldehyde production (Shoujin Su et al., 1994; Usachev et al., 2004; Osugi and Uchiyama, 1977) for the aqueous route via methanol and formaldehyde by dehydrogenation of methanol (MeOH DEHY). Exergy flows are given for 1 kg of $OME_{3\text{-}5}$.

Exergy flow	**Value**	**Unit**
In		
MeOH	−28.48	MJ
Heat at 650 °C	−1.45	MJ
Electricity	−0.64	MJ
Out		
FA/MeOH/H_2O (56/34/10 wt%)	21.44	MJ
H_2 recycle to MeOH	6.65	MJ
Heat export to $OME_{3\text{-}5}$ at 200 °C	0.67	MJ
Loss	1.81	MJ

Table C.34: Exergy balance of $OME_{3\text{-}5}$ production (Held et al., 2019) for the aqueous route via methanol and formaldehyde by dehydrogenation of methanol (MeOH DEHY). Exergy flows are given for 1 kg of $OME_{3\text{-}5}$.

Exergy flow	**Value**	**Unit**
In		
FA/MeOH/H_2O (56/34/10 wt%)	−21.44	MJ
Heat import from MeOH at 650/200 °C	−1.93	MJ
Heat import from FA at 200 °C	−0.67	MJ
Heat at 197 °C	−1.20	MJ
Out		
$OME_{3\text{-}5}$	20.97	MJ
Loss	4.27	MJ

C.3.2 Fleet analysis

The fleet analysis is conducted for blending $OME_{3\text{-}5}$ and diesel for the entire fleet (Section C.3.2.1) and using $OME_{3\text{-}5}$ and diesel separately in the fleet (Section C.3.2.2).

C.3.2.1 Blend for All: Blending $OME_{3\text{-}5}$ and diesel for the entire fleet

We estimate the current annual mileage of the diesel passenger car fleet in the EU ($MILEAGE^{\text{EU, annual}}_{\text{Diesel cars}}$) as the product of the amount of diesel passenger cars ($n^{\text{EU}}_{\text{Diesel cars}}$) and the average annual mileage per passenger car in the EU ($MILEAGE^{\text{EU, annual}}_{\text{Car, avg}}$):

$$MILEAGE^{\text{EU, annual}}_{\text{Diesel cars}} = n^{\text{EU}}_{\text{Diesel cars}} \cdot MILEAGE^{\text{EU, annual}}_{\text{Car, avg}}. \tag{C.2}$$

The annual mileage of the EU fleet of diesel passenger cars results in 1.34×10^{12} km with 95.7×10^{6} diesel passenger cars (Eurostat, 2020b) and an estimated average annual mileage of 14×10^{3} km in the EU (Siegemund et al., 2017). The transportation demand is proportional to the total enthalpy of combustion of the diesel-$OME_{3\text{-}5}$ blend ($H^{\text{Blend}}_{\text{comb}}$), assuming equal energy consumptions ($e_{\text{Diesel car}}$) for all diesel passenger cars:

$$H^{\text{Blend}}_{\text{comb}} = MILEAGE^{\text{EU, annual}}_{\text{Diesel cars}} \cdot e_{\text{Diesel car}}. \tag{C.3}$$

The mass of produced $OME_{3\text{-}5}$ ($m_{OME_{3\text{-}5}}$) is determined by the amount of available electricity ($W^{\text{available}}_{\text{el}}$) and the specific electricity consumption to produce 1 kg of $OME_{3\text{-}5}$ ($w^{OME_{3\text{-}5}}_{\text{el}}$):

$$m_{OME_{3\text{-}5}} = \frac{W^{\text{available}}_{\text{el}}}{w^{OME_{3\text{-}5}}_{\text{el}}}. \tag{C.4}$$

The enthalpy of combustion of $OME_{3\text{-}5}$ ($H^{OME_{3\text{-}5}}_{\text{comb}}$) is proportional to the mass of produced $OME_{3\text{-}5}$ and the specific LHV of $OME_{3\text{-}5}$ ($LHV_{OME_{3\text{-}5}}$):

$$H^{OME_{3\text{-}5}}_{\text{comb}} = m_{OME_{3\text{-}5}} \cdot LHV_{OME_{3\text{-}5}}. \tag{C.5}$$

The sum of the enthalpies of combustion of $OME_{3\text{-}5}$ and diesel ($H^{\text{Diesel}}_{\text{comb}}$) equals the total enthalpy of combustion of the diesel-$OME_{3\text{-}5}$ blend (Figure C.2), assuming ideal mixing and equal energy consumptions per km. Therefore, the enthalpy of combustion of diesel can be calculated as follows:

$$H_{\text{comb}}^{\text{Diesel}} = H_{\text{comb}}^{\text{Blend}} - H_{\text{comb}}^{\text{OME}_{3\text{-}5}}. \tag{C.6}$$

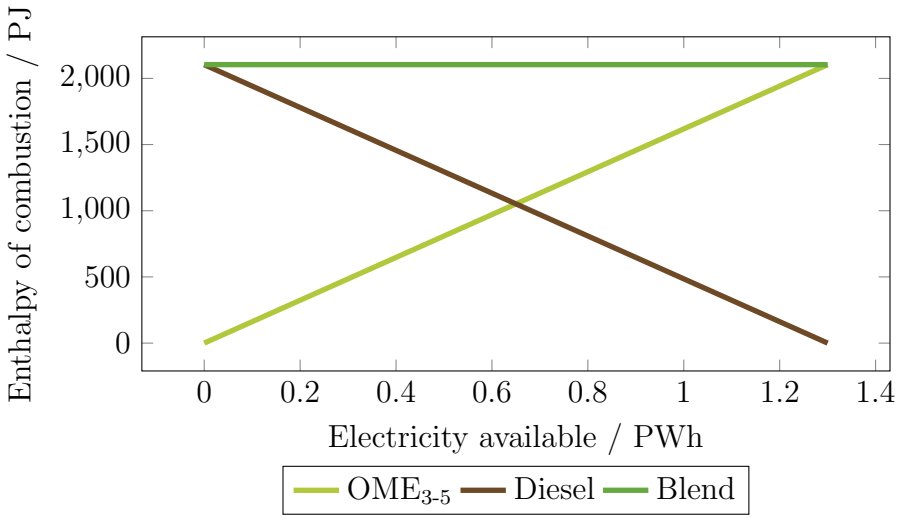

Figure C.2: Energy balance of the enthalpy of combustion of $\text{OME}_{3\text{-}5}$, diesel, and blends of both as function of the available electricity.

The mass of produced diesel (m_{Diesel}) is proportional to the enthalpy of combustion and the specific lower heating value of diesel (LHV_{Diesel}):

$$m_{\text{Diesel}} = \frac{H_{\text{comb}}^{\text{Diesel}}}{LHV_{\text{Diesel}}}. \tag{C.7}$$

The total blend mass (m_{Blend}) is the sum of the $\text{OME}_{3\text{-}5}$ and diesel masses:

$$m_{\text{Blend}} = m_{\text{OME}_{3\text{-}5}} + m_{\text{Diesel}}. \tag{C.8}$$

The total blend mass increases with increasing mass of produced $\text{OME}_{3\text{-}5}$ (Figure C.3). This is due to the lower specific lower heating value of $\text{OME}_{3\text{-}5}$ compared to that of fossil diesel: Substituting 1.0 kg of fossil diesel requires 2.2 kg of $\text{OME}_{3\text{-}5}$ to provide the same amount of enthalpy of combustion, assuming a constant energy consumption of the passenger car for both fuels. Note that we neglect the effect of increasing fuel mass on the mileage.

The mass fractions of $\text{OME}_{3\text{-}5}$ ($y_{\text{OME}_{3\text{-}5}}^{\text{Blend}}$) and diesel ($y_{\text{Diesel}}^{\text{Blend}}$) within the blend are calculated as follows:

$$y_{\text{OME}_{3\text{-}5}}^{\text{Blend}} = \frac{m_{\text{OME}_{3\text{-}5}}}{m_{\text{Blend}}}, \tag{C.9}$$

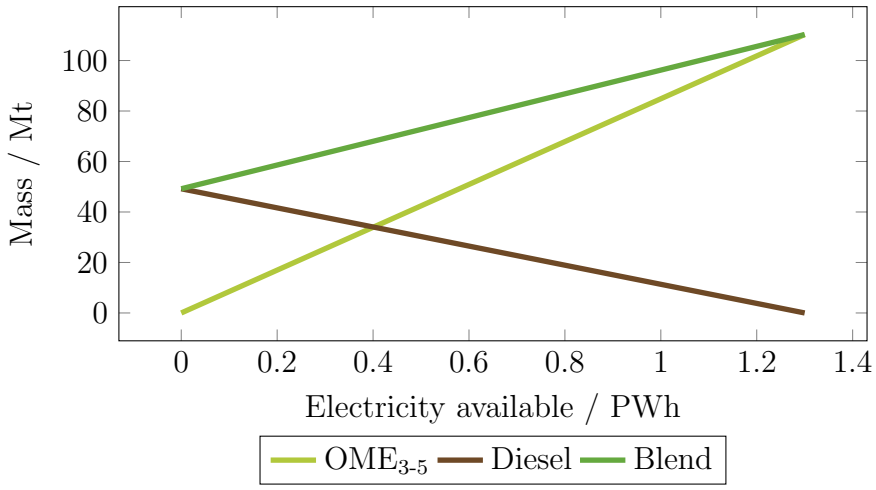

Figure C.3: The mass of $OME_{3\text{-}5}$, diesel, and blends of both as function of the available electricity.

$$y_{\text{Diesel}}^{\text{Blend}} = 1 - y_{\text{OME}_{3\text{-}5}}^{\text{Blend}}. \tag{C.10}$$

As stated above, the total blend mass increases with increasing mass of produced $OME_{3\text{-}5}$. This results in nonlinear functions of available electricity for both mass fractions (Figure C.4). The mass fraction of $OME_{3\text{-}5}$, which equals the specific blending ratio of $OME_{3\text{-}5}$, is a concave function of the amount of available electricity. A blending component with higher LHV than fossil diesel would instead result in a convex function, while a blending component with equal LHV as fossil diesel would result in a linear function.

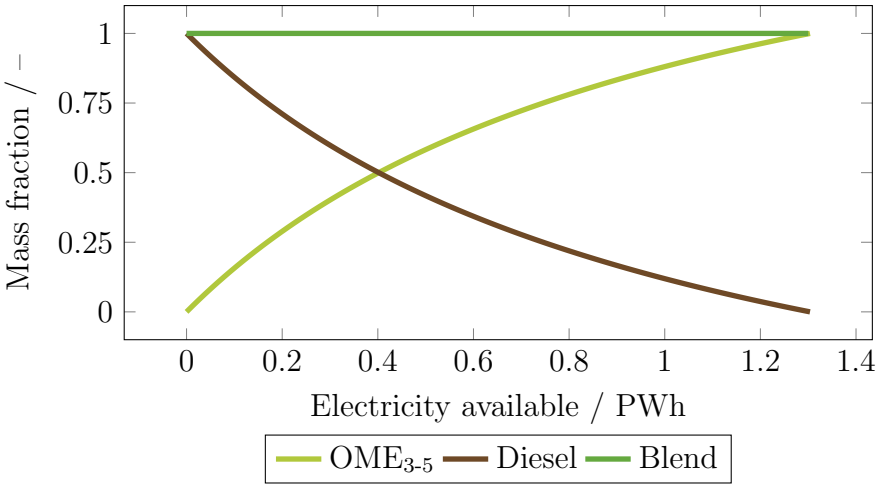

Figure C.4: The mass fraction of $OME_{3\text{-}5}$, diesel, and blends of both as function of the available electricity.

The specific blending ratio of $OME_{3\text{-}5}$ (BR_{spec}) equals the mass fraction of $OME_{3\text{-}5}$ within the blend:

$$BR_{\text{spec}} = \frac{m_{\text{OME}_{3\text{-}5}}}{m_{\text{Blend}}} = y^{\text{Blend}}_{\text{OME}_{3\text{-}5}}. \tag{C.11}$$

The volumetric blending ratio of $\text{OME}_{3\text{-}5}$ (BR_{vol}) is the ratio of the $\text{OME}_{3\text{-}5}$ volume ($V_{\text{OME}_{3\text{-}5}}$) and the total blend volume (V_{Blend}). The total blend volume is the sum of the $\text{OME}_{3\text{-}5}$ and diesel volume (V_{Diesel}). Both the $\text{OME}_{3\text{-}5}$ and diesel volume are proportional to the ratios of their masses and densities (ρ):

$$BR_{\text{vol}} = \frac{V_{\text{OME}_{3\text{-}5}}}{V_{\text{Blend}}} = \frac{V_{\text{OME}_{3\text{-}5}}}{V_{\text{OME}_{3\text{-}5}} + V_{\text{Blend}}} = \frac{\frac{m_{\text{OME}_{3\text{-}5}}}{\rho_{\text{OME}_{3\text{-}5}}}}{\frac{m_{\text{OME}_{3\text{-}5}}}{\rho_{\text{OME}_{3\text{-}5}}} + \frac{m_{\text{Diesel}}}{\rho_{\text{Diesel}}}}. \tag{C.12}$$

The LHV of the blend (LHV_{Blend}) is obtained by the sum of the products of each component's mass fraction and LHV:

$$LHV_{\text{Blend}} = \sum_i y^{\text{Blend}}_i \cdot LHV_i = y^{\text{Blend}}_{\text{OME}_{3\text{-}5}} \cdot LHV_{\text{OME}_{3\text{-}5}} + y^{\text{Blend}}_{\text{Diesel}} \cdot LHV_{\text{Diesel}}. \tag{C.13}$$

The LHV of the diesel-$\text{OME}_{3\text{-}5}$ blend is a convex, monotonically decreasing function of the amount of available electricity and ranges in the interval of the LHVs of both pure fuels (Figure C.5). The environmental impact of the "Blend for All" fleet ($EI^{\text{Blend for All}}_{\text{Fleet}}$) follows from emission measurements for each volumetric blending ratio (see Section 5.3.2 and Section C.4).

C.3.2.2 Pure for Few: Using $\text{OME}_{3\text{-}5}$ and diesel separately in the fleet

For "Pure for Few," we calculate the mileage of diesel passenger cars with pure $\text{OME}_{3\text{-}5}$ as the fraction of the enthalpy of combustion of $\text{OME}_{3\text{-}5}$ and the energy consumption of diesel passenger cars. The enthalpy of combustion of $\text{OME}_{3\text{-}5}$ follows from the amount of produced $\text{OME}_{3\text{-}5}$, depending on available electricity for $\text{OME}_{3\text{-}5}$ production (Equations C.4 and C.5).

$$MILEAGE_{\text{OME}_{3\text{-}5}} = \frac{H^{\text{OME}_{3\text{-}5}}_{\text{comb}}}{e_{\text{Diesel car}}}. \tag{C.14}$$

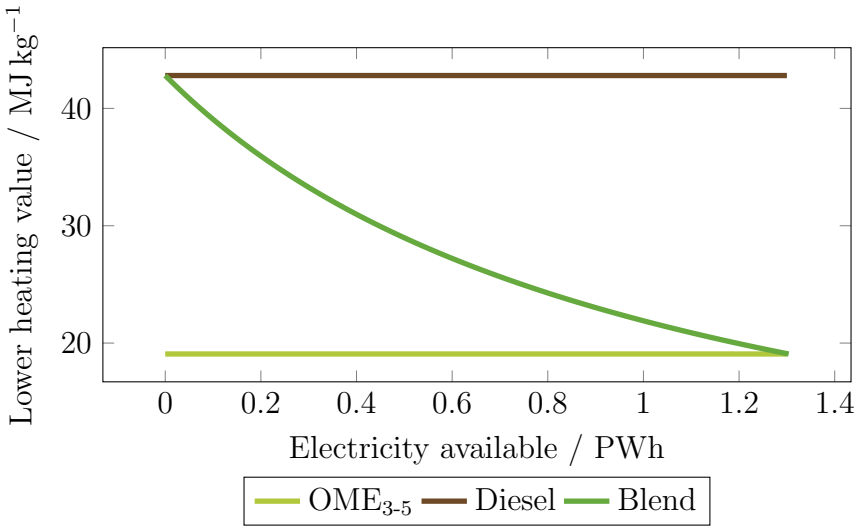

Figure C.5: The lower heating value of OME$_{3\text{-}5}$, diesel, and blends of both as function of the available electricity.

We estimate the mileage of diesel passenger cars with pure fossil diesel by subtracting the mileage of diesel passenger cars with pure OME$_{3\text{-}5}$ from the current annual mileage of the EU fleet of diesel passenger cars (Equation C.2):

$$MILEAGE_{\text{Diesel}} = MILEAGE^{\text{EU, annual}}_{\text{Diesel cars}} - MILEAGE_{\text{OME}_{3\text{-}5}}. \tag{C.15}$$

The mileage shares ($SHARE$) of pure OME$_{3\text{-}5}$ and pure fossil diesel can be calculated as follows:

$$SHARE^{\text{Mileage}}_{\text{OME}_{3\text{-}5}} = \frac{MILEAGE_{\text{OME}_{3\text{-}5}}}{MILEAGE^{\text{EU, annual}}_{\text{Diesel cars}}}, \tag{C.16}$$

$$SHARE^{\text{Mileage}}_{\text{Diesel}} = 1 - SHARE^{\text{Mileage}}_{\text{OME}_{3\text{-}5}}. \tag{C.17}$$

The environmental impact of the "Pure for Few" fleet ($EI^{\text{Pure for Few}}_{\text{Fleet}}$) is the sum of the products of the mileage shares and the environmental impacts of driving a diesel passenger car with pure OME$_{3\text{-}5}$ ($EI_{\text{OME}_{3\text{-}5}}$) and pure fossil diesel (EI_{Diesel}), respectively (Equation C.18). The environmental impacts of pure OME$_{3\text{-}5}$ and pure fossil diesel stem from emission measurements (see Section 5.3.2 and Section C.4).

$$EI^{\text{Pure for Few}}_{\text{Fleet}} = SHARE^{\text{Mileage}}_{\text{OME}_{3\text{-}5}} \cdot EI_{\text{OME}_{3\text{-}5}} + SHARE^{\text{Mileage}}_{\text{Diesel}} \cdot EI_{\text{Diesel}} \tag{C.18}$$

C.4 Emission measurements

In Table C.35–C.39, further details regarding the emission measurements and tailpipe emissions are given.

Table C.35: Measuring devices for species concentration, air mass flow, and fuel mass flow in the $OME_{3\text{-}5}$ study.

Emission	**Measuring principle**	**Device**
Soot	Filter paper method	AVL 415s
Particle number and size	Differential electrical mobility separation	TSI Engine exhaust particle sizer 3090
NO_x	Chemiluminescence detector	EcoPysics CLD 700 EL
HC as C_3H_8 equivalent	Flame ionization detector	Rosemount – NGA 2000
CO and CO_2	Non-dispersive infrared	Rosemount – NGA 2000
O_2	Paramagnetic detector	Rosemount – NGA 2000
Formaldehyde and CH_4	FTIR	FEV EmissionRate
Fuel mass flow	Coriolis	FEV FuelRate
Air mass flow	Ultrasonic	FEV AirRate

Table C.36: Specifications of the single-cylinder engine in the $OME_{3\text{-}5}$ study.

Feature	**Unit**	**Value**
Bore	mm	75
Stroke	mm	88.3
Displacement	L	0.39
Compression ratio	–	15:1
Swirl number	–	1.25
Max. injection pressure	bar	2000
Max. boost pressure (abs.)	bar	4
Peak firing pressure	bar	220
Max. engine speed	min^{-1}	5500
Piston bowl geometry	–	Aluminum piston with ω-shaped reentrant

Table C.37: Data for the vehicle, engine, and after-treatment system model in the $OME_{3\text{-}5}$ study.

Parameter name	**Value**	**Unit**
Vehicle mass	1590	kg
Gears	7	–
1^{st} gear ratio	4.00	–
2^{nd} gear ratio	2.10	–
3^{rd} gear ratio	1.38	–
4^{th} gear ratio	1.00	–
5^{th} gear ratio	0.78	–
6^{th} gear ratio	0.65	–
7^{th} gear ratio	0.52	–
Final drive ratio	2.93	–
Rolling resistance curve	$0.04\,\nu^2 - 0.32\,\nu + 175$	N
Drive train efficiency	0.95	–
Wheel diameter	61	cm
Engine displacement	1600	cm^3
Inertia of turbine and compressor wheel	5×10^{-5}	$kg\,m^2$
DPF volume	3000	cm^3
SCR volume	3600	cm^3
DOC volume	1300	cm^3
Initial temperature of aftertreatment system	300	K

Table C.38: Tailpipe emissions of diesel, $OME_{3\text{-}5}$, and diesel-$OME_{3\text{-}5}$ blends and the energy consumption of the passenger car in the $OME_{3\text{-}5}$ study.

Fuel	**NO_x emissions**	**PM emissions**	**CO_2 emissions**	**Energy consumption**
–	$mg\,km^{-1}$	$mg\,km^{-1}$	$g\,km^{-1}$	$MJ\,km^{-1}$
Fossil diesel	58	0.56	115	
20 vol% $OME_{3\text{-}5}$ in fossil diesel	40	0.40	117	
35 vol% $OME_{3\text{-}5}$ in fossil diesel	31	0.23	119	1.57
50 vol% $OME_{3\text{-}5}$ in fossil diesel	25	0.08	121	
$OME_{3\text{-}5}$	25	0.00	131	

Table C.39: Variation domain for the design of experiment approach in the $OME_{3\text{-}5}$ study.

Variation parameter	**Range**	**Distribution**	**Constraints**
$OME_{3\text{-}5}$ content in fuel	0–100 %	Predefined	0 vol%, 35 vol%, 100 vol%
Engine speed	1000–2750 rpm	In steps of 250 rpm	No constraints
Imep of the high pressure cycle	1.5–19.5 bar	In steps of 2 bar	Constrained by full load at low engine speeds
Center of combustion	5–20 °CAaTDC	Random	±5 °CAaTDC from basis value for corresponding load point
Rail pressure	200–2000 bar	Random	±300 bar from basis value for corresponding load point
Pilot energizing time	180–300 μs	Random	No constraints
Pilot offset relative to main injection	800–3000 μs	Random	Constrained to −30 °CAaTDC
Boost pressure	1–3 bar	Random	±0.3 bar from basis value for corresponding load point
EGR rate	0–70 %	Random	Constrained by $\lambda > 1.1$ for diesel and by $\lambda > 0.9$ for pure $OME_{3\text{-}5}$

C.5 Life cycle impact assessment

In the following, life cycle impact assessment results are presented for the fuel production (Section C.5.1) and entire life cycle (Section C.5.2–C.5.3) of $OME_{3\text{-}5}$.

C.5.1 Fuel production

This section presents the life cycle impact assessment results for fuel production in the worst-case scenario and the best-case scenario with CO_2 from direct air capture.

Worst-case scenario

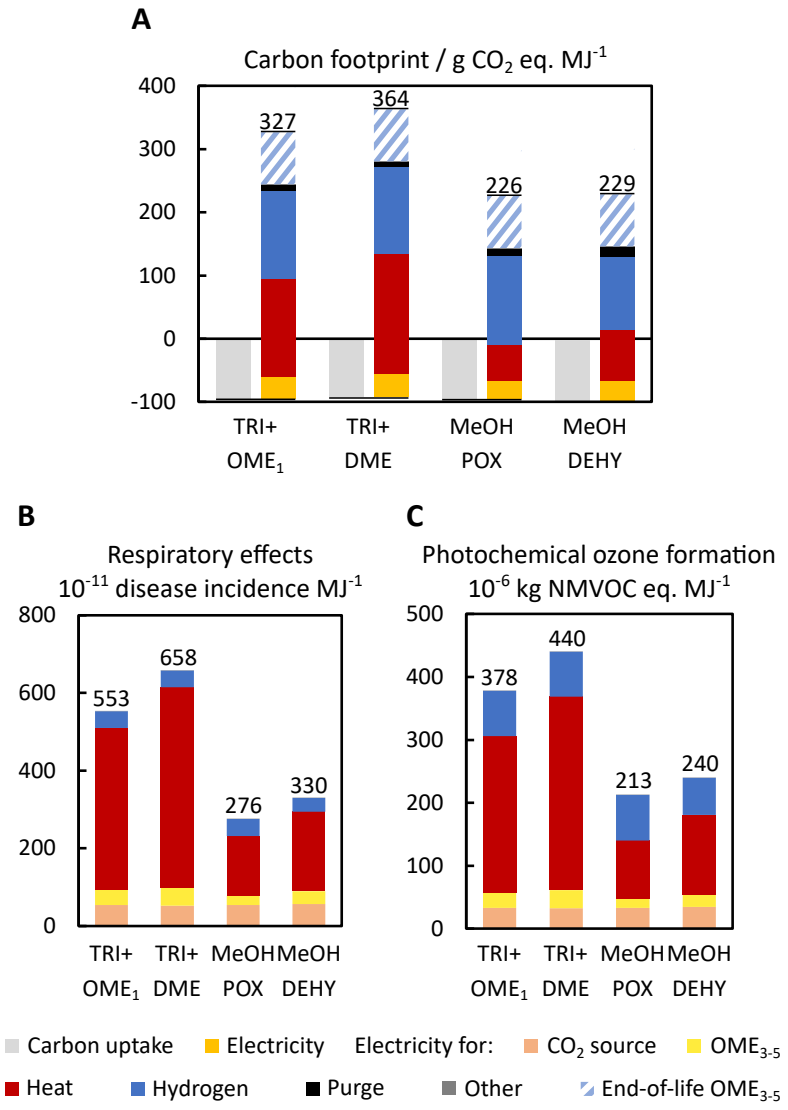

Figure C.6: Well-to-tank (A) carbon footprint in g CO_2 eq. per MJ, (B) respiratory effects in 10^{-11} disease incidence per MJ, and (C) photochemical ozone formation in 10^{-6} kg NMVOC eq. per MJ of $OME_{3\text{-}5}$ production routes in the worst-case scenario. The carbon uptake has a negative carbon footprint due to CO_2 utilization while all other processes have positive environmental impacts. Electricity supply is further subdivided in electricity for CO_2 and $OME_{3\text{-}5}$ supply in (B) and (C). Although not inside the system boundary of a well-to-tank analysis, we additionally indicate the end-of-life emissions from $OME_{3\text{-}5}$ combustion for the carbon footprint.

Best-case scenario with CO_2 from direct air capture

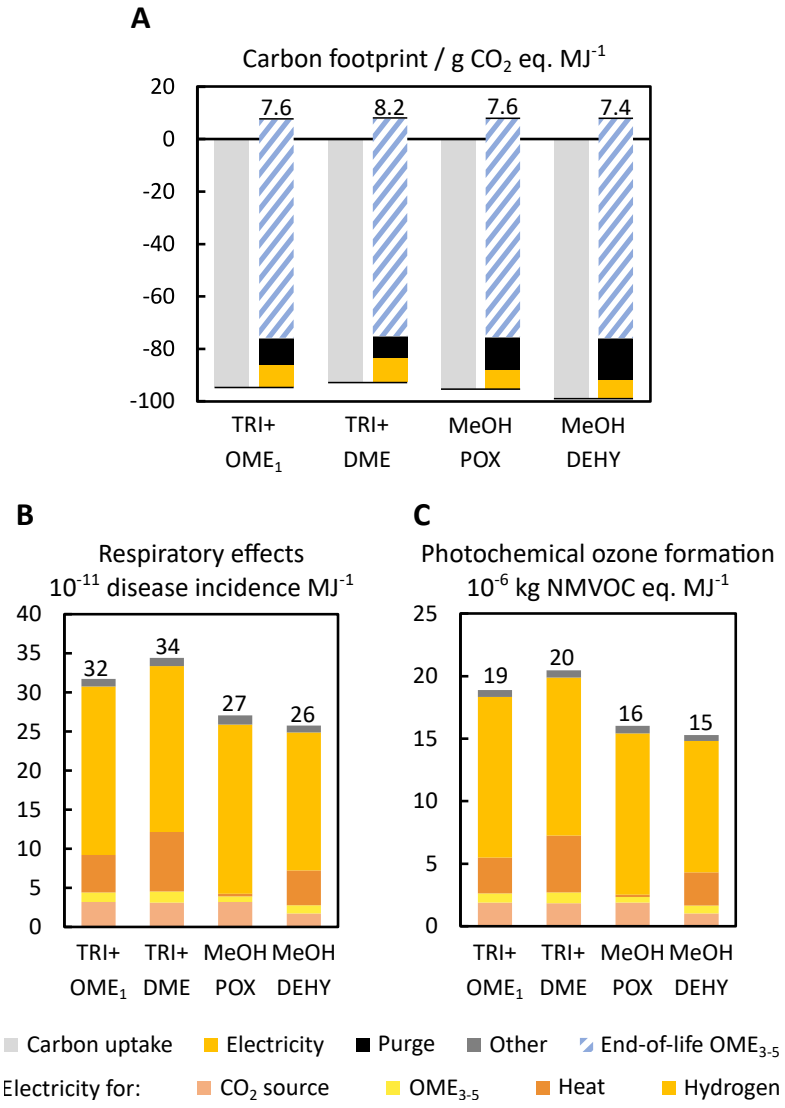

Figure C.7: Well-to-tank (A) carbon footprint in g CO_2 eq. per MJ, (B) respiratory effects in 10^{-11} disease incidence per MJ, and (C) photochemical ozone formation in 10^{-6} kg NMVOC eq. per MJ of $OME_{3\text{-}5}$ production routes in the best-case scenario with CO_2 from direct air capture. The carbon uptake has a negative carbon footprint due to CO_2 utilization while all other processes have positive environmental impacts. Electricity supply is further subdivided in electricity for CO_2, $OME_{3\text{-}5}$, heat, and hydrogen supply in (B) and (C). Although not inside the system boundary of a well-to-tank analysis, we additionally indicate the end-of-life emissions from $OME_{3\text{-}5}$ combustion for the carbon footprint.

C.5.2 Entire life cycle

Here, life cycle impact assessment results are presented for the entire life cycle in the worst-case scenario. For CO_2 from direct air capture, we additionally show results for the best-case scenario as well as the sensitivity and fleet analyses.

Worst-case scenario

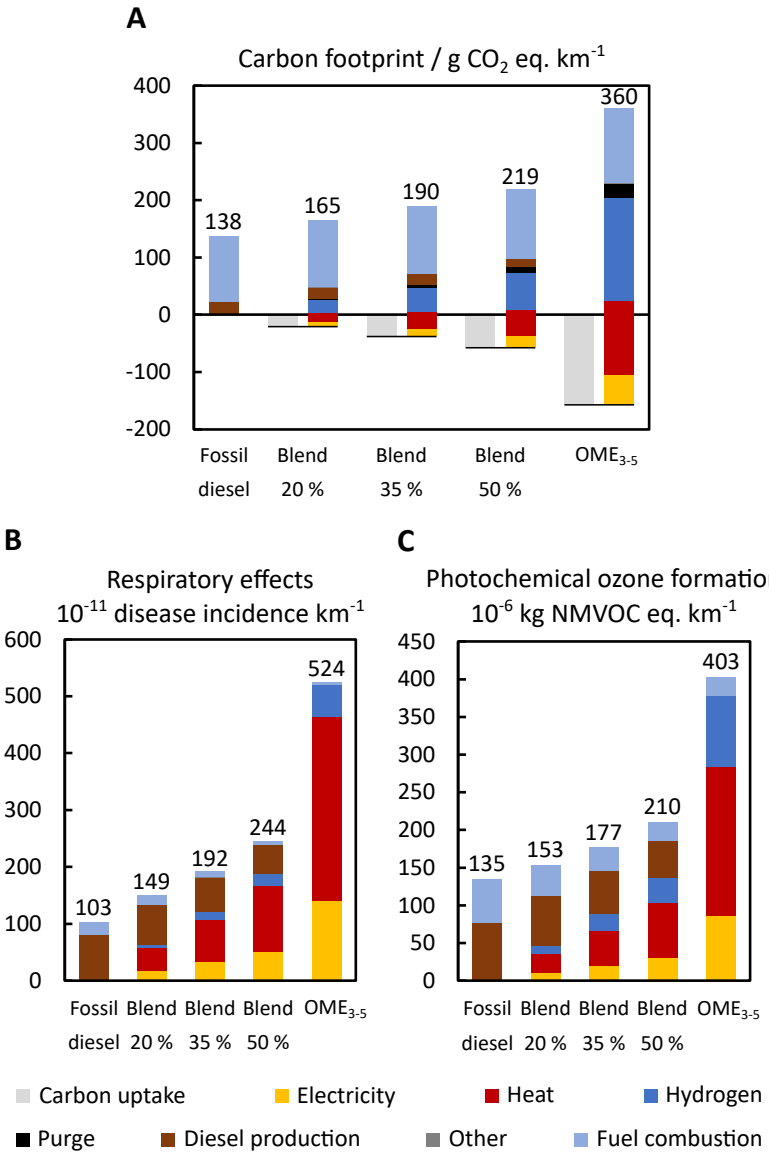

Figure C.8: Well-to-wheel (A) carbon footprint in g CO_2 eq. per km, (B) respiratory effects in 10^{-11} disease incidence per km, and (C) photochemical ozone formation in 10^{-6} kg NMVOC eq. per km of diesel-$OME_{3\text{-}5}$ blends in the worst-case scenario. $OME_{3\text{-}5}$ is produced via the MeOH DEHY route. The carbon uptake has a negative carbon footprint due to CO_2 utilization while all other processes have positive environmental impacts.

Best-case scenario with CO_2 from direct air capture

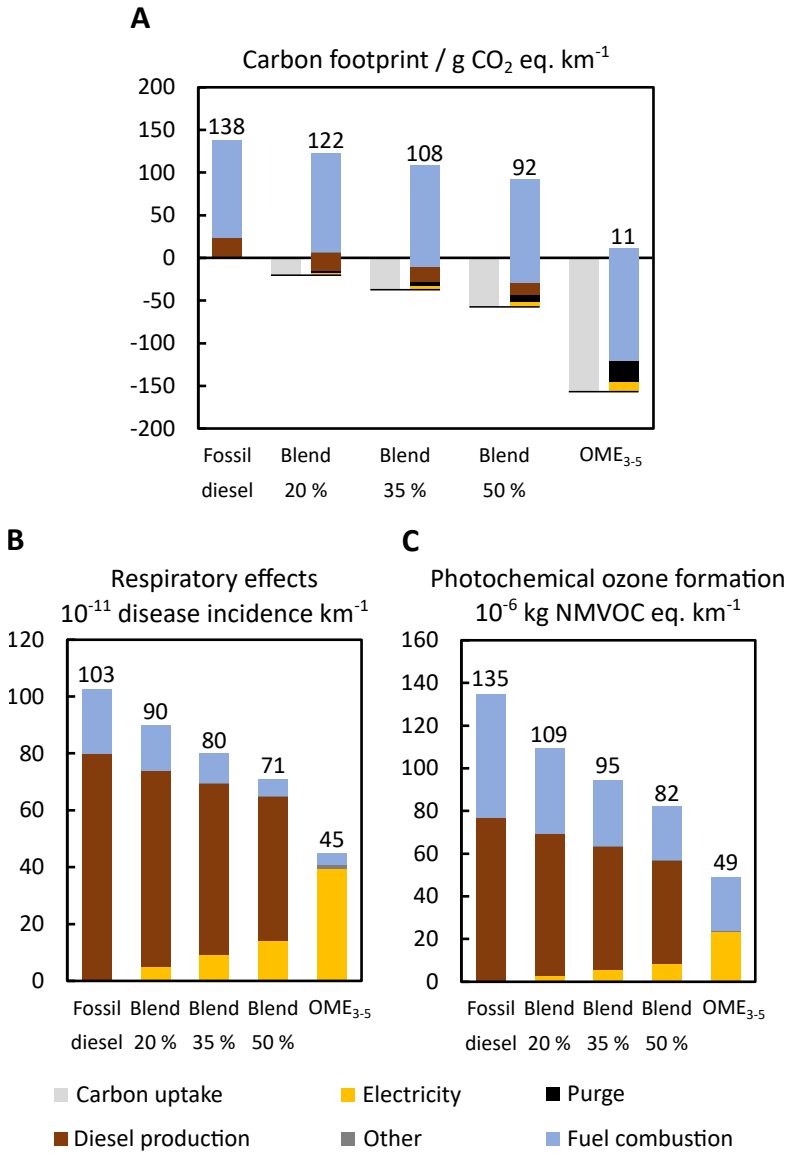

Figure C.9: Well-to-wheel (A) carbon footprint in g CO_2 eq. per km, (B) respiratory effects in 10^{-11} disease incidence per km, and (C) photochemical ozone formation in 10^{-6} kg NMVOC eq. per km of diesel-$OME_{3\text{-}5}$ blends in the best-case scenario with CO_2 from direct air capture. $OME_{3\text{-}5}$ is produced via the MeOH DEHY route. The carbon uptake has a negative carbon footprint due to CO_2 utilization while all other processes have positive environmental impacts.

Sensitivity analysis of electricity supply with CO_2 from direct air capture

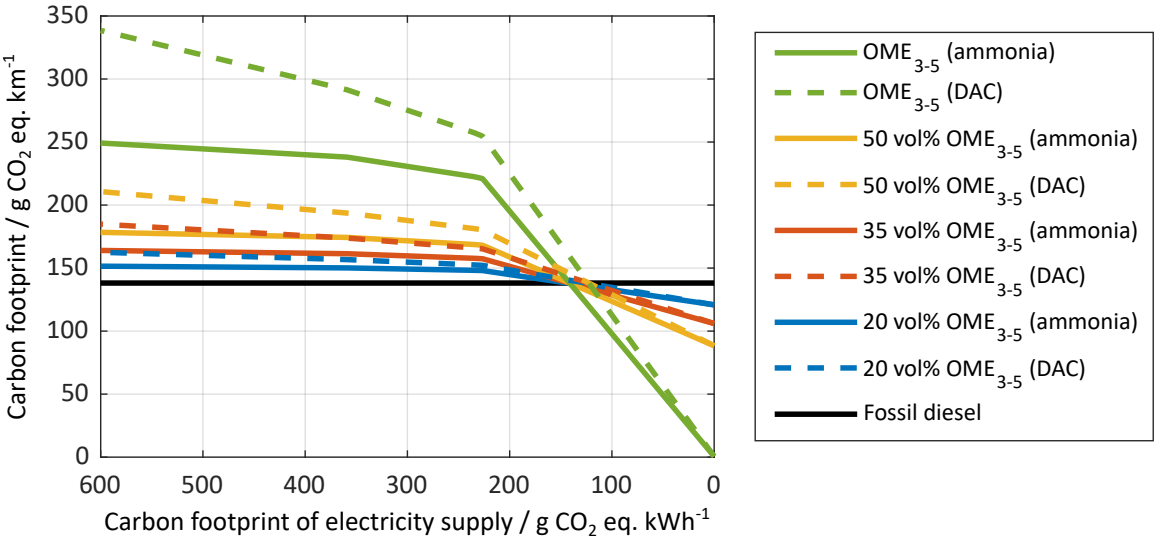

Figure C.10: Well-to-wheel carbon footprint in g CO_2 eq. per km of diesel-$OME_{3\text{-}5}$ blends as function of the carbon footprint of electricity supply. Results are shown for CO_2 from an ammonia plant (solid) and from DAC (dashed). $OME_{3\text{-}5}$ is produced via the MeOH DEHY route.

Fleet analysis with CO_2 from direct air capture

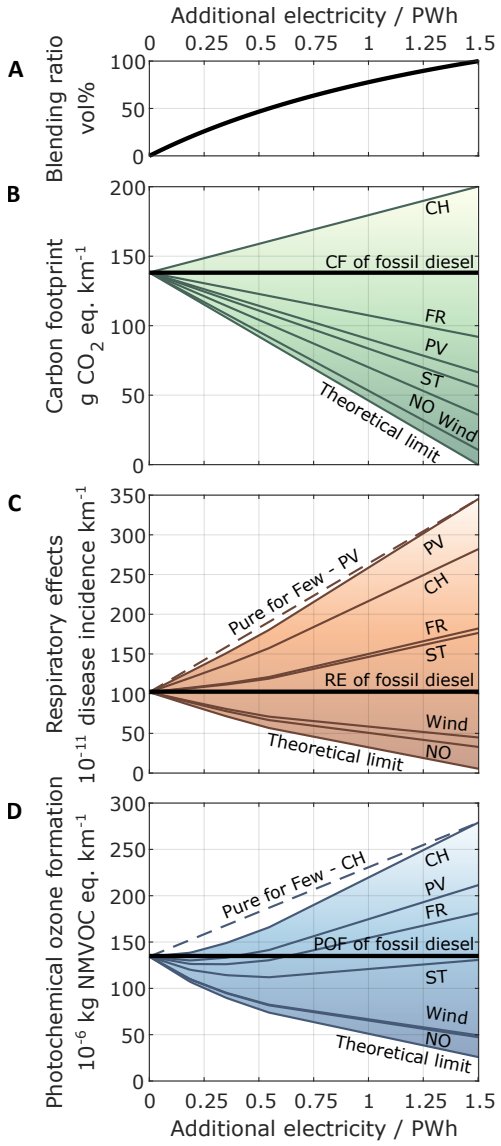

Figure C.11: (A) The volumetric blending ratio, the well-to-wheel (B) carbon footprint (CF), (C) respiratory effects (RE), and (D) photochemical ozone formation (POF) as function of available electricity for $OME_{3\text{-}5}$ production. Results are presented for country- and technology-specific environmental impacts of electricity. Solid curves indicate environmental impacts of blending $OME_{3\text{-}5}$ with fossil diesel for the entire fleet ("Blend for All"). Dashed lines show the results for switching only some diesel passenger cars to pure $OME_{3\text{-}5}$ usage ("Pure for Few"). "Pure for Few" is the linear combination of pure diesel and pure $OME_{3\text{-}5}$ and is, for the sake of better readability, shown for only two examples. For reference, black bold lines indicate environmental impacts of pure fossil diesel. $OME_{3\text{-}5}$ is produced via the MeOH DEHY route. CO_2 is supplied by direct air capture. CH: Switzerland, FR: France, NO: Norway, PV: photovoltaic, ST: solar-thermal. The theoretical limit of burden-free electricity is included as lower bound.

C.5.3 Contribution analyses

In this section, we present contribution analyses of the environmental impacts for the case "Blend for All" and various electricity supplies as function of the additionally available electricity for $OME_{3\text{-}5}$ production.

Note that respiratory effects and photochemical ozone formation are significantly higher with electricity from photovoltaic (Figure C.14) than from wind power (Figure C.17). The considered LCA datasets of the LCA database GaBi assume manufacturing of photovoltaic modules mostly in China, whereas most wind turbine components are assumed to be produced in Europe. In contrast to Europe, China's electricity mix has a higher proportion of coal-fired power plants with higher specific NO_x, sulphur dioxide, and PM emissions, increasing both environmental impacts strongly (GaBi, 2019).

Furthermore, photochemical ozone formation shows a minimum between 0.0 PWh and 0.5 PWh of additional electricity for Switzerland, France, and photovoltaic (Figure C.12–C.14). For these electricity supplies, emissions from electricity production overcompensate the nonlinear reduction of NO_x emissions during fuel combustion at these minima.

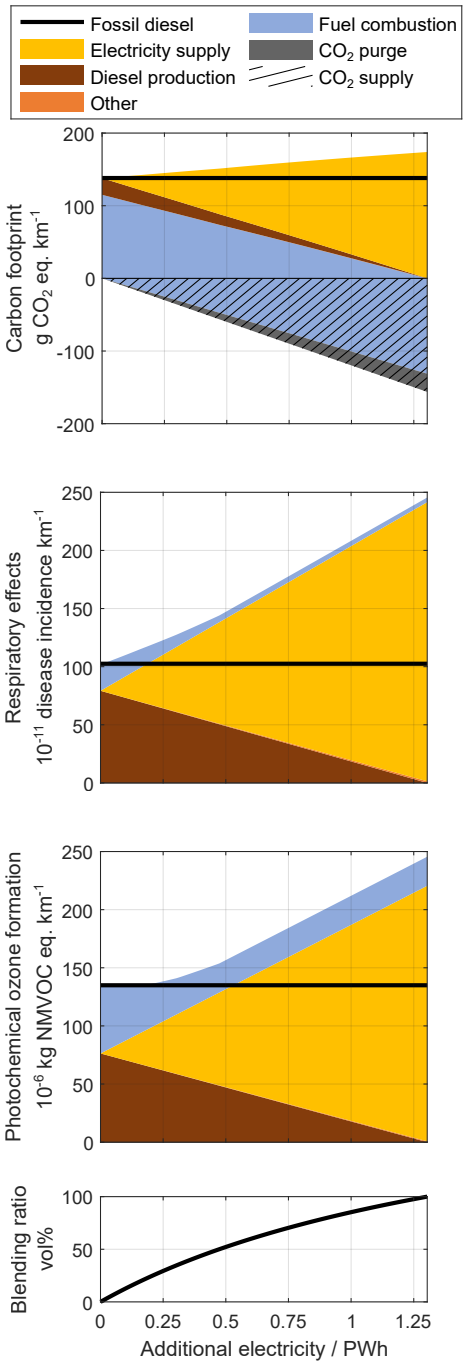

Figure C.12: Well-to-wheel carbon footprint, respiratory effects, photochemical ozone formation, and the volumetric blending ratio as functions of additionally available electricity for $OME_{3\text{-}5}$ production. Results are shown for the electricity supply of *Switzerland (CH)*. The well-to-wheel impacts include emissions along the entire life cycle of diesel-$OME_{3\text{-}5}$ blends. The black bold line represents the environmental impacts of the conventional fossil diesel system. $OME_{3\text{-}5}$ is produced via the MeOH DEHY route. CO_2 is supplied by an ammonia plant.

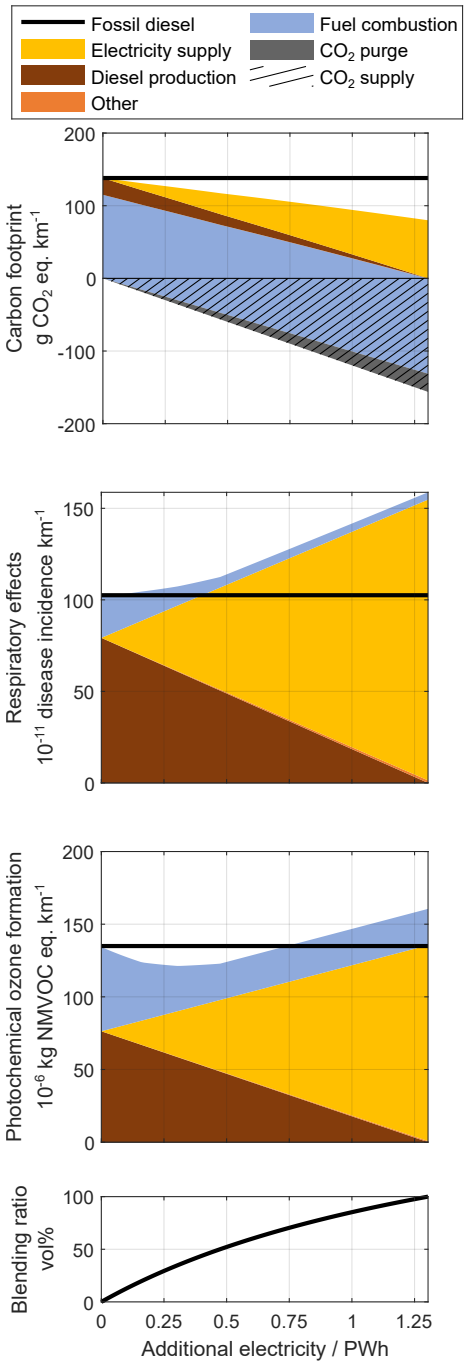

Figure C.13: Well-to-wheel carbon footprint, respiratory effects, photochemical ozone formation, and the volumetric blending ratio as functions of additionally available electricity for $OME_{3\text{-}5}$ production. Results are shown for the electricity supply of *France (FR)*. The well-to-wheel impacts include emissions along the entire life cycle of diesel-$OME_{3\text{-}5}$ blends. The black bold line represents the environmental impacts of the conventional fossil diesel system. $OME_{3\text{-}5}$ is produced via the MeOH DEHY route. CO_2 is supplied by an ammonia plant.

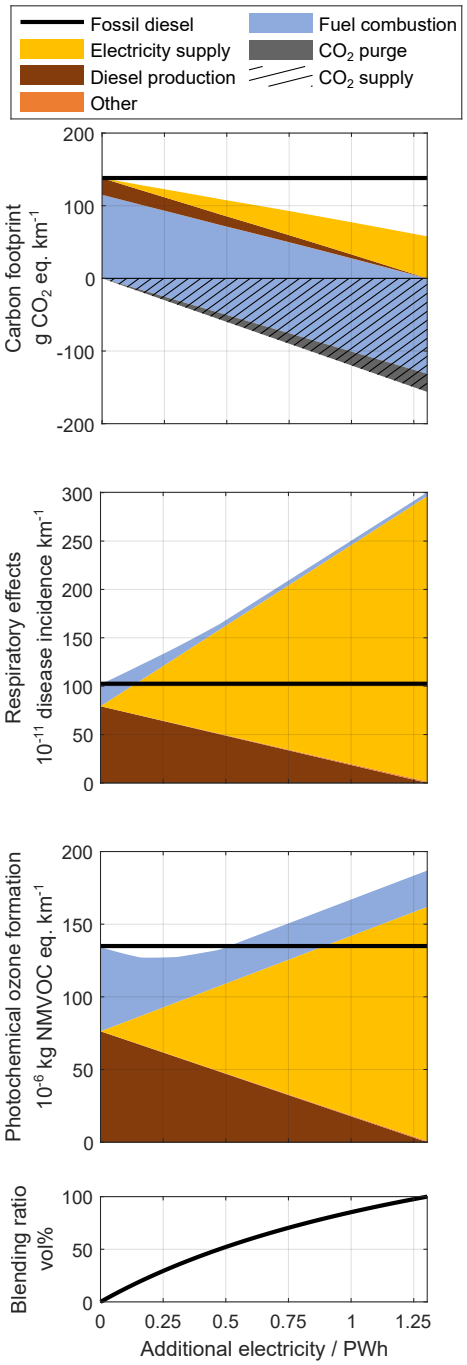

Figure C.14: Well-to-wheel carbon footprint, respiratory effects, photochemical ozone formation, and the volumetric blending ratio as functions of additionally available electricity for $OME_{3\text{-}5}$ production. Results are shown for electricity supply by *photovoltaic (PV)*. The well-to-wheel impacts include emissions along the entire life cycle of diesel-$OME_{3\text{-}5}$ blends. The black bold line represents the environmental impacts of the conventional fossil diesel system. $OME_{3\text{-}5}$ is produced via the MeOH DEHY route. CO_2 is supplied by an ammonia plant.

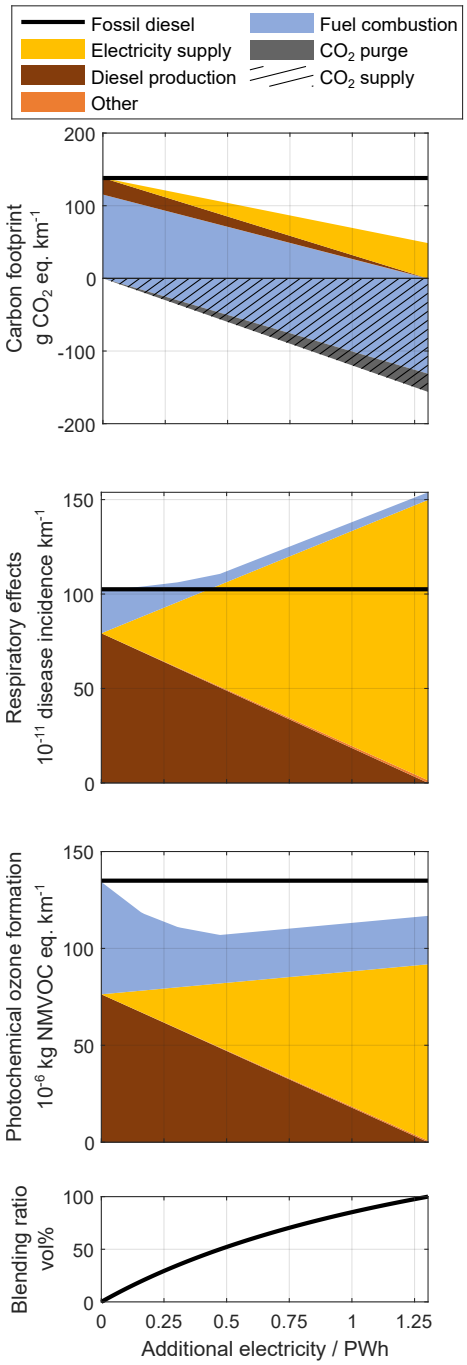

Figure C.15: Well-to-wheel carbon footprint, respiratory effects, photochemical ozone formation, and the volumetric blending ratio as functions of additionally available electricity for $OME_{3\text{-}5}$ production. Results are shown for electricity supply by *solar-thermal (ST) energy*. The well-to-wheel impacts include emissions along the entire life cycle of diesel-$OME_{3\text{-}5}$ blends. The black bold line represents the environmental impacts of the conventional fossil diesel system. $OME_{3\text{-}5}$ is produced via the MeOH DEHY route. CO_2 is supplied by an ammonia plant.

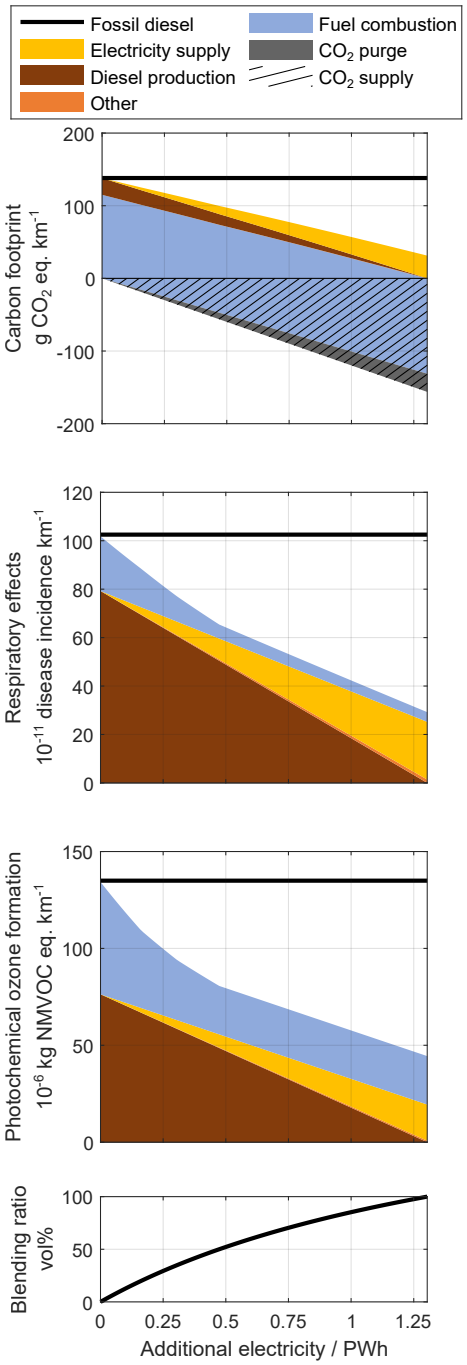

Figure C.16: Well-to-wheel carbon footprint, respiratory effects, photochemical ozone formation, and the volumetric blending ratio as functions of additionally available electricity for $OME_{3\text{-}5}$ production. Results are shown for the electricity supply of *Norway (NO)*. The well-to-wheel impacts include emissions along the entire life cycle of diesel-$OME_{3\text{-}5}$ blends. The black bold line represents the environmental impacts of the conventional fossil diesel system. $OME_{3\text{-}5}$ is produced via the MeOH DEHY route. CO_2 is supplied by an ammonia plant.

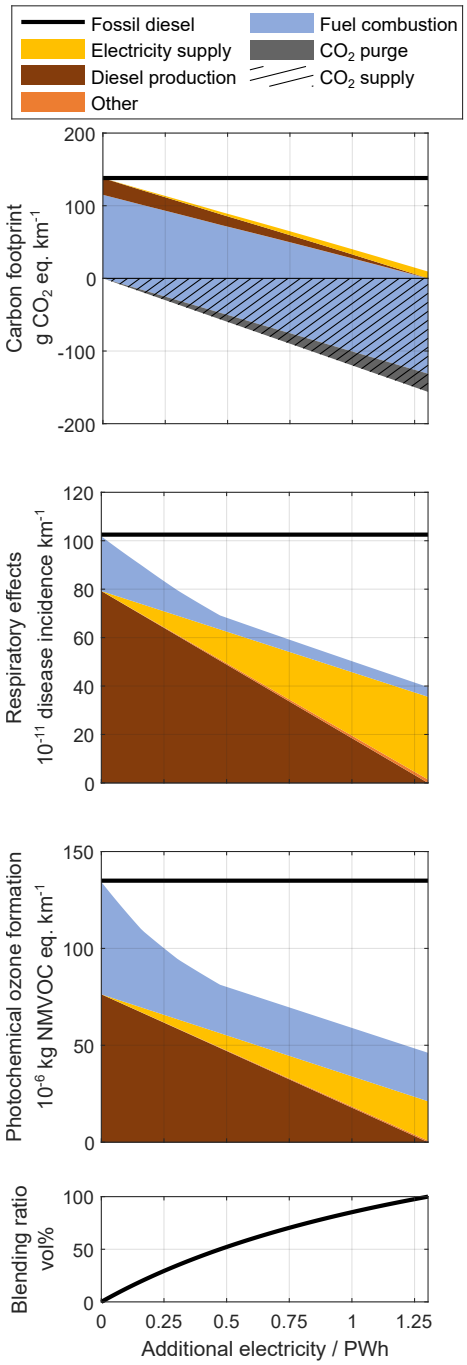

Figure C.17: Well-to-wheel carbon footprint, respiratory effects, photochemical ozone formation, and the volumetric blending ratio as functions of additionally available electricity for $OME_{3\text{-}5}$ production. Results are shown for electricity supply by *wind power*. The well-to-wheel impacts include emissions along the entire life cycle of diesel-$OME_{3\text{-}5}$ blends. The black bold line represents the environmental impacts of the conventional fossil diesel system. $OME_{3\text{-}5}$ is produced via the MeOH DEHY route. CO_2 is supplied by an ammonia plant.

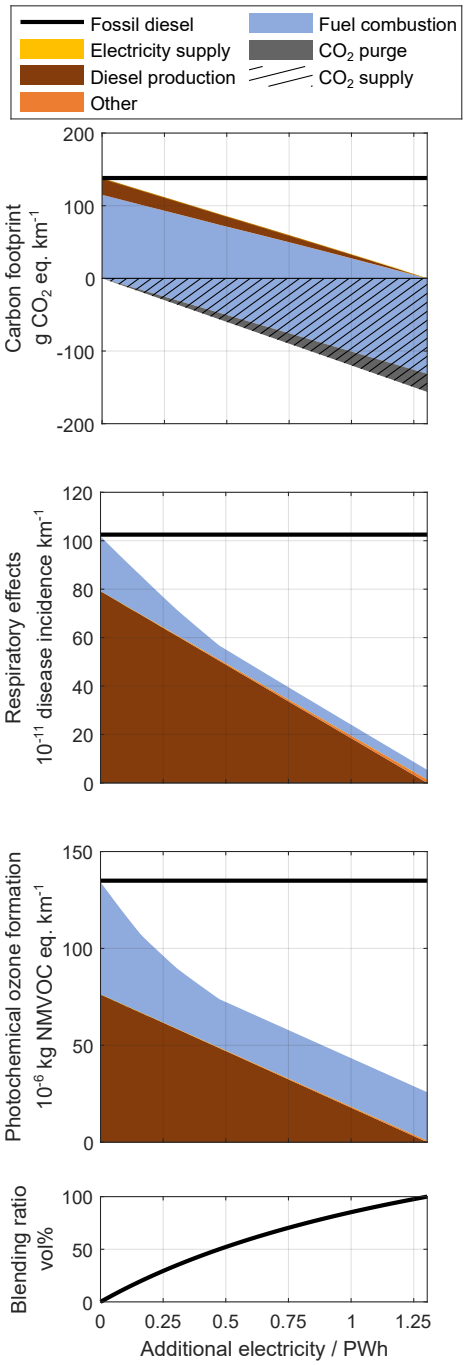

Figure C.18: Well-to-wheel carbon footprint, respiratory effects, photochemical ozone formation, and the volumetric blending ratio as functions of additionally available electricity for $OME_{3\text{-}5}$ production. Results are shown for the *theoretical limit of burden-free electricity*. The well-to-wheel impacts include emissions along the entire life cycle of diesel-$OME_{3\text{-}5}$ blends. The black bold line represents the environmental impacts of the conventional fossil diesel system. $OME_{3\text{-}5}$ is produced via the MeOH DEHY route. CO_2 is supplied by an ammonia plant.

Appendix D

Publications and student theses

List of publications

Journal papers

Völker, S., Ackermann, P., Granderath, M., Kortmann, C., Viell, J., Mitsos, A., and von der Aßen, N. (2024). Identifying key environmental objectives for integrated process and fuel design. *Sustainable Energy & Fuels*, **8**(9), 1966-1982.

Völker, S., Groll, N., Bachmann, M., Müller, L., Neumann, M., Kossioris, T., Muthyala, P., Lehrheuer, B., Hofmeister, M., Vorholt, A., Schmitz, K., Pischinger, S., Leitner, W., and Bardow, A. (2024). Towards carbon-neutral and clean propulsion in heavy-duty transportation with hydroformylated Fischer-Tropsch fuels. *Nature Energy*, **9**(10), 1220-1229.

Bachmann, M., Völker, S., Kleinekorte, J., and Bardow, A. (2023). Syngas from what? Comparative Life Cycle Assessment for Syngas Production from Biomass, CO_2, and steel mill off-gases. *ACS Sustainable Chemistry & Engineering*, **11**(14), 5356–5366.

Leow, W. R., Völker, S., Meys, R., Huang, J. E., Jaffer, S. A., Bardow, A., and Sargent, E. H. (2023). Electrified hydrocarbon-to-oxygenates coupled to hydrogen evolution for efficient greenhouse gas mitigation. *Nature Communications*, **14**(1), 1954.

Völker, S., Deutz, S., Burre, J., Bongartz, D., Omari, A., Lehrheuer, B., Mitsos, A., Pischinger, S., Bardow, A., and von der Aßen, N. (2022). Blend for all or pure for

few? Well-to-wheel life cycle assessment of blending electricity-based $OME_{3–5}$ with fossil diesel. *Sustainable Energy & Fuels*, **6**(8), 1959-1973.

Mantei, F., Ali, R. E., Baensch, C., Völker, S., Haltenort, P., Burger, J., Dietrich, R., von der Aßen, N., Schaadt, A., Sauer, J., and Salem, O. (2022). Techno-economic assessment and carbon footprint of processes for the large-scale production of oxymethylene dimethyl ethers from carbon dioxide and hydrogen. *Sustainable Energy & Fuels*, **6**(3), 528-549.

Ackermann, P., Braun, K., Burkardt, P., Heger, S., König, A., Morsch, P., Lehrheuer, B., Surger, M., Völker, S., Blank, L., Du, M., Heufer, K. A., Roß-Nickoll, M., Viell, J., von der Aßen, N., Mitsos, A., Pischinger, S., and Dahmen, M. (2021). Designed to Be Green, Economic, and Efficient: A Ketone-Ester-Alcohol-Alkane Blend for Future Spark-Ignition Engines. *ChemSusChem*, **14**(23), 5254-5264.

Burre, J., Bongartz, D., Deutz, S., Mebrahtu, C., Osterthun, O., Sun, R., Völker, S., Bardow, A., Klankermayer, J., Palkovits, R., and Mitsos, A. (2021). Comparing pathways for electricity-based production of dimethoxymethane as a sustainable fuel. *Energy & Environmental Science*, **14**(7), 3686-3699.

Roh, K., Bardow, A., Bongartz, D., Burre, J., Chung, W., Deutz, S., Han, D., Heßelmann, M., Kohlhaas, Y., König, A., Lee, J., Meys, R., Völker, S., Wessling, M., Lee, J., and Mitsos, A. (2020). Early-stage evaluation of emerging CO_2 utilization technologies at low technology readiness levels. *Green Chemistry*, **22**(12), 3842-3859.

Sick, V., Armstrong, K., Cooney, G., Cremonese, L., Eggleston, A., Faber, G., Hackett, G., Kätelhön, A., Keoleian, G., Marano, J., Marriott, J., McCord, S., Miller, S., Mutchek, M., Olfe-Kräutlein, B., Ravikumar, D., Roper, L., Schaidle, J., Skone, T., Smith, L., Strunge, T., Styring, P., Tao, L., Völker, S., and Zimmermann, A. (2019). The Need for and Path to Harmonized Life Cycle Assessment and Techno-Economic Assessment for Carbon Dioxide Capture and Utilization. *Energy Technology*, **8**(11), 1901034.

Conference contributions

Völker, S., Groll, N., Bachmann, M., Müller, L., Neumann, M., Kossioris, T., Muthyala, P., Lehrheuer, B., Hofmeister, M., Vorholt, A., Schmitz, K., Pischinger,

S., Leitner, W., and Bardow, A. (2023). The drop-in potential of hydroformylated Fischer-Tropsch fuels from CO_2. *Gordon Research Conference - Carbon Capture, Utilization and Storage*. Poster presentation. Les Diablerets, Switzerland.

Völker, S., Ackermann, P., Viell, J., Mitsos, A., and von der Aßen, N. (2023). Identifying the key environmental objectives for integrated fuel and process design. *11th International Conference on "Fuel Science - From Production to Propulsion"*. Oral presentation. Aachen, Germany.

Völker, S., Groll, N., Bachmann, M., Müller, L., Neumann, M., Kossioris, T., Muthyala, P., Lehrheuer, B., Hofmeister, M., Vorholt, A., Schmitz, K., Pischinger, S., Leitner, W., and Bardow, A. (2023). Towards sustainable transport with hydroformylated Fischer-Tropsch fuels as drop-in fuels employing drop-in technology. *11th International Conference on "Fuel Science - From Production to Propulsion"*. Oral presentation. Aachen, Germany.

Völker, S., Deutz, S., Burre, J., Bongartz, D., Omari, A., Lehrheuer, B., Pischinger, S., Mitsos, A., Bardow, A., and von der Aßen, N. (2022). Environmental potential of CO_2-based polyoxymethylene ethers as diesel blends. *19th International Conference on Carbon Dioxide Utilization (ICCDU)*. Oral presentation. Princeton, USA.

Völker, S., Ackermann, P., Viell, J., Mitsos, A., and von der Aßen, N. (2022). Integrated fuel and process design combined with life cycle assessment. *10th International Conference on "Fuel Science - From Production to Propulsion"*. Poster presentation. Aachen, Germany.

Dahmen, M., Burkardt, P., Ackermann, P., Braun, K., Heger, S., König, A., Morsch, P., Surger, M., Völker, S., Blank, L., Du, M., Heufer, K. A., Roß-Nickoll, M., Viell, J., von der Aßen, N., Mitsos, A., and Pischinger, S. (2021). Design and Multi-Disciplinary Assessment of a New FSC Blend for Ultra-High Efficiency Engines. *9th International Conference on "Fuel Science - From Production to Propulsion"*. Oral presentation. Aachen, Germany.

Völker, S., Deutz, S., Burre, J., Bongartz, D., Omari, A., Lehrheuer, B., Pischinger, S., Mitsos, A., Bardow, A., and von der Aßen, N. (2021). Well-to-Wheel Life Cycle Assessment of Blending $OME_{3\text{-}5}$ With Fossil Diesel. *9th International Conference on "Fuel Science - From Production to Propulsion"*. Oral presentation. Aachen, Germany.

Roh, K., Bardow, A., Bongartz, D., Burre, J., Chung, W., Deutz, S., Han, D., Heßelmann, M., Kohlhaas, Y., König, A., Lee, J. H., Lee, J. S., Meys, R., Völker, S., Wessling, M., and Mitsos, A. (2020). Early-stage evaluation procedure for CO_2 utilization technologies at low TRLs: A case study for electrochemical production of ethylene. *AIChE Annual Meeting 2020*. Oral presentation. Online.

Burre, J., Bongartz, D., Deutz, S., Völker, S., Bardow, A., and Mitsos, A. (2019). Comparison of Processes for Producing OME_1 - An Efficient, Economic, and Environmentally Sustainable e-Fuel?. *AIChE Annual Meeting 2019*. Oral presentation. Orlando, USA.

Student theses supervised during this work

Kipke, R. (2023). Simulative Prozessentwicklung und -bewertung von Methanol to Olefin-Verfahren im Kontext der synthetischen Kerosinherstellung. Master's thesis at the Institute of Electrochemical Process Engineering (IEK-14), Forschungszentrum Jülich GmbH, RWTH Aachen University.

Kortmann, C. J. (2022). Objective Reduction in Integrated Product and Process Optimization with embedded Life Cycle Assessment. Bachelor's thesis, RWTH Aachen University.

Granderath, M. (2022). Ökologische und ökonomische Optimierung einer Fahrzeugflotte unter der Berücksichtigung von Mobilitätsbedarfen privater Haushalte (in German). Bachelor's thesis, RWTH Aachen University.

Kalousdian, A. A. (2021). Life cycle assessment model of the supply chain from crude oil to commodity chemicals. Master's thesis at Carbon Minds GmbH, RWTH Aachen University.

Frohmann, J. (2020). CFD modeling and analysis of the effect of flow disturbers on the conditions in a fixed-bed Fischer-Tropsch reactor. Project thesis at the Energy Research Laboratory, University of California, Davis, RWTH Aachen University.

Pellny, Y. (2020). Potenzialanalyse von synthetischen Brennstoffen für ein zukünftiges Energiesystem (in German). Bachelor's thesis at the Institute of High Voltage Equipment and Grids, Digitalization and Energy Economics, RWTH Aachen University.

Bibliography

Aatola, H., Larmi, M., Sarjovaara, T., and Mikkonen, S. (2009). Hydrotreated Vegetable Oil (HVO) as a Renewable Diesel Fuel: Trade-off between NOx, Particulate Emission, and Fuel Consumption of a Heavy Duty Engine. *SAE International Journal of Engines*, 1(1):1251–1262.

Ackermann, P., Braun, K. E., Burkardt, P., Heger, S., König, A., Morsch, P., Lehrheuer, B., Surger, M., Völker, S., Blank, L. M., Du, M., Heufer, K. A., Roß-Nickoll, M., Viell, J., von der Aßen, N., Mitsos, A., Pischinger, S., and Dahmen, M. (2021). Designed to Be Green, Economic, and Efficient: A Ketone–Ester–Alcohol–Alkane Blend for Future Spark–Ignition Engines. *ChemSusChem*, 14(23):5254–5264.

Agora Verkehrswende (2017). *Transforming Transport to Ensure Tomorrow's Mobility: 12 Insights into the Verkehrswende.*

Agora Verkehrswende (2018). *Agora Energiewende and Frontier Economics: The Future Cost of Electricity-Based Synthetic Fuels.*

Aikawa, K., Sakurai, T., and Jetter, J. J. (2010). Development of a Predictive Model for Gasoline Vehicle Particulate Matter Emissions. *SAE International Journal of Fuels and Lubricants*, 3(2):610–622.

Ail, S. S. and Dasappa, S. (2016). Biomass to liquid transportation fuel via Fischer Tropsch synthesis – Technology review and current scenario. *Renewable and Sustainable Energy Reviews*, 58:267–286.

Albrecht, F. G., König, D. H., Baucks, N., and Dietrich, R.-U. (2017). A standardized methodology for the techno-economic evaluation of alternative fuels – A case study. *Fuel*, 194:511–526.

Alhyari, M., Al-Salaymeh, A., Irshidat, M., Kaltschmitt, M., and Neuling, U. (2019). The Impact of Energy Source on the Life-Cycle Assessment of Power-to-Liquid Fuels. *Journal of Ecological Engineering*, 20(4):239–244.

Alleman, T. L. and McCormick, R. L. (2003). Fischer-Tropsch Diesel Fuels - Properties and Exhaust Emissions: A Literature Review. In *SAE Technical Paper Series*, SAE Technical Paper Series, Warrendale, PA, United States. SAE International.

Ampelli, C., Perathoner, S., and Centi, G. (2015). CO2 utilization: an enabling element to move to a resource- and energy-efficient chemical and fuel production. *Philosophical transactions. Series A, Mathematical, physical, and engineering sciences*, 373(2037).

Anderson, K. and Peters, G. (2016). The trouble with negative emissions. *Science (New York, N.Y.)*, 354(6309):182–183.

Antipova, E., Boer, D., Cabeza, L. F., Guillén-Gosálbez, G., and Jiménez, L. (2013). Uncovering relationships between environmental metrics in the multi-objective optimization of energy systems: A case study of a thermal solar Rankine reverse osmosis desalination plant. *Energy*, 51:50–60.

Arcoumanis, C., Bae, C., Crookes, R., and Kinoshita, E. (2008). The potential of di-methyl ether (DME) as an alternative fuel for compression-ignition engines: A review. *Fuel*, 87(7):1014–1030.

Artz, J., Müller, T. E., Thenert, K., Kleinekorte, J., Meys, R., Sternberg, A., Bardow, A., and Leitner, W. (2018). Sustainable Conversion of Carbon Dioxide: An Integrated Review of Catalysis and Life Cycle Assessment. *Chemical reviews*, 118(2):434–504.

Arvidsson, R., Persson, S., Fröling, M., and Svanström, M. (2011). Life cycle assessment of hydrotreated vegetable oil from rape, oil palm and Jatropha. *Journal of Cleaner Production*, 19(2-3):129–137.

Azizi, Z., Rezaeimanesh, M., Tohidian, T., and Rahimpour, M. R. (2014). Dimethyl ether: A review of technologies and production challenges. *Chemical Engineering and Processing - Process Intensification*, 82:150–172.

Bachmann, M., Kätelhön, A., Winter, B., Meys, R., Müller, L. J., and Bardow, A. (2021). Renewable carbon feedstock for polymers: environmental benefits from synergistic use of biomass and CO2. *Faraday discussions*, 230:227–246.

Bachmann, M., Völker, S., Kleinekorte, J., and Bardow, A. (2023a). Syngas from What? Comparative Life-Cycle Assessment for Syngas Production from Biomass, CO2, and Steel Mill Off-Gases. *ACS Sustainable Chemistry & Engineering*, 11(14):5356–5366.

Bachmann, M., Zibunas, C., Hartmann, J., Tulus, V., Suh, S., Guillén-Gosálbez, G., and Bardow, A. (2023b). Towards circular plastics within planetary boundaries. *Nature Sustainability*, 6(5):599–610.

Baranowski, C. J., Bahmanpour, A. M., and Kröcher, O. (2017). Catalytic synthesis of polyoxymethylene dimethyl ethers (OME): A review. *Applied Catalysis B: Environmental*, 217:407–420.

Barbaro, P. and Bianchini, C., editors (2009). *Catalysis for Sustainable Energy Production*. Wiley.

Bareiß, K., de La Rua, C., Möckl, M., and Hamacher, T. (2019). Life cycle assessment of hydrogen from proton exchange membrane water electrolysis in future energy systems. *Applied Energy*, 237:862–872.

Bargiacchi, E., Antonelli, M., and Desideri, U. (2019). A comparative assessment of Power-to-Fuel production pathways. *Energy*, 183:1253–1265.

Bartoo, R. K. (1984). Removing Acid Gas by The Benfield Process. *Chemical Engineering Progress*, pages 35–39.

Baumgärtner, N., Deutz, S., Reinert, C., Nolzen, N., Kuepper, L. E., Hennen, M., Hollermann, D. E., and Bardow, A. (2021). Life-Cycle Assessment of Sector-Coupled National Energy Systems: Environmental Impacts of Electricity, Heat, and Transportation in Germany Till 2050. *Frontiers in Energy Research*, 9.

Bausa, J., Watzdorf, R. v., and Marquardt, W. (1998). Shortcut methods for nonideal multicomponent distillation: I. Simple columns. *AIChE Journal*, 44(10):2181–2198.

Becker, T., Wolff, M., Linzenich, A., Engelmann, L., Arning, K., Ziefle, M., and Walther, G. (2024). An integrated bi-objective optimization model accounting for the social acceptance of renewable fuel production networks. *European Journal of Operational Research*, 315(1):354–367.

Blanco, H., Nijs, W., Ruf, J., and Faaij, A. (2018). Potential for hydrogen and Power-to-Liquid in a low-carbon EU energy system using cost optimization. *Applied Energy*, 232:617–639.

Bokinge, P., Heyne, S., and Harvey, S. (2020). Renewable OME from biomass and electricity—Evaluating carbon footprint and energy performance. *Energy Science & Engineering*, 8(7):2587–2598.

Bongartz, D., Burre, J., and Mitsos, A. (2019). Production of Oxymethylene Dimethyl Ethers from Hydrogen and Carbon Dioxide—Part I: Modeling and Analysis for OME 1. *Industrial & Engineering Chemistry Research*, 58(12):4881–4889.

Bongartz, D., Doré, L., Eichler, K., Grube, T., Heuser, B., Hombach, L. E., Robinius, M., Pischinger, S., Stolten, D., Walther, G., and Mitsos, A. (2018). Comparison of light-duty transportation fuels produced from renewable hydrogen and green carbon dioxide. *Applied Energy*, 231:757–767.

Börner, A. and Franke, R. (2016). *Hydroformylation*. Wiley-VCH Verlag GmbH & Co. KGaA, Weinheim, Germany.

Borning, M., Doré, L., Wolff, M., Walter, J., Becker, T., Walther, G., and Moser, A. (2020). Opportunities and Challenges of Flexible Electricity-Based Fuel Production for the European Power System. *Sustainability*, 12(23):9844.

Borrion, A. L., McManus, M. C., and Hammond, G. P. (2012). Environmental life cycle assessment of bioethanol production from wheat straw. *Biomass and Bioenergy*, 47:9–19.

Borugadda, V. B., Kamath, G., and Dalai, A. K. (2020). Techno-economic and life-cycle assessment of integrated Fischer-Tropsch process in ethanol industry for biodiesel and bio-gasoline production. *Energy*, 195:116985.

Breitkreuz, C. F., Schmitz, N., Ströfer, E., Burger, J., and Hasse, H. (2018). Design of a Production Process for Poly(oxymethylene) Dimethyl Ethers from Dimethyl Ether and Trioxane. *Chemie Ingenieur Technik*, 90(10):1489–1496.

Breuer, J., Scholten, J., Koj, J., Schorn, F., Fiebrandt, M., Samsun, R., Albus, R., Görner, K., Stolten, D., and Peters, R. (2022). An Overview of Promising Alternative Fuels for Road, Rail, Air, and Inland Waterway Transport in Germany. *Energies*, 15(4):1443–1507.

Brill, E. D., Chang, S.-Y., and Hopkins, L. D. (1982). Modeling to Generate Alternatives: The HSJ Approach and an Illustration Using a Problem in Land Use Planning. *Management Science*, 28(3):221–235.

Brill, E. D., Flach, J. M., Hopkins, L. D., and Ranjithan, S. (1990). MGA: a decision support system for complex, incompletely defined problems. *IEEE Transactions on Systems, Man, and Cybernetics*, 20(4):745–757.

Brockhoff, D. and Zitzler, E. (2006). Are All Objectives Necessary? On Dimensionality Reduction in Evolutionary Multiobjective Optimization. In Hutchison, D., Kanade, T., Kittler, J., Kleinberg, J. M., Mattern, F., Mitchell, J. C., Naor, M., Nierstrasz, O., Pandu Rangan, C., Steffen, B., Sudan, M., Terzopoulos, D., Tygar, D., Vardi, M. Y., Weikum, G., Runarsson, T. P., Beyer, H.-G., Burke, E., Merelo-Guervós, J. J., Whitley, L. D., Yao, X., and Burke, E. K., editors, *Parallel Problem Solving from Nature - PPSN IX*, volume 4193 of *SpringerLink Bücher*, pages 533–542. Springer Berlin Heidelberg, Berlin, Heidelberg.

Brockhoff, D. and Zitzler, E. (2009). Objective reduction in evolutionary multiobjective optimization: theory and applications. *Evolutionary computation*, 17(2):135–166.

Brunet, R., Guillén-Gosálbez, G., and Jiménez, L. (2012). Cleaner Design of Single-Product Biotechnological Facilities through the Integration of Process Simulation, Multiobjective Optimization, Life Cycle Assessment, and Principal Component Analysis. *Industrial & Engineering Chemistry Research*, 51(1):410–424.

Brynolf, S., Hansson, J., Anderson, J. E., Skov, I. R., Wallington, T. J., Grahn, M., Korberg, A. D., Malmgren, E., and Taljegård, M. (2022). Review of electrofuel feasibility—prospects for road, ocean, and air transport. *Progress in Energy*, 4(4):042007.

Brynolf, S., Taljegard, M., Grahn, M., and Hansson, J. (2018). Electrofuels for the transport sector: A review of production costs. *Renewable and Sustainable Energy Reviews*, 81:1887–1905.

Bui, M., Adjiman, C. S., Bardow, A., Anthony, E. J., Boston, A., Brown, S., Fennell, P. S., Fuss, S., Galindo, A., Hackett, L. A., Hallett, J. P., Herzog, H. J., Jackson, G., Kemper, J., Krevor, S., Maitland, G. C., Matuszewski, M., Metcalfe, I. S., Petit, C., Puxty, G., Reimer, J., Reiner, D. M., Rubin, E. S., Scott, S. A., Shah, N., Smit, B., Trusler, J. P. M., Webley, P., Wilcox, J., and Mac Dowell, N. (2018). Carbon capture and storage (CCS): the way forward. *Energy & Environmental Science*, 11(5):1062–1176.

Burger, J., Siegert, M., Ströfer, E., and Hasse, H. (2010). Poly(oxymethylene) dimethyl ethers as components of tailored diesel fuel: Properties, synthesis and purification concepts. *Fuel*, 89(11):3315–3319.

Burger, J., Ströfer, E., and Hasse, H. (2012). Chemical Equilibrium and Reaction Kinetics of the Heterogeneously Catalyzed Formation of Poly(oxymethylene) Dimethyl

Ethers from Methylal and Trioxane. *Industrial & Engineering Chemistry Research*, 51(39):12751–12761.

Burger, J., Ströfer, E., and Hasse, H. (2013). Production process for diesel fuel components poly(oxymethylene) dimethyl ethers from methane-based products by hierarchical optimization with varying model depth. *Chemical Engineering Research and Design*, 91(12):2648–2662.

Burre, J., Bongartz, D., Deutz, S., Mebrahtu, C., Osterthun, O., Sun, R., Völker, S., Bardow, A., Klankermayer, J., Palkovits, R., and Mitsos, A. (2021). Comparing pathways for electricity-based production of dimethoxymethane as a sustainable fuel. *Energy Environ. Sci.*, 14(7):3686–3699.

Burre, J., Bongartz, D., and Mitsos, A. (2019). Production of Oxymethylene Dimethyl Ethers from Hydrogen and Carbon Dioxide—Part II: Modeling and Analysis for OME 3–5. *Industrial & Engineering Chemistry Research*, 58(14):5567–5578.

Carreras, J., Pozo, C., Boer, D., Guillén-Gosálbez, G., Caballero, J. A., Ruiz-Femenia, R., and Jiménez, L. (2016). Systematic approach for the life cycle multi-objective optimization of buildings combining objective reduction and surrogate modeling. *Energy and Buildings*, 130(3):506–518.

Chen, L., Debnath, D., Zhong, J., Ferin, K., VanLoocke, A., and Khanna, M. (2021). The economic and environmental costs and benefits of the renewable fuel standard. *Environmental Research Letters*, 16(3):034021.

Chu, K., Liu, W., She, Y., Hua, Z., Tan, M., Liu, X., Gu, L., and Jia, Y. (2018). Modified Principal Component Analysis for Identifying Key Environmental Indicators and Application to a Large-Scale Tidal Flat Reclamation. *Water*, 10(1):69.

Colelli, L., Segneri, V., Bassano, C., and Vilardi, G. (2023). E-fuels, technical and economic analysis of the production of synthetic kerosene precursor as sustainable aviation fuel. *Energy Conversion and Management*, 288:117165.

Copado-Méndez, P. J., Guillén-Gosálbez, G., and Jiménez, L. (2014). MILP-based decomposition algorithm for dimensionality reduction in multi-objective optimization: Application to environmental and systems biology problems. *Computers & Chemical Engineering*, 67(19):137–147.

Copado-Méndez, P. J., Pozo, C., Guillén-Gosálbez, G., and Jiménez, L. (2016). Enhancing the epsilon-constraint method through the use of objective reduction and

random sequences: Application to environmental problems. *Computers & Chemical Engineering*, 87:36–48.

Cornils, B., Börner, A., Franke, R., Zhang, B., Wiebus, E., and Schmid, K. (2018). Hydroformylation. In Cornils, B., Herrmann, W. A., Beller, M., and Paciello, R., editors, *Applied homogeneous catalysis with organometallic compounds*, pages 23–90. Wiley-VCH Verlag GmbH & Co. KGaA, Weinheim.

Cornils, B., Herrmann, W. A., Zanthoff, H.-W., and Wong, C.-H. (2013). *Catalysis from A to Z*. Wiley-VCH Verlag GmbH & Co. KGaA, Weinheim, Germany.

Čuček, L., Klemeš, J. J., and Kravanja, Z. (2014). Objective dimensionality reduction method within multi-objective optimisation considering total footprints. *Journal of Cleaner Production*, 71:75–86.

Cuéllar-Franca, R., García-Gutiérrez, P., Dimitriou, I., Elder, R. H., Allen, R. W., and Azapagic, A. (2019). Utilising carbon dioxide for transport fuels: The economic and environmental sustainability of different Fischer-Tropsch process designs. *Applied Energy*, 253:113560–113579.

da Silva, A. R. G., Torres Ortega, C. E., and Rong, B.-G. (2016). Techno-economic analysis of different pretreatment processes for lignocellulosic-based bioethanol production. *Bioresource technology*, 218(2):561–570.

Dahmen, M. and Marquardt, W. (2016). Model-Based Design of Tailor-Made Biofuels. *Energy & Fuels*, 30(2):1109–1134.

Dahmen, M. and Marquardt, W. (2017). Model-Based Formulation of Biofuel Blends by Simultaneous Product and Pathway Design. *Energy & Fuels*, 31(4):4096–4121.

Das, D. D., St. John, P. C., McEnally, C. S., Kim, S., and Pfefferle, L. D. (2018). Measuring and predicting sooting tendencies of oxygenates, alkanes, alkenes, cycloalkanes, and aromatics on a unified scale. *Combustion and Flame*, 190:349–364.

David, A., Mathiesen, B. V., Averfalk, H., Werner, S., and Lund, H. (2017). Heat Roadmap Europe: Large-Scale Electric Heat Pumps in District Heating Systems. *Energies*, 10(4):578.

Daylan, B. and Ciliz, N. (2016). Life cycle assessment and environmental life cycle costing analysis of lignocellulosic bioethanol as an alternative transportation fuel. *Renewable Energy*, 89:578–587.

de Jong, S., Antonissen, K., Hoefnagels, R., Lonza, L., Wang, M., Faaij, A., and Junginger, M. (2017). Life-cycle analysis of greenhouse gas emissions from renewable jet fuel production. *Biotechnology for biofuels*, 10:64–81.

Deb, K. and Saxena, D. K. (2005). On finding pareto-optimal solutions through dimensionality reduction for certain large-dimensional multi-objective optimization problems: Kangal report, 2005011. pages 1–19.

Deb, K. and Saxena, D. K. (2006). Searching for Pareto-optimal solutions through dimensionality reduction for certain large-dimensional multi-objective optimization problems. In *Proceedings of the world congress on computational intelligence (WCCI-2006)*, pages 3352–3360.

Decker, M., Schorn, F., Samsun, R. C., Peters, R., and Stolten, D. (2019). Off-grid power-to-fuel systems for a market launch scenario – A techno-economic assessment. *Applied Energy*, 250:1099–1109.

Delgado, H. E., Cappello, V., Zang, G., Sun, P., Ng, C., Vyawahare, P., Elgowainy, A. A., Wendt, D. S., Boardman, R. D., and Marcinkoski, J. (2023). Techno-economic analysis and life cycle analysis of e-fuel production using nuclear energy. *Journal of CO2 Utilization*, 72:102481.

Deutz, S. and Bardow, A. (2021). Life-cycle assessment of an industrial direct air capture process based on temperature–vacuum swing adsorption. *Nature Energy*, 6:203–213.

Deutz, S., Bongartz, D., Heuser, B., Kätelhön, A., Schulze Langenhorst, L., Omari, A., Walters, M., Klankermayer, J., Leitner, W., Mitsos, A., Pischinger, S., and Bardow, A. (2018). Cleaner production of cleaner fuels: wind-to-wheel – environmental assessment of CO 2 -based oxymethylene ether as a drop-in fuel. *Energy & Environmental Science*, 11(2):331–343.

Dharma, S., Ong, H. C., Masjuki, H. H., Sebayang, A. H., and Silitonga, A. S. (2016). An overview of engine durability and compatibility using biodiesel–bioethanol–diesel blends in compression-ignition engines. *Energy Conversion and Management*, 128(Part B):66–81.

Dieterich, V., Buttler, A., Hanel, A., Spliethoff, H., and Fendt, S. (2020). Power-to-liquid via synthesis of methanol, DME or Fischer–Tropsch-fuels: a review. *Energy & Environmental Science*, 13(10):3207–3252.

Dietrich, R.-U., Albrecht, F. G., Maier, S., König, D. H., Estelmann, S., Adelung, S., Bealu, Z., and Seitz, A. (2018). Cost calculations for three different approaches of biofuel production using biomass, electricity and CO2. *Biomass and Bioenergy*, 111:165–173.

Dimitriou, I., Goldingay, H., and Bridgwater, A. V. (2018). Techno-economic and uncertainty analysis of Biomass to Liquid (BTL) systems for transport fuel production. *Renewable and Sustainable Energy Reviews*, 88:160–175.

Drünert, S., Neuling, U., Zitscher, T., and Kaltschmitt, M. (2020). Power-to-Liquid fuels for aviation – Processes, resources and supply potential under German conditions. *Applied Energy*, 277:115578.

Dry, M. E. and Steynberg, A. P. (2006). Commercial FT Process Applications. In Steynberg, A. and Dry, M., editors, *Fischer-Tropsch technology*, volume 152 of *Studies in Surface Science and Catalysis*, pages 406–481. Elsevier, Amsterdam.

Dubois, L. and Thomas, D. (2018). Comparison of various configurations of the absorption-regeneration process using different solvents for the post-combustion CO2 capture applied to cement plant flue gases. *International Journal of Greenhouse Gas Control*, 69:20–35.

Dunn, J. B., Mueller, S., Kwon, H.-Y., and Wang, M. Q. (2013). Land-use change and greenhouse gas emissions from corn and cellulosic ethanol. *Biotechnology for biofuels*, 6(1):51.

Dunn, R. J. H., Stanitski, D. M., Gobron, N., and Willett, K. M. (2020). Global Climate: [in "State of the Climate in 2019"]. *Bulletin of the American Meteorological Society*, 101(8):S9–S127.

El-Halwagi, M. M. (2012). Overview of Process Economics. In *Sustainable Design Through Process Integration*, volume 91, pages 15–61. Elsevier.

El-Seesy, A. I., El-Zoheiry, R. M., Fouad, A. K., Hussien, A. M., Elshabrawy, S. O. M., He, Z., and Nasser, A. (2021). Impacts of octanol and decanol addition on the solubility of methanol/hydrous methanol/diesel/biodiesel/Jet A-1 fuel ternary mixtures. *RSC advances*, 11(30):18213–18224.

European Commission (2011). *International reference life cycle data system (ILCD) handbook: General guide for life cycle assessment: provisions and action steps*, volume 24571 of *EUR, Scientific and technical research series*. Publications Office, Luxembourg, first edition edition.

European Commission (2015). *Best Available Techniques (BAT) Reference Document for the Refining of Mineral Oil and Gas: Industrial Emissions Directive 2010/75/EU (Integrated Pollution Prevention and Control).* Publications Office, Luxembourg.

European Commission (2017). *Technology readiness level: guidance principles for renewable energy technologies: final report.* Publications Office.

European Commission (2018a). Directive (EU) 2018/2001 of the European Parliament and of the Council of 11 December 2018 on the promotion of the use of energy from renewable sources.

European Commission (2018b). *Supporting information to the characterisation factors of recommended EF Life Cycle Impact Assessment methods: Version 2, from ILCD to EF 3.0.* Publications Office of the European Union.

European Commission (2019). Regulation (EU) 2019/631 of the European Parliament and of the Council of 17 April 2019 setting CO2 emission performance standards for new passenger cars and for new light commercial vehicles, and repealing Regulations (EC) No 443/2009 and (EU) No 510/2011.

European Environment Agency (2018). *Air quality in Europe: 2018 report: EEA report No 12/2018*, volume No 12/2018. Publications Office of the European Union, Luxembourg.

Eurostat (2020a). Electricity production, consumption and market overview.

Eurostat (2020b). Passenger cars in the EU.

Fargione, J., Hill, J., Tilman, D., Polasky, S., and Hawthorne, P. (2008). Land clearing and the biofuel carbon debt. *Science (New York, N.Y.)*, 319(5867):1235–1238.

Farla, J. C. M., Hendriks, C. A., and Blok, K. (1995). Carbon dioxide recovery from industrial processes. *Climatic Change*, 29(4):439–461.

Fazal, M. A., Haseeb, A., and Masjuki, H. H. (2011). Biodiesel feasibility study: An evaluation of material compatibility; performance; emission and engine durability. *Renewable and Sustainable Energy Reviews*, 15(2):1314–1324.

Fenton, O. and Ó hUallacháin, D. (2012). Agricultural nutrient surpluses as potential input sources to grow third generation biomass (microalgae): A review. *Algal Research*, 1(1):49–56.

Fernández-Dacosta, C., Shen, L., Schakel, W., Ramirez, A., and Kramer, G. J. (2019). Potential and challenges of low-carbon energy options: Comparative assessment of alternative fuels for the transport sector. *Applied Energy*, 236:590–606.

Fioroni, G., Fouts, L., Luecke, J., Vardon, D., Huq, N., Christensen, E., Huo, X., Alleman, T., McCormick, R., Kass, M., Polikarpov, E., Kukkadapu, G., and Whitesides, R. A. (2019). Screening of Potential Biomass-Derived Streams as Fuel Blendstocks for Mixing Controlled Compression Ignition Combustion. *SAE International Journal of Advances and Current Practices in Mobility*, 1(3):1117–1138.

Fleitmann, L., Ackermann, P., Schilling, J., Kleinekorte, J., Rittig, J. G., vom Lehn, F., Schweidtmann, A. M., Pitsch, H., Leonhard, K., Mitsos, A., Bardow, A., and Dahmen, M. (2023). Molecular Design of Fuels for Maximum Spark-Ignition Engine Efficiency by Combining Predictive Thermodynamics and Machine Learning. *Energy & Fuels*, 37(3):2213–2229.

Franke, R., Selent, D., and Börner, A. (2012). Applied hydroformylation. *Chemical reviews*, 112(11):5675–5732.

Freire Ordóñez, D., Shah, N., and Guillén-Gosálbez, G. (2021). Economic and full environmental assessment of electrofuels via electrolysis and co-electrolysis considering externalities. *Applied Energy*, 286:116488.

Frischknecht, R. (1998). *Life cycle inventory analysis for decision-making: scope-dependent inventory system models and context-specific joint product allocation*. PhD thesis, ETH Zurich, Zurich.

Fuss, S., Lamb, W. F., Callaghan, M. W., Hilaire, J., Creutzig, F., Amann, T., Beringer, T., de Oliveira Garcia, W., Hartmann, J., Khanna, T., Luderer, G., Nemet, G. F., Rogelj, J., Smith, P., Vicente, J. L. V., Wilcox, J., del Mar Zamora Dominguez, M., and Minx, J. C. (2018). Negative emissions—Part 2: Costs, potentials and side effects. *Environmental Research Letters*, 13(6):063002.

GaBi (2019). *GaBi 9.2.0.58: Software-System and Database for Life Cycle Engineering, DB 8.7 - SP 39*. thinkstep AG, Leinfelden-Echterdingen, Germany.

Gal, T. and Leberling, H. (1977). Redundant objective functions in linear vector maximum problems and their determination. *European Journal of Operational Research*, 1(3):176–184.

Gao, R., Wang, L., Zhang, L., Zhang, C., Jun, K.-W., Ki Kim, S., Park, H.-G., Zhao, T., Gao, Y., Zhu, Y., Wan, H., and Guan, G. (2022). Upcycling of CO2 into sustainable hydrocarbon fuels via the integration of Fe-based Fischer-Tropsch synthesis and olefin oligomerization: A comparative case study. *Fuel*, 325(12):124855.

Gao, R., Zhang, C., Jun, K.-W., Kim, S. K., Park, H.-G., Zhao, T., Wang, L., Wan, H., and Guan, G. (2021). Green liquid fuel and synthetic natural gas production via CO2 hydrogenation combined with reverse water-gas-shift and Co-based Fischer-Tropsch synthesis. *Journal of CO2 Utilization*, 51(5):101619.

García, A., Monsalve-Serrano, J., Villalta, D., Zubel, M., and Pischinger, S. (2018). Potential of 1-octanol and di-n-butyl ether (DNBE) to improve the performance and reduce the emissions of a direct injected compression ignition diesel engine. *Energy Conversion and Management*, 177(3):563–571.

Gnanasekaran, L., Priya, A. K., Thanigaivel, S., Hoang, T. K., and Soto-Moscoso, M. (2023). The conversion of biomass to fuels via cutting-edge technologies: Explorations from natural utilization systems. *Fuel*, 331:125668.

Gnansounou, E. and Dauriat, A. (2010). Techno-economic analysis of lignocellulosic ethanol: A review. *Bioresource technology*, 101(13):4980–4991.

Gong, E., Ali, S., Hiragond, C. B., Kim, H. S., Powar, N. S., Kim, D., Kim, H., and In, S.-I. (2022). Solar fuels: research and development strategies to accelerate photocatalytic CO2 conversion into hydrocarbon fuels. *Energy & Environmental Science*, 15(3):880–937.

González-García, S., Iribarren, D., Susmozas, A., Dufour, J., and Murphy, R. J. (2012). Life cycle assessment of two alternative bioenergy systems involving Salix spp. biomass: Bioethanol production and power generation. *Applied Energy*, 95:111–122.

González-García, S., Moreira, M. T., and Feijoo, G. (2010). Comparative environmental performance of lignocellulosic ethanol from different feedstocks. *Renewable and Sustainable Energy Reviews*, 14(7):2077–2085.

Grube, T. and Höhlein, B. (2014). Kosten der Wasserstoffbereitstellung in Versorgungssystemen auf Basis erneuerbarer Energien. In Lehmann, J. and Töpler, J., editors, *Wasserstoff und Brennstoffzelle*, SpringerLink Bücher, pages 225–239. Springer Vieweg, Berlin, Heidelberg.

Grünert, A., Losch, P., Ochoa-Hernández, C., Schmidt, W., and Schüth, F. (2018). Gas-phase synthesis of oxymethylene ethers over Si-rich zeolites. *Green Chemistry*, 20(20):4719–4728.

Grützner, T., Hasse, H., Lang, N., Siegert, M., and Ströfer, E. (2007). Development of a new industrial process for trioxane production. *Chemical Engineering Science*, 62(18-20):5613–5620.

Gschwend, D., Soltic, P., Wokaun, A., and Vogel, F. (2019). Review and Performance Evaluation of Fifty Alternative Liquid Fuels for Spark-Ignition Engines. *Energy & Fuels*, 33(3):2186–2196.

Guillén-Gosálbez, G. (2011). A novel MILP-based objective reduction method for multi-objective optimization: Application to environmental problems. *Computers & Chemical Engineering*, 35(8):1469–1477.

Gutiérrez, E., Lozano, S., and Adenso-Díaz, B. (2010). Dimensionality Reduction and Visualization of the Environmental Impacts of Domestic Appliances. *Journal of Industrial Ecology*, 14(6):878–889.

Haimes, Y. Y., Lasdon, L. S., and Wismer, D. A. (1971). On a Bicriterion Formulation of the Problems of Integrated System Identification and System Optimization. *IEEE Transactions on Systems, Man, and Cybernetics*, SMC-1(3):296–297.

Hank, C., Lazar, L., Mantei, F. K., Ouda, M., White, R. J., Smolinka, T., Schaadt, A., Hebling, C., and Henning, H.-M. (2019). Comparative Well-to-Wheel Life Cycle Assessment of OME3-5 synfuels production via the Power-to-Liquids pathway. *Sustainable Energy & Fuels*, 3(11):3219–3233.

Hartikka, T., Kuronen, M., and Kiiski, U. (2012). Technical Performance of HVO (Hydrotreated Vegetable Oil) in Diesel Engines. In *SAE Technical Paper Series*, SAE Technical Paper Series, Warrendale, PA, United States. SAE International.

Hashim, H., Narayanasamy, M., Yunus, N. A., Shiun, L. J., Muis, Z. A., and Ho, W. S. (2017). A cleaner and greener fuel: Biofuel blend formulation and emission assessment. *Journal of Cleaner Production*, 146(2):208–217.

Hasse, H., Hahnenstein, I., and Maurer, G. (1990). Revised vapor-liquid equilibrium model for multicomponent formaldehyde mixtures. *AIChE Journal*, 36(12):1807–1814.

Held, M., Tönges, Y., Pélerin, D., Härtl, M., Wachtmeister, G., and Burger, J. (2019). On the energetic efficiency of producing polyoxymethylene dimethyl ethers from CO2 using electrical energy. *Energy & Environmental Science*, 12(3):1019–1034.

Hennen, M., Postels, S., Voll, P., Lampe, M., and Bardow, A. (2017). Multi-objective synthesis of energy systems: Efficient identification of design trade-offs. *Computers & Chemical Engineering*, 97:283–293.

Hernandez, B. and Martin, M. (2018). Optimization for biogas to chemicals via tri-reforming. Analysis of Fischer-Tropsch fuels from biogas. *Energy Conversion and Management*, 174:998–1013.

Herz, G., Reichelt, E., and Jahn, M. (2017). Design and evaluation of a Fischer-Tropsch process for the production of waxes from biogas. *Energy*, 132:370–381.

Herz, G., Reichelt, E., and Jahn, M. (2018). Techno-economic analysis of a co-electrolysis-based synthesis process for the production of hydrocarbons. *Applied Energy*, 215:309–320.

Herz, G., Rix, C., Jacobasch, E., Müller, N., Reichelt, E., Jahn, M., and Michaelis, A. (2021). Economic assessment of Power-to-Liquid processes – Influence of electrolysis technology and operating conditions. *Applied Energy*, 292:116655.

Heuser, B., Vorholt, A., Prieto, G., Graziano, B., Schönfeld, S., Messagie, M., Cardellini, G., Tuomi, S., Sittinger, N., Hermanns, R., Ramawamy, S., Kosuru, C. K., Hoffmann, H., Schulz, L., Yadav, J., Weide, M., and Schnorbus, T. (2020). REDIFUEL: Robust and Efficient processes and technologies for Drop-In renewable FUELs for road transport. *Proceedings of 8th Transport Research Arena TRA 2020, April 27-30, 2020, Helsinki, Finland*.

Hoekman, S. K. and Robbins, C. (2012). Review of the effects of biodiesel on NOx emissions. *Fuel Processing Technology*, 96(1):237–249.

Hombach, L. E., Doré, L., Heidgen, K., Maas, H., Wallington, T. J., and Walther, G. (2019). Economic and environmental assessment of current (2015) and future (2030) use of E-fuels in light-duty vehicles in Germany. *Journal of Cleaner Production*, 207:153–162.

Hong, G. H., Lee, J., Cho, Y., and Hwang, S. (2023). Techno-economic analysis of CO2/steam co-electrolysis process and synfuel production process coupled with steel manufacturing process. *Korean Journal of Chemical Engineering*, 40(4):740–753.

Hosseinzadeh-Bandbafha, H., Kiehbadroudinezhad, M., Aghbashlo, M., Gupta, V. K., Mohammadi, P., Amiri, H., Nizami, A.-S., and Tabatabaei, M. (2024). Life cycle sustainability assessment of higher alcohol: energy, environmental, and social indicators. In *Higher Alcohols Production Platforms*, volume 16, pages 271–303. Elsevier.

Huo, X., Huq, N. A., Stunkel, J., Cleveland, N. S., Starace, A. K., Settle, A. E., York, A. M., Nelson, R. S., Brandner, D. G., Fouts, L., St. John, P. C., Christensen, E. D., Luecke, J., Mack, J. H., McEnally, C. S., Cherry, P. A., Pfefferle, L. D., Strathmann, T. J., Salvachúa, D., Kim, S., McCormick, R. L., Beckham, G. T., and Vardon, D. R. (2019). Tailoring diesel bioblendstock from integrated catalytic upgrading of carboxylic acids: a "fuel property first" approach. *Green Chemistry*, 21(21):5813–5827.

Hydrocarbon Processing (2008). *2008 Refining Processes Handbook*.

IEA (2021). *Key World Energy Statistics 2021*. International Energy Agency, Paris.

IEA (2023a). *Energy Technology Perspectives 2023*. International Energy Agency, Paris.

IEA (2023b). *Net Zero Roadmap: A global pathway to keep the 1.5 degree celsius goal in reach: 2023 Update*. International Energy Agency, Paris.

IEA (2023c). *World Energy Outlook 2023*. IEA, Paris.

IHS Markit, editor (2018). *Process Economics Program (PEP) Yearbook*.

İnci, M., Büyük, M., Demir, M. H., and İlbey, G. (2021). A review and research on fuel cell electric vehicles: Topologies, power electronic converters, energy management methods, technical challenges, marketing and future aspects. *Renewable and Sustainable Energy Reviews*, 137(12):110648.

International Energy Agency (2017). *Energy Technology Perspectives 2017: Catalysing Energy Technology Transformations*. IEA, Paris.

ISO (2006a). ISO 14040: Environmental Management: Life Cycle Assessment: Principles and Framework.

ISO (2006b). ISO 14044: Environmental Management: Life Cycle Assessment: Requirements and Guidelines.

Jacobsen, E., Skov, S. M., Singlitico, A., and Frandsen, H. L. (2023). Techno-economic analysis of green aviation fuel production using an integrated electrolyzer and a "biomass-battery" storage system. *International Journal of Hydrogen Energy*, 139:1173.

Jaramillo, P., Kahn Ribeiro, S., Newman, P., Dhar, S., Diemuodeke, O. E., Kajino, T., Lee, D. S., Nugroho, S. B., and Ou, X. (2022). Transport. In IPCC, editor, *Climate Change 2022: Contribution of Working Group III to the Sixth Assessment Report of the Intergovernmental Panel on Climate Change*, pages 1049–1160. Cambridge University Press, Cambridge, UK and New York, USA.

Jarvis, S. M. and Samsatli, S. (2018). Technologies and infrastructures underpinning future CO2 value chains: A comprehensive review and comparative analysis. *Renewable and Sustainable Energy Reviews*, 85:46–68.

Jeerh, G., Zhang, M., and Tao, S. (2021). Recent progress in ammonia fuel cells and their potential applications. *Journal of Materials Chemistry A*, 9(2):727–752.

Jeske, K., Kizilkaya, A. C., López-Luque, I., Pfänder, N., Bartsch, M., Concepción, P., and Prieto, G. (2021). Design of Cobalt Fischer-Tropsch Catalysts for the Combined Production of Liquid Fuels and Olefin Chemicals from Hydrogen-Rich Syngas. *ACS Catalysis*, 11(8):4784–4798.

Jeske, K., Rösler, T., Belleflamme, M., Rodenas, T., Fischer, N., Claeys, M., Leitner, W., Vorholt, A. J., and Prieto, G. (2022). Direct Conversion of Syngas to Higher Alcohols via Tandem Integration of Fischer–Tropsch Synthesis and Reductive Hydroformylation. *Angewandte Chemie*, 134(31):1–9.

Johansson, M., Yang, J., Ochoterena, R., Gjirja, S., and Denbratt, I. (2013). NOx and soot emissions trends for RME, SME and PME fuels using engine and spray experiments in combination with simulations. *Fuel*, 106:293–302.

Julis, J. and Leitner, W. (2012). Synthesis of 1-octanol and 1,1-dioctyl ether from biomass-derived platform chemicals. *Angewandte Chemie (International ed. in English)*, 51(34):8615–8619.

Kalakul, S., Zhang, L., Fang, Z., Choudhury, H. A., Intikhab, S., Elbashir, N., Eden, M. R., and Gani, R. (2018). Computer aided chemical product design – ProCAPD and tailor-made blended products. *Computers & Chemical Engineering*, 116(1):37–55.

Karavalakis, G., Jiang, Y., Yang, J., Durbin, T., Nuottimäki, J., and Lehto, K. (2016). Emissions and Fuel Economy Evaluation from Two Current Technology Heavy-Duty Trucks Operated on HVO and FAME Blends. *SAE International Journal of Fuels and Lubricants*, 9(1):177–190.

Kätelhön, A., Meys, R., Deutz, S., Suh, S., and Bardow, A. (2019). Climate change mitigation potential of carbon capture and utilization in the chemical industry. *Proceedings of the National Academy of Sciences of the United States of America*, 116(23):11187–11194.

Katiyo, M., Gudukeya, L., Kanganga, M., and Sukdeo, N. (2023). Techno-Economic Assessment of Biogas to Liquid Fuel Conversion via Fischer-Tropsch Synthesis: A Case Study of Biogas Generated from Municipal Sewage. In Kohl, H., Seliger, G., and Dietrich, F., editors, *Manufacturing Driving Circular Economy*, volume 7 of *Lecture Notes in Mechanical Engineering*, pages 729–737. Springer International Publishing, Cham.

Kleinekorte, J., Fleitmann, L., Bachmann, M., Kätelhön, A., Barbosa-Póvoa, A., von der Assen, N., and Bardow, A. (2020). Life Cycle Assessment for the Design of Chemical Processes, Products, and Supply Chains. *Annual review of chemical and biomolecular engineering*, 11:203–233.

Klerk, A. d. (2003). Fischer-Tropsch Process. In Kirk, R. E. and Othmer, D. F., editors, *Encyclopedia of chemical technology*. Wiley, New York, NY.

Klerk, A. d. (2011). *Fischer-Tropsch refining*. Wiley-VCH, Weinheim, online-ausg edition.

Klerk, A. d. and Furimsky, E. (2010). *Catalysis in the Refining of Fischer-Tropsch Syncrude*. Royal Society of Chemistry, Cambridge.

Kohl, A. L. and Nielsen, R. B. (1997). Alkaline Salt Solutions for Acid Gas Removal. In Kohl, A. L. and Nielsen, R., editors, *Gas purification*, pages 330–414. Gulf Publishing Company An Imprint of Elsevier, Houston, Texas.

König, A., Neidhardt, L., Viell, J., Mitsos, A., and Dahmen, M. (2020). Integrated design of processes and products: Optimal renewable fuels. *Computers & Chemical Engineering*, 134:106712.

König, A., Siska, M., Schweidtmann, A. M., Rittig, J. G., Viell, J., Mitsos, A., and Dahmen, M. (2021). Designing production-optimal alternative fuels for conven-

tional, flexible-fuel, and ultra-high efficiency engines. *Chemical Engineering Science*, 237:116562.

König, A., Ulonska, K., Mitsos, A., and Viell, J. (2019). Optimal Applications and Combinations of Renewable Fuel Production from Biomass and Electricity. *Energy & Fuels*, 33(2):1659–1672.

König, D. H., Baucks, N., Dietrich, R.-U., and Wörner, A. (2015a). Simulation and evaluation of a process concept for the generation of synthetic fuel from CO2 and H2. *Energy*, 91:833–841.

König, D. H., Freiberg, M., Dietrich, R.-U., and Wörner, A. (2015b). Techno-economic study of the storage of fluctuating renewable energy in liquid hydrocarbons. *Fuel*, 159:289–297.

Kostin, A., Guillén-Gosálbez, G., and Jiménez, L. (2015). Dimensionality reduction applied to the simultaneous optimization of the economic and life cycle environmental performance of supply chains. *International Journal of Production Economics*, 159:223–232.

Kostin, A., Guillén-Gosálbez, G., Mele, F. D., and Jiménez, L. (2012). Identifying Key Life Cycle Assessment Metrics in the Multiobjective Design of Bioethanol Supply Chains Using a Rigorous Mixed-Integer Linear Programming Approach. *Industrial & Engineering Chemistry Research*, 51(14):5282–5291.

Kuronen, M., Mikkonen, S., Aakko, P., and Murtonen, T. (2007). Hydrotreated Vegetable Oil as Fuel for Heavy Duty Diesel Engines. In *SAE Technical Paper Series*, SAE Technical Paper Series, Warrendale, PA, United States. SAE International.

Kwon, H., Liu, X., Dunn, J. B., Mueller, S., Wander, M. M., and Wang, M. (2021). Carbon Calculator for Land Use and Land Management Change from Biofuels Production (CCLUB), Users' Manual and Technical Documentation (No. ANL/ESD/12-5 Rev. 7).

Ladner, D. R. (2011). Performance and Mass vs. Operating Temperature for Pulse Tube and Stirling Cryocoolers. In Miller, S. D., editor, *Cryocoolers 16*, Boulder, Colo. ICC Press.

Landälv, I., Gebart, R., Marke, B., Granberg, F., Furusjö, E., Löwnertz, P., Öhrman, O. G. W., Sørensen, E. L., and Salomonsson, P. (2014). Two years experience of the BioDME project—A complete wood to wheel concept. *Environmental Progress & Sustainable Energy*, 33(3):744–750.

Lappas, A. and Heracleous, E. (2016). Production of biofuels via Fischer–Tropsch synthesis. In Lin, C. S. K., Clark, J. H., Wilson, K., and Luque, R., editors, *Handbook of biofuels production*, Woodhead Publishing in energy, pages 549–593. Woodhead Publishing, Duxford, UK.

Lapuerta, M., Villajos, M., Agudelo, J. R., and Boehman, A. L. (2011). Key properties and blending strategies of hydrotreated vegetable oil as biofuel for diesel engines. *Fuel Processing Technology*, 92(12):2406–2411.

Lark, T. J., Hendricks, N. P., Smith, A., Pates, N., Spawn-Lee, S. A., Bougie, M., Booth, E. G., Kucharik, C. J., and Gibbs, H. K. (2022). Environmental outcomes of the US Renewable Fuel Standard. *Proceedings of the National Academy of Sciences of the United States of America*, 119(9).

Lautenschütz, L., Oestreich, D., Haltenort, P., Arnold, U., Dinjus, E., and Sauer, J. (2017). Efficient synthesis of oxymethylene dimethyl ethers (OME) from dimethoxymethane and trioxane over zeolites. *Fuel Processing Technology*, 165:27–33.

Lecksiwilai, N., Gheewala, S. H., Sagisaka, M., and Yamaguchi, K. (2016). Net Energy Ratio and Life cycle greenhouse gases (GHG) assessment of bio-dimethyl ether (DME) produced from various agricultural residues in Thailand. *Journal of Cleaner Production*, 134:523–531.

Lee, R. A. and Lavoie, J.-M. (2013). From first- to third-generation biofuels: Challenges of producing a commodity from a biomass of increasing complexity. *Animal Frontiers*, 3(2):6–11.

Lee, S.-Y., Andert, J., Neumann, D., Querel, C., Scheel, T., Aktas, S., Miccio, M., Schaub, J., Koetter, M., and Ehrly, M. (2018). Hardware-in-the-Loop-Based Virtual Calibration Approach to Meet Real Driving Emissions Requirements. *SAE Int. J. Engines*, 11(6):1479–1504.

Lee, S.-Y., Andert, J., Pischinger, S., Ehrly, M., Schaub, J., Koetter, M., and Ayhan, A. S. (2019). Scalable Mean Value Modeling for Real-Time Engine Simulations with Improved Consistency and Adaptability. *SAE Technical Paper Series 2019-01-0195*.

Lehrheuer, B., Zubel, M., Neumann, D., Heuser, B., Thenert, K., Leitner, W., and Pischinger, S. (2018). Alternative Kraftstoffe aus Fischer-Tropsch-Synthese in Kombination mit Hydroformylierung für verbrauchs- und emissionsarme Verbrennungsmotoren von heute und morgen. In Krahl, J., Munack, A., Eilts, P., and

Bünger, J., editors, *Kraftstoffe für die Mobilität von morgen*, Fuels Joint Research Group, pages 76–88. Cuvillier Verlag, Göttingen.

Leitner, W., Klankermayer, J., Pischinger, S., Pitsch, H., and Kohse-Höinghaus, K. (2017). Advanced Biofuels and Beyond: Chemistry Solutions for Propulsion and Production. *Angewandte Chemie (International ed. in English)*, 56(20):5412–5452.

Leow, W. R., Völker, S., Meys, R., Huang, J. E., Jaffer, S. A., Bardow, A., and Sargent, E. H. (2023). Electrified hydrocarbon-to-oxygenates coupled to hydrogen evolution for efficient greenhouse gas mitigation. *Nature communications*, 14(1):1954.

Li, B., Li, J., Tang, K., and Yao, X. (2015). Many-Objective Evolutionary Algorithms. *ACM Computing Surveys*, 48(1):1–35.

Linzenich, A., Arning, K., Bongartz, D., Mitsos, A., and Ziefle, M. (2019). What fuels the adoption of alternative fuels? Examining preferences of German car drivers for fuel innovations. *Applied Energy*, 249:222–236.

Liu, C. M., Sandhu, N. K., McCoy, S. T., and Bergerson, J. A. (2020). A life cycle assessment of greenhouse gas emissions from direct air capture and Fischer–Tropsch fuel production. *Sustainable Energy & Fuels*, 4(6):3129–3142.

Liu, H., Wang, Z., Li, Y., Zheng, Y., He, T., and Wang, J. (2019). Recent progress in the application in compression ignition engines and the synthesis technologies of polyoxymethylene dimethyl ethers. *Applied Energy*, 233-234(10–11):599–611.

Liu, W., Wang, J., Bhattacharyya, D., Jiang, Y., and DeVallance, D. (2017). Economic and environmental analyses of coal and biomass to liquid fuels. *Energy*, 141:76–86.

López Jaimes, A., Coello Coello, C. A., and Chakraborty, D. (2008). Objective reduction using a feature selection technique. In Ryan, C., editor, *Proceedings of the 10th annual conference on Genetic and evolutionary computation*, ACM Conferences, pages 673–680, New York, NY. ACM.

Loulou, R. (2008). ETSAP-TIAM: the TIMES integrated assessment model. part II: mathematical formulation. *Computational Management Science*, 5(1-2):41–66.

Loulou, R. and Labriet, M. (2008). ETSAP-TIAM: the TIMES integrated assessment model Part I: Model structure. *Computational Management Science*, 5(1-2):7–40.

Luecke, J. and Zigler, B. T. (2021). Rapid prediction of fuel research octane number and octane sensitivity using the AFIDA constant-volume combustion chamber. *Fuel*, 301:120969–120980.

Luk, H. T., Mondelli, C., Ferré, D. C., Stewart, J. A., and Pérez-Ramírez, J. (2017). Status and prospects in higher alcohols synthesis from syngas. *Chemical Society reviews*, 46(5):1358–1426.

Lundberg, S., Fagerström, A., and Johansson, K. (2020). *Life Cycle Assessment of Gasification-based Fischer-Tropsch Bio Jet Fuel production: Retrieved from IVL Svenska Miljöinstitutet website: http://urn.kb.se/resolve?urn=urn:nbn:se:ivl:diva-2792*, volume B2377 of *B report*. IVL Svenska Miljöinstitutet.

Luyben, W. L. (2017). Estimating refrigeration costs at cryogenic temperatures. *Computers & Chemical Engineering*, 103:144–150.

Ma, F., Guo, L., Li, Z., Zeng, X., Zheng, Z., Li, W., Zhao, F., and Yu, W. (2023). A Review of Current Advances in Ammonia Combustion from the Fundamentals to Applications in Internal Combustion Engines. *Energies*, 16(17):6304.

Madhu, K., Pauliuk, S., Dhathri, S., and Creutzig, F. (2021). Understanding environmental trade-offs and resource demand of direct air capture technologies through comparative life-cycle assessment. *Nature Energy*, 6(11):1035–1044.

Mahbub, N., Oyedun, A. O., Kumar, A., Oestreich, D., Arnold, U., and Sauer, J. (2017). A life cycle assessment of oxymethylene ether synthesis from biomass-derived syngas as a diesel additive. *Journal of Cleaner Production*, 165:1249–1262.

Mahieux, J. (1969). Make Trioxane Continuously. *Hydrocarbon Process., Int. Ed.*, 48:163–164.

Maitlis, P. M. and Klerk, A. d., editors (2013). *Greener Fischer-Tropsch processes for fuels and feedstocks*. Wiley-VCH, Weinheim, 1. aufl. edition.

Mancini, N. D. and Mitsos, A. (2011). Conceptual design and analysis of ITM oxy-combustion power cycles. *Phys. Chem. Chem. Phys.*, 13(48):21351–21361.

Mantei, F., Ali, R. E., Baensch, C., Völker, S., Haltenort, P., Burger, J., Dietrich, R.-U., von der Aßen, N., Schaadt, A., Sauer, J., and Salem, O. (2022). Techno-economic assessment and carbon footprint of processes for the large-scale production of oxymethylene dimethyl ethers from carbon dioxide and hydrogen. *Sustainable Energy & Fuels*, 6(3):528–549.

Marchese, M., Buffo, G., Santarelli, M., and Lanzini, A. (2021). CO2 from direct air capture as carbon feedstock for Fischer-Tropsch chemicals and fuels: Energy and economic analysis. *Journal of CO2 Utilization*, 46:101487.

Marler, R. T. and Arora, J. S. (2004). Survey of multi-objective optimization methods for engineering. *Structural and Multidisciplinary Optimization*, 26(6):369–395.

Marvin, W. A., Rangarajan, S., and Daoutidis, P. (2013). Automated Generation and Optimal Selection of Biofuel-Gasoline Blends and Their Synthesis Routes. *Energy & Fuels*, 27(6):3585–3594.

Matzen, M. and Demirel, Y. (2016). Methanol and dimethyl ether from renewable hydrogen and carbon dioxide: Alternative fuels production and life-cycle assessment. *Journal of Cleaner Production*, 139:1068–1077.

Maurer, G. (1986). Vapor-liquid equilibrium of formaldehyde-and water-containing multicomponent mixtures. *AIChE Journal*, 32(6):932–948.

Mavrotas, G. (2009). Effective implementation of the epsilon-constraint method in Multi-Objective Mathematical Programming problems. *Applied Mathematics and Computation*, 213(2):455–465.

McCormick, R. L., Fioroni, G., Fouts, L., Christensen, E., Yanowitz, J., Polikarpov, E., Albrecht, K., Gaspar, D. J., Gladden, J., and George, A. (2017). Selection Criteria and Screening of Potential Biomass-Derived Streams as Fuel Blendstocks for Advanced Spark-Ignition Engines. *SAE International Journal of Fuels and Lubricants*, 10(2):442–460.

McQueen, N., Gomes, K. V., McCormick, C., Blumanthal, K., Pisciotta, M., and Wilcox, J. (2021). A review of direct air capture (DAC): scaling up commercial technologies and innovating for the future. *Progress in Energy*, 3(3):032001.

Medrano-García, J. D., Charalambous, M. A., and Guillén-Gosálbez, G. (2022). Economic and Environmental Barriers of CO2 -Based Fischer–Tropsch Electro-Diesel. *ACS Sustainable Chemistry & Engineering*, 10(36):11751–11759.

Mekhilef, S., Saidur, R., and Safari, A. (2012). Comparative study of different fuel cell technologies. *Renewable and Sustainable Energy Reviews*, 16(1):981–989.

Meyers, R. A., editor (2004). *Handbook of petroleum refining processes*. McGraw-Hill's AccessEngineering. McGraw-Hill, New York, 3rd ed. edition.

Meys, R., Kätelhön, A., Bachmann, M., Winter, B., Zibunas, C., Suh, S., and Bardow, A. (2021). Achieving net-zero greenhouse gas emission plastics by a circular carbon economy. *Science (New York, N.Y.)*, 374(6563):71–76.

Mohr, A. and Raman, S. (2013). Lessons from first generation biofuels and implications for the sustainability appraisal of second generation biofuels. *Energy Policy*, 63(100):114–122.

Müller, L. J., Kätelhön, A., Bachmann, M., Zimmermann, A., Sternberg, A., and Bardow, A. (2020a). A Guideline for Life Cycle Assessment of Carbon Capture and Utilization. *Frontiers in Energy Research*, 8:1–20.

Müller, L. J., Kätelhön, A., Bringezu, S., McCoy, S., Suh, S., Edwards, R., Sick, V., Kaiser, S., Cuéllar-Franca, R., El Khamlichi, A., Lee, J. H., von der Assen, N., and Bardow, A. (2020b). The carbon footprint of the carbon feedstock CO2. *Energy & Environmental Science*, 13(9):2979–2992.

Müller-Langer, F., Majer, S., and O'Keeffe, S. (2014). Benchmarking biofuels—a comparison of technical, economic and environmental indicators. *Energy, Sustainability and Society*, 4(1).

Muñoz, I., Flury, K., Jungbluth, N., Rigarlsford, G., i Canals, L. M., and King, H. (2014). Life cycle assessment of bio-based ethanol produced from different agricultural feedstocks. *The International Journal of Life Cycle Assessment*, 19(1):109–119.

Murtonen, T., Aakko-Saksa, P., Kuronen, M., Mikkonen, S., and Lehtoranta, K. (2009). Emissions with Heavy-duty Diesel Engines and Vehicles using FAME, HVO and GTL Fuels with and without DOC+POC Aftertreatment. *SAE International Journal of Fuels and Lubricants*, 2(2):147–166.

Muthukumar, M., Rengarajan, N., Velliyangiri, B., Omprakas, M. A., Rohit, C. B., and Kartheek Raja, U. (2021). The development of fuel cell electric vehicles – A review. *Materials Today: Proceedings*, 45(2):1181–1187.

Navas-Anguita, Z., Cruz, P. L., Martín-Gamboa, M., Iribarren, D., and Dufour, J. (2019). Simulation and life cycle assessment of synthetic fuels produced via biogas dry reforming and Fischer-Tropsch synthesis. *Fuel*, 235:1492–1500.

Neuling, U. and Kaltschmitt, M. (2018). Techno-economic and environmental analysis of aviation biofuels. *Fuel Processing Technology*, 171:54–69.

Neumann, D., Muthyala, P., Frenken, C., Schaub, J., Jörg, C., and Kötter, M. (2019). Flex-fuel capability via advanced digital combustion rate shaping and airpath control. In Liebl, J., Beidl, C., and Maus, W., editors, *Internationaler Motorenkongress 2019*, Proceedings, pages 333–350. Springer Fachmedien Wiesbaden, Wiesbaden.

Neumann, D., Pischinger, S., Zubel, M., Heuser, B., Thenert, K., Leitner, W., Schönen, M., Schaub, J., and Jörg, C. (2018). Power-to-Liquids - Kompensation variierender E-Fuel Zusammensetzungen mittels Digital Rate Shaping /Power-to-Liquids - Compensation of Varying E-Fuel Compositions via Digital Rate Shaping. In Geringer, B. and Lenz, H.-P., editors, *39. Internationales Wiener Motorensymposium 26.-27. April 2018*, pages 230–258. VDI Verlag, Düsseldorf.

Niethammer, B., Wodarz, S., Betz, M., Haltenort, P., Oestreich, D., Hackbarth, K., Arnold, U., Otto, T., and Sauer, J. (2018). Alternative Liquid Fuels from Renewable Resources. *Chemie Ingenieur Technik*, 90(1-2):99–112.

Ockwig, N. W. and Nenoff, T. M. (2007). Membranes for hydrogen separation. *Chemical reviews*, 107(10):4078–4110.

Okeke, I. J. and Mani, S. (2017). Techno–economic assessment of biogas to liquid fuels conversion technology via Fischer–Tropsch synthesis. *Biofuels, Bioproducts and Biorefining*, 11(3):472–487.

Okeke, I. J., Sahoo, K., Kaliyan, N., and Mani, S. (2020). Life cycle assessment of renewable diesel production via anaerobic digestion and Fischer-Tropsch synthesis from miscanthus grown in strip-mined soils. *Journal of Cleaner Production*, 249:119358–119368.

Okolie, J. A., Awotoye, D., Tabat, M. E., Okoye, P. U., Epelle, E. I., Ogbaga, C. C., Güleç, F., and Oboirien, B. (2023). Multi-criteria decision analysis for the evaluation and screening of sustainable aviation fuel production pathways. *iScience*, 26(6):106944.

Oliva, D. G., Guillén-Gosálbez, G., Mateo-Sanz, J. M., and Jiménez-Esteller, L. (2013). MILP-based clustering method for multi-objective optimization: Application to environmental problems. *Computers & Chemical Engineering*, 56:202–217.

Omari, A. (2021). *Characterization of Polyoxymethylen Dimethyl Ether for Diesel Engine Applications*. PhD thesis (in press), RWTH Aachen University, Aachen.

Omari, A., Heuser, B., and Pischinger, S. (2017a). Potential of oxymethylenether-diesel blends for ultra-low emission engines. *Fuel*, 209:232–237.

Omari, A., Heuser, B., Pischinger, S., and Rüdinger, C. (2019). Potential of long-chain oxymethylene ether and oxymethylene ether-diesel blends for ultra-low emission engines. *Applied Energy*, 239:1242–1249.

Omari, A., Pischinger, S., Bhardwaj, O. P., Holderbaum, B., Nuottimäki, J., and Honkanen, M. (2017b). Improving Engine Efficiency and Emission Reduction Potential of HVO by Fuel-Specific Engine Calibration in Modern Passenger Car Diesel Applications. *SAE International Journal of Fuels and Lubricants*, 10(3).

Ostovari, H., Müller, L., Mayer, F., and Bardow, A. (2022). A climate-optimal supply chain for CO2 capture, utilization, and storage by mineralization. *Journal of Cleaner Production*, 360:131750.

Ostovari, H., Sternberg, A., and Bardow, A. (2020). Rock 'n' use of CO2 : carbon footprint of carbon capture and utilization by mineralization. *Sustainable Energy & Fuels*.

Osugi, M. and Uchiyama, T. (1977). Process for the preparation for formaldehyde: US Patent 4,054,609.

Ouda, M., Mantei, F., Hesterwerth, K., Bargiacchi, E., Klein, H., and White, R. J. (2018a). A hybrid description and evaluation of oxymethylene dimethyl ethers synthesis based on the endothermic dehydrogenation of methanol. *Reaction Chemistry & Engineering*, 3(5):676–695.

Ouda, M., Mantei, F. K., Elmehlawy, M., White, R. J., Klein, H., and Fateen, S.-E. K. (2018b). Describing oxymethylene ether synthesis based on the application of non-stoichiomsetric Gibbs minimisation. *Reaction Chemistry & Engineering*, 3(3):277–292.

Ouda, M., Yarce, G., White, R. J., Hadrich, M., Himmel, D., Schaadt, A., Klein, H., Jacob, E., and Krossing, I. (2017). Poly(oxymethylene) dimethyl ether synthesis – a combined chemical equilibrium investigation towards an increasingly efficient and potentially sustainable synthetic route. *Reaction Chemistry & Engineering*, 2(1):50–59.

Pal, M., Saha, S., and Bandyopadhyay, S. (2018). DECOR: Differential Evolution using Clustering based Objective Reduction for many-objective optimization. *Information Sciences*, 423(1):200–218.

Papong, S. and Malakul, P. (2010). Life-cycle energy and environmental analysis of bioethanol production from cassava in Thailand. *Bioresource technology*, 101 Suppl 1:S112–8.

Paris, B., Papadakis, G., Janssen, R., and Rutz, D. (2021). Economic analysis of advanced biofuels, renewable gases, electrofuels and recycled carbon fuels for the Greek transport sector until 2050. *Renewable and Sustainable Energy Reviews*, 144:111038.

Park, S. H. and Lee, C. S. (2014). Applicability of dimethyl ether (DME) in a compression ignition engine as an alternative fuel. *Energy Conversion and Management*, 86:848–863.

Patel, P. D., Lakdawala, A., Chourasia, S., and Patel, R. N. (2016). Bio fuels for compression ignition engine: A review on engine performance, emission and life cycle analysis. *Renewable and Sustainable Energy Reviews*, 65(4):24–43.

Pedersen, T. T., Victoria, M., Rasmussen, M. G., and Andresen, G. B. (2021). Modeling all alternative solutions for highly renewable energy systems. *Energy*, 234(2):121294.

Pélerin, D., Gaukel, K., Härtl, M., Jacob, E., and Wachtmeister, G. (2020). Potentials to simplify the engine system using the alternative diesel fuels oxymethylene ether OME1 and OME3−6 on a heavy-duty engine. *Fuel*, 259:116231–116240.

Pellegrini, L., Marchionna, M., Patrini, R., and Florio, S. (2013). Emission Performance of Neat and Blended Polyoxymethylene Dimethyl Ethers in an Old Light-Duty Diesel Car. In *SAE Technical Paper Series*, SAE Technical Paper Series. SAE International400 Commonwealth Drive, Warrendale, PA, United States.

Perez-Gallardo, J. R., Azzaro-Pantel, C., and Astier, S. (2018). Combining Multi-Objective Optimization, Principal Component Analysis and Multiple Criteria Decision Making for ecodesign of photovoltaic grid-connected systems. *Sustainable Energy Technologies and Assessments*, 27:94–101.

Peters, R., Wegener, N., Samsun, R. C., Schorn, F., Riese, J., Grünewald, M., and Stolten, D. (2022). A Techno-Economic Assessment of Fischer–Tropsch Fuels Based on Syngas from Co-Electrolysis. *Processes*, 10(4):699.

Piccolo, C. and Bezzo, F. (2009). A techno-economic comparison between two technologies for bioethanol production from lignocellulose. *Biomass and Bioenergy*, 33(3):478–491.

Postels, S., von der Assen, N., Voll, P., and Bardow, A. (2015). Reducing dimensionality in multi-objective LCA-based optimization of energy systems - The impact normalization variants and weighting factors. In *28th International Conference on Efficiency, Cost, Optimization, Simulation and Environmental Impact of Energy Systems (ECOS 2015)*, pages 787–798, Red Hook, NY. Curran Associates Inc.

Pozo, C., Ruíz-Femenia, R., Caballero, J., Guillén-Gosálbez, G., and Jiménez, L. (2012). On the use of Principal Component Analysis for reducing the number of environmental objectives in multi-objective optimization: Application to the design of chemical supply chains. *Chemical Engineering Science*, 69(1):146–158.

Prabhu, A. K. and Oyama, S. (2000). Highly hydrogen selective ceramic membranes: application to the transformation of greenhouse gases. *Journal of Membrane Science*, 176(2):233–248.

Pramuanjaroenkij, A. and Kakaç, S. (2023). The fuel cell electric vehicles: The highlight review. *International Journal of Hydrogen Energy*, 48(25):9401–9425.

Puricelli, S., Cardellini, G., Casadei, S., Faedo, D., van den Oever, A., and Grosso, M. (2021). A review on biofuels for light-duty vehicles in Europe. *Renewable and Sustainable Energy Reviews*, 137:110398.

Püschel, S., Hammami, E., Rösler, T., Ehmann, K. R., Vorholt, A. J., and Leitner, W. (2022a). Auto-tandem catalytic reductive hydroformylation with continuous multiphase catalyst recycling. *Catalysis Science & Technology*, 12(3):728–736.

Püschel, S., Sadowski, J., Rösler, T., Ehmann, K. R., Vorholt, A. J., and Leitner, W. (2022b). Auto-Tandem Catalytic Reductive Hydroformylation in a CO2-Switchable Solvent System. *ACS Sustainable Chemistry & Engineering*, 10(11):3749–3756.

Püschel, S., Störtte, S., Topphoff, J., Vorholt, A. J., and Leitner, W. (2021). Green Process Design for Reductive Hydroformylation of Renewable Olefin Cuts for Drop-In Diesel Fuels. *ChemSusChem*, 14:5226–5234.

Putta, K. R., Pandey, U., Gavrilovic, L., Rout, K. R., Rytter, E., Blekkan, E. A., and Hillestad, M. (2022). Optimal Renewable Energy Distribution Between Gasifier and Electrolyzer for Syngas Generation in a Power and Biomass-to-Liquid Fuel Process. *Frontiers in Energy Research*, 9.

Qin, Y. J., Zheng, J. H., Li, Z., and Wu, Q. H. (2020). Reduction of non-linear many objectives for coordinated operation of integrated energy systems. *International Journal of Electrical Power & Energy Systems*, 117:105657.

Quader, M. A., Ahmed, S., Raja Ghazilla, R. A., Ahmed, S., and Dahari, M. (2016). Evaluation of criteria for CO2 capture and storage in the iron and steel industry using the 2-tuple DEMATEL technique. *Journal of Cleaner Production*, 120(3):207–220.

Rafati, M., Wang, L., Dayton, D. C., Schimmel, K., Kabadi, V., and Shahbazi, A. (2017). Techno-economic analysis of production of Fischer-Tropsch liquids via biomass gasification: The effects of Fischer-Tropsch catalysts and natural gas co-feeding. *Energy Conversion and Management*, 133:153–166.

Redina, E. A., Vikanova, K. V., Kapustin, G. I., Mishin, I. V., Tkachenko, O. P., and Kustov, L. M. (2019). Selective Room-Temperature Hydrogenation of Carbonyl Compounds under Atmospheric Pressure over Platinum Nanoparticles Supported on Ceria-Zirconia Mixed Oxide. *European Journal of Organic Chemistry*, 2019(26):4159–4170.

Reinert, C., Deutz, S., Minten, H., Dörpinghaus, L., von Pfingsten, S., Baumgärtner, N., and Bardow, A. (2020). Environmental Impacts of the Future German Energy System from Integrated Energy Systems Optimization and Life Cycle Assessment. In Pierucci, S., Manenti, F., Bozzano, G. L., and Manca, D., editors, *30th European Symposium on Computer Aided Process Engineering*, volume 48 of *Computer-aided chemical engineering*, pages 241–246. Elsevier, Amsterdam.

Reinert, C., Schellhas, L., Mannhardt, J., Shu, D. Y., Kämper, A., Baumgärtner, N., Deutz, S., and Bardow, A. (2022). SecMOD: An Open-Source Modular Framework Combining Multi-Sector System Optimization and Life-Cycle Assessment. *Frontiers in Energy Research*, 10.

Reuss, G., Disteldorf, W., Gamer, A. O., and Hilt, A. (2000). Formaldehyde. In Ullmann, editor, *Ullmann's Encyclopedia of Industrial Chemistry*, volume 19, page 377. Wiley-VCH Verlag GmbH & Co. KGaA, Weinheim, Germany.

Reuß, M., Grube, T., Robinius, M., Preuster, P., Wasserscheid, P., and Stolten, D. (2017). Seasonal storage and alternative carriers: A flexible hydrogen supply chain model. *Applied Energy*, 200:290–302.

Riazi, M. R., Eser, S., Agrawal, S. S., and Peña Díez, J. L. (2013). *Petroleum refining and natural gas processing*, volume 58 of */ASTM manual series], MNL*. ASTM International, West Conshohocken, PA.

Richter, B. (2014). Evaluation of Stability Tests for Elastomeric Materials and Seals. *International Polymer Science and Technology*, 41(5):1–6.

Richter, B. (2022). Bewertung von Beständigkeitstests von Elastomeren Werkstoffen mit Getriebe- und Motorölen bezüglich des Funktionsverhalten von Radialwellendichtringen.

Richter, G. and Zellbeck, H. (2017). OME als Kraftstoffersatz im Pkw-Dieselmotor. *MTZ - Motortechnische Zeitschrift*, 78(12):66–73.

Rittig, J. G., Ritzert, M., Schweidtmann, A. M., Winkler, S., Weber, J. M., Morsch, P., Heufer, K. A., Grohe, M., Mitsos, A., and Dahmen, M. (2023). Graph machine learning for design of high–octane fuels. *AIChE Journal*, 69(4).

Rodríguez Vallejo, D. F. and Klerk, A. d. (2013). Improving the Interface between Fischer–Tropsch Synthesis and Refining. *Energy & Fuels*, 27(6):3137–3147.

Rodríguez-Vallejo, D. F., Valente, A., Guillén-Gosálbez, G., and Chachuat, B. (2021). Economic and life-cycle assessment of OME3-5 as transport fuel: A comparison of production pathways. *Sustainable Energy & Fuels*, 5(9):2504–2516.

Roh, K., Bardow, A., Bongartz, D., Burre, J., Chung, W., Deutz, S., Han, D., Heßelmann, M., Kohlhaas, Y., König, A., Lee, J. S., Meys, R., Völker, S., Wessling, M., Lee, J. H., and Mitsos, A. (2020). Early-stage evaluation of emerging CO2 utilization technologies at low technology readiness levels. *Green Chemistry*, 22(12):3842–3859.

Rösler, T., Ehmann, K. R., Köhnke, K., Leutzsch, M., Wessel, N., Vorholt, A. J., and Leitner, W. (2021). Reductive hydroformylation with a selective and highly active rhodium amine system. *Journal of Catalysis*, 400:234–243.

Rudin, M. (2018). *Isocracking technology review*.

Ruth, M. (2011). *Hydrogen Production Cost Estimate Using Biomass Gasification: Independent Review: Technical Report DE-AC36-08GO28308, National Renewable Energy Laboratory (NREL)*. National Renewable Energy Lab. (NREL), Golden, CO (United States).

Sabatino, F., Grimm, A., Gallucci, F., van Sint Annaland, M., Kramer, G. J., and Gazzani, M. (2021). A comparative energy and costs assessment and optimization for direct air capture technologies. *Joule*, 5(8):2047–2076.

Sabio, N., Kostin, A., Guillén-Gosálbez, G., and Jiménez, L. (2012). Holistic minimization of the life cycle environmental impact of hydrogen infrastructures using multi-objective optimization and principal component analysis. *International Journal of Hydrogen Energy*, 37(6):5385–5405.

Sacchi, R., Bauer, C., Cox, B., and Mutel, C. (2022). When, where and how can the electrification of passenger cars reduce greenhouse gas emissions? *Renewable and Sustainable Energy Reviews*, 162:112475–112486.

Saini, J. K., Saini, R., and Tewari, L. (2015). Lignocellulosic agriculture wastes as biomass feedstocks for second-generation bioethanol production: concepts and recent developments. *3 Biotech*, 5(4):337–353.

Samavati, M., Martin, A., Santarelli, M., and Nemanova, V. (2018). Synthetic Diesel Production as a Form of Renewable Energy Storage. *Energies*, 11(5):1223.

Sassner, P., Galbe, M., and Zacchi, G. (2008). Techno-economic evaluation of bioethanol production from three different lignocellulosic materials. *Biomass and Bioenergy*, 32(5):422–430.

Saxena, D. K. and Deb, K. (2007). Non-linear Dimensionality Reduction Procedures for Certain Large-Dimensional Multi-objective Optimization Problems: Employing Correntropy and a Novel Maximum Variance Unfolding. In Obayashi, S., editor, *Evolutionary Multi-Criterion Optimization*, volume 4403 of *Lecture Notes in Computer Science Ser*, pages 772–787. Springer Berlin / Heidelberg, Berlin, Heidelberg.

Saxena, D. K., Duro, J. A., Tiwari, A., Deb, K., and Zhang, Q. (2013). Objective Reduction in Many-Objective Optimization: Linear and Nonlinear Algorithms. *IEEE Transactions on Evolutionary Computation*, 17(1):77–99.

Sazali, N., Wan Salleh, W. N., Jamaludin, A. S., and Mhd Razali, M. N. (2020). New Perspectives on Fuel Cell Technology: A Brief Review. *Membranes*, 10(5).

Schakel, W., Oreggioni, G., Singh, B., Strømman, A., and Ramírez, A. (2016). Assessing the techno-environmental performance of CO2 utilization via dry reforming of methane for the production of dimethyl ether. *Journal of CO2 Utilization*, 16:138–149.

Schaub, J., Ehrly, M., Vogt, K., Kansy, W., Lindemann, B., Sammito, G., Lingemann, P., Muthyala, P. P., and Pischinger, S. (2020a). Hybrid Powertrain Concepts for Light Commercial Vehicles. *29th Aachen Colloquium Sustainable Mobility*.

Schaub, J., Pieper, M., Klopstein, S., Übbing, M., Knappe, P., Muthyala, P., and Schmidt, T. (2020b). Electrified efficiency – diesel hybrid powertrain concepts for light commercial vehicles. In Liebl, J., Beidl, C., and Maus, W., editors, *Internationaler Motorenkongress 2020*, Proceedings, pages 335–352. Springer Fachmedien Wiesbaden, Wiesbaden.

Schemme, S., Breuer, J. L., Köller, M., Meschede, S., Walman, F., Samsun, R. C., Peters, R., and Stolten, D. (2019). H2-based synthetic fuels: A techno-economic comparison of alcohol, ether and hydrocarbon production. *International Journal of Hydrogen Energy*, 45(8):5395–5414.

Schemme, S., Breuer, J. L., Samsun, R. C., Peters, R., and Stolten, D. (2018). Promising catalytic synthesis pathways towards higher alcohols as suitable transport fuels based on H2 and CO2. *Journal of CO2 Utilization*, 27:223–237.

Schemme, S., Samsun, R. C., Peters, R., and Stolten, D. (2017). Power-to-fuel as a key to sustainable transport systems – An analysis of diesel fuels produced from CO2 and renewable electricity. *Fuel*, 205:198–221.

Schmidt, P., Batteiger, V., Roth, A., Weindorf, W., and Raksha, T. (2018). Power-to-Liquids as Renewable Fuel Option for Aviation: A Review. *Chemie Ingenieur Technik*, 90(1-2):127–140.

Schmitz, N., Burger, J., and Hasse, H. (2015a). Reaction Kinetics of the Formation of Poly(oxymethylene) Dimethyl Ethers from Formaldehyde and Methanol in Aqueous Solutions. *Industrial & Engineering Chemistry Research*, 54(50):12553–12560.

Schmitz, N., Burger, J., Ströfer, E., and Hasse, H. (2016). From methanol to the oxygenated diesel fuel poly(oxymethylene) dimethyl ether: An assessment of the production costs. *Fuel*, 185:67–72.

Schmitz, N., Homberg, F., Berje, J., Burger, J., and Hasse, H. (2015b). Chemical Equilibrium of the Synthesis of Poly(oxymethylene) Dimethyl Ethers from Formaldehyde and Methanol in Aqueous Solutions. *Industrial & Engineering Chemistry Research*, 54(25):6409–6417.

Schmitz, N., Ströfer, E., Burger, J., and Hasse, H. (2017). Conceptual Design of a Novel Process for the Production of Poly(oxymethylene) Dimethyl Ethers from Formaldehyde and Methanol. *Industrial & Engineering Chemistry Research*, 56(40):11519–11530.

Schröder, J. and Görsch, K. (2020). Storage Stability and Material Compatibility of Poly(oxymethylene) Dimethyl Ether Diesel Fuel. *Energy & Fuels*, 34(1):450–459.

Seidenspinner, P., Härtl, M., Wilharm, T., and Wachtmeister, G. (2015). Cetane Number Determination by Advanced Fuel Ignition Delay Analysis in a New Constant Volume Combustion Chamber. *SAE Technical Paper 2015-01-0798*, pages 1–12.

Shaharun, M. S., Dutta, B. K., Mukhtar, H., and Maitra, S. (2010). Hydroformylation of 1-octene using rhodium–phosphite catalyst in a thermomorphic solvent system. *Chemical Engineering Science*, 65(1):273–281.

Shahir, S. A., Masjuki, H. H., Kalam, M. A., Imran, A., Fattah, I. R., and Sanjid, A. (2014). Feasibility of diesel–biodiesel–ethanol/bioethanol blend as existing CI engine fuel: An assessment of properties, material compatibility, safety and combustion. *Renewable and Sustainable Energy Reviews*, 32:379–395.

Sharaf, O. Z. and Orhan, M. F. (2014). An overview of fuel cell technology: Fundamentals and applications. *Renewable and Sustainable Energy Reviews*, 32:810–853.

Shen, W.-J., Jun, K.-W., Choi, H.-S., and Lee, K.-W. (2000). Thermodynamic investigation of methanol and dimethyl ether synthesis from CO2 Hydrogenation. *Korean Journal of Chemical Engineering*, 17(2):210–216.

Shoujin Su, Philippe Zaza, and Albert Renken (1994). Catalytic dehydrogenation of methanol to water–free formaldehyde. *Chemical Engineering & Technology*, 17(1):34–40.

Shukla, P. R., Skea, J., Slade, R., Al Khourdajie, A., van Diemen, R., McCollum, D., Pathak, M., Some, S., Vyas, P., Fradera, R., Belkacemi, M., Hasija, A., Lisboa, G., Luz, S., and Malley, J., editors (2022). *Climate Change 2022: Mitigation of Climate Change. Contribution of Working Group III to the Sixth Assessment Report of the Intergovernmental Panel on Climate Change*. Cambridge University Press, Cambridge, United Kingdom and New York, NY, USA.

Sick, V., Armstrong, K., Cooney, G., Cremonese, L., Eggleston, A., Faber, G., Hackett, G., Kätelhön, A., Keoleian, G., Marano, J., Marriott, J., McCord, S., Miller, S. A., Mutchek, M., Olfe-Kräutlein, B., Ravikumar, D., Roper, L. K., Schaidle, J., Skone, T., Smith, L., Strunge, T., Styring, P., Tao, L., Völker, S., and Zimmermann, A. (2019). The Need for and Path to Harmonized Life Cycle Assessment and Techno–Economic Assessment for Carbon Dioxide Capture and Utilization. *Energy Technology*, 8(11):1901034.

Siegemund, S., Trommler, M., Kolb, O., and Zinnecker, V. (2017). *E-fuels study: The potential of electricity-based fuels for low-emission transport in the EU: An expertise by LBST and dena*. Deutsche Energie-Agentur GmbH (dena), Berlin.

Simons, A. (2016). Road transport: new life cycle inventories for fossil-fuelled passenger cars and non-exhaust emissions in ecoinvent v3. *The International Journal of Life Cycle Assessment*, 21(9):1299–1313.

Sims, R. E. H., Mabee, W., Saddler, J. N., and Taylor, M. (2010). An overview of second generation biofuel technologies. *Bioresource technology*, 101(6):1570–1580.

Singh, H. K., Isaacs, A., and Ray, T. (2011). A Pareto Corner Search Evolutionary Algorithm and Dimensionality Reduction in Many-Objective Optimization Problems. *IEEE Transactions on Evolutionary Computation*, 15(4):539–556.

Skov, I. R. and Schneider, N. (2022). Incentive structures for power-to-X and e-fuel pathways for transport in EU and member states. *Energy Policy*, 168:113121.

Snehesh, A. S., Mukunda, H. S., Mahapatra, S., and Dasappa, S. (2017). Fischer-Tropsch route for the conversion of biomass to liquid fuels - Technical and economic analysis. *Energy*, 130:182–191.

Steinmann, Z. J. N., Schipper, A. M., Hauck, M., and Huijbregts, M. A. J. (2016). How Many Environmental Impact Indicators Are Needed in the Evaluation of Product Life Cycles? *Environmental science & technology*, 50(7):3913–3919.

Sternberg, A. and Bardow, A. (2015). Power-to-What? – Environmental assessment of energy storage systems. *Energy & Environmental Science*, 8(2):389–400.

Sternberg, A. and Bardow, A. (2016). Life Cycle Assessment of Power-to-Gas: Syngas vs Methane. *ACS Sustainable Chemistry & Engineering*, 4(8):4156–4165.

Sternberg, A., Jens, C. M., and Bardow, A. (2017). Life cycle assessment of CO2-based C1-chemicals. *Green Chemistry*, 19(9):2244–2259.

Sun, R., Delidovich, I., and Palkovits, R. (2019). Dimethoxymethane as a Cleaner Synthetic Fuel: Synthetic Methods, Catalysts, and Reaction Mechanism. *ACS Catalysis*, 9(2):1298–1318.

Surisetty, V. R., Dalai, A. K., and Kozinski, J. (2011). Alcohols as alternative fuels: An overview. *Applied Catalysis A: General*, 404(1-2):1–11.

Thavornprasert, K.-a., Capron, M., Jalowiecki-Duhamel, L., and Dumeignil, F. (2016). One-pot 1,1-dimethoxymethane synthesis from methanol: a promising pathway over bifunctional catalysts. *Catalysis Science & Technology*, 6(4):958–970.

Thoai, N. V. (2012). Criteria and dimension reduction of linear multiple criteria optimization problems. *Journal of Global Optimization*, 52(3):499–508.

Tornatore, C., Marchitto, L., Sabia, P., and de Joannon, M. (2022). Ammonia as Green Fuel in Internal Combustion Engines: State-of-the-Art and Future Perspectives. *Frontiers in Mechanical Engineering*, 8.

Tsalidis, G. A., Discha, F. E., Korevaar, G., Haije, W., de Jong, W., and Kiel, J. (2017). An LCA-based evaluation of biomass to transportation fuel production and utilization pathways in a large port's context. *International Journal of Energy and Environmental Engineering*, 8(3):175–187.

Tsongidis, N. I., Asimakopoulou, A. G., Pantoleontos, G., and Konstandopoulos, A. G. (2019). Transportation and solar-aided utilization of CO2: Technoeconomic analysis of spanning routes of CO2 conversion to solar fuels. *Journal of CO2 Utilization*, 30:142–157.

Tsubaki, N., Sun, S., and Fujimoto, K. (2001). Different Functions of the Noble Metals Added to Cobalt Catalysts for Fischer–Tropsch Synthesis. *Journal of Catalysis*, 199(2):236–246.

Tu, J.-l., Ding, M.-y., Zhang, Q., Zhang, Y.-l., Wang, C.-g., Wang, T.-j., Ma, L.-l., and Li, X.-j. (2015). Design of Carbon-Encapsulated Fe3O4 Nanocatalyst with Enhanced Performance for Fischer-Tropsch Synthesis. *ChemCatChem*, 7(15):2323–2327.

Uddin, M. M., Simson, A., and Wright, M. M. (2020). Techno-economic and greenhouse gas emission analysis of dimethyl ether production via the bi-reforming pathway for transportation fuel. *Energy*, 211(5):119031.

Ueckerdt, F., Hirth, L., Luderer, G., and Edenhofer, O. (2013). System LCOE: What are the costs of variable renewables? *Energy*, 63(1):61–75.

Ullmann, editor (2000). *Ullmann's Encyclopedia of Industrial Chemistry*. Wiley-VCH Verlag GmbH & Co. KGaA, Weinheim, Germany.

Ulonska, K., Skiborowski, M., Mitsos, A., and Viell, J. (2016). Early-stage evaluation of biorefinery processing pathways using process network flux analysis. *AIChE Journal*, 62(9):3096–3108.

UNEP (2020). *Emissions Gap Report 2020*, volume 2020 of *The emissions gap report*. United Nations Environment Programme, Nairobi.

UNEP (2022). *Emissions Gap Report 2022: The closing window: Climate crisis calls for rapid transformation of societies*, volume 2022 of *The emissions gap report*. United Nations Environment Programme, Nairobi.

U.S. Environmental Protection Agency (2022). Our Nation's Air: Status and Trends Through 2022: Annual Air Trends Report [interactive web application] available via https://www.epa.gov/air-trends. Accessed November 07, 2023.

Usachev, N. Y., Krukovskii, I. M., and Kanaev, S. A. (2004). The nonoxidative methanol dehydrogenation to formaldehyde (A review). *Petroleum Chemistry*, 44(6):379–394.

van Biert, L., Godjevac, M., Visser, K., and Aravind, P. V. (2016). A review of fuel cell systems for maritime applications. *Journal of Power Sources*, 327(D17):345–364.

Van-Dal, É. S. and Bouallou, C. (2013). Design and simulation of a methanol production plant from CO2 hydrogenation. *Journal of Cleaner Production*, 57:38–45.

van de Loosdrecht, J., Botes, F. G., Ciobica, I. M., Ferreira, A., Gibson, P., Moodley, D. J., Saib, A. M., Visagie, J. L., Weststrate, C. J., and Niemantsverdriet, J. W. (2013). Fischer–Tropsch Synthesis: Catalysts and Chemistry. In Reedijk, J., editor, *Comprehensive inorganic chemistry II*, pages 525–557. Elsevier, Amsterdam.

van den Oever, A., Costa, D., and Messagie, M. (2022). *Deliverable report: Comparison of BtL drop-in biofuels with transport fuels: REDIFUEL project.*

van den Oever, A., Costa, D., and Messagie, M. (2023). Prospective life cycle assessment of alternatively fueled heavy-duty trucks. *Applied Energy*, 336:120834–120845.

van Grinsven, A., van den Toorn, E., van der Veen, R., Kampman, B., and Oil, C. (2020). Used Cooking Oil (UCO) as biofuel feedstock in the EU. *CE Delft: Delft, The Netherlands*, pages 1–64.

Vaskan, P., Guillén-Gosálbez, G., and Jiménez, L. (2012). Multi-objective design of heat-exchanger networks considering several life cycle impacts using a rigorous MILP-based dimensionality reduction technique. *Applied Energy*, 98:149–161.

Vaskan, P., Guillén-Gosálbez, G., Turkay, M., and Jiménez, L. (2014). Multiobjective Optimization of Utility Plants under Several Environmental Indicators Using an MILP-Based Dimensionality Reduction Approach. *Industrial & Engineering Chemistry Research*, 53(50):19559–19572.

Vázquez, D., Fernández-Torres, M. J., Ruiz-Femenia, R., Jiménez, L., and Caballero, J. A. (2018a). MILP method for objective reduction in multi-objective optimization. *Computers & Chemical Engineering*, 108:382–394.

Vázquez, D., Ruiz-Femenia, R., Jiménez, L., and Caballero, J. A. (2018b). MILP models for objective reduction in multi-objective optimization: Error measurement considerations and non-redundancy ratio. *Computers & Chemical Engineering*, 115:323–332.

Vázquez, D., Ruiz-Femenia, R., Jiménez, L., and Caballero, J. A. (2018c). Multiobjective Early Design of Complex Distillation Sequences Considering Economic and Inherent Safety Criteria. *Industrial & Engineering Chemistry Research*, 57(20):6992–7007.

Vázquez, F. V., Koponen, J., Ruuskanen, V., Bajamundi, C., Kosonen, A., Simell, P., Ahola, J., Frilund, C., Elfving, J., Reinikainen, M., Heikkinen, N., Kauppinen, J., and Piermartini, P. (2018d). Power-to-X technology using renewable electricity and carbon dioxide from ambient air: SOLETAIR proof-of-concept and improved process concept. *Journal of CO2 Utilization*, 28:235–246.

Verhelst, S., Turner, J. W. G., Sileghem, L., and Vancoillie, J. (2019). Methanol as a fuel for internal combustion engines. *Progress in Energy and Combustion Science*, 70(26 May - 1 June 2017):43–88.

Völker, F. (1990). *Ein Verfahren zur Vorhersage des dynamischen Betriebsverhaltens von Schützen mit elektromagnetischem Antrieb*. PhD thesis, University of Duisburg-Essen, Duisburg.

Völker, S., Ackermann, P., Granderath, M., Kortmann, C., Viell, J., Mitsos, A., and von der Assen, N. (2024a). Identifying key environmental objectives for integrated process and fuel design. *Sustainable Energy & Fuels*, 8(9):1966–1982.

Völker, S., Deutz, S., Burre, J., Bongartz, D., Omari, A., Lehrheuer, B., Mitsos, A., Pischinger, S., Bardow, A., and von der Assen, N. (2022). Blend for all or pure for few? Well-to-wheel life cycle assessment of blending electricity-based OME3–5 with fossil diesel. *Sustainable Energy & Fuels*, 6(8):1959–1973.

Völker, S., Groll, N., Bachmann, M., Mueller, L., Neumann, M., Kossioris, T., Muthyala, P., Lehrheuer, B., Hofmeister, M., Vorholt, A., Schmitz, K., Pischinger, S., Leitner, W., and Bardow, A. (2024b). Towards carbon-neutral and clean propulsion in heavy-duty transportation with hydroformylated Fischer–Tropsch fuels. *Nature Energy*, 9(10):1220–1229.

Voll, A. and Marquardt, W. (2012). Reaction network flux analysis: Optimization-based evaluation of reaction pathways for biorenewables processing. *AIChE Journal*, 58(6):1788–1801.

vom Lehn, F., Cai, L., Tripathi, R., Broda, R., and Pitsch, H. (2021). A property database of fuel compounds with emphasis on spark-ignition engine applications. *Applications in Energy and Combustion Science*, 5:100018.

von der Assen, N. and Bardow, A. (2014). Life cycle assessment of polyols for polyurethane production using CO2 as feedstock: insights from an industrial case study. *Green Chemistry*, 16(6):3272–3280.

von der Assen, N., Müller, L. J., Steingrube, A., Voll, P., and Bardow, A. (2016). Selecting CO2 Sources for CO2 Utilization by Environmental-Merit-Order Curves. *Environmental science & technology*, 50(3):1093–1101.

Wang, L., Littlewood, J., and Murphy, R. J. (2013). Environmental sustainability of bioethanol production from wheat straw in the UK. *Renewable and Sustainable Energy Reviews*, 28:715–725.

Wang, L., Wu, W.-T., Chen, T., Chen, Q., and He, M.-Y. (2014). Ion-Exchange Resin–Catalyzed Synthesis of Polyoxymethylene Dimethyl Ethers: A Practical and Environmentally Friendly Way to Diesel Additive. *Chemical Engineering Communications*, 201(5):709–717.

Wang, Q., Huang, R., Ni, J., and Chen, Q. (2021). Potential Improvement in PM-NOX Trade-Off in a Compression Ignition Engine by n-Octanol Addition and Injection Pressure. *Processes*, 9(2):310.

Warmeling, H., Hafki, D., von Söhnen, T., and Vorholt, A. J. (2017a). Kinetic investigation of lean aqueous hydroformylation – An engineer's view on homogeneous catalysis. *Chemical Engineering Journal*, 326:298–307.

Warmeling, H., Janz, D., Peters, M., and Vorholt, A. J. (2017b). Acceleration of lean aqueous hydroformylation in an innovative jet loop reactor concept. *Chemical Engineering Journal*, 330:585–595.

Weidert, J.-O., Burger, J., Renner, M., Blagov, S., and Hasse, H. (2017). Development of an Integrated Reaction–Distillation Process for the Production of Methylal. *Industrial & Engineering Chemistry Research*, 56(2):575–582.

Wernet, G., Bauer, C., Steubing, B., Reinhard, J., Moreno-Ruiz, E., and Weidema, B. (2016). The ecoinvent database version 3 (part I): overview and methodology: [online]. *The International Journal of Life Cycle Assessment*, 21(9):1218–1230.

Westbrook, C. K., Pitz, W. J., and Curran, H. J. (2006). Chemical kinetic modeling study of the effects of oxygenated hydrocarbons on soot emissions from diesel engines. *The journal of physical chemistry. A*, 110(21):6912–6922.

Weyand, J., Habermeyer, F., and Dietrich, R.-U. (2023). Process design analysis of a hybrid power-and-biomass-to-liquid process – An approach combining life cycle and techno-economic assessment. *Fuel*, 342(4):127763.

Wheeler, J., Caballero, J. A., Ruiz-Femenia, R., Guillén-Gosálbez, G., and Mele, F. D. (2017). MINLP-based Analytic Hierarchy Process to simplify multi-objective problems: Application to the design of biofuels supply chains using on field surveys. *Computers & Chemical Engineering*, 102(4):64–80.

Wiese, K.-D. and Obst, D. (2006). Hydroformylation. In Beller, M., editor, *Catalytic Carbonylation Reactions*, volume 18 of *Topics in organometallic chemistry*, pages 1–33. Springer Berlin Heidelberg.

Wouters, C., Burkardt, P., Steeger, F., Fleischmann, M., and Pischinger, S. (2023). Comprehensive assessment of methanol as an alternative fuel for spark-ignition engines. *Fuel*, 340(Part 5):127627.

Wouters, C., Lehrheuer, B., Heuser, B., and Pischinger, S. (2020). Gasoline Blends with Methanol, Ethanol and Butanol. *MTZ worldwide*, 81(3):16–21.

Wu, J., Zhu, H., Wu, Z., Qin, Z., Yan, L., Du, B., Fan, W., and Wang, J. (2015). High Si/Al ratio HZSM-5 zeolite: an efficient catalyst for the synthesis of polyoxymethylene dimethyl ethers from dimethoxymethane and trioxymethylene. *Green Chemistry*, 17(4):2353–2357.

Wu, Q., Wang, M., Hao, Y., Li, H., Zhao, Y., and Jiao, Q. (2014). Synthesis of Polyoxymethylene Dimethyl Ethers Catalyzed by Brønsted Acid Ionic Liquids with Alkanesulfonic Acid Groups. *Industrial & Engineering Chemistry Research*, 53(42):16254–16260.

Wu, Y., Li, Z., and Xia, C. (2016). Silica-Gel-Supported Dual Acidic Ionic Liquids as Efficient Catalysts for the Synthesis of Polyoxymethylene Dimethyl Ethers. *Industrial & Engineering Chemistry Research*, 55(7):1859–1865.

Wu, Y.-p. G., Lin, Y.-f., and Chang, C.-T. (2007). Combustion characteristics of fatty acid methyl esters derived from recycled cooking oil. *Fuel*, 86(17-18):2810–2816.

Wyatt, V. T., Hess, M. A., Dunn, R. O., Foglia, T. A., Haas, M. J., and Marmer, W. N. (2005). Fuel properties and nitrogen oxide emission levels of biodiesel produced from animal fats. *Journal of the American Oil Chemists' Society*, 82(8):585–591.

Xu, D., Gu, X., and Dai, Y. (2023). Concentrating solar assisted biomass-to-fuel conversion through gasification: A review. *Frontiers in Energy Research*, 10.

Ying, W., Genbao, L., Wei, Z., and Longbao, Z. (2008). Study on the application of DME/diesel blends in a diesel engine. *Fuel Processing Technology*, 89(12):1272–1280.

Yunus, N. A., Gernaey, K. V., Woodley, J. M., and Gani, R. (2014). A systematic methodology for design of tailor-made blended products. *Computers & Chemical Engineering*, 66:201–213.

Zang, G., Sun, P., Elgowainy, A., Bafana, A., and Wang, M. (2021a). Life Cycle Analysis of Electrofuels: Fischer–Tropsch Fuel Production from Hydrogen and Corn Ethanol Byproduct CO2. *Environmental Science & Technology*, 55(6):3888–3897.

Zang, G., Sun, P., Elgowainy, A. A., Bafana, A., and Wang, M. (2021b). Performance and cost analysis of liquid fuel production from H2 and CO2 based on the Fischer-Tropsch process. *Journal of CO2 Utilization*, 46:101459.

Zang, G., Sun, P., Yoo, E., Elgowainy, A., Bafana, A., Lee, U., Wang, M., and Supekar, S. (2021c). Synthetic Methanol/Fischer-Tropsch Fuel Production Capacity, Cost, and Carbon Intensity Utilizing CO2 from Industrial and Power Plants in the United States. *Environmental science & technology*, 55(11):7595–7604.

Zhang, L., Kalakul, S., Liu, L., Elbashir, N. O., Du, J., and Gani, R. (2018a). A Computer-Aided Methodology for Mixture-Blend Design. Applications to Tailor-Made Design of Surrogate Fuels. *Industrial & Engineering Chemistry Research*, 57(20):7008–7020.

Zhang, Y., Sahir, A. H., Tan, E. C. D., Talmadge, M. S., Davis, R., Biddy, M. J., and Tao, L. (2018b). Economic and environmental potentials for natural gas to enhance biomass-to-liquid fuels technologies. *Green Chemistry*, 20(23):5358–5373.

Zhou, H., Qian, Y., Kraslawski, A., Yang, Q., and Yang, S. (2017). Life-cycle assessment of alternative liquid fuels production in China. *Energy*, 139:507–522.

Zubel, M., Bhardwaj, O. P., Heuser, B., Holderbaum, B., Doerr, S., and Nuottimäki, J. (2016). Advanced Fuel Formulation Approach using Blends of Paraffinic and

Oxygenated Biofuels: Analysis of Emission Reduction Potential in a High Efficiency Diesel Combustion System. *SAE International Journal of Fuels and Lubricants*, 9(3):481–492.

Zubel, M., Heuser, B., and Pischinger, S. (2017a). 1-Octanol Tailor-made Fuel for Lower Soot Emissions. *MTZ worldwide*, 78(3):58–61.

Zubel, M., Ottenwälder, T., Heuser, B., Herudek, C., Maas, H., and Willems, W. (2019). DME – A Sustainable Fuel Solution for Clean and Closed CO2-Cycle-Mobility for CI Powertrain. In Maus, W., editor, *Zukünftige Kraftstoffe*, ATZ/MTZ-Fachbuch Ser, pages 783–798. Springer Berlin/Heidelberg, Berlin/Heidelberg.

Zubel, M., Ottenwälder, T., Heuser, B., and Pischinger, S. (2021). Combustion system optimization for dimethyl ether using a genetic algorithm. *International Journal of Engine Research*, 22(1):22–38.

Zubel, M., Pischinger, S., and Heuser, B. (2017b). Assessment of the Full Thermodynamic Potential of C8-Oxygenates for Clean Diesel Combustion. *SAE International Journal of Fuels and Lubricants*, 10(3):913–923.

Aachener Beiträge zur Technischen Thermodynamik

ABTT 1
Philip Voll
Automated Optimization-Based Synthesis of Distributed Energy Supply Systems
1. Auflage 2014
ISBN 978-3-86130-474-6

ABTT 2
Johannes Jung
Comparative Life Cycle Assessment of Industrial Multi-Product Processes
1. Auflage 2014
ISBN 978-3-86130-471-5

ABTT 3
Franz Lanzerath
Modellgestützte Entwicklung von Adsorptionswärmepumpen
1. Auflage 2014
ISBN 978-3-86130-472-2

ABTT 4
Thorsten Brands
Einfluss der Gemischzusammensetzung auf die Verbrennung im Diesel- und GCAI-Motor
1. Auflage 2014
ISBN 978-3-95886-006-3

ABTT 5
Dominique Dechambre
Efficient Measurement of Liquid-Liquid Equilibria using Automation and Optimal Experimental Design
1. Auflage 2016
ISBN 978-395886-077-3

ABTT 6
Niklas von der Aßen
From Life-Cycle Assesement towards life-Cycle Design of Carbon Dioxide Capture and Utilization
1. Auflage 2016
ISBN 978-3-95886-080-3

ABTT 7
Matthias Lampe
Integrated Process and Organic Rankine Cycle Working Fluid Design in the Continuous-Molecular Targeting Framework
1. Auflage 2016
ISBN 978-3-95886-086-5

ABTT 8
Thomas Hülser
Optische Untersuchung der Zündvorgänge und deren Auswirkung auf die Verbrennung in PKW-Motoren
1. Auflage 2016
ISBN 978-3-95886-090-2

Aachener Beiträge zur Technischen Thermodynamik

ABTT 16
Bastian Liebergesell
A Milliliter-Scale Setup for the Efficient Characterization of Multicomponent Vapor-Liquid Equilibria Using Raman Spectroscopy
1. Auflage 2018
ISBN 978-3-95886-247-0

ABTT 17
Stefan Wilhelm Graf
A Design Approach for Adsorption Energy Systems Integrating Dynamic Modeling with Small-Scale Experiments
1. Auflage 2018
ISBN 978-3-95886-258-6

ABTT 18
Sebastian Kaminski
Quantum-Mechanics-Based Prediction of SAFT Parameters for Non-Associating and Associating Molecules Containing Carbon, Hydrogen, Oxygen and Nitrogen
1. Auflage 2019
ISBN 978-3-95886-270-8

ABTT 19
Maike Renate Hennen
Decision Support for the Synthesis of Energy Systems by Analysis of the Near-Optimal Solution Space
1. Auflage 2019
ISBN 978-3-95886-277-7

ABTT 20
Peyman Yamin
COSMO-RS-Based Methods for Improved Modelling of Complex Chemical Systems
1. Auflage 2019
ISBN 978-3-95886-288-3

ABTT 21
Meltem Erdogan
Assessement of Adsorbents for Drying by Experiments and Dynamic Simulations
1. Auflage 2019
ISBN 978-3-95886-303-3

ABTT 22
Christian Schulz
SRS/LIF-Messungen zur Charakterisierung rußarmer dieselähnlicher Flammen von alternativen Kraftstoffen und n-Heptan
1. Auflage 2019
ISBN 978-3-91886-310-1

ABTT 23
Peter Beumers
Physically-Based Models for the Analysis of Raman Spectra
1. Auflage 2019
ISBN 978-3-95886-319-4

Aachener Beiträge zur Technischen Thermodynamik

ABTT 24
Arne Kätelhön
Technology Choice Model for Consequential Life Cycle Assessment
1. Auflage 2019
ISBN 978-3-95886-324-8

ABTT 25
Christine Peters
Measurement of Multicomponent Diffusion in Liquids Using Raman Microspectroscopy and Microfluidics
1. Auflage 2020
ISBN 978-3-95886-337-8

ABTT 26
Dinah Elena Hollermann
Reliable and Robust Optimal Design of Sustainable Energy Systems
1. Auflage 2020
ISBN 978-3-95886-346-0

ABTT 27
Thomas Raffius
Laserspektroskopische Analyse von selbstzündenden motorischen Einspritzstrahlen alternativer Biokraftstoffe
1. Auflage 2020
ISBN 978-3-95886-358-3

ABTT 28
Johannes Schilling
Integrated Thermo-Economic Design of Processes and Molecules Using PC-SAFT
1. Auflage 2020
ISBN 978-3-95886-368-2

ABTT 29
Nils Julius Baumgärtner
Optimization of Low-Carbon Energy Systems from Industrial to National Scale
1. Auflage 2020
ISBN 978-3-95886-385-9

ABTT 30
Ludger Wolff
From Model-based Experimental Design and Analysis of Diffusion and Liquid-Liquid Equilibria to Process Applications
1. Auflage 2020
ISBN 978-3-95886-402-3

ABTT 31
Andrej Gibelhaus
A Model-based Framework for Optimal Systems Integration of Adsorption Chillers
1. Auflage 2021
ISBN 978-3-95886-406-1

ABTT 32
Jan Seiler
Debottlenecking the Evaporator in Water-Based Adsorption Chillers
1. Auflage 2021
ISBN 978-3-95886-407-8

Aachener Beiträge zur Technischen Thermodynamik

ABTT 33
Leif Kröger
Prediction of Reaction Rate Constants for the Synthesis of Microgels
1. Auflage 2021
ISBN 978-395886-425-2

ABTT 34
Sarah von Pfingsten
Uncertainty Analysis in Matrix-Based Life Cycle Assessment
1. Auflage 2022
ISBN 978-3-95886-431-3

ABTT 35
Ludger Leenders
Optimization Methods for Integrating Energy and Production Systems
1. Auflage 20022
ISBN 978-3-95886-445-0

ABTT 36
Leonard Müller
Harmonized Life Cycle Assessment of Technologies for Carbon Capture and Utilization
1. Auflage 2022
ISBN 978-3-95886-434-4

ABTT 37
Fritz Röben
Decarbonization of Copper Production by Optimal Demand Response
and Power-to-Hydrogen
1. Auflage 2022
ISBN 978-3-95886-458-0

ABTT 38
Johanna Kleinekorte
Predictive Life Cycle Assessment for Chemical Processes using Machine Learing
1. Auflage 2022
ISBN 978-3-95886-461-0

ABTT 39
Raoul Meys
Designing Pathways for Net-Zero Greenhouse Gas Emission Plastics with Life Cycle Optimization
1. Auflage 2022
ISBN 978-3-95886-463-4

ABTT 40
Lukas Krep
Novel Acceleration Methods and Improved Transition State Finding Approaches for the Automatic Exploration of Reaction Networks
1. Auflage 2023
ISBN 978-3-95886-480-1

ABTT 41
Andreas Kämper
Data-driven Modeling and Optimization of Multi-Energy Systems
1. Auflage 2023
ISBN 978-3-95886-488-7

Aachener Beiträge zur Technischen Thermodynamik

ABTT 42
Chriatiane Reinert
Optimization and Life-Cycle Assessment of Low-Carbon Energy systems from Industrial to International Scale
1. Auflage 2023
ISBN 978-3-95886-498-6

ABTT 43
Sarah Deutz
Life-Cycle Assessment of Low-Carbon Technologies from Screening to Integrated Energy system Design
1. Auflage 2023
ISBN 978-3-95886-499-6

ABTT 44
Hesam Ostovari
From Life Cycle Assessment to Optimal Supply Chains of CO2 Mineralization
1. Auflage 2023
ISBN 978-3-95886-509-9

ABTT 45
Justus Wöhl
Extension of Indirect Hard Modeling for the User-Independent and Automated Spectral Analysis of Reactive and Interacting Mixtures
1. Auflage 2023
ISBN 978-3-95886-511-2

ABTT 46
Carsten Flake
Automated Measurement Modeling and Interpretation of Diffusion Coefficients in Aqueous Multicomponent Mixtures
1. Auflage 2024
ISBN 978-95886-516-7

ABTT 47
Raphael Dewor
Laseroptische Untersuchungen von Verbrennungsprozessen bio-hybrider Kraftstoffe
1. Auflage 2024
ISBN 978-3-95886-522-8

ABTT 48
Christian Zibunas
Life Cycle Optimization towards Environmentally and Economically Sustainable Chemicals and Plastics
1. Auflage 2024
ISBN 978-3-95886-525-9

ABTT 49
Christoph Gertig
Computer-Aided Design of Molecules and Reactive Chemical Processes based on Quantum Chemistry
1. Auflage 2024
ISBN 978-95886-528-0

Aachener Beiträge zur Technischen Thermodynamik

ABTT 50
Marvin Bachmann
From Life Cycle Assessment to Absolute Environment Sustainability of Plastics from Alternative Carbon Feedstocks
1. Auflage 2024
ISBN 978-3-95886-530-3

ABTT 51
Mirko Engelpracht
Experimental Demonstration and Model-Based Optimization of Adsorption Heat Transformation for Waste Heat Upgrading
1. Auflage 2024
ISBN 978-3-95886-533-4

ABTT 52
David Müller
In-Line Monitoring and Control of Bioprocesses Using Raman Spectroscopy and Indirect Hard Modeling
1. Auflage 2024
ISBN 978-3-95886-537-2

ABTT 53
Matthias Henninger
Optimal Design of Small-Scale Experiments for Model-Based Scale-Up of Adsorption Chillers
1. Auflage 2024
ISBN 978-95886-539-6

ABTT 54
Julia Thien
A Microfluidic Platform for the Efficient Determination of Liquid-Liquid Equilibria Using Raman Microspectroscopy
1. Auflage 2025
ISBN 978-3-95886-542-6

ABTT 55
Simon Völker
Multi-Scale Life Cycle Design of Synthetic Fuels for Sustainable Mobility
1. Auflage 2025
ISBN 978-3-95886-544-0

Aachener Beiträge zur Technischen Thermodynamik